Experimental investigations of flame-cooling air interaction in an effusion cooled pressurized single sector model gas turbine combustor

Vom Fachbereich Maschinenbau
der Technischen Universität Darmstadt

zur Erlangung des Grades eines
Doktors der Ingenieurwissenschaften (Dr.-Ing.)
genehmigte

Dissertation

von

Max Jakob Karl Greifenstein, M.Sc.

aus Dieburg

Berichterstatter:	Prof. Dr. rer. nat. A. Dreizler
Mitberichterstatterin:	Prof. S. Hochgreb, PhD
Tag der Einreichung:	25.01.2021
Tag der mündlichen Prüfung:	27.04.2021

Darmstadt 2021

Zwei Dinge sind zu unserer Arbeit nötig:
Unermüdliche Ausdauer und die Bereitschaft, etwas,
in das man viel Zeit und Arbeit gesteckt hat, wieder wegzuwerfen.

Albert Einstein

Danksagung

Mit dem Abschluss des Verfassens dieser Dissertationsschrift neigt sich meine Zeit als Doktorand am Fachgebiet Reaktive Strömungen und Messtechnik ihrem Ende zu. Inklusive der Bachelor- und Masterarbeit blicke ich auf 10 Jahre vielfältiger Erfahrungen am Fachgebiet zurück. Obwohl die Messkampagnen für diese Dissertation weitestgehend in Eigenregie durchgeführt wurden, wäre all das ohne die Unterstützung einer Vielzahl von Personen nicht möglich gewesen.

Zunächst möchte ich meinem Doktorvater Prof. Dr. Andreas Dreizler danken. Ohne Dich, lieber Andreas, als mein Dienstvorgesetzter und Mentor, wäre ich bei Weitem nicht an dem Punkt, an dem ich mich jetzt befinde. Ich danke Dir für das über all die Jahre entgegengebrachte Vertrauen, die Ermöglichung der Promotion und deine uneingeschränkte Unterstützung aller meiner Vorhaben im Labor und die Freiheiten, die ich am Fachgebiet genießen durfte.

Weiterhin möchte ich mich bei Prof. Dr. Simone Hochgreb für die Übernahme des Koreferats bedanken. Dass Sie diese Aufgabe übernehmen, trotz der ohnehin schon hohen Arbeitsbelastung im Rahmen Ihrer Tätigkeit als Leiterin der Arbeitsgruppe für *Reacting Flows* an der University of Cambridge, weiß ich sehr zu schätzen.

Meinen derzeitigen und ehemaligen Kolleginnen und Kollegen am Fachgebiet möchte ich für die fachliche und moralische Unterstützung danken, die für den erfolgreichen Abschluss der Dissertation unerlässlich war. Besonders hervorheben möchte ich an dieser Stelle Dr. Jens Hermann, meinen Vorgänger am Druckbrennkammerprüfstand und Mitbetreuer meiner Bachelorarbeit. Gerne erinnere ich mich an zwei intensive gemeinsame Jahre im Labor, in denen ich sehr viel von Deinen Erfahrungen lernen konnte. Für zahlreiche Diskussionen und Erfahrungsaustausch möchte ich Florian Zentgraf, Johannes Emmert, Dr. Johannes Weinkauff, Dr. Carl-Philipp Ding, Christopher Geschwindner, Marius Schmidt, Dr. Jhon Pareja Restrepo und Dr. Hidemasa Kosaka danken. Pascal Johe danke ich für die Bereitschaft, mich an diesem Prüfstand mit all seinen Schönheiten und Fehlern zu beerben. Ich bin froh, die Anlage in guten Händen zu wissen und ich wünsche Dir viel Erfolg in den kommenden Jahren. Auch außerhalb des Fachgebietes habe ich fachliche Unterstützung erfahren. Dr. Johannes Heinze vom Institut für Antriebstechnik am Deutschen Zentrum für Luft- und Raumfahrt möchte ich besonders erwähnen. In zwei gemeinsamen Messkampagnen im Rahmen des CORNET Projektes und zahlreichen, teils stundenlangen Telefonaten konnte ich viel von Dir, lieber Johannes, lernen. Dafür danke ich Dir.

Für den Betrieb und die Wartung eines solchen Prüfstandes, ist die Bedeutung einer guten und zuverlässigen Werkstatt nicht zu unterschätzen. Ich möchte mich an dieser Stelle herzlich für die stets freundliche und unkomplizierte Bearbeitung aller meiner Anliegen, wie kurzfristig sie auch umzusetzen waren, bei Roland Berntheisel und seinem Team, insbesondere Dirk Feldmann, Mathias Felter und Sebastian Feuerbach, bedanken. Weiterhin möchte ich Andreas Ludwig danken, der mir als Ansprechpartner für alle infrastrukturellen Fragen und seiner langjährigen Erfahrung eine große Hilfe für meine Zeit im Labor war.

Meinen Eltern Hans und Karin Greifenstein möchte ich für die Unterstützung während der letzten 33 Jahre danken. Ihr habt mir nicht nur das Studium ermöglicht, sondern mich auch stets auf meinem Lebensweg begleitet und mich jederzeit darin bestärkt, meinen Weg zu finden und zu beschreiten. Abschließend gilt mein größter Dank meiner Frau Miriam Fleischhacker. Ohne Dich, liebe Miriam, wäre das alles nicht gegangen. Deine unendliche Geduld mit mir und dem Prüfstand, dessen Unwägbarkeiten so oft unser gemeinsames Leben mitbestimmt haben, waren unverzichtbar. Du bist mit mir durch die hohen Höhen und tiefen Tiefen dieser Zeit gegangen, du hast den teils großen Druck, den diese Arbeit mit sich gebracht hat, gemeinsam mit mir ausgehalten. Dafür und für so viel Weiteres, bin ich Dir von Herzen dankbar.

Darmstadt, Dezember 2020 Max Greifenstein

Abstract

Within this thesis, the mutual interaction between the flame and cooling air within an effusion cooled single sector model gas turbine combustor is investigated at elevated pressure. Although effusion cooling has been widely studied in the last decades with respect to heat transfer and total film cooling effectiveness, fundamental aspects of the interaction mechanisms with the reacting main flow are not yet well understood.

Typically, experimental investigations are conducted either by reducing the complexity by placing an effusion cooling plate in a test section downstream of a hot gas source, which allows a good experimental accessibility and well controlled boundary conditions, or by reducing the complexity on the diagnostics side, e.g. by using sampling probe measurements at the exhaust of a close-to-reality test rig. The first approach does not facilitate investigations of the interaction mechanisms between the reacting main flow and effusion cooling air, as they are spatially separated. The second approach on the other hand includes all mechanisms, but measurements are not conducted spatially resolved within the test section. Within this work, an effusion cooling plate is mounted within a generic test rig which features a swirl-stabilized turbulent flame at elevated inlet temperature and pressure to fully capture the influence of unsteady heat release, convection, radiation and chemical reactions in the vicinity of the liner.

Quantitative and semi-quantitative advanced laser diagnostics with high temporal and spatial resolution are employed to identify sensitivities of flame-cooling air interaction with respect to important boundary conditions that affect the flow and temperature field and cooling performance. Mixing between the reacting main flow and effusion cooling air is investigated by a combination of quantitative planar laser-induced fluorescence of the hydroxyl radical (OH) and nitric oxide, seeded to the effusion cooling air. This data allows to identify the relative occurrence of mixing processes before, during and after reaction. Furthermore, measurements of the thermochemical state, as represented by the carbon monoxide (CO) mole fraction and the gas phase temperature, were conducted using combined quantitative CO laser induced fluorescence (LIF) and ro-vibrational coherent anti-Stokes Raman spectroscopy with nitrogen as a resonant species. Simultaneous LIF measurements of OH, CO and formaldehyde (CH_2O) were executed to investigate the sensitivity of CO production and oxidation near reaction zones to the boundary conditions.

The acquired data shows that interaction processes between the flame and cooling air locally influence the structure of the premixed flame across the preheating zone, main reaction zone and the exhaust. Spatially, these interaction processes are not limited to the area close to the effusion cooled liner but extend into the primary zone by recirculation.

Kurzfassung

Im Rahmen der vorliegenden Arbeit wird die gegenseitige Beeinflussung von Flamme und Kühlluft in einem effusionsgekühlten Eindüsensektor-Brennkammerprüfstand unter erhöhtem Druck untersucht. Obwohl Effusionskühlung in den vergangenen Jahrzehnten hinsichtlich Wandwärmeübergängen und totaler Filmkühleffektivität intensiv untersucht wurde, sind fundamentelle Aspekte der Interaktionsmechanismen der Kühlluft mit der reagierenden Hauptströmung noch weitgehend unverstanden.

Typischerweise werden experimentelle Untersuchungen bei reduzierter Komplexität im Vergleich zu realen Anlagen durchgeführt. Entweder wird eine Effusionskühlplatte stromab einer Heißgasquelle platziert, was eine gute experimentelle Zugänglichkeit und eine hohe Reproduzierbarkeit der Randbedingungen erwirkt. Interaktionsmechanismen zwischen Kühlluft und reagierender Hauptströmungen können in diesen Konfigurationen konzeptbedingt nicht untersucht werden. Alternative Ansätze reduzieren die Komplexität auf messtechnischer Seite, z.B. indem Abgasuntersuchungen an realitätsnahen Anlagen durchgeführt werden. Bei diesen Ansätzen sind Rückschlüsse auf die zugrundeliegenden Mechanismen nicht möglich, da Messungen weder räumlich noch zeitlich aufgelöst innerhalb der Brennkammer erfolgen. In dieser Arbeit wird eine Effusionskühlplatte als Wandsegment in einem generischen Verbrennungsprüfstand eingesetzt, welcher sich durch eine Drall-stabilisierte turbulente Flamme bei erhöhter Einlasstemperatur und erhöhtem Druck auszeichnet. Hierduch werden Einflüsse durch instationäre Wärmefreisetzung, Konvektion und Strahlung sowie chemische Reaktionen vollständig abgebildet.

Quantitative und semi-quantitative Laser-basierte Messtechniken mit hoher räumlicher und zeitlicher Auflösung werden eingesetzt, um eine Sensitivität der zu untersuchenden Flamme-Kühlluft Interaktion hinsichtlich wichtiger Randbedingungen zu identifizieren, die das Strömungs- und Temperaturfeld sowie die Kühlung an sich betreffen. Mischungsprozesse zwischen der reagierenden Hauptströmung und der Effusionskühlluft werden mit Hilfe einer Kombination aus quantitativer Laser induzierter Fluoreszenz des Hydroxyl Radikals (OH) und Stickstoffmonoxid, mit welchem die Kühlluft dotiert wird, untersucht. Die erhobenen Daten lassen Rückschlüsse darauf zu, wie häufig eine Mischung der Stoffströme vor, während oder nach dem chemischen Umsatz des Brennstoffs vorliegt. Messungen des thermochemischen Zustandes, representiert durch den lokalen Kohlenstoffmonoxid (CO) Molenbruch und die Temperatur der Gasphase, werden mittels Kombination von CO Laser induzierter Fluoreszenz (LIF) und rotations-vibrations kohärenter anti-Stokes Raman Spektroskopie mit Stickstoff als resonanter Spezies durchgeführt. Simultane Messungen von OH-, CO- und Formaldehyd-LIF erlauben die Untersuchung von Sensitivitäten auf den CO Produktions- und Oxidationsablauf in Bezug auf die untersuchten parametrischen Variationen der Randbedingungen.

Die gewonnenen Daten zeigen, dass Interaktionen zwischen der Flamme und der Effusionskühlluft lokal die Struktur der Vormischflamme innerhalb der Vorwärmzone, der Hauptreaktionszone und im Abgas beeinflussen. Räumlich sind diese Beeinflussungen nicht nur auf den Bereich nahe der effusionsgekühlten Wand beschränkt, sondern erstrecken sich durch Rezirkulation bis in die Primärzone.

Contents

List of Tables

List of Figures

Nomenclature

Lower-case Latin letters		Unit
$b_{J'J''}$	Placzek-Teller coefficients	-
c_p	Heat capacity at constant pressure	$\mathrm{J\,kg^{-1}\,K}$
f	Boltzmann fraction	-
g	Laser line overlap integral	$\mathrm{cm^{-1}}$
h	Specific enthalpy	$\mathrm{J\,kg^{-1}}$
k	CH_2O-LIF temperature correction factor	-
k	Reaction rate constant	-
k	Wave vector	$\mathrm{cm^{-1}}$
k_{ij}	Absorption coefficient of transition ij	$\mathrm{cm^{-1}}$
l	Characteristic length	m
m	Mass	kg
n	Line width multiplier	-
p	Pressure	$\mathrm{N\,m^{-2}}$
u	Velocity	$\mathrm{m\,s^{-1}}$
v	Vibrational quantum number	-
x,y,z	Spatial coordinates	m

Upper-case Latin letters		Unit
$\tilde{I}$	Photon flux	$\mathrm{s^{-1}}$
A	Line-of-sight integrated absorption	-
A	Pre-exponential factor	-
A_{ij}	Einstein A-coefficient for transition ij	$\mathrm{s^{-1}}$
B_{ij}	Einstein B-coefficient for transition ij	$\mathrm{m^3\,J^{-1}\,s^{-2}}$
C_i	Image-side contrast	-
C_o	Object-side contrast	-
D	Diffusion coefficient	$\mathrm{m^2\,s^{-1}}$
D_i	Degeneracy of initial state i	-
E	Energy reference	-
E_a	Activation energy	J
F	Rotational energy levels	$\mathrm{cm^{-1}}$

$F_{\alpha,\gamma}$	Hermann-Wallis Factors	-
G	Vibrational energy levels	cm^{-1}
$G^{(2)}$	Second-order intensity correlation factor	-
G_i	Apparatus function for CARS measurements	cm^{-1}
I	Momentum ratio	-
I_L	Laser intensity	$\mathrm{GW\,cm}^{-2}$
J	Rotational quantum number	-
L	Absorption path length	cm
M	Blowing ratio	-
M_k	Molar mass of species k	$\mathrm{g\,mol}^{-1}$
N_k	Number density of species k	cm^{-3}
Q	Quenching rate	s^{-1}
$Q_{e,v,r}$	Electronic, vibrational and rotational partition function	-
R	Density ratio	-
R	Residual	-
R_i	Photoionization rate	s^{-1}
Re	Reynolds number	-
RR	Normalized reaction rate	-
S	Swirl number	-
S_k	Simulated LIF intensity of species k	s^{-1}
$S_{J'J''}$	Hönl-London-Factors	-
SR	Staging ratio	-
T	Temperature	K
T_ν	Fractional transmission at frequency ν	-
T_m	Fractional transmission at pixel m	-
X_k	Mole fraction of species k	-
Y_k	Mass fraction of species k	-

Lower-case Greek letters		**Unit**
$\chi^{(3)}$	Third order susceptibility	$\mathrm{cm}^3\,\mathrm{erg}^{-1}\,\mathrm{amagat}^{-1}$
δ_F	Flame front thickness	m
δ_{ij}	Kronecker symbol	-
$\dot{\omega}_k$	Source term of species k	$\mathrm{kg\,m}^{-3}\,\mathrm{s}^{-1}$
$\epsilon_{N,T}$	Relative uncertainty for OH number density and temperature	-
η	Fluorescence quantum yield	-
$\hat{\sigma}^{(2)}$	Two-photon absorption cross-section	cm^4
ν	Kinematic viscosity	-
ν_L	Laser center frequency	-
ν_{ij}	Center frequency of transition ij	cm^{-1}

ω	Angular frequency	s^{-1}
ρ	Density	$\mathrm{kg\,m}^{-3}$
$\sigma_i^{J'}$	Ionization cross-section	cm^2
$\sigma_{Q,i}$	Quenching cross-section for collision with species i	cm^2
τ_{ij}	Stress tensor	$\mathrm{kg\,m}^{-2}\,\mathrm{s}^{-1}$
ξ	LIF detection efficiency	-

Upper-case Greek letters **Unit**

$\Delta\nu_L$	Laser line width	cm^{-1}
$\Delta\sigma_C$	Collisional broadening	cm^{-1}
$\Delta\sigma_D$	Doppler broadening	cm^{-1}
$\Delta\sigma_S$	Collisional shift	cm^{-1}
Δ_q	Differential Boltzmann fraction for transition q	-
Γ_q	Line width of transition q	cm^{-1}
Φ	Equivalence ratio	-
Φ_{ij}	Normalized line shape of transition ij	-
Φ_L	Normalized laser line shape	-

Indices

$'$	Excited state
$''$	Ground state
ad	Adiabatic
h, c	Hot and cold side of effusion cooled liner
i,j,k	Integer index
ij	Transition $j \leftarrow i$
ref	Reference
u	Unburnt

Operators and Mathematical symbols

$*$	Convolution
$\Im$	Imaginary part of complex number
H	Heaviside function
$\Re$	Real part of complex number
$\star$	Cross-correlation

Physical constants		**Value**
c	Speed of light	$299\,792\,458\,\mathrm{m\,s^{-1}}$
h	Planck's constant	$6.626 \times 10^{-34}\,\mathrm{J\,s}$
k_B	Boltzmann's constant	$1.3806 \times 10^{-23}\,\mathrm{J\,K^{-1}}$
R	Ideal gas constant	$8.3145\,\mathrm{J\,mol^{-1}\,K}$

Abbreviations

CARS	Coherent anti-Stokes Raman spectroscopy
CCD	Charge Coupled Device
CMOS	Complementary Metal–Oxide–Semiconductor
CTF	Contrast Transfer Function
FCAI	Flame-Cooling Air Interaction
FOV	Field of View
FWHM	Full-width Half Maximum
HR	High Resolution
HRR	Heat Release Rate
IRZ	Inner Recirculation Zone
ISL	Inner Shear Layer
LDV	Laser Doppler Velocimetry
LIF	Laser Induced Fluorescence
LR	Low Resolution
MFC	Mass Flow Controller
MI-GA	Mixed Integer Genetic Algorithm
MTF	Modulation Transfer Function
OPO	Optical Parametric Oscillator
ORZ	Outer Recirculation Zone
OSL	Outer Shear Layer
PAH	Polycyclic Aromatic Hydrocarbons
PIV	Particle Image Velocimetry
PLIF	Planar Laser Induced Fluorescence
PMT	Photomultiplier Tube
PSF	Point Spread Function
RET	Rotational Energy Transfer
ROI	Region of Interest
RR	Reaction Rate

RSM	Reaktive Strömungen und Messtechnik
SNR	Signal-to-Noise Ratio
SSC	Single Sector Combustor
TBC	Thermal Barrier Coating
VET	Vibrational Energy Transfer
VUV	Vacuum Ultra Violet
YAG	Yttrium Aluminium Garnet
YASSES	Yet Another Siemens Star Evaluation Script

Chapter 1

Introduction

Although the COVID-19 pandemic, which has shocked the societies and economies across the globe since the beginning of 2020, has led to a drastic reduction in passenger air traffic, it is assumed that the aviation sector will recover on its original track in the years ahead. The German Aerospace Center (Deutsches Zentrum für Luft- und Raumfahrt; DLR) forecasted a rise in passenger number from 4 Billion per year in 2016 to more than 9.4 Billion per year in 2040, or equivalently, 3.7% annually [43]. Quite obviously, this has severe environmental ramifications. Consequently, future development of aero engine propulsion systems is strongly influenced by reaching stringent emission goals to make a step towards more sustainable aviation. Although most companies with a major market share for civil aero engines, such as Airbus [3], Rolls-Royce [131], Safran [136] and GE [88], have visions for electric propulsion systems, there are numerous technological challenges that are yet to be overcome. While the power density of modern electrical propulsion systems compares well with their combustion counterpart, the energy storage density poses significant issues. In 2019, Rolls-Royce started the project *Accelerating the Electrification of Flight* (ACCEL) with the goal to set a new record with a target speed of $480\,\mathrm{km\,h^{-1}}$, previously set by Siemens with their Extra 330LE which reached a top speed of approximately $342\,\mathrm{km\,h^{-1}}$ in 2017 [67]. This goal is to be reached using an electrical propulsion system with 750 kW peak power, supplied from 6000 battery cells, enough to fly 200 nautical miles or supply 250 homes with electricity [131]. Comparing these numbers to an Airbus A340-300, which flies 295 passengers across 6700 nautical miles with a top speed of approximately $900\,\mathrm{km\,h^{-1}}$, demonstrates - keeping in mind that the aforementioned electric planes feature only *one* seat - how dramatic the difference in technology readiness level is.

Even though electrification may begin to play a role in aviation in the years ahead, especially in smaller vessels, it remains a long-term perspective. Short- and mid-term, traditional combustion propulsion systems need considerable attention and development to improve their emission performance in terms of green house gas emissions as well as pollutants and noise. Flightpath 2050 demands to reduce emissions of CO_2 by 75%, nitric oxides (NOx) by 90% and perceived noise by 65% per passenger kilometer relative to a typical aircraft in 2020 [40]. Assuming a high degree of burnout, CO_2 emissions are directly linked to the total cycle efficiency which may be increased with higher overall pressure ratios or by minimizing losses within the engine e.g. due to excessive cooling. A reduction of NOx emissions to this extent is impossible with traditional Rich-Quench-Lean (RQL)

combustors due to the high peak temperatures in the primary zone which result in a high thermal NOx formation due to the Zeldovich mechanism [169]. A promising approach is the development of lean combustion concepts in order to lower the global temperature level which consequently reduces NOx formation. However, as more compressed air is supplied via the injector, an increased demand for efficient cooling techniques is evident as less air is available [14, 101, 139]. This is further aggravated by increased compressor outlet temperatures at higher overall pressure ratios for improved cycle efficiency. Additionally, reduced temperature in the combustion chamber may have an adverse effect on CO emission performance [96]. One possible approach for efficient liner cooling is the concept of *effusion cooling*, where air is supplied via a perforated plate featuring an array of slanted holes with diameters typically in the sub-millimeter range. The focus of this work is the investigation of the mutual interaction between the flame and cooling air within the combustion chamber itself. The following section summarizes the current state of research on this topic from which the aim and structure of this thesis is derived.

1.1 Current State of Research

This section summarizes the current state of research concerning experimental studies of effusion cooling for gas turbine combustors.[1] The gas-phase temperatures occurring in the combustor core of an aeroengine by far exceed the allowed operating limits of metallic materials used for combustor liner design [100]. For this reason, combustor liner cooling has been subject to scientific research for over 60 years. Due to the limited experimental and numerical accessibility of real geometries, investigations are typically conducted in generic configurations to gain insight on the underlying phenomena. Behrendt and Hassa classify test rigs used for cooling related states in three categories based on their complexity and the closeness to a real combustor [14].

Rigs of the first category are characterized by non-reactive flows at ambient pressure with a comparably small temperature difference between main and cooling flow. The low level of complexity allows an excellent experimental and numerical accessibility with reduced uncertainties arising from well-controllable boundary conditions. By keeping the governing similarity parameters, such as blowing ratio, as well as the Reynolds, Nusselt and Biot numbers comparable to a real combustor, the findings are considered representative and may be used for improved liner design. Due to the limited availability of experimental methods, most of the early publications in the second half of the 20th century fall into this category, such as publications by Weighardt in 1946 [164] and Goldstein et al. [62], Metzger et al. [116] and Le Brocq et al. [102] in the early 1970s, in which the influence of blowing ratio, momentum ratio and the way cooling air is supplied to the test section on the total film cooling effectiveness was investigated. Starting in the late 1990s, Gritsch et al. investigated the influence of cooling air inflow and hole geometry on the wall heat flux within the holes in wind tunnel experiments [65, 66, 154].

[1] This literature survey is taken in part from previous publications with permission from the respective journals [E4, E5, E8, E9].

Test rigs of the second category are similar in nature, but approach more realistic temperature levels and associated density ratios for the main flow by using either an electrically heated main flow or the exhaust of a flame located upstream of the test section. Within this category, the vast majority of publications, such as by Leger [105], Behrendt [14] and Huang [87], investigate the dependence of total film cooling effectiveness on various parameters, such as blowing ratios, momentum ratios or hole pattern and geometry. Jackowski et al. published investigations on adiabatic effectiveness with innovative bent cooling holes, manufactured by direct metal laser sintering [89]. Investigations presented by Wurm et al. [166, 167] and the group around Andreini [7, 9] include swirling flows, albeit under non-reacting conditions. In some of the studies, advanced laser diagnostics to provide a high spatial and temporal resolution, are used in conjunction with more traditional techniques such as exhaust sampling probes, thermocouples, infrared thermography and temperature sensitive paints. One prominent example is a study bei Schreivogel et al., who conducted thermographic particle image velocimetry measurements of the flow emerging from a single effusion hole in a heated wind tunnel [138]. Compared to test rigs of the first category, the more realistic temperature and flow fields lead to a better comparability to a real configuration. However, interaction between flame and cooling air as well as the influence of unsteady heat release is not accounted for.

Within test rigs of the third category, an effusion cooled plate is used as a liner inside a pressurized combustor in the vicinity of a swirl-stabilized flame to capture the full complexity by unsteady heat release from turbulent combustion, convection, mixing and radiation in realistic flow and temperature fields. As the experimental and numerical complexity is drastically increased, the literature on this topic is yet very sparse. Wall temperature measurements in a category three test rig using thermographic phosphor thermometry were demonstrated by Feist et al. [56]. Combined measurements of flow field and hydroxyl (OH) distributions by means of particle image velocimetry (PIV) and planar laser induced fluorescence (PLIF) were conducted by Lange et al. [101]. In their publication, the importance of high spatial and temporal resolution was highlighted as they encountered a strong intermittency in the observed phenomena such as local rupture of the cooling air film. Unfortunately, no parametric variations were reported within their study, such that sensitivities of observed phenomena with respect to boundary conditions are unclear. Ji et al. demonstrated measurements of wall temperature in an atmospheric combustor by means of infrared thermography with varying equivalence ratios. A significantly lower total film cooling effectiveness, also reported by Andreini [8], was encountered in the area where the flame impinges on the effusion cooled liner, highlighting the importance of investigations in test rigs of the third category. Färber et al. investigated the stability limits of an atmospheric swirl-stabilized flame in the presence of cooling air and impingement cooling [55] by means of Laser Doppler Velocimetry (LDV). Quantitative CO emissions using exhaust sampling probes under varying mass flows through discrete cooling holes in the liner were performed by Smith et al. [149] and Andrews et al. [10]. While both observed an increase in CO mole fraction at the exhaust with increasing amounts of cooling air, they proposed quite different explanations for the cause. While Smith et al. suspected that injection of compressor discharge air causes increased CO emissions due to chemical quenching, Andrews et al. argued, that this change is simply explained by the fact that more air flow through the liner results in less air flow through

the fuel injector, consequently increasing the equivalence ratio which leads to increased CO concentrations. Within their test rigs, it was impossible to separately condition the air flows through the injector and the cooling holes, such that both arguments seem plausible. As only measurements in the exhaust - as opposed to spatially and temporally resolved measurements *within* the test section - are presented, this conflict of statements cannot be resolved. First demonstrations of quantitative CO concentration measurements by means of CO-LIF in an effusion cooled single sector gas turbine combustor were reported by Voigt et al. [158, 159]. However, as their publication is at its core only a demonstration of the applicability of the method, only results far from the effusion cooled liner were reported and no systematic variation of boundary conditions was conducted. Consequently, no information on the interaction mechanisms between main flow and cooling air can be extracted. Extensive studies were conducted by Hermann [84] [E8, E9]. In a single sector model gas turbine combustor, which has also been used for the investigations presented in this thesis, parametric variations of swirl number, effusion cooling air mass flow and fuel staging were conducted. Non-reacting and reacting flow fields were measured using PIV. Additionally, qualitative OH-PLIF measurements were conducted to visualize the instantaneous location of the flame brush. Wall- and gas-phase temperatures were measured using thermographic phosphor thermometry and ro-vibrational coherent anti-Stokes Raman spectroscopy (CARS) using N_2 as resonant species. From the acquired data, the dependence of the total film cooling effectiveness on swirl, staging and effusion cooling air mass flow was derived. As all measurements were conducted in separate experiments, findings may only be combined using statistical approaches.

Summarizing the current state of research, most effusion cooling related studies in gas turbine combustors are conducted with a focus on wall heat transfer and film cooling effectiveness in test rigs with significant reduction of complexity. Studies that include the full complexity under reacting conditions are sparse, consequently, interaction mechanisms between flame and cooling air are yet not well understood. Against the background of stringent goals on lowering pollutant emissions in aviation and at the same time predicted rising passenger numbers and freight volumes, the urgent need for intensive research and development in this sector becomes apparent.

1.2 Aim and Structure of this Work

The current state of research on combustor cooling does not yet include the influence of relevant boundary conditions on the local thermochemical state, important reaction rates and pollutant formation. This work provides experimental investigations using advanced laser diagnostics in a category three test rig to help filling this research gap. The experiments carried out are intended, on the one hand, to deepen the understanding of the underlying processes and, on the other hand, to provide urgently needed validation data for the development of numerical models that are essential for the design of future gas turbine combustors. The aim of this thesis is to test the validity of the following working hypotheses, which result from the summary of the current state of research:

1. The interaction of effusion cooling air and main flow locally influences the structure of premixed flames across the preheating zone, reaction zone and post-flame zone.
2. Spatially, the interaction is not limited to an area close to the effusion cooled liner, but extends into the primary zone through recirculation.

These working hypotheses are to be tested experimentally. For this purpose, minimally invasive advanced laser diagnostics are used to (a) examine the mixture of effusion cooling air and main flow, (b) investigate the local thermochemical state, represented by CO mole fraction and gas-phase temperature and (c) infer the dependence of the CO chemistry on relevant boundary conditions within the primary zone and in the flame-cooling air interaction (FCAI) area, where the flame impinges on the effusion cooled liner. The choice of CO as an important pollutant over other species like NO or NO_2 was made based on the better experimental accessibility using advanced laser diagnostics. Furthermore, CO is not only to be seen as a pollutant with regulated emissions, but is also an important intermediate species within the reaction zone with mole fractions up to 4% as is later discussed in the fundamentals section. For every investigation, a systematic variation of boundary conditions relevant for cooling, flow field and combustion mode is conducted by varying the cooling air mass flow, swirl number and fuel staging.

Within Chapt. 2, fundamental aspects concerning fluid dynamics, basic principles of combustion and specifics important for gas turbine combustion and cooling are outlined, followed by a presentation of the principles of the employed diagnostics.

The test rig and the investigated operating conditions are described in Chapt. 3.

In Chapt. 4, mixing between effusion cooling air and main flow is investigated. For this purpose, nitric oxide (NO) is seeded to the effusion cooling air and visualized using planar laser induced fluorescence (NO-PLIF). Simultaneously, the instantaneous location of the flame front is inferred from quantitative OH-PLIF measurements. From the spatial superposition of the acquired data, it can be concluded in which areas of the combustor an influence of effusion cooling air is expected. Furthermore, it allows to estimate the relative occurrence of mixing events *before*, *during* or *after* chemical reaction.

In Chapt. 5, a combined approach of N_2 ro-vibrational coherent anti-Stokes Raman spectroscopy (CARS) and two-photon laser induced fluorescence of carbon monoxide (CO-LIF) is used to infer the local CO mole fraction and gas phase temperature, representing the local thermochemical state.

Influence on reaction rates are presented in Chapt. 6, where three scalar measurements are combined to gain a deeper understanding on the influence of the chosen boundary conditions on CO chemistry. In this investigation, measurements of OH-PLIF and CO-LIF are used in conjunction with formaldehyde (CH_2O) LIF which serves as a marker for low temperature chemistry, allowing to separate the CO production and oxidation phases.

Chapt. 7 summarizes the presented results and a discussion on the transferability of the findings to real combustor cores is included. Additionally, the author's perspective on remaining open questions for further research is outlined.

Chapter 2

Fundamentals

2.1 Research Object

This section covers fundamental aspects relating to the research object, i.e. turbulent combustion within an effusion cooled model single sector gas turbine combustor. The first two subsections addresses the dynamics of turbulent flows and basic principles of combustion that are relevant for this work. The discussion of these is kept brief, as it presents knowledge readily available in various textbooks, such as *Turbulent Flows* by S. Pope [125] and *Combustion* by J. Warnatz [162]. Furthermore, specifics for low emission gas turbine combustors, such as the design of flow field and lean premixed combustion is discussed. In a last subsection, the basic idea behind effusion cooling is outlined.

2.1.1 Fluid Dynamics

The set of governing equations for describing non-reactive turbulent flows, commonly referred to as the Navier-Stokes equations, consists of the conservation of mass and momentum given in Eq. (2.1) with the expression for the stress tensor τ_{ij} for a Newtonian fluid defined in Eq. (2.2) as a function of the velocity gradients and the kinematic viscosity ν.

$$\frac{\partial \rho}{\partial t} + \frac{\partial}{\delta x_i}\left(\rho u_i\right) = 0 \tag{2.1a}$$

$$\frac{\partial}{\partial t}\left(\rho u_i\right) + \frac{\partial}{\delta x_j}\left(\rho u_i u_j\right) = -\frac{\partial p}{\partial x_i} + \frac{\partial \tau_{ij}}{\delta x_j} + \rho g_i \tag{2.1b}$$

$$\tau_{ij} = \rho\nu\left[\left(\frac{\partial u_j}{\partial x_i} + \frac{\partial u_i}{\partial x_j}\right) - \frac{2}{3}\frac{\partial u_k}{\partial x_k}\delta_{ij}\right] \tag{2.2}$$

In these equations, the Einstein notation is used and δ_{ij} describes the Kronecker delta, i.e. $\delta_{ij} = 1$ for $i = j$. Tor a turbulent flow field in three spatial dimensions x_i, Eq. (2.1) describes a set of four equations for the six independent variables density ρ, pressure p, kinematic viscosity ν and velocities v_i. For isothermal flows, the kinematic viscosity is a material constant. Furthermore, with the low-Mach number approximation ($\mathrm{Ma} \leq 0.3$) and negligible acoustic effects, the density of the fluid may be assumed to be constant. Under these conditions, the set of equations (2.1) is determined.

In chemically reactive flows, such as combustion systems, temperature - and thus density and viscosity - are not constant. Consequently, the set of equations becomes under determined. Additionally, chemical reactions within the fluid domain have to be accounted for. This is realized by introducing transport equations for the mass fraction Y of a chemical species k as given by Eq. (2.3).

$$\frac{\partial}{\partial t}\left(\rho Y_k\right) + \frac{\partial}{\partial x_i}\left(\rho Y_k u_i\right) = -\frac{\partial}{\partial x_i}\left(\rho D_i \frac{\partial Y_k}{\partial x_i}\right) + \dot{\omega}_k \tag{2.3}$$

This type of transport equation consists of an unsteady term and a convection term on the left hand side and a diffusion term and source term on the right hand side. Diffusion processes are described by Fick's law, where the diffusive flux is proportional to the spatial gradient of the species concentration and the corresponding diffusion coefficient D_k. While reacting flows still obey conservation of mass, chemical reactions cause conversions between molecules, i.e. chemical species may be either produced or consumed, described by the source term $\dot{\omega}_k$. In addition to the transport equations for chemical species, a transport equation for energy has to be introduced. In principle, various thermodynamic parameters that represent energy may be used, such as temperature, internal energy or enthalpy. Eq. (2.4) shows the energy transport equation based on the enthalpy h.

$$\frac{\partial}{\partial t}\left(\rho h\right) + \frac{\partial}{\partial x_i}\left(\rho h u_i\right) = -\frac{\partial}{\partial x_i}\left(c_p \rho D_\alpha \frac{\partial T}{\partial x_i}\right) + \dot{\omega}_T + \dot{Q} \tag{2.4}$$

Here, c_p describes the heat capacity at constant pressure, D_α the thermal diffusion coefficient, $\dot{\omega}_T$ the net heat release due to chemical reactions and $\dot{Q}$ external enthalpy gain or loss.

An important notion of the described set of equations is its strong sensitivity to boundary conditions and the associated susceptibility to instabilities leading to the phenomenon of turbulence. The onset of turbulence is commonly described by the Reynolds number given in Eq. (2.5), where l describes a characteristic length.

$$Re = \frac{lv}{\nu} \tag{2.5}$$

The Reynolds number may be interpreted as the ratio between inertial and viscous forces within the fluid flow. Below a critical Reynolds number Re_{crit}, viscous forces dominate, which dampen instabilities and maintain a laminar flow. Above Re_{crit}, the flow becomes turbulent due to increased inertial forces. As turbulence strongly increases convective transport and mixing within a flow, it is of high importance for practical applications such as gas turbines.

2.1.2 Basic Principles of Combustion

Combustion describes a self-sustaining energy conversion process where a selected fuel is oxidized in an exothermic reaction. During this process, chemically bound energy is released to the surrounding fluid in form of heat. Within this work, natural gas with a methane (CH_4) content of $\geq 90\%$ is oxidized using air. For the discussion of the

fundamentals and laminar flame simulations used during the investigations in Sections 4-6, it is assumed that the chemistry is adequately described by replacing natural gas with methane.

2.1.2.1 Equivalence Ratio

The global reaction describing stoichiometric methane-air combustion is given in Eq. (2.6).

$$\mathrm{CH_4} + 2\,\mathrm{O_2} \longrightarrow \mathrm{CO_2} + 2\,\mathrm{H_2O} \tag{2.6}$$

In this one-step reaction mechanism, the ratio between fuel and oxidizer is chosen to exactly convert the entire amount of fuel with the necessary amount of oxidizer to form the main products CO_2 and H_2O.

For mixtures that deviate from that composition, one of the most important concepts for combustion applications, namely the equivalence ratio Φ as defined by Eq. (2.7), is introduced. The equivalence ratio is defined by the air-to-fuel mass fraction for stoichiometric conditions divided by the air-to-fuel mass fraction ratio for the actual mixture.

$$\Phi = \frac{(Y_{air}/Y_{\mathrm{CH_4}})_{st}}{Y_{air}/Y_{\mathrm{CH_4}}} \tag{2.7}$$

By definition, $\Phi = 1$ corresponds to stoichiometric mixtures. For $\Phi < 1$, the mixture contains more oxidizer than necessary for stoichiometric combustion and is designated as *lean*. Conversely, a mixture is called *rich* for equivalence ratios $\Phi > 1$, i.e. there is a surplus of fuel after reaction.

2.1.2.2 Reaction Kinetics

While the one-step reaction in Eq. (2.6) describes the global reaction from educts to major product species, the entire mechanism is more complex and consists of many elementary reactions to describe the production and consumption of intermediate species within the reaction zone.

Within this work, the GRI-MECH 3.0 mechanism [148] is used to describe elementary reactions of methane-air combustion. This mechanism contains 325 reactions and 53 species. Forward reaction rates RR are modeled using Eq. (2.8).

$$RR_i \propto k(T) \prod_i N_i \tag{2.8}$$

Here, $k(T)$ denotes the rate constant calculated by the Arrhenius equation given in Eq. (2.9) and N_i denotes the number density of species i that are involved in the reaction.

$$k(T) = A \exp\left(\frac{-E_a}{k_B T}\right) \tag{2.9}$$

Within the Arrhenius equation, E_a denotes the activation energy and A the pre-exponential factor for a given reaction. T refers to the temperature and k_B to the Boltzmann constant, respectively.

2.1.2.3 Structure of Premixed Flames

Premixed flames are characterized by complete mixing of oxidizer and fuel prior to the onset of chemical reactions. In a steady flow with $v = 0$, the flame propagates with the laminar flame speed s_L into the mixture. For a one-dimensional laminar flame with $v = -s_L$, i.e. the flow has a velocity with magnitude s_L with opposite direction, a stationary flame front is observed. This flame front may be separated in three zones [61]:

Preheating zone: This zone is characterized by low temperature chemistry. Heat and intermediate species from the reaction zone diffuse into the preheating zone.

Reaction zone: This zone is driven by high temperature chemistry and is characterized by the peak heat release rate.

Post flame zone: In this region, the chemical composition approaches its equilibrium concentration and temperature gradients decline until the adiabatic flame temperature is reached.

Different definitions of the flame front thickness are available in the literature. Hasse et al. define the flame front thickness δ_F by the ratio of the temperature increase from unburnt temperature T_U to the adiabatic temperature T_{ad} to the maximum spatial temperature gradient $\partial T/\partial z$ as given in Eq. (2.10) [78].

$$\delta_F = \frac{T_{ad} - T_u}{\max\left(\partial T/\partial z\right)} \tag{2.10}$$

Throughout this work, laminar adiabatic flame simulations are - unless otherwise noted - conducted using CANTERA [63]. As described later in Sect. 3, the operating conditions used in this work include an elevated unburnt gas temperature T_u to mimic increased combustor inlet temperature due to isentropic compression in a real engine. Due to the temperature sensitivity of the reaction rate constant $k(T)$, see Eq. (2.9), reaction rates are increased for higher temperatures. Additionally, reactions take place at elevated pressure, which, due to the number density dependence of Eq. (2.8), also increases reaction rates. Consequently, these factors have a strong influence on the structure of premixed flames. Fig. 2.1 shows the temperature and mole fraction profiles as well as the mole fractions in state-space, i.e. against temperature, of selected species relevant for this work. These are formaldehyde (CH_2O), carbon monoxide (CO) and the hydroxyl radical (OH). Shown are simulations of a $\Phi = 0.75$ laminar adiabatic flame with $T_u = 300\,\mathrm{K}$ at atmospheric pressure in comparison to a case with $T_u = 623\,\mathrm{K}$ at $p = 2.5\,\mathrm{bar}$.

As can be seen from Fig. 2.1, the increase in T_u and p leads to a narrower structure in spatial domain. Consequently, gradients in species mole fractions and temperature are increased. The flame thickness δ_F as calculated using Eq. (2.10) is reduced from $\approx 600\,\mu\mathrm{m}$ to $\approx 200\,\mu\mathrm{m}$ for the high pressure and high inlet temperature case, posing stringent requirements on the spatial resolution of the employed diagnostics. With respect to temperature, profiles are slightly compressed and shifted towards higher temperatures at increased mole fraction values.

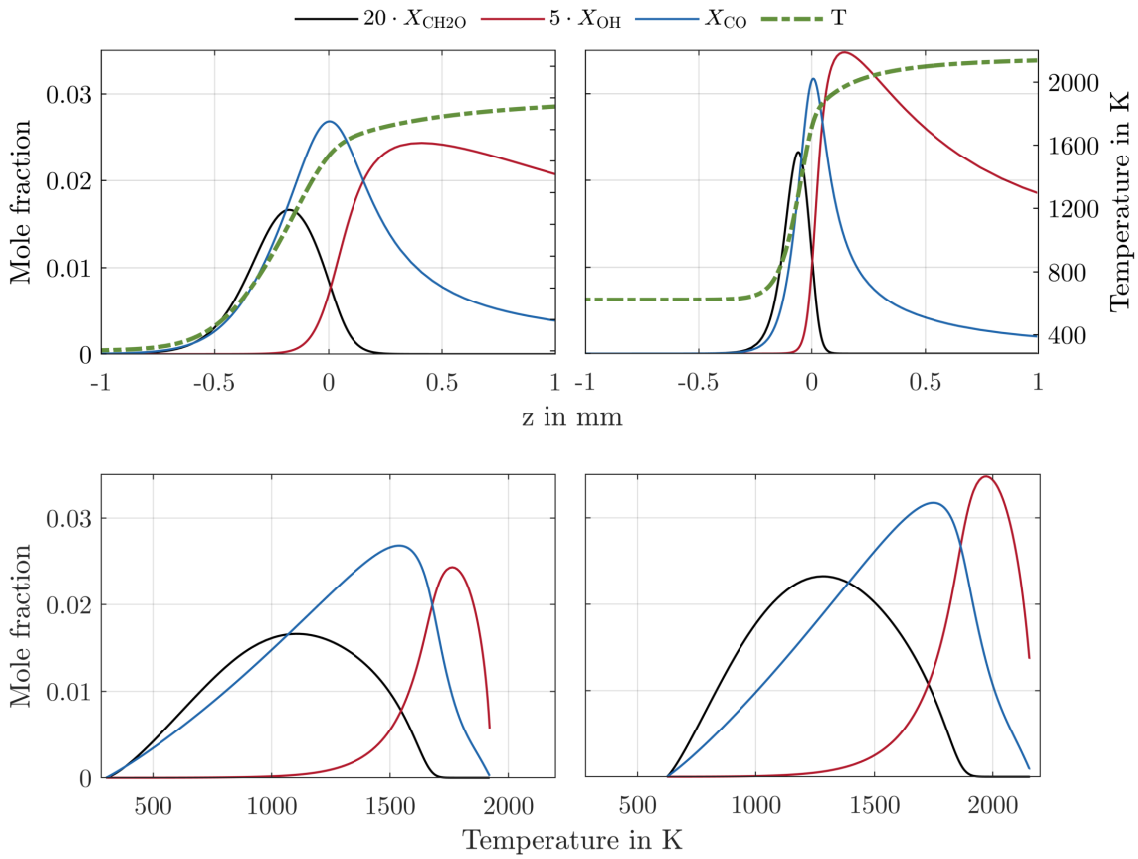

Figure 2.1: Comparison of laminar flame simulations with different inlet temperatures and pressure levels. Left column: $T_u = 300\,\mathrm{K}$ at atmospheric pressure. Right column: $T_u = 623\,\mathrm{K}$ at 2.5 bar. Mole fractions are plotted against spatial dimension ($z \equiv 0$ at peak heat release rate, top row) and temperature (bottom row). OH and CH_2O have been scaled to fit on the same axis as CO.

2.1.3 Gas Turbine Combustion

Main design goals for the development of aero engine combustor cores are a high degree of burnout, low pollutant emission, stable operation in a wide range of operating conditions, compact geometry and safe (re-)ignition [25]. Nearly all modern gas turbine combustors use swirl stabilization to achieve these design goals. The topic of swirl-stabilized flames has been subject to scientific research for decades and numerous articles are available that cover the fundamentals, e.g. by Huang et al. [86] or the review article on *Dynamics of Swirling Flames* by Candel et al. [30].

The principal idea is to impress an axial flow with a tangential component to produce a swirling flow. To achieve this, a component referred to as *swirler* is placed into the inlet duct to the combustor to partially deflect the flow in tangential direction. The swirl number, defined as the ratio of axial flux of tangential momentum G_θ to the axial flux of axial momentum G_z times a characteristic length R, most commonly the outer radius of

the swirler, is given in Eq. (2.11).

$$S = \frac{G_\theta}{RG_z} = \frac{\int_0^\infty \rho u_z u_\theta r^2 \mathrm{d}r}{R \int_0^\infty \left[\rho u^2 + (p - p_\infty)\right] r \mathrm{d}r} \tag{2.11}$$

A priori, the actual swirl number is unknown due to the fact that the flow field is typically unavailable at this design stage. Instead, a geometric swirl number may be defined based on the geometry of the swirler. This approach is also followed in the present work, see Sect. 3.

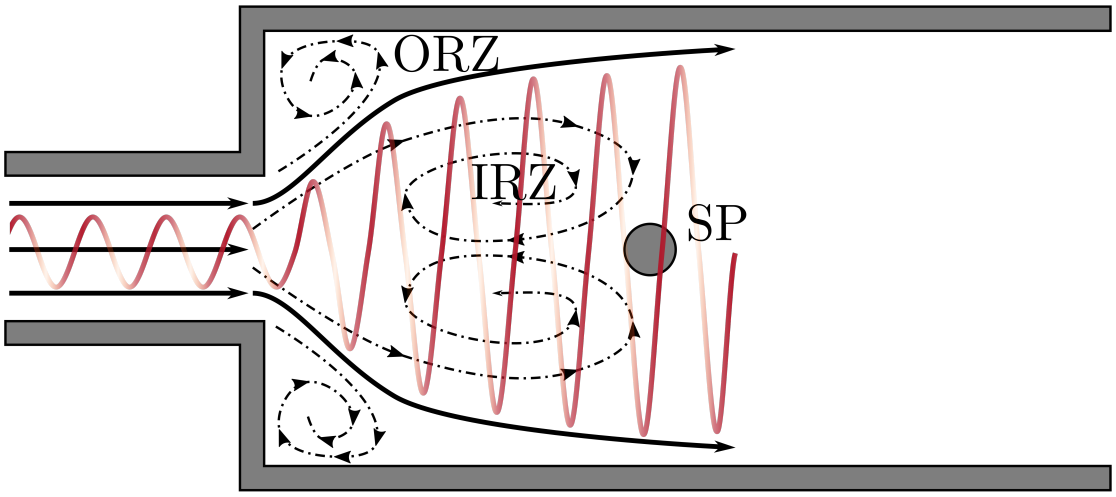

Figure 2.2: Sketch of a typical swirl induced flow field within a gas turbine combustor. Black dashed lines represent inner (IRZ) and outer (ORZ) recirculation zones. Thick black lines show expanding main flow. SP: Stagnation point. Figure adapted from [84].

Fig. 2.2 schematically shows the typical flow field within a swirl-stabilized combustor. The rotational movement around the central axis causes a centrifugal force on fluid elements within the swirling flow. This centrifugal force causes a positive radial and axial pressure gradient. For a critical swirl number $S > 0.6$, the axial momentum of the main flow is no longer capable to overcome the increase in axial pressure gradient [68]. Consequently, this results in a local flow reversal that establishes an inner recirculation zone (IRZ). The IRZ expands radially with increasing axial distance, which leads to a reduction of the axial pressure gradient. As a result, the pressure gradient has a zero-crossing at the *stagnation point* (SP), which limits the axial length of the IRZ. This length is strongly dependent on the geometry of the inlet duct [53]. Additionally, in a confined combustor, an outer recirculation zone (ORZ) is formed near the shear layer between the combustor liner and the main inflow. In the shear layers of the IRZ and ORZ, flow velocities are significantly reduced compared to the bulk outlet velocity. This allows the flame to stabilize in these areas.

2.1.4 Effusion Cooling

This section covers fundamental aspects regarding liner design and heat transfer processes occurring within the combustor. The necessity of wall cooling is outlined, followed by a brief description of the concept of effusion cooling.

Typically, high temperature alloys such as Hastelloy X, Nimonic 75 or Inconel are used for the liner which resist temperatures up to 1100 K. These materials are usually coated with a thin layer of ceramic *thermal barrier coating* (TBC), consisting of e.g. yttrium stabilized zirconium, which leads to a reduction of the metal temperature by approximately $40 - 70$ K. As the gas phase temperatures exceed this limit by far, the combustor liner has to be cooled. Considering that for a modern engine, up to 40% of the air flow from the compressor is used for cooling [25], the need for efficient cooling techniques becomes obvious. Increasing the pressure ratio to achieve higher cycle efficiency aggravates this need due to the increased temperature of the air flow due to compression, which leads both to higher adiabatic flame temperatures, see Sect. 2.1.2.3, and increased cooling air temperature which drastically lowers the cooling efficiency [25].

One of the most promising approaches is the use of effusion cooling using angled holes as shown in Fig. 2.3. Within this approach, the combustor liner features a regular pattern of closely spaced holes with diameters in the sub-mm range. Compressor bleed air is injected trough this hole array which provides two dominant cooling mechanisms: (I) Heat is removed from the effusion cooled liner due to forced convection within the holes. Using angled holes greatly increases the surface area within the holes, maximizing the amount of heat that can be extracted. E.g. a hole drilled at 20° has almost threefold surface area compared to a hole drilled perpendicular to the wall [104]. (II) Providing the spacing between holes is close enough and the emerging jets from the holes do not penetrate too far into the combustor, a film is formed along the surface of the wall which isolates the wall from the hot products of the flame [104].

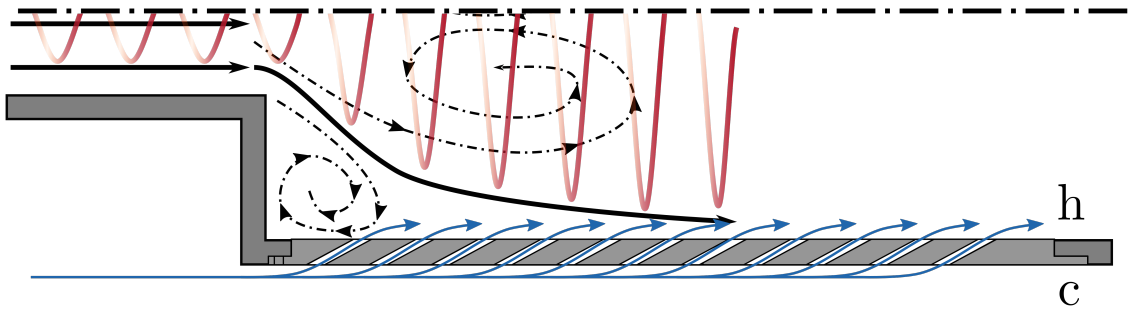

Figure 2.3: Sketch of a flow through angled effusion cooling holes (blue). Hot and cold gas side indicated by h and c.

Typically, effusion cooling is described using dimensionless similarity parameters. These are the blowing ratio M, momentum ratio I and density ratio R given in Eq. (2.12), where ρ and v denote the density and the velocity on the hot (h) and cold (c) side of the effusion cooled liner [100].

$$M = \frac{v_c \rho_c}{v_h \rho_h} \tag{2.12a}$$

$$I = \frac{v_c^2 \rho_c}{v_h^2 \rho_h} \tag{2.12b}$$

$$R = \frac{\rho_c}{\rho_h} \tag{2.12c}$$

The blowing ratio describes the ratio of the mass flux between the hot and cold side of the effusion cooled liner. The momentum ratio is a measure for the tendency of the cooling air jets to lift off the wall. Tab. 2.1 summarizes the investigated ranges of blowing, momentum and density ratios obtained from selected publications in the literature to provide a guideline of typical values. Unfortunately, typical ranges for these parameters from commercial combustors are not readily available due to intellectual property rights (IPR) issues. One notable exception is the dissertation of Martiny [113], where $M = 0.5-3$ and $I = 0 - 3.83$ is reported for the BR-715 by Rolls-Royce.

Table 2.1: Investigated range of blowing and momentum ratios for selected publications. Asterisks denote values that have been calculated using Eq. (2.12) based on the reported parameters.

Author	M	I	R
Andreini et al. [9]	0.5-5	0.16-25*	1-1.5
Behrendt et al. [14]	0.5-4.2	0.03-9.38*	1.88*
Huang et al. [87]	0.5-2.5	0.187-4.7	1.33*
Kakade et al. [95]	0.48-2	0.23-4*	0.97-1.47
Scrittore et al. [141]	3.2-5.0	10.2-25*	1-1.08
Martin et al. [112]	0.3-1.5	0.06-2.1*	1.065-1.4

2.2 Diagnostics

Within this work, minimally intrusive advanced laser diagnostics are used to investigate the phenomena involved in flame-cooling air interaction. This section summarizes fundamental principles of the employed methods. These are laser induced fluorescence (LIF) of carbon monoxide (CO), nitric oxide (NO), hydroxyl radical (OH) and formaldehyde (CH_2O), and ro-vibrational coherent anti-Stokes Raman spectroscopy (CARS) with N_2 as a resonant species. Additionally, the influence of optical resolution of the used imaging systems on spatial gradients is discussed. The description focuses on aspects that are relevant for the understanding of the experimental investigations performed in this thesis rather than providing information about the underlying fundamental physics, such as quantum mechanics and electrodynamics, which are described in great detail in the literature, e.g. in the fundamental textbooks [41, 42, 74, 85, 115].

2.2.1 Laser Induced Fluorescence

This section describes the fundamentals of laser induced fluorescence (LIF) and addresses important notions regarding the molecules of interest for this work, which are carbon monoxide (CO), nitric oxide (NO), formaldehyde (CH_2O) and the hydroxyl radical (OH), respectively. As the investigations presented in Sections 4, 5 and 6 partially rely on simulation of LIF signals and excitation spectra, these aspects are discussed in detail.

2.2.1.1 General Description

For all molecules of interest, an electronic transition is excited by resonant absorption of an incident laser photon. This absorption process defines the high selectivity of LIF measurements, as transitions may be selected that have no to little influence on other molecules within the measurement volume. The excitation to an electronically higher eigenstate causes a change in the Boltzmann distribution which does no longer correspond to the distribution for thermal equilibrium. Population distributions outside thermal equilibrium have a short lifetime and relaxation processes start to re-establish thermal equilibrium. These processes have to obey conservation of energy, i.e. the excess energy has to be transferred. The most dominant relaxation processes are collisional quenching, rotational and vibrational energy transfer (RET, VET) and spontaneous emission, the latter being the LIF signal that is to be measured. This is summarized in the definition of the *fluorescence quantum yield*, which is described by the ratio of spontaneous emission rate to the sum of rates of the concurring processes. Precise knowledge of this parameter is usually inaccessible experimentally, as it involves measuring the local temperature and species mole fractions of all major colliders. Spectroscopically, molecular transitions are not infinitely sharp but are - in addition to their natural line width - subject to broadening mechanisms such as Doppler or collisional broadening. Additionally, the lasers used for excitation also have a finite bandwidth which has to be accounted for as it impacts the efficiency with which a transition is excited. Spontaneous emission is an isotropic process and as such the detected signal intensity depends on the collection angle and efficiency of the detector which imposes the constraint, that LIF measurements are never calibration-free [74].

2.2.1.2 CO-LIF

In Sect. 5, quantitative CO mole fraction measurements by means of CO-LIF are presented to investigate the influence of effusion cooling air mass flow on the thermochemical state within various regions of the combustor. Due to the low number densities expected at the given conditions, see Sect. 2.1.2.3, stringent requirements on sensitivity as well as precision and accuracy are imposed onto the measurements. To achieve acquisition of high quality data, detailed knowledge of the spectroscopy of CO is required, as discussed in the following. The calibration procedure and a discussion on the resulting uncertainties is presented in Sect. 5.

Fig. 2.4 shows the energy levels of the first three electronic eigenstates of the CO molecule and two different excitation/detection schemes. Exciting the transition $A^1\Pi \leftarrow X^2\Sigma^+$ by

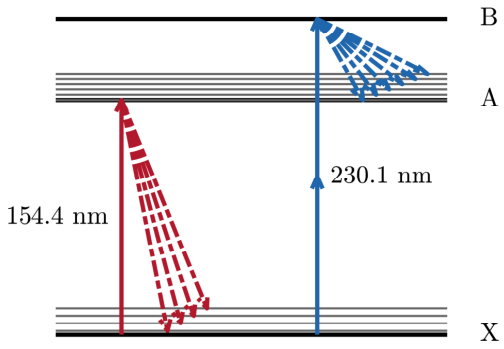

Figure 2.4: Electronic and vibrational energy levels of the CO molecule. Solid lines: Excitation; Dashed lines: Emission. Red: single-photon excitation $A^1\Pi \leftarrow X^2\Sigma^+$, Blue: two-photon excitation $B^1\Sigma^+ \leftarrow\leftarrow X^1\Sigma^+$.

absorption of a single photon would require a wavelength of $\approx 154\,\text{nm}$, i.e. in the vacuum-UV (VUV) region. This is impractical for several reasons: VUV radiation is absorbed nearly immediately in the optically dense medium within a gas turbine combustor [159]. Additionally, the transmission efficiency of the quartz glass windows surrounding the measurement volume, see Sect. 3, is significantly reduced for wavelengths shorter than 220 nm [84]. Furthermore, subsequent fluorescence from the A state to the vibrational bands in the electronic ground state is also in the VUV regime, which poses problems with common imaging systems.

As an alternative, a scheme may be employed that excites the $B^1\Sigma^+ \leftarrow\leftarrow X^1\Sigma^+$ transition in the Hopfield-Birge system by simultaneous absorption of two photons around 230.1 nm with subsequent detection of fluorescence in the Ångström band, i.e. from the excited B state to the vibrational levels of the electronic A state. This approach is widely used in combustion research, e.g. in [13, 54, 59, 79, 114, 142], and has also been successfully used for atmospheric investigations on flame-wall interaction at RSM[2], e.g. in [90, 97, 110, 146]. Unlike for other molecules such as OH and NO, there is no spectroscopic simulation code publicly available for CO. For this reason, a code has been developed that closely follows the procedures described in the dissertation of Carrivain [31] and a publication by Voigt et al. [159] which have been validated within the required temperature and pressure range relevant to this work. Individual parts of the code as well as resulting excitation and emission spectra are verified against available data from these references.

Spectral simulation The CO-LIF signal intensity in s^{-1} can be expressed using Eq. 2.13, where ξ characterizes the net detection efficiency due to transmission losses and limited collection angle. N_{CO}, $\hat{\sigma}^{(2)}$, I_L, ν_L and $\eta(T,p)$ denote the CO number density, the two-photon absorption cross-section, the laser intensity, the laser center frequency and the fluorescence quantum yield, respectively [31, p. 44]. Note that the equation does not

[2]Reaktive Strömungen und Messtechnik / Reactive Flows and Diagnostics.

yet include the laser line overlap integral, which is later included via convolution.

$$S_{CO} = N_{CO}\hat{\sigma}^{(2)} \left(\frac{I_L}{h\nu_L}\right)^2 \eta(T,p)\xi \tag{2.13}$$

The fluorescence quantum yield η is computed using the Stern-Volmer equation given in Eq. (2.14) and includes contributions from the Einstein-A coefficient, quenching rate Q and the photoionization rate R_i [159]. The latter describes the concurring process of *resonance enhanced multi-photon ionization* (REMPI), a process that involves ionization within the B-state by absorption of an additional photon [47]. Influence from predissociation and stimulated emission is neglected as the quenching and ionization rates dominate at pressures above 100 mbar. Unfortunately, VET and RET rates for CO are insufficiently studied for the B-state. Comes et al. report a cross section of $6.1\,\text{Å}^2$ for VET from $A^2\Pi(v'=1)$ to $A^2\Pi(v'=0)$ induced by collisions with N_2 [35]. Sun et al. report a RET cross section of $3.13\,\text{Å}^2$ for energy transfer from $J'=2$ to $J'=1$ within the $A^1\Pi(v'=3)$ state from collisions with Ar [151]. It is assumed that the VET and RET cross sections for the B-states are in a similar order and thus small compared to those of electronic quenching.

$$\eta(T,p) = \frac{A_{B-A}}{A_{tot} + Q + R_i} \tag{2.14}$$

For the calculation of the quenching rate, quenching cross-sections and their temperature dependence for collisions with Ar, Kr, Xe, H_2, N_2, O_2, CO, H_2O, CO_2 and CH_4 are taken from Settersten et al. [143]. The quenching rate is calculated using Eq. (2.15), where N_i is the number density of the collider with the temperature dependent quenching cross-section $\sigma_{Q,i}$ at a mean relative intramolecular velocity of $\bar{v_i}$, where M_i denotes the molar mass and R the ideal gas constant.

$$\begin{aligned} Q(T,p) &= \sum_i N_i \bar{v_i} \sigma_{Q,i}(T) \quad \text{with} \\ \bar{v_i} &= \sqrt{\frac{8RT}{\pi}\left(\frac{1}{M_{CO}} + \frac{1}{M_i}\right)} \end{aligned} \tag{2.15}$$

Fig. 2.5 shows the temperature dependent quenching cross-sections for the included species and resulting total quenching rates at 1800 K in the pressure range $1-10$ bar. In comparison to the data from Carrivain, no difference in the calculated quenching cross-sections is observed. Total quenching rates calculated using Eq. (2.15) are slightly below the values reported by Carrivain, which might be an artifact arising from digitizing Fig. 2.24 in [31].

The photoionization rate is expressed by the product of the ionization cross section $\sigma_i^{J'}$ and the photon flux $\tilde{I} = {}^{I_L}/_{h\nu}$, see Eq. (2.16).

$$R = \sigma_i^{J'} \cdot \tilde{I} \tag{2.16}$$

Within this work, the ionization cross-section is assumed to be J''-independent. A constant value of $1 \times 10^{-17}\,\text{cm}^{-2}$ is used, which corresponds to the J''-averaged value for $J''=0-8$ and $J''=12$ [44]. Voigt et al. report a deviation from the J'-averaged value

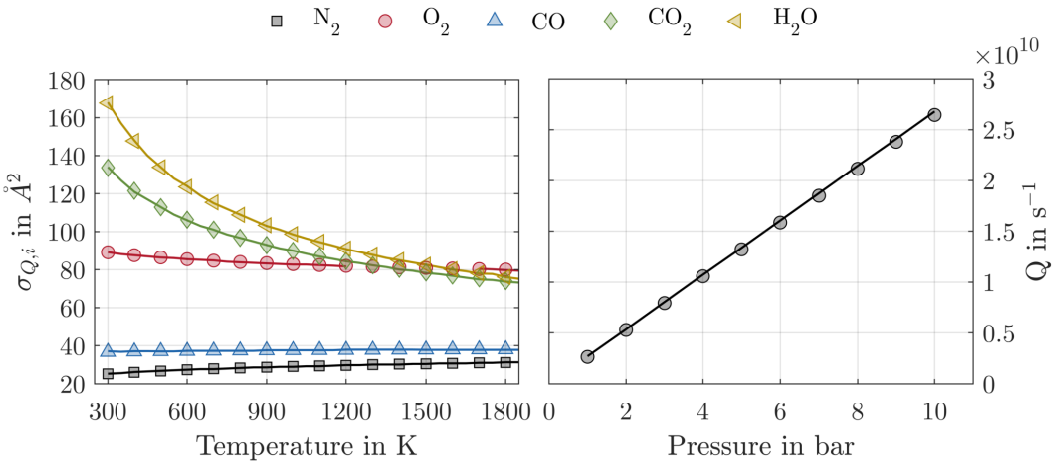

Figure 2.5: Collisional quenching cross-sections for implemented species at varying temperature and atmospheric pressure (left) and resulting quenching rate Q for varying pressure at 1800 K (right). Chemical composition: 78% N_2, 8% CO_2, 10% H_2O, 4% CO. Symbols: calculated values. Lines: comparison data from Fig. 2.23 and 2.24 in [31].

of $\approx 40 - 60\%$ for $J'' = 9 - 11$ within their experiment [159]. However, no systematic investigation is conducted whether this deviation is linear with the photon flux, thus it is not clear if the reported variation in ionization cross section is of fundamental nature. As this effect is only relevant for the comparison between excitation scans and simulations and not for signal computations with a fixed excitation frequency, no impact on the simulated LIF signal is to be expected.

Fig. 2.6 shows the resulting variation of the fluorescence quantum yield η with respect to temperature, pressure and laser intensity. As can be observed, increased photo-ionization reduces the dependency on collisional quenching at the cost of reduced net fluorescence quantum yield. The obtained values agree well with those reported in Fig. 2.26 [31].

The two-photon absorption cross-section $\hat{\sigma}^{(2)}$ for a given transition in ground state $v = 0, J''$ is modeled using Eq. (2.17) [31, p. 34]. Note that the definition of the laser line overlap integral is omitted at this step and included later.

$$\hat{\sigma}^{(2)} = \sigma_0^{(2)} G^{(2)} f_{J''} \frac{S^{(2)}_{J'J''}}{2J'' + 1} \tag{2.17}$$

In this equation, $\sigma_0^{(2)}$ denotes the spectrally integrated 2-photon cross section with a value of $1.5 \times 10^{-35}\,\mathrm{cm}^4$ [45]. In accordance with [31] and [159], the second-order intensity correlation factor $G^{(2)}$ is set to a value of 2. $f_{J''}$ represents the ground state Boltzmann fraction. Assuming linear polarization of the excitation source, the two-photon Hönl-London factors for the O, Q and S branch of a ${}^1\Sigma^+ \leftarrow\leftarrow {}^1\Sigma^+$ transition may be simplified by assuming that the transition dipole moment for linear polarization is much larger than for circular polarization, i.e. $\mu_l \gg \mu_c$ [107]. This assumption yields the Hönl-London-Factors $S^{(2)}_{J'J''}$ for the $O-$, $Q-$ and $S-$branch transitions given in Eq. (2.18), where the

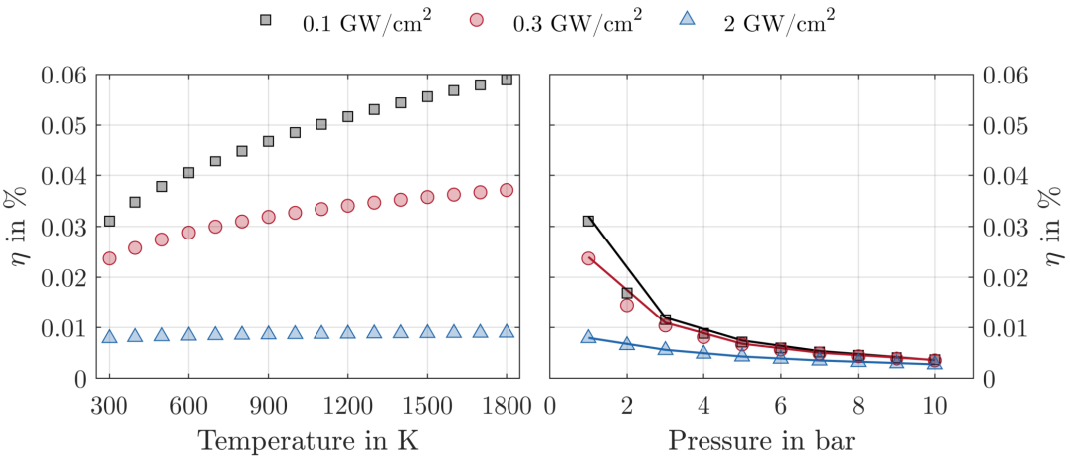

Figure 2.6: Variation of fluorescence quantum yield η at varying temperature and atmospheric pressure (left) and varying pressure at 1800 K (right) for three different laser intensities. 2.6% CO in dry air atmosphere for both cases. Symbols: data created using Eq. (2.14). Lines: comparison data from Fig 2.26 in [31]. Note that the difference at 2 bar is an artifact from linear interpolation of the data from [31], which does not include a value at this pressure.

subscript $J'J''$ was omitted for simplicity.

$$\begin{aligned} S_O^{(2)} &= 0 \\ S_Q^{(2)} &= \frac{2J''+1}{9} \\ S_S^{(2)} &= 0 \end{aligned} \tag{2.18}$$

Effectively, this suppresses S- and O-branch transitions and the term $S^{(2)}_{J'J''}/(2J''+1)$ in Eq. (2.17) is reduced to the J''-independent value 1/9 for Q-branch transitions. This implies that the J'' dependence of the 2-photon absorption cross-section is determined by the Boltzmann fraction $f_{J''}$ only. Calculating line positions and Boltzmann fractions requires a model for the rotational, vibrational and electronic eigenstates of CO. Rotational energies F and vibrational energies G are computed using Eq. (2.19). Constants for the computation are listed in Tab. 2.2.

$$\begin{aligned} F(v'',J'') &= B_v J''(J''+1) - D_v J''^2(J''+1)^2 + H_v J''^3(J''+1)^3 + L_v J''^4(J''+1)^4 \\ G(v'') &= \omega_e(v''+0.5) - \omega_e x_e(v''+0.5)^2 \end{aligned} \tag{2.19}$$

Boltzmann fractions $f_{J''}$ are calculated using Eq. (2.20), which assumes validity of the Born-Oppenheimer approximation.

$$f_{J''} = (2J''+1)\exp\left(-{}^{hc}/_{kT}\,(F(0,J'')+G(0))\right)\frac{1}{Q_e Q_v Q_r} \tag{2.20}$$

Here, Q_e, Q_v and Q_r denote the electronic, vibrational and rotational partition function, respectively. Vibrational and rotational partition functions are computed by the sum of

Table 2.2: Constants for rotational and vibrational energy levels of the CO molecule for electronic ground state X and excited state B in cm^{-1}.

Const.	X	B	Ref.
B_v	1.9225	1.9481153	[156], [6]
D_v	6.1211×10^{-6}	6.7133×10^{-6}	[156], [6]
H_v	5.7536×10^{-12}	–	[156]
L_v	1.0340×10^{-17}	–	[156]
ω_e	2169.81	2161.75	[51]
$\omega_e x_e$	15.164	39.84	[51]

states of the first four vibrational bands $v'' = 0 - 3$ and $J'' = 0 - 65$ for the rotational energies within the electronic ground-state ($Q_e = 1$). Even at a temperature of 2500 K, higher states are not significantly occupied. The relative population of states with $v'' \geq 3$ is $\leq 1.8\%$ and ≤ 0.13 for $J'' \geq 65$ at $v'' = 0$.

Due to broadening mechanisms, the transitions are not strictly sharp but show a finite linewidth. In the relevant temperature and pressure range for most applications, Doppler and collisional broadening are the dominant broadening mechanisms. The appropriate line shape for Doppler broadening for a given transition i is a Gaussian with a FWHM value of $\Delta\sigma_D$ given in Eq. (2.21) [31].

$$\Delta\sigma_{D,i} = 2\nu_i \sqrt{\frac{2kT\ln(2)}{m_{CO}c^2}} \tag{2.21}$$

Here, ν_i denotes the center frequency of transition i in cm^{-1} and m_{CO} the mass of a CO molecule in kg.

Collisional broadening $\Delta\sigma_C$ and shift $\Delta\sigma_S$ are simulated using Eq. (2.22) with data for collisions with N_2, CO_2 and CO from Di Rosa et al. [46]. Unfortunately, no data is available for collisions with O_2 and H_2O. Following the argumentation of Carrivain [31], the values for broadening and shift from N_2 are used for O_2 as well due to the similar dipole moment. For collisions with H_2O, 30% higher values as obtained for N_2 are used.[3]

$$\begin{aligned} \Delta\sigma_C &= p \sum_i X_i 2\gamma_i \\ \Delta\sigma_S &= p \sum_i X_i \delta_i \end{aligned} \tag{2.22}$$

$\Delta\sigma_C$ is used as a FHWM value for a Lorentzian form function that is used for a convolution of every transition. Transition center frequencies are shifted individually by the values obtained for $\Delta\sigma_S$. Fig. 2.7 shows results for Doppler and collisional broadening as

[3] In [31] the reasoning is, that CO $B - X$ transitions are similar to NO $A - X$ transitions, judged by their dipole moment. Additionally, intermolecular forces are equivalent for $CO(X) - N_2$ and $NO(X) - N_2$. H_2O as a molecule with high polarity lead to stronger broadening and shift due to higher intermolecular interaction potential. For $NO(X) - H_2O$ collisions, the broadening and shift values are 30% higher as for $NO(X) - N_2$. This relative increase is assumed to be true for $CO(X) - H_2O$ as well allowing to extrapolate the broadening and shift parameters from N_2 to H_2O.

obtained by Eq. (2.21) and Eq. (2.22) for a temperature range between 300 K and 1800 K at atmospheric pressure as well as collisonal broadening at 1800 K with pressure varying from 1 bar to 10 bar for a comparison with data[4] reported in [31].

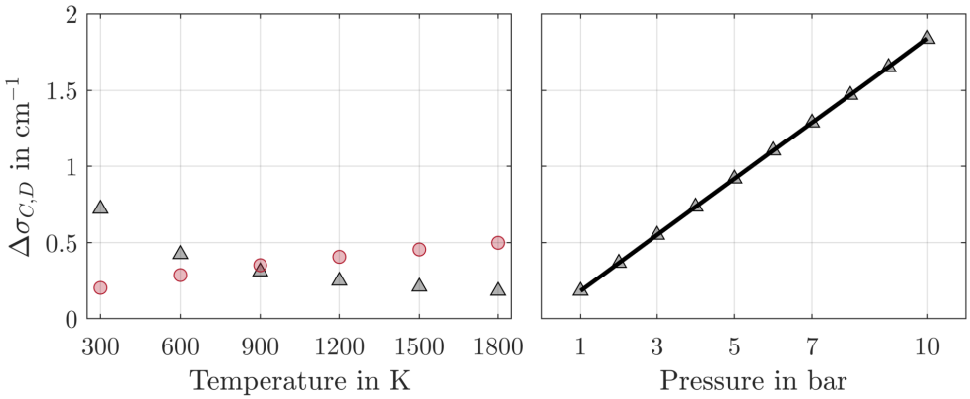

Figure 2.7: Collisional (black triangles) and mean Doppler broadening (red circles) for Q-branch transitions in the $B-X$ system of CO at varying temperature and atmospheric pressure (left) and varying pressure at 1800 K (right). 5% CO in N_2 atmosphere for both cases. For verification, the right plot shows data extracted from Table 2.22 in [31] (line) and computation using the implemented code (circles).

To create the excitation spectrum, Eq. (2.13) is solved for Q-branch transitions with $v'' = 0$ and $J'' = 0 - 65$. A stick spectrum is generated by creating a wavenumber array for each transition with a resolution of $0.005\,\mathrm{cm}^{-1}$ and assigning the J'' dependent intensity at the closest match of the center frequency $\nu_{J''}$ on the wavenumber grid. Q-branch transition center frequencies are calculated by subtracting the energies obtained for the B-state from those obtained for the X-state using Eq. (2.23).

$$\nu_{J''} = T_e + G(v',J') - G(v'',J'') + F(v',J') - F(v'',J'') \tag{2.23}$$

In this equation, $T_e + G(v',J') - G(v'',J'')$ corresponds to the electronic energy of the B state plus the difference in vibrational energy for $v'' = v' = 0$ amongst the involved electronic states which is $86\,916.198\,\mathrm{cm}^{-1}$ [6]. The individual transitions are shifted by $\Delta\sigma_s$ to account for collisional shift and subsequently convolved with the line shape functions for Doppler and collisional broadening. In a last step, the final spectrum is created by summation over all transitions and convolution with the laser bandwidth, which is assumed to be Gaussian. For a two-photon process, the appropriate width is $\Delta\hat{\nu}_L = \sqrt{2}\Delta\nu_L$ as a consequence of the convolution of the laser line shape with itself. Fig. 2.8 shows the simulation of excitation spectra step-by-step.

In addition to excitation spectra, the code optionally allows to simulate LIF emission spectra to aid the design process of a bandpass filter used in the detection system. Emission from the B to the A state follows the selection rules for one-photon transitions,

[4]Doppler broadening is also given in Table 2.22 in [31], but it is assumed that the reported value of $0.353\,\mathrm{cm}^{-1}$ is incorrect as it is inconsistent with the data in Fig. 2.20 on the same page. Plotted Doppler broadening values agree with calculated values using Eq. (2.21).

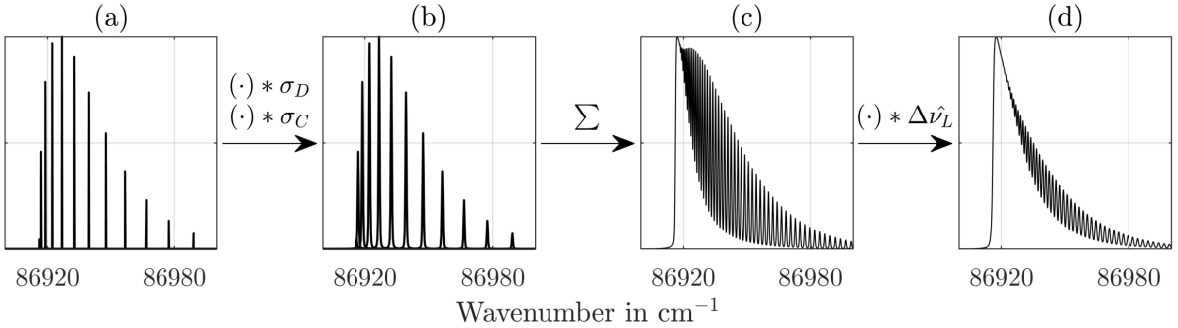

Figure 2.8: Step-wise demonstration of the simulation of two-photon excitation spectra for CO $B - X$ transitions. (a) shows the stick spectrum which is convolved with the appropriate line shapes for collisional and Doppler broadening after accounting for collisional shift to create spectrum (b). For better visibility, only every 5^{th} J'' is shown. Spectrum (c) is generated by summation over all J'' transitions. This is subsequently convolved with the appropriate laser line shape function to generate the final excitation spectrum (d). Conditions for the simulation: atmospheric pressure, $T = 2000\,\text{K}$, $\Delta\nu_L = 0.5\,\text{cm}^{-1}$.

i.e. $\Delta J = -1{,}0{,}+1$, giving rise to a P, Q and R-branch. As VET and RET processes are neglected, fluorescence results from a single laser excited state. Intensities for these branches are calculated using Eq. (2.24) [31].

$$I_{v',J'} = A_{v'v''}\frac{S_{J'J''}}{2J''+1}g_{J''} \tag{2.24}$$

Here, $A_{v'v''}$ denote the Einstein-A coefficients for a vibrational transition from $A(v') \leftarrow B(v'')$ and $S_{J'J''}$ the Hönl-London-factors for $^1\Pi \leftarrow ^1\Sigma^+$ transitions given in Eq. 2.25 [31].

$$\begin{aligned} S_P &= \frac{J''-1}{4} \\ S_Q &= \frac{2J''+1}{4} \\ S_R &= \frac{J''+2}{4} \end{aligned} \tag{2.25}$$

Due to a finite bandwidth of the excitation laser, typically multiple overlapping J'' are excited. This is especially true when exciting near the band head to achieve high signal intensities. Thus, the laser line overlap integral $g_{J''}$ is used to weigh individually created emission spectra for every $B - X$ transition with $J'' = 0 - 65$ to create a final spectrum. Creating the emission spectrum is similar to the process described for the excitation spectra. Transition center frequencies are obtained by subtracting the energy levels in the B-state from the respective A-state levels using Eq. 2.23. For the calculation of A state energies, constants from Le Floch are used [103]. Einstein-A coefficients for the vibrational transitions are extracted from Da Silva et al. [38]. The used values are summarized in Tab. 2.3. Lambda-doubling in the $A^1\Pi$ state is typically accounted for by the parameter q_v by introducing a term $\pm\frac{1}{2}q_v J''(J''+1)$ to $F(v'',J'')$ in Eq. (2.19). In this context, Lambda-doubling is ignored due to the fact that the wavenumber resolution for the simulation of

Table 2.3: Constants for energy levels of the CO molecule within the A-state in cm^{-1} and corresponding Einstein-A coefficients in s^{-1}.

v'	0	1	2	3	4	5
$T_{v'}$	64 748.1333	66 230.3506	67 677.5003	69 089.9702	70 467.5285	–
$B_{v'}$	1.604147	1.581374	1.558362	1.535046	1.511619	–
$D_{v'} \times 10^6$	7.351	7.462	7.584	7.700	7.879	–
$H_{v'} \times 10^{11}$	−1.08	−1.37	−1.37	–	–	–
$q_{v'} \times 10^5$	2.3	−2.85	–	−1.44	−2.61	–
$A_{v'v''} \times 10^6$	1.171	2.321	2.579	2.104	1.407	0.819

emission spectra is limited by the resolution of a typical spectrometer and can thus be assumed larger than the typical energy difference introduced by Lambda-doubling. To extend emission spectra simulation to transitions with $v' = 0 - 5$, values in Tab. 2.3 have been linearly extrapolated to extract constants for $v' = 5$. Emission spectra are simulated on a wavenumber grid with $0.05\,\mathrm{cm}^{-1}$ resolution for accurate placement of the center frequencies of $B - A$ transitions to create stick spectra. These spectra are subsequently summed and convolved with a Lorentzian line shape with $\approx 1\,\mathrm{nm}$ FWHM to approximate the apparatus function of a typical spectrometer. The choice of the line shape is somewhat arbitrary. The justification to use a Lorentzian rather than a Gaussian is that it gives a better fit to experimental data available in the literature, see Fig. 2.13. Fig. 2.9 shows examples of resulting simulated emission spectra after excitation of different ground state J''. A strong dependence with respect to center frequencies of the vibrational bands is

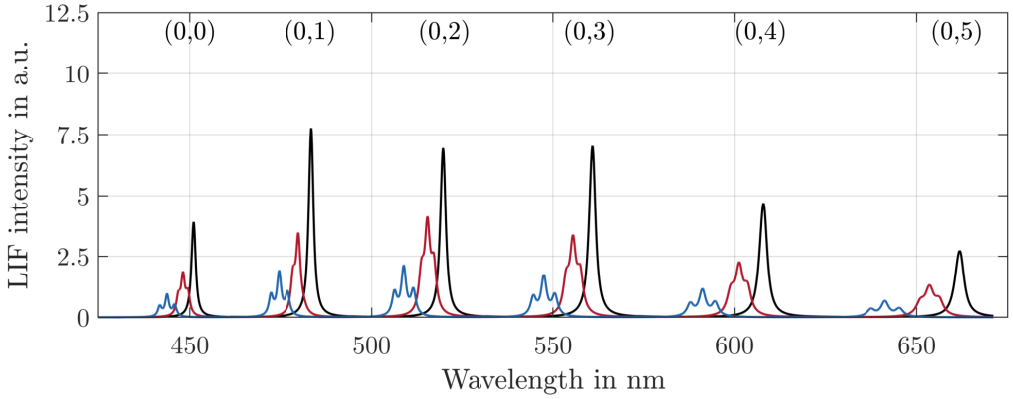

Figure 2.9: Simulated emission spectra with varying excitation frequencies at $\Delta\nu_L = 0.5\,\mathrm{cm}^{-1}$. Black: $J'' = 0 - 6$. Multiple transitions excited due to close spacing of rotational lines near the band head; Red: $J'' = 20$; Blue: $J'' = 32$. Other simulation conditions: $T = 2000\,\mathrm{K}$, atmospheric pressure, 2.6% CO in dry air, $0.1\,\mathrm{GW\,cm}^{-2}$ laser intensity. Spectrometer resolution $60\,\mathrm{cm}^{-1}$.

observed depending on the excitation center frequency. Exciting higher J'' leads to a shift towards lower wavelengths and visible splitting of P-, Q- and R-branches. E.g. within the (0,1) vibrational band, which is commonly used in detection due to its high Einstein-A coefficient and reduced interference with C_2 Swan-band emission, the Q-branch emission

wavelength is shifted by $\approx 9\,\mathrm{nm}$. This is an important point to consider when using narrow-band filters for detection when doing line scan measurements. Fig. 2.10 shows the potential impact of different detection schemes on measured excitation spectra. For

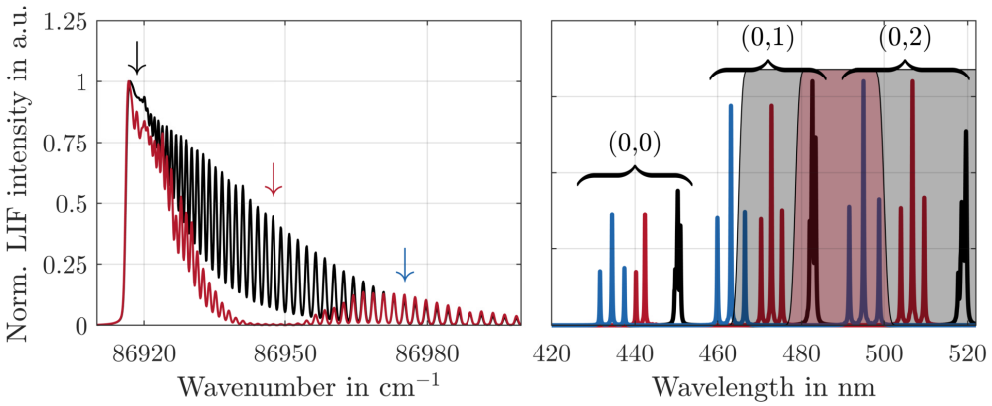

Figure 2.10: Simulated CO two-photon LIF excitation scans with two different simulated detection filters. Left: excitation scans obtained with a longpass filter (black) and bandpass filter (red); Right: Emission spectra for three selected transitions $J'' = 10$ (black), $J'' = 36$ (red) $J'' = 50$ (blue). Locations of these transitions indicated by colored arrows in left plot. Filter pass bands represented by shaded areas.

this analysis, two different filter types are simulated: (a) a longpass filter with a rising edge at 465 nm and (b) a bandpass filter with a pass band between 478 nm and 500 nm. Both filters are simulated with an edge steepness of 2 nm. While the excitation scan with the longpass filter approximates the ideal excitation spectrum very well, significant impact is observed for the simulated bandpass filter, where the measured spectrum features a characteristic drop of the LIF signal in the region of $J'' = 10 - 45$. This behavior results from the shift of vibrational emission bands when exciting higher ground state J''s. Exciting near the band head at $J'' = 10$, the (0,1) transition is well isolated within the pass band. At $J'' = 36$, the (0,1) vibrational band is shifted outside of the pass band towards lower wavelength and the (0,2) is not yet shifted far enough to enter the pass band at the falling edge of the filter. Exciting even higher J''s, the (0,2) vibrational band - starting with the R-branch - enters the pass band, consequently the excitation scan signal recovers. At $J'' = 50$, the (0,2) vibrational band is completeley within the pass band. As a validation of the influence arising from spectral filtering, Fig. 2.11 shows a measured excitation scan in the exhaust of a fuel rich methane-air flame[5] compared to the bandpass filter simulation. As can be seen, the characteristic drop for intermediate J'' values is also visible in the experiment. Note that the exact experimental laser line width is unknown, leading to differences in peak-to-valley contrast of rotational lines. The simulated spectrum is computed with $\Delta\nu_L = 0.3\,\mathrm{cm}^{-1}$.

As further validation of the simulation code, a comparison to measured excitation and emission spectra is presented in the following. Fig. 2.12 shows a comparison to excitation

[5] $T = 2127\,\mathrm{K}$, $P = 1\,\mathrm{bar}$, $X_{CO_2} = 0.062$, $X_{N_2} = 0.67$, $X_{H_2O} = 0.19$, $X_{CO} = 0.045$, $X_{H_2} = 0.0273$. Equilibrium mole fractions and temperature calculated using CANTERA [63] in conjunction with GRI-MECH 3.0 reaction mechanism [148]. Thanks to Florian Zentgraf for providing the experimental data.

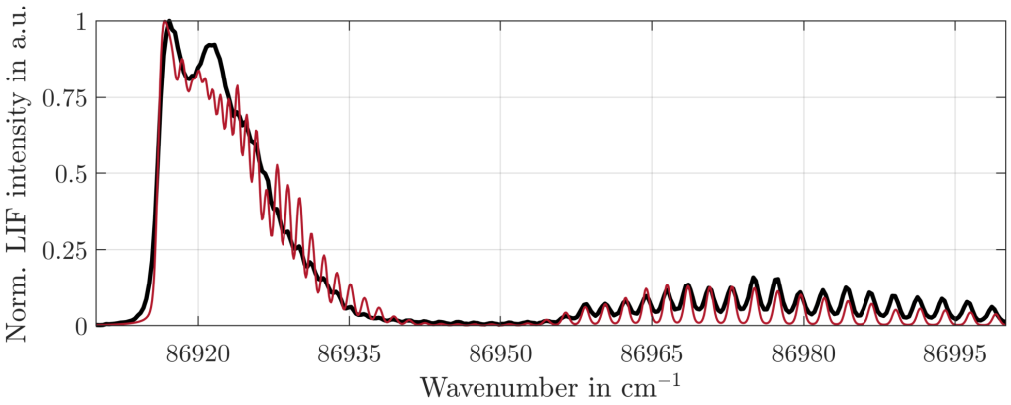

Figure 2.11: Comparison of simulated and measured excitation spectra for CO two-photon LIF. Red: simulated excitation scan with bandpass filter, cf. Fig. 2.10; Black: Measured CO excitation spectrum using a comparable bandpass filter.

spectra at $1 - 5\,\text{bar}$ acquired in the exhaust of a pressurized McKenna burner operated with a fuel-rich methane-air flame ($\Phi = 1.4$) using an excitation laser with a band width of $0.05\,\text{cm}^{-1}$ FWHM.[6] For the simulation, the chemical composition has been calculated using CANTERA, see Sect. 2.1.2.3. With a residual in the order of ± 0.1 of the peak

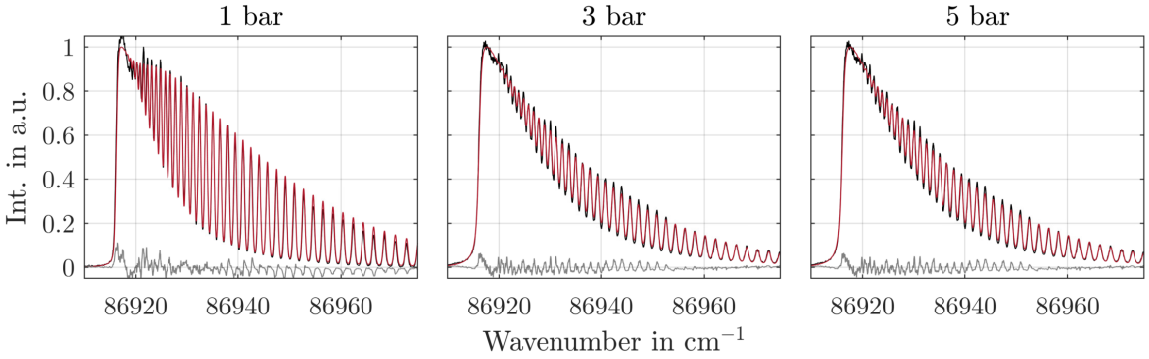

Figure 2.12: Verification of CO two-photon LIF excitation spectra at three different pressure levels. Black: experiment; Red: simulation; Gray: residual. Curves normalized to peak of simulated spectra.

normalized spectra, the simulation agrees reasonably well with the experiment. The oscillations visible in the residual resemble the structure of the rotational lines. This suggests that the line shape is inadequately computed which might be a result of a different temperature - which affects Doppler *and* collisional broadening - and/or chemical composition - that affects collisional broadening - between experiment and simulation, e.g. due to heat loss of the flame.

Fig. 2.13 shows a comparison between simulated emission spectra and data from Rosell et al. [132] and Voigt et al. [159]. In comparison to Rosell's data, the agreement between

[6] Thanks to Dr. Johannes Heinze, DLR Cologne, for providing the experimental data.

simulation and experiment is within 10%. For the first three vibrational bands, this uncertainty arises mainly from the shape of the transition dominated by the spectrometer resolution. For the (0,3) vibrational band, the peak is over estimated by $\approx 12\%$. This may be a result of uncertainties in the relative variation of Einstein-A coefficients or inaccuracies in the measured spectra. Additionally, peaks left and right of the (0,0) transition result form residual radiation of the fundamental frequency of the used Optical Parametric Oscillator (OPO) for excitation which impacts the measured spectral shape of the (0,0) and (0,1) transition. In Voigt et al. [159], no wavelength dependent detection efficiency is reported, thus a comparison of the intensities between simulation and experiment can not be conducted. However, this comparison verifies the wavelength shift in emission spectra introduced due to a different excitation scheme. In their paper, they use sum-frequency mixing of the third harmonic of an injection seeded pulsed Nd:YAG laser and the fundamental wavelength of a dye laser at 654 nm to generate radiation around 230.1 nm with a bandwidth of $\Delta\nu_L \leq 0.05\,\mathrm{cm}^{-1}$ which is below the rotational line width even at atmospheric pressure, allowing to excite single J'' transitions. The emission spectrum is recorded after excitation of $J'' = 32$. The difference in location of Q-branch transition peaks between simulation and experiment is ≤ 0.5 nm. Note that this difference may as well be a result of digitizing the plot published in [159].

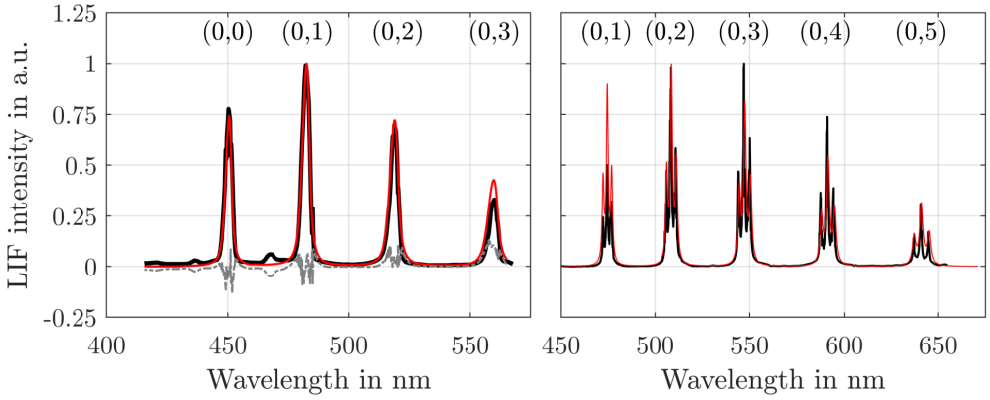

Figure 2.13: Left: comparison between simulated spectra using the proposed code and data from Rosell et al. [132]. Solid lines represent measurements at 0.1 bar pure CO after excitation around 230.1 nm with a bandwidth of $\Delta\nu_L = 4\,\mathrm{cm}^{-1}$ ($J'' = 0 - 17$). Red line shows simulated emission spectrum with $60\,\mathrm{cm}^{-1}$ resolution using the proposed code multiplied by the efficiency curve reported in Fig. 3 of [132] to account for their wavelength dependent detection efficiency. Right: Comparison to Voigt et al. [159] with narrow-band excitation of $Q(23)$ with $\Delta\nu_L = 0.05\,\mathrm{cm}^{-1}$. No wavelength dependent detection efficiency reported. For both cases, spectra have been peak-normalized. Data digitized from publications using [130].

Interferences Aside from the desired CO fluorescence signal, interferences may arise from different sources, which under certain circumstances limit the applicability of the method. Two of these interferences is C_2-LIF and C_2 chemiluminescence. While the latter may easily be suppressed by temporal gating of the detection system, interference from

C_2-LIF is superimposed on the CO-LIF signal on the same time scale. Even though C_2 is only a minor species in the presented premixed methane-air flames in Sect. 2.1.2.3, C_2 may be photolytically produced by UV radiation around 230.1 nm [23]. For this reason, commonly the (0,1) vibrational band is isolated using a narrow bandpass filter around 484 nm to minimize this influence on the detection side by suppressing C_2 Swan-band emission at the cost of reduced signal intensity. Additionally, photolytic production of CO by dissociation of CO_2 may introduce an artificial increase in the measured LIF signal [118]. This effect is further investigated and discussed in Sect. 5.

2.2.1.3 NO-PLIF

In this work, NO-PLIF is used for the investigation of mixing effects in Sect. 4 by seeding the effusion cooling air with NO. As LIF signals are proportional to the *number density* rather than the *mole fraction*, a careful excitation line selection must be made to achieve proportionality between the measured LIF signal and the quantity of interest, namely the *effusion air mole fraction*. This is achieved by simulating excitation and emission spectra of NO using LIFSim 3.17 by Bessler et al. [16]. The following paragraphs describe the features of LIFSim and the general structure how spectra are simulated. The procedure of selecting a proper transition is described in Sect. 4.

Spectral simulation LIFSim uses a three-level non-transient linear model for simulation of excitation spectra and LIF signals. The code features temperature dependent collisional broadening and shifting using data from [46] and [32] for collisions with O_2, H_2O and N_2. For CO_2, CO and CH_4, calculated values from semi-classical phase-shift theory are used. Electronic quenching is accounted for by using temperature dependent cross-sections from a harpoon model [122] for collisions with N_2, O_2, CO_2, CO, H_2O, NO, NO_2, N_2O, NH_3, NH, O, H, OH and CH. The model assumes, that the fluores-

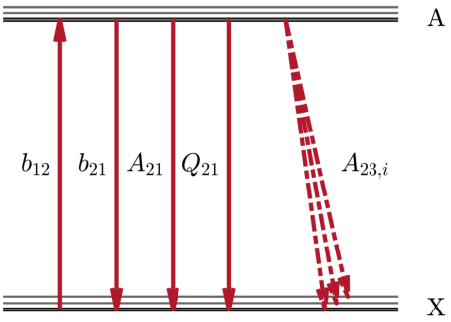

Figure 2.14: Energylevels of the NO molecule for spectral simulation with LIFSim. b_{12}, b_{21} and Q_{21} denote the stimulated absorption, stimulated emission and quenching rate between the lower state 1 and upper state 2. $A_{23,i}$ corresponds to the Einstein-A coefficients from the laser excited state to rovibrational states within the electronic ground state. Figure adapted from [16].

cence quantum yield is dominated by electronic quenching, i.e. no other non-radiative

loss mechanisms such as VET or RET are implemented. Consequently, emission spectra result from relaxation from a single upper state to all possible rotational and vibrational levels within the electronic ground state, see Fig. 2.14. LIFSim supports transitions from $v'' = 0-11$ to $v' = 0-1$ with $J'' \leq 50.5$[7] within the $A^2\Sigma^+ \leftarrow X^2\Pi$ system. The laser line shape is modeled as a Voigt profile, where the Gaussian and Lorentzian contribution may be parametrized indiviudally. For multiple overlapping transitions, the code computes the line overlap and integral for all contributing tranisitions to compute the total LIF signal and the corresponding emission spectrum [16].

Fig. 2.15 shows an example of an excitation spectrum in the wavelength region between $44\,150\,\mathrm{cm}^{-1}$ and $44\,300\,\mathrm{cm}^{-1}$ and an emission spectrum after excitation around $44\,227.5\,\mathrm{cm}^{-1}$.

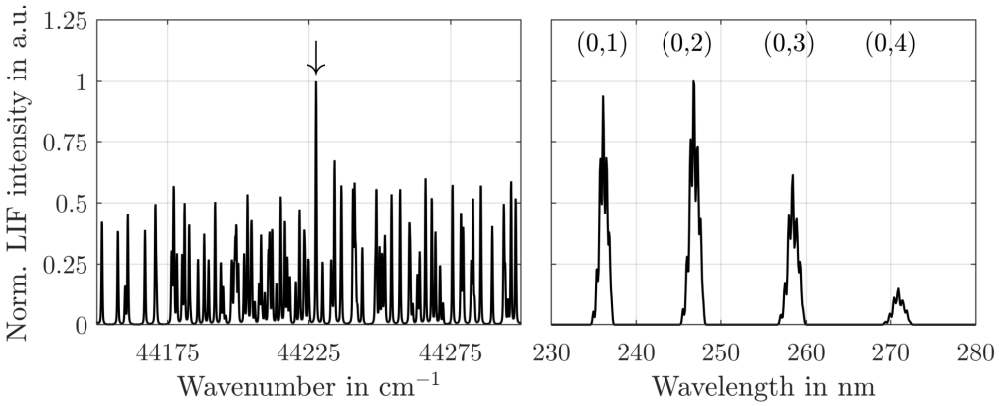

Figure 2.15: Excitation and emission spectrum - after excitation of the transition indicated with a black arrow - of NO simulated with LIFSim. $T = 2000\,\mathrm{K}$, $p = 1\,\mathrm{bar}$, Gaussian laser line shape with $0.2\,\mathrm{cm}^{-1}$ FWHM.

2.2.1.4 OH-PLIF

OH-PLIF is likely to be one of the most common measurement techniques in laser based combustion diagnostics.[8] For this reason, the spectroscopy of OH is well-known and various codes to simulate excitation and emission spectra, such as LIFBASE by Luque et al. [108] or LASKIN by Bülter et al. [28], are publicly available.

Three different excitation schemes are commonly employed in the literature which vary in their respective vibrational band used for excitation. Exciting the (0,0) band in the $A-X$ electronic system around 308 nm has the advantage of the highest Franck-Condon factors, yielding high signal strength. However, absorption of incident photons for excitation and re-absorption of fluorescence photons, an effect known as *signal trapping*, poses issues especially under circumstances with high OH number densities and long absorption path lengths. Excitation of the (3,0) band around 248 nm shows strong predissociation and

[7] LIFSim uses Hund's case (a) for notation of rotational lines.

[8] As of October 2020, the search term OH laser induced fluorescence combustion returns 50.300 results at Google Scholar.

consequently low fluorescence quantum yields. Additionally, interference from O_2 LIF may not be negligible in lean flames, particularly at increased pressure levels [11]. For these reasons, the excitation of (1,0) transitions in the $A^2\Sigma \leftarrow X^2\Pi$ system using frequency-doubled dye lasers has become the de facto standard in OH-LIF measurements. This excitation scheme was also selected for the investigations presented in Sect. 4 and 6.

Within this work, OH-PLIF is used in conjunction with absorption measurements to achieve quantitative OH number density measurements. This approach, which is further discussed in Sect. 4, requires detailed knowledge about the spectroscopy and influencing factors for the LIF signals which is presented in the following paragraph.

Spectral simulation The intensity of the OH-LIF signal S_{OH} may be expressed by Eq. (2.26) [83].

$$S_{\mathrm{OH}} = I N_{\mathrm{OH}} f_i(T) D_i B_{ij} \eta_{ij}(p,T) g_{ij}(P,T) \xi \tag{2.26}$$

Here, I and N_{OH} denote the laser intensity and OH number density, respectively. For a given transition from ground state i to excited state j, $f_i(T)$, D_i, B_{ij}, η_{ij}, g_{ij} describe the Boltzmann fraction and degeneracy of the ground state, the Einstein-B coefficient, fluorescence quantum yield and laser line overlap integral, respectively. The parameter ξ accounts for the efficiency of the detection system due to limited collection angle and transmission losses.

For flames at atmospheric pressure and above, electronic quenching is the dominant loss mechanism for the fluorescence quantum yield, reducing the definition given in Eq. (2.14) to Eq. (2.27), where $A_{v'v''}$ denotes the Einstein-A coefficient within the detection pass-band and $\sum A_{v'v''}$ the total emission rate. Q refers to the quenching rate which depends on temperature, pressure and chemical composition, see Eq. (2.15).

$$\eta_{ij}(p,T) = \frac{A_{v'v''}}{\sum A_{v'v''} + Q(p,T)} \tag{2.27}$$

Quenching cross-sections for collisions with N_2, O_2, H_2O, H_2, CO_2, CO, CH_4, H and OH are obtained from Tamura et al. [152]. Spectroscopic constants such as Einstein coefficients, temperature dependent Boltzmann factors and line positions are calculated using LIFBASE [108].

Calculating the laser line overlap integral requires a model for the transitional line shapes, which are dominated by Doppler, see Eq. (2.21), and collisional broadening. Collisional broadening is modeled with a Lorentzian line shape with an FWHM calculated using a power law of the form [74]:

$$2\gamma_c = 2\gamma_0 \frac{p}{p_{ref}} \left(\frac{T_{ref}}{T} \right)^n \tag{2.28}$$

Due to lack of detailed collisional broadening coefficients for major colliders, data from Atakan et al. [11] was used. In their publication, they report a second order polynomial dependent on the rotational quantum number N of the initial state for the FWHM $2\gamma_0$ at

a reference temperature of $T_{ref} \approx 2000\,\mathrm{K}$ for gas atmospheres encountered in the exhaust of a stoichiometric methane-air flame:

$$\frac{2\gamma_0}{p_{ref}} = 0.083 - 0.0026N + 8 \cdot 10^{-5} N^2\,\mathrm{cm}^{-1}/\mathrm{bar} \tag{2.29}$$

For the exponent n, Rea et al. report a value of 0.66 for the (0,0) vibrational band [129]. It is assumed that this value is also valid for the transitions in the (1,0) vibrational band. This uncertainty is later addressed in section 4.2.6.1.

For simulation of excitation spectra in a wider range and subsequent comparison with line scan measurements, LIFBASE is used. For the calculation of the spectral overlap, the spectral region of interest is simulated with a custom code that greatly simplifies the process because of a missing programming interface with LIFBASE. Additionally, LIFBASE only allows to export spectra which are summed over all transitions, i.e. calculating the spectral overlap of overlapping line pairs is possible, albeit respective contribution of the transitions cannot be inferred. The code has the aforementioned equations implemented and equivalence with LIFBASE has been verified by comparison of the simulated excitation spectra. Fig. 2.16 shows an example excitation spectrum simulated with LIFBASE for (1,0) vibrational band transitions within the $A - X$ system.

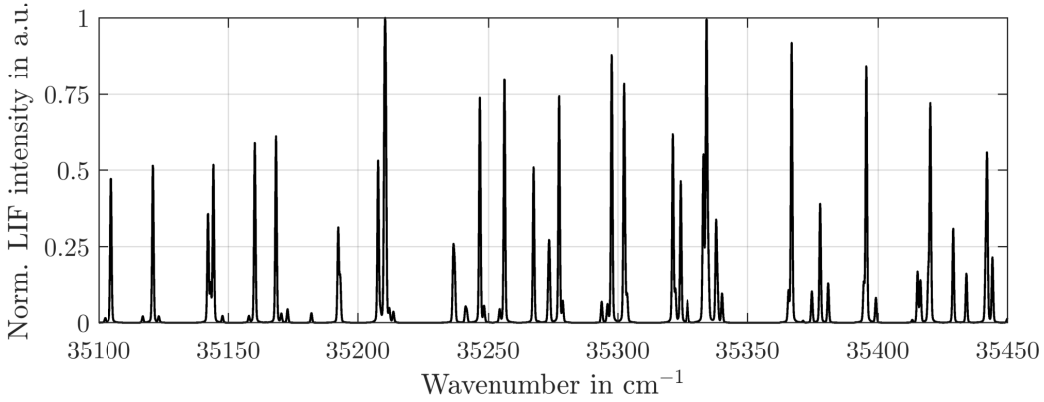

Figure 2.16: OH-LIF excitation spectrum simulated with LIFBASE for (1,0) vibrational band transitions within the $A - X$ system in the spectral region between $35\,100\,\mathrm{cm}^{-1}$ and $35\,450\,\mathrm{cm}^{-1}$.

Absorption spectroscopy Resonant absorption of light when passing through a sample with the absorption coefficient $k_{ij}(\nu)$ for a transition ij and absorption path length L is commonly described using the Beer-Lambert-Bouguer law of absorption given in Eq. (2.30), where T_ν describes the fractional transmission at frequency ν, i.e. the ratio of the transmitted light intensity I and the incident intensity I_0 at any given frequency ν [74, p. 117].

$$T_\nu = \left(\frac{I}{I_0}\right)_\nu = \exp\left(-k_{ij}(\nu)L\right) \tag{2.30}$$

The differential form of Beer's Law is given in Eq. (2.31), where dx denotes an infinitesimal increment of the path length L:

$$\mathrm{d}I_\nu = -I_\nu k_{ij}(\nu)\mathrm{d}x \tag{2.31}$$

The fact that absorption spectroscopy is used in conjunction with OH-PLIF imposes the following conditions:

(a) The OH-PLIF signal is recorded using an intensified CCD camera and as such is discretized on a uniform pixel grid.

(b) Absorption is measured by an energy reference that is spectrally integrated.

(c) The used laser has a spectral bandwidth that is in the order of the molecular transitions.

Condition (a) requires to introduce a discrete form of Eq. (2.31). For sufficiently fine discretization, a Taylor-series expansion with only the linear term provides a good approximation of the absorption profile. The linearized discrete differential form of Beer's Law is given in Eq. (2.32), where m represents the index on a uniform grid and Δx corresponds to the grid spacing.

$$I_m = I_{m-1}\left(1 - k_{ij,m}(\nu)\Delta x\right) \tag{2.32}$$

This equation describes the local intensity I at index m by subtracting the absorbed fraction from the local incident intensity I_{m-1}.

The absorption coefficient $k_{ij}(\nu)$ can be described by Eq. (2.33), where h, k, c and T are Planck's constant, Boltzmann's constant, the speed of light and the local temperature, respectively. N_i corresponds to the number density of the absorbing molecule in ground state i. B_{ij}, ν_{ij} and $\Phi_{ij}(\nu)$ represent the Einstein-B coefficient, the central frequency and the normalized spectral line shape of transition ij [74, p. 119].

$$k_{ij}(\nu) = \frac{h\nu_{ij}}{c} N_i B_{ij}\left(1 - \exp\left(-h\nu_{ij}/kT\right)\right)\Phi_{ij}\left(\nu\right) \tag{2.33}$$

This equation can be further simplified for electronic transitions, where $h\nu_{ij} \gg kT$ and as such $\exp\left(-h\nu_{ij}/kT\right) \approx 0$. With this, the spectrally integrated equation for k_{ij} may be written as:

$$k_{ij} \approx \frac{h\nu_{ij}}{c} N_i B_{ij} g_{ij} \tag{2.34}$$

Here, the laser line overlap integral g is introduced to account for the normalized line shape $\Phi_L(\nu) = \phi_L(\nu)/\int_{-\infty}^{\infty}\phi_L(\nu)\mathrm{d}\nu$ of the excitation laser with finite bandwidth:

$$g_{ij} = \int_{-\infty}^{\infty} \Phi_{ij}\left(\nu\right)\Phi_L\left(\nu\right)\mathrm{d}\nu \tag{2.35}$$

Combining Eq. (2.32) with Eq. (2.34) yields Eq. (2.36):

$$I_m = I_{m-1}\left(1 - \sum_q \frac{h\nu_{ij}}{c} N_{i,m} B_{ij} g_{ij,m}\Delta x\right) \tag{2.36}$$

The summation over all transitions q is introduced to account for all transitions that are excited within the bandwidth of the laser.

For high line-of-sight absorption, the overlap integral g varies with the spatial coordinate as the laser line shape exhibits a modulation when the absorption line width and the laser line width are in a similar order [83]. This is modeled by modifying the spectral shape of the laser by subtracting fractions r of the absorption line such that the integral of the laser line shape *prior to normalization* corresponds to the local laser intensity T_m:

$$\int_{-\infty}^{\infty} \phi_{L,m} d\nu = \int_{-\infty}^{\infty} \mathrm{H}(\phi_{L,m-1}(\nu) - r\Phi_{ij,m-1}(\nu)) d\nu \equiv T_m \tag{2.37}$$

H denotes the Heaviside function to prevent the model from returning negative values for the spectral shape of the laser. During evaluation, the parameter r is optimized in a non-linear least squares fit to ensure the resulting spectral integral of the laser line shape corresponds to the local laser intensity.

Fig. 2.17 shows the impact of the change in spectral overlap due to the modulation of the laser line shape when passing through a cell with $L = 10\,\mathrm{cm}$ and a homogeneous OH number density of $1 \times 10^{16}\,\mathrm{cm}^{-3}$ at $T = 2000\,\mathrm{K}$ for various simulated laser linewidths. For this visualization, a normalized line shape with a Doppler width of $0.3\,\mathrm{cm}^{-1}$ and collisional broadening of $0.15\,\mathrm{cm}^{-1}$ has been assumed, see Eq. (2.29) and (2.21). For a very narrow

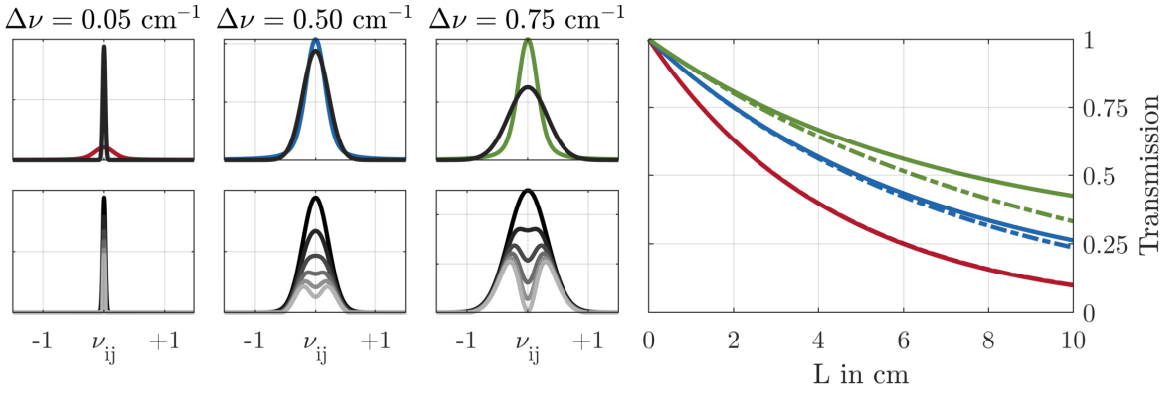

Figure 2.17: Impact of variation in local spectral overlap integral on the absorption profile in a homogeneous cell. The left group shows the simulated absorption line in color and the spectral profile of the laser in black for three different laser line widths (top) and the variation of the laser profile due to absorption at various local intensities (bottom). On the right, absorption profiles for all laser line widths are plotted with respect to the absorption path length L without (dash-dotted) and including the effect of local change in g (solid).

spectral profile of the laser, the spectral overlap integral does not vary significantly. With increasing spectral width, the modulation of the laser profile becomes increasingly stronger as the efficiency of absorption is reduced in the wings of the transitional line shape. As a consequence, the transitional line shape is *imprinted* in the laser line shape at high

absorption levels. At $\Delta\nu = 0.5\,\mathrm{cm}^{-1}$, the line of sight integrated absorption deviates by 12%. At $0.75\,\mathrm{cm}^{-1}$, the deviation amounts to 28%.

2.2.1.5 CH_2O-LIF

Within this work, CH_2O-LIF is used in Sect. 6 as a marker for regions with significant low-temperature chemistry. Formaldehyde is an organic compound occurring as an intermediate species in the reaction mechanism of hydrocarbon fuels, see Sect. 2.1.2.3. In its ground-state, CH_2O is a planar molecule with $N_A = 4$ atoms, leading to $3N_A - 6 = 6$ vibrational degrees of freedom [163]. The vibrational modes are schematically presented in Fig. 2.18. From all molecules of interest, CH_2O is the only non-diatomic and as such spectroscopically the most difficult due to the many degrees of freedom leading to a high spectral density of transitions. Despite the complexity, the electronic spectrum of formaldehyde is well understood and described in the literature [24, 33, 48, 117, 150]. For

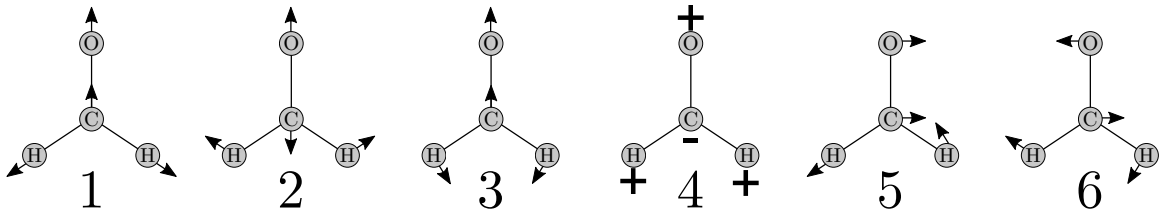

Figure 2.18: The six normal vibrations of $\tilde{X}^1A_1$ CH_2O. Figure adapted from [117].

further details regarding the molecular structure of CH_2O, the reader is referred to the cited literature. Due to the complexity of the molecule, the nomenclature for rovibronic transitions deviates from the notation used in the previous sections for diatomics. As upper-case latin letters are used to symbolize the symmetry type, e.g. A_1, electronic states are notated with a tilde, e.g. $\tilde{X}^1$ for the electronic ground state and $\tilde{A}^1$ for the first excited state. Vibrational transitions are denoted by $i^{v_i'}_{v_i''}$, which corresponds to a transition of normal vibration i from $v_i' \leftarrow v_i''$. If multiple normal vibrational modes are excited simultaneously, these bands are concatenated, leading to $i^{v_i'}_{v_i''} j^{v_j'}_{v_j''}$ as a notation for a simultaneous transition of normal vibration mode i from $v_i' \leftarrow v_i''$ and j from $v_j' \leftarrow v_j''$. For example, the 4^1_0 band within the $\tilde{A}^1A_1 \leftarrow \tilde{X}^1A_1$ electronic system denotes a transition of vibrational mode 4 from $v'' = 0$ to $v' = 1$.

In the literature, three excitation schemes are commonly used:

(a) Excitation within the 4^1_0 band using XeF excimer lasers at 353 nm, e.g. [18, 27, 29].

(b) Excitation within the 4^1_0 band using the frequency-tripled output of an Nd:YAG laser at 355 nm, e.g. [22, 58, 69, 75].

(c) Excitation within the overlapping $2^1_0 4^1_0$ and $4^2_0 6^1_0$ bands using the frequency doubled output of dye laser at 339 nm, e.g. [52, 97, 137, 145].

Due to availability of equipment, a choice between excitation at 355 nm (b) and 339 nm (c) has to be made. Excitation scheme (c) has several advantages over scheme (b): As

radiation at 355 nm overlaps with rather weak rotational lines of CH_2O only, an ≥ 10 times higher signal is expected for excitation around 339 nm. This is partly compensated by the fact that Nd:YAG lasers typically emit higher pulse energies [122]. Furthermore, cross-talk from polyaromatic hydrocarbons (PAH), which exhibit a broad excitation spectrum in the UV, is reduced with excitation sources with a narrow band width such as dye lasers [58]. In principle, this could as well be achieved by injection seeding of the Nd:YAG laser. However, such a laser is unavailable for the experiment. Another advantage of selecting transitions at lower wavelengths is the better separation from broadband fluorescence between 380 nm and 550 nm, reducing requirements on edge steepness of detection side bandpass filters [122].

Spectral simulation To simulate LIF signals and excitation spectra, an approach similar to the one described in Coriton et al. [36], which also has been used by Popp et al. [126] and Kosaka et al. [98], is employed.

In principle, as CH_2O-LIF is a one-photon transition, the LIF signal may be expressed similar to Eq. (2.26). For a given transition ij, this equation may be written as:

$$S_{CH_2O} \propto N_{\mathrm{CH_2O}} \underbrace{f_i(T)\eta_{ij}(T)g(T)}_{=k(T)} \tag{2.38}$$

Here, $N_{\mathrm{CH_2O}}$ describes the number density of CH_2O, $f_i(T)$, $\eta_{ij}(T)$ and $g(T)$ correspond to the Boltzmann fraction, fluorescence quantum yield and laser liner overlap integral. Unfortunately, no collider specific information regarding collisional quenching and broadening is available in the literature. Thus, it is assumed that every species has an equal quenching cross-section and contribution to collisional broadening. Consequently, $f_i(T)$, $\eta_{ij}(T)$ and $g(T)$ only depend on temperature and may be summarized in a single temperature-dependent correction factor $k(T)$.

Assuming a constant quenching cross-section for every collider, the quenching rate Q may be expressed by (2.39) with $\sigma_i \equiv \text{const}$:

$$\begin{aligned} Q &= \underbrace{N_{tot}}_{\propto T^{-1}} \underbrace{\sum_i X_i \sigma_i \left(\frac{8kT}{\pi \mu_i}\right)^{0.5}}_{\propto T^{0.5}} \\ Q &\propto T^{-0.5} \end{aligned} \tag{2.39}$$

Furthermore it is assumed, that quenching is the dominant loss mechanism and as such $\eta_{ij}(T) \propto 1/Q \propto T^{0.5}$.

For the calculation of the temperature dependent Boltzmann fraction and laser line overlap integral, AsyrotWin [94] with spectroscopic data from Clouthier et al. [33] is used to simulate absorption spectra in the temperature range between 300 K and 2000 K. The procedure to create absorption spectra is as follows:

(a) Create stick spectra of all transitions in the spectral region of interest between 338 nm and 340 nm within the $\tilde{A}^1A_2 \leftarrow \tilde{X}^1A_1$ system, including contributions from the $2_0^1 4_0^1$ and $4_0^2 6_0^1$ band.

(b) Convolve every transition with a Gaussian of appropriate Doppler width as calculated using Eq. (2.21) and sum all transitions.

(c) Convolve the summed Doppler-broadened spectrum using a Lorentzian to account for collisional broadening.

(d) Convolve with another Gaussian with the spectral bandwidth of the excitation laser to include the laser line overlap in the simulation.

Fig. 2.19 shows an example absorption spectrum of CH_2O around 339 nm.

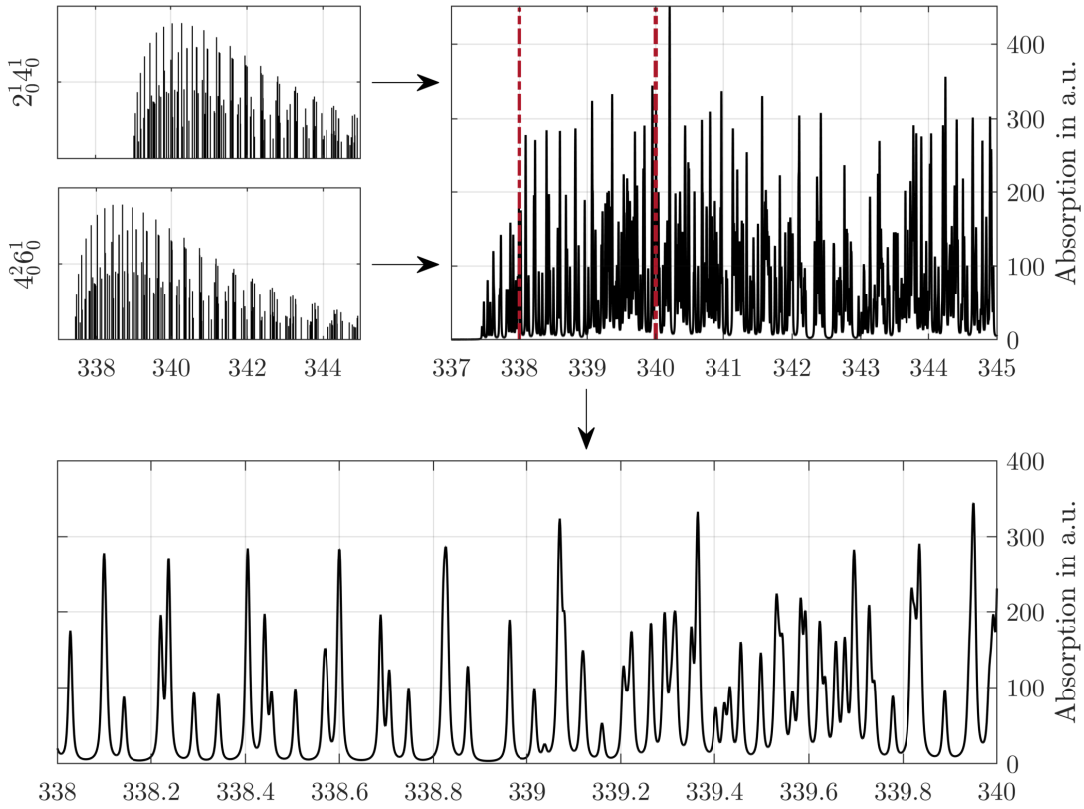

Figure 2.19: Example absorption spectrum of CH_2O simulated with AsyrotWin [94] at $T = 300\,\mathrm{K}$. Upper row shows construction of spectrum with contributions from the $2_0^1 4_0^1$ and $4_0^2 6_0^1$ band with subsequent broadening. Doppler broadening $0.07\,\mathrm{cm}^{-1}$; Collisional broadening $0.5\,\mathrm{cm}^{-1}$; Laser line width $0.5\,\mathrm{cm}^{-1}$. All values FWHM. Bottom plot shows zoomed in window between dashed lines at 338 nm and 340 nm.

In principle, this procedure includes variations in ground-state Boltzmann population and the laser line overlap integral from Eq. (2.38). Unfortunately, spectroscopic data for accurate simulation of the line shape of transitions in the $\tilde{A}^1A_2 \leftarrow \tilde{X}^1A_1$ system is unavailable in the literature. Thus, a Monte-Carlo simulation is conducted to provide a sensitivity analysis of the temperature dependency arising from uncertainties in the laser line shape (Gaussian) and collisional broadening (Lorentzian) contributions to the transitional line widths. Within the Monte-Carlo simulation, the spectral simulation is coupled with a laminar flame simulation as described in Sect. 2.1.2.3. This allows to estimate the error

induced by various uncertainties in the spectral simulation on identification of regions with significant low-temperature chemistry.

The parameters varied in the Monte-Carlo simulation are collisional broadening, as modeled using the power-law given in Eq. (2.28), with $2\gamma_0/P_{ref} \in [0.045,0.45]\,\mathrm{cm^{-1}\,bar^{-1}}$ and various temperature exponents $n \in [0,1]$. The range for collisional broadening coefficients is based on Co et al. [34], who reported a pressure broadening coefficient of $1.8 \times 10^{-4}\,\mathrm{cm^{-1}\,Torr^{-1}} = 0.135\,\mathrm{cm^{-1}\,bar^{-1}}$ for transitions in the spectral region between 351 nm and 356 nm. It is assumed that the spectral region around 339 nm presents values in the same order of magnitude. The defined range for the collisional broadening coefficient reaches from 1/3 to 3 times the value reported by Co. The reasoning for the variation of the temperature exponent is to include a high degree of uncertainty of interaction mechanisms. A temperature exponent of $n = 0$ corresponds to a case where the collisional broadening coefficient $2\gamma_0$ is entirely independent of temperature whereas $n = 1$ implies density driven interaction, i.e. strong reduction of collisional broadening with temperature due to increased mean free path length. In the following example, this leads to variations in FWHM values for the Lorentzian used for collisional broadening between $0.0005\,\mathrm{cm^{-1}}$ and $1\,\mathrm{cm^{-1}}$. Gaussian contribution is varied using FWHM values between $0.002\,\mathrm{cm^{-1}}$ and $2\,\mathrm{cm^{-1}}$ for the laser line width.

As a representative example, a Monte-Carlo simulation with 10^4 realizations as described above for the temperature dependency of the transition at 339.069 nm is shown in Fig. 2.20. The temperature dependency is extracted from the simulations by extracting the value at the peak of the selected transition for all temperatures and subsequent multiplication by $T^{0.5}$ to approximate influence from quenching as discussed above. The temper-

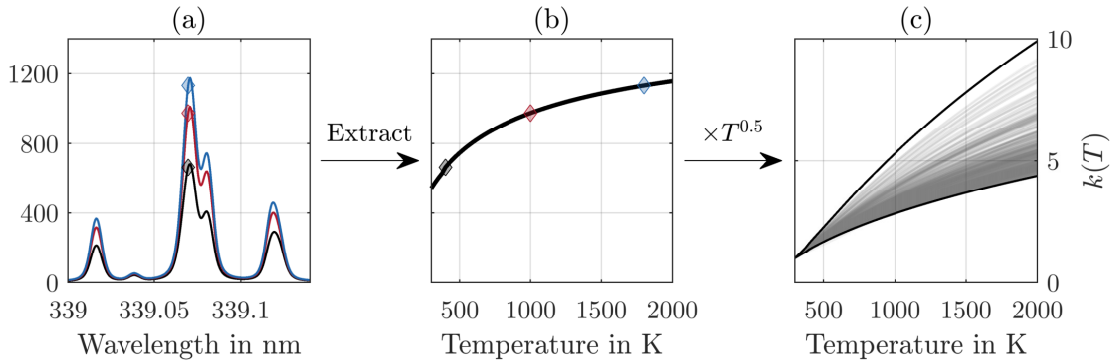

Figure 2.20: Monte-Carlo simulation of the temperature dependence of the CH_2O-LIF signal after excitation at 339.069 nm. Step-wise derivation of temperature dependent correction factor $k(T)$: (a) Simulation of absorption spectra with varying temperature and extraction at central excitation wavelength (b). (c) shows the variation of total $k(T)$ including $\eta \propto T^{0.5}$ as approximated by the Monte-Carlo simulation. Correction factor normalized to $k(T) \equiv 1$ at 300 K.

ature dependency shows a monotonically increasing slope[9] which is strongly affected by

[9]This seems inconsistent with Kosaka et al. [97]. Apparently, Kosaka uses the mole fraction rather than the number density of CH_2O for the calculation of S_{CH_2O}, which adds an additional T^{-1} dependency.

the uncertainties included in the Monte-Carlo simulation. The maximum relative error of $k(T)$ at 2000 K is a factor of ≈ 2. However, the influence on measured CH_2O profiles is less prominent as these values suggest. Fig. 2.21 shows a comparison between the spatial profile of N_{CH_2O} and S_{CH_2O} as computed with the temperature dependent correction factors $k(T)$ from all Monte-Carlo realizations. Effectively, as CH_2O is an intermediate

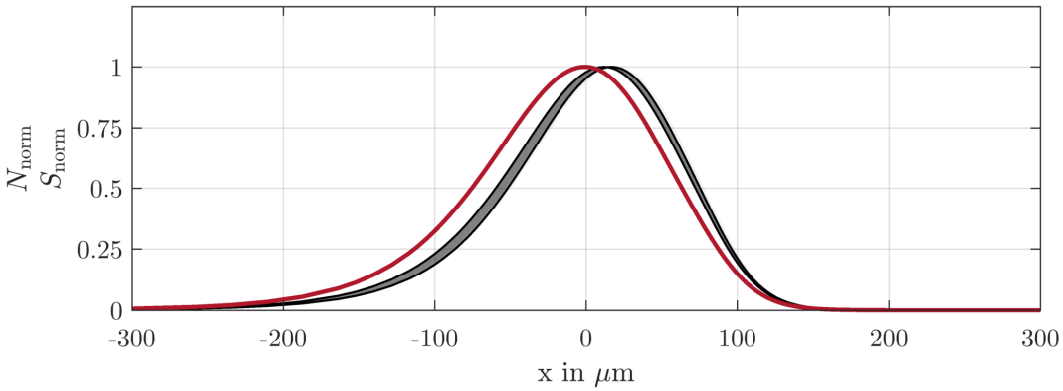

Figure 2.21: Impact of temperature dependency of CH_2O-LIF signals when comparing to laminar flame simulations. Red: Peak-normalized N_{CH_2O} from laminar flame simulation; Grey: simulated LIF signals with various $k(T)$ results from Monte-Carlo simulation. $x \equiv 0$ at peak simulated number density, i.e. unburnt fresh gas at $x < 0$ and burnt region at $x > 0$.

species which has only significant number densities in a narrow temperature range, the deviation between a simulated LIF signal and the underlying number density may be described by a shift of approximately 20 µm towards the high temperature region within the reaction zone. Even when artificial temperature dependencies $k(T) = T^p$ with $p \in [-2,2]$ are adopted, the deviation between the peak location of CH_2O number density and the measured LIF signal is - as a first-order approximation - only shifted by 35 µm towards higher temperatures for T^2 or 41 µm towards lower temperatures for T^{-2}, see Fig. 2.22. This deviation is in the order of or even below the spatial resolution commonly achieved with imaging systems, see Sect. 2.2.3, and as such may safely be ignored in this context.

2.2.2 Coherent Anti-Stokes Raman Spectroscopy

Single-shot ro-vibrational coherent anti-Stokes Raman spectroscopy with N_2 as a resonant species using a broadband Stokes laser is used for point-wise measurements of the gas-phase temperature in Sect. 5. In the following, a general description of the CARS process is given followed by a derivation of the spectrally resolved CARS signal intensity, which is subsequently used to derive temperature information by means of a spectral fit. In previous publications, CARSFT [120] was used for the process of spectral fitting [E8, E9]. Due to the rather inefficient process which involves passing data via ASCII files to CARSFT

Including this in the calculation of $k(T)$ yields a calibration curve that closely resembles the one obtained by Kosaka.

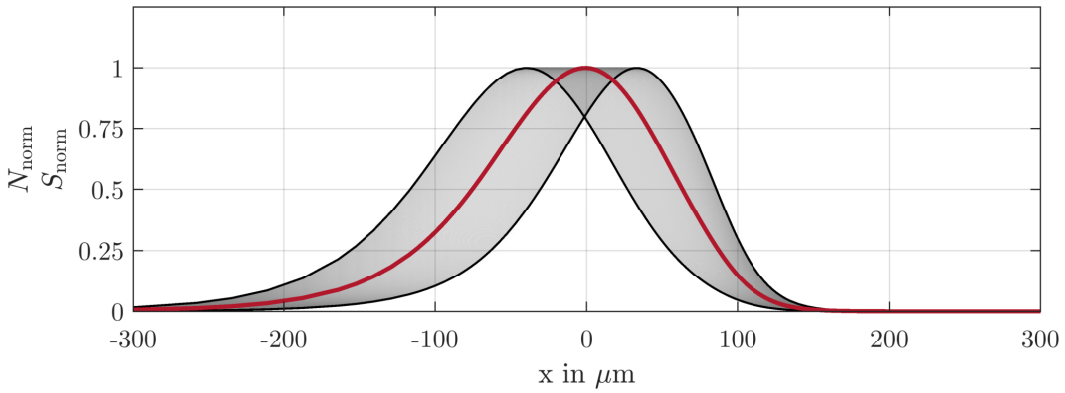

Figure 2.22: Impact of artificial temperature dependencies of CH_2O-LIF signals when comparing to laminar flame simulations. Red: N_{CH_2O} from laminar flame simulation; Grey: simulated LIF signals with various $k(T)$ results from Monte-Carlo simulation. $x \equiv 0$ at peak simulated number density, i.e. unburnt fresh gas at $x < 0$ and burnt region at $x > 0$.

that uses a gradient-based solver for fitting, which in addition is very susceptible to local minima, a novel fitting strategy based on precomputed library spectra in conjunction with a mixed-integer genetic algorithm (MI-GA) was implemented in MATLAB. The code, named MARSFT[10], has been published[11] under MIT license for further community based development. A detailed description of the method may be found in [E6] licensed under CC BY 4.0 [1].

2.2.2.1 General Description

Coherent anti-Stokes Raman spectroscopy is a technique that has been widely used in combustion research [70]. In principle, CARS probes the same Raman active modes as spontaneous Raman spectroscopy (SRS) but has the advantage of producing a coherent signal and thus has comparably high signal intensities [50]. This is realized by a four-wave mixing process which obeys the energy and momentum balance given in Eq. (2.40), where ω_{1-4} denotes the frequency of the pump, Stokes and probe laser and the CARS signal with corresponding wave vectors $\vec{k}_i = 2\pi/\lambda_i$ [49].

$$\begin{aligned} \omega_1 - \omega_2 + \omega_3 - \omega_4 &= 0 \\ \vec{k}_1 - \vec{k}_2 + \vec{k}_3 - \vec{k}_4 &= 0 \end{aligned} \tag{2.40}$$

Fig. 2.23 schematically shows the fundamental CARS principle represented by the energy levels involved in the process. The pump beam with frequency ω_1 excites the molecule of interest to a virtual state – i.e. not an eigenstate – which is left by stimulated emission using the probe beam ω_2, leaving the molecule in a coherently excited ro-vibrational state. The probe beam scatters from these coherences, generating the CARS signal with

[10]The name *MARSFT* (MATLAB-based coherent anti-Stokes Raman Fitting Tool) was chosen to honor the extraordinary amount of effort that went into the development of CARSFT at Sandia National Labs.
[11]https://github.com/tudarsm/marsft

frequency ω_4. To drive such a non-linear optical process, high peak intensities are necessary such that commonly CARS is only applied point-wise, i.e. 0D. Recent developments in ulta-short-pulse laser systems enabled 1D measurements and even 2D measurements [19, 20, 93]. Due to equipment availability, gas-phase temperature measurements in Sect. 5 are performed with a nanosecond laser system and are thus limited to point-wise measurements. Typically, for reduced experimental complexity, the same laser is used as

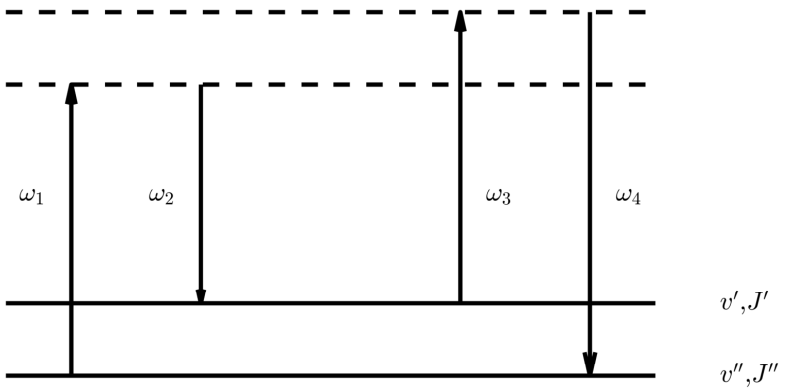

Figure 2.23: CARS energy level diagram. Solid lines represent eigenstates of the molecule of interest, dashed lines correspond to virtual, i.e. *forbidden* states. Figure adapted from [74].

a pump and probe source although dual-pump configurations are described in the literature, which allow to extend the number of species probed simultaneously [37, 73, 119, 153]. For measurements in Sect. 5, only N_2 is selected as a a resonant species, i.e. $\omega_1 = \omega_3$.

Conservation of momentum, i.e. the balance of wave vectors in Eq. (2.40), imposes a condition commonly referred to as *phase matching* depicted in Fig. 2.24. This condition requires, that the beams are overlapped in the measurement volume at a certain angle that allows constructive interference of the emerging coherent signal. Aside the trivial

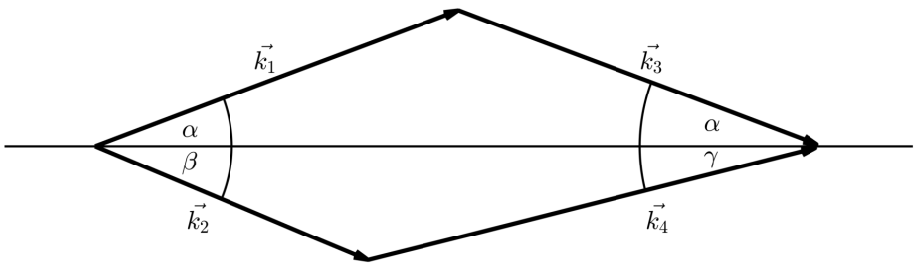

Figure 2.24: Phase-matching of the wave vectors involved in the CARS process with $\omega_1 = \omega_3$.

solution $\alpha = \beta = \gamma = 0$, beams may be arranged in a BOXCARS configuration to reduce the interaction length and thus improving spatial resolution in the principal direction [49].

To excite resonances of the probed molecule, the frequency difference $\omega_1 - \omega_2$ has to be chosen adequately to match the transitions of the molecule of interest. These transitions may either be purely rotational or additionally include a change in the vibrational state, i.e. ro-vibrational transitions. For single-shot measurements of ro-vibrational CARS spectra, the Stokes laser is designed with a broad spectral width of around $100\,\mathrm{cm}^{-1}$, to allow excitation of multiple transitions with a single pulse. Subsequently, the CARS signal is dispersed in a spectrometer and recorded with a CCD camera. Temperature information is then evaluated by fitting a physical model to the acquired data. The following subsection describes the physical model for ro-vibrational N_2 CARS spectra used in this work.

2.2.2.2 Simulation of Spectra

The spectral shape of the CARS signal arises from the squared modulus of the complex third order susceptibility $\chi^{(3)}$ given in Eq. (2.41). Here, a_q, Γ_q and $\Delta\omega_q = \omega_q - \omega_1 + \omega_2$ correspond to the amplitude and line width of transition q and the detuning from the Raman resonance at ω_q. These terms are used to model individual transitions with a Lorentzian line shape which are subsequently summed within the spectral region of interest. $\chi^{(3)}_{NR}$ denotes the non-resonant susceptibility which is wavelength independent, purely real and depends on the gas composition, as every species in the measurement volume contributes with its mole fraction weighted non-resonant susceptibility.

$$\begin{aligned} |\chi^{(3)}|^2 &= |\sum_q \frac{a_q}{\Delta\omega_q - i\Gamma_q/2} + \chi^{(3)}_{NR}|^2 \\ I_{CARS}/I_{Stokes} &= I^*_{CARS} \propto G_i * |\chi^{(3)}|^2 \end{aligned} \tag{2.41}$$

Typically, the spectral profile of the Stokes laser is not flat. To account for this intensity distribution, the measured CARS signal is normalized to a non-resonant signal acquired in a medium that has no nearby Raman resonances, e.g. CH_4 or Ar. Due to finite resolution of the spectrometer and finite bandwidth of the pump and probe beam, the normalized CARS signal I^*_{CARS} is proportional to the squared modulus convolved with the apparatus function G_i. To solve Eq. (2.41), information on the amplitude, position and line width of every transition is required. The individual components and resulting spectra are compared to computations using CARSFT which in addition to spectral simulations has the option to write information on the involved transitions to a file which are used to verify the implementation.

Line positions The spectral position of a given transition is calculated by subtracting the energy level of the ground state at v'', J'' from the energy level of the excited state at v', J', see Eq. (2.42). Energy levels for a given vibrational and rotational quantum number are calculated using the respective equations in Eq. (2.19) with spectroscopic

constants for N_2 taken from the documentation of CARSFT [120].

$$\omega_q = G(v') + F(v',J') - G(v'') - F(v'',J'') \tag{2.42}$$

These energy levels are also used to compute the Boltzmann fractions required for the calculation of the amplitudes a_q for a given initial state v'', J'' using Eq. (2.20) extended with the different degeneracies for even and odd J'' values (6 and 3, respectively).

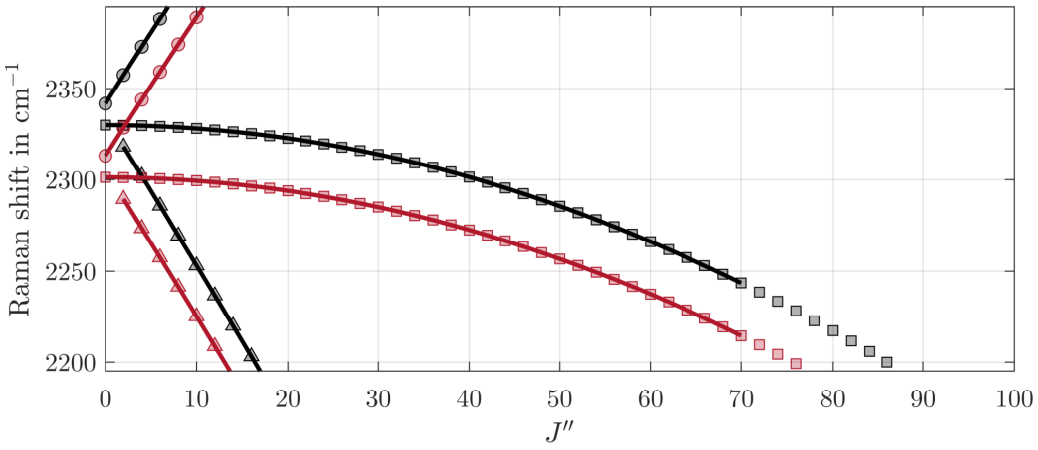

Figure 2.25: Line positions calculated for N_2 CARS spectra. Circles, squares and triangles represent O-, Q- and S-branches as calculated from Eq. (2.42), respectively. Shown are the first two vibrational bands $v'' = 0$ (black) and $v'' = 1$ (red). Solid lines represent the line positions as computed with CARSFT for comparison. Only every second J'' value shown for better readability.

Amplitudes The amplitude of transition q is expressed by Eq. (2.43), where N is the number density of the resonant species, c the speed of light, $\hbar$ the reduced Planck's constant, ω_S the Stokes wavenumber. These terms are constant for every ground-state v'' and J''. The differential Boltzmann fraction Δ_q and the differential Raman cross-section $\frac{\delta\sigma}{\delta\Omega}\Big|_q$ on the other hand depend on the vibrational and rotational quantum number.

$$a_q = \frac{Nc^4}{\hbar\omega_S^4}\Delta_q \left.\frac{\delta\sigma}{\delta\Omega}\right|_q \tag{2.43}$$

For ro-vibrational CARS spectra of N_2, the selection rules are $\Delta v = 1$, $\Delta J = -2, 0, +2$ (O-,Q- and S-branch), with corresponding differential Raman cross-sections given in Eq.

(2.44) for parallel and perpendicular polarization of pump and probe beam [26, 91, 111].

$$
\begin{aligned}
\left.\frac{\delta\sigma}{\delta\Omega}\right|_{\substack{v''+1\leftarrow v''\\ J''-2\leftarrow J''}} &= \frac{\hbar\omega_S^4}{2\omega_e c^4 M}\times\left(\frac{2}{15}b^O_{J',J''}F^O_\gamma\gamma^2\right)(v''+1) && \mathrm{O}_\parallel\\
\left.\frac{\delta\sigma}{\delta\Omega}\right|_{\substack{v''+1\leftarrow v''\\ J''\leftarrow J''}} &= \frac{\hbar\omega_S^4}{2\omega_e c^4 M}\times\left(F^Q_\alpha\alpha^2+\frac{4}{45}b^Q_{J',J}F^Q_\gamma\gamma^2\right)(v''+1) && \mathrm{Q}_\parallel\\
\left.\frac{\delta\sigma}{\delta\Omega}\right|_{\substack{v''+1\leftarrow v''\\ J''+2\leftarrow J''}} &= \frac{\hbar\omega_S^4}{2\omega_e c^4 M}\times\left(\frac{2}{15}b^S_{J',J''}F^S_\gamma\gamma^2\right)(v''+1) && \mathrm{S}_\parallel\\
\left.\frac{\delta\sigma}{\delta\Omega}\right|_{\substack{v''+1\leftarrow v''\\ J''-2\leftarrow J''}} &= \frac{\hbar\omega_S^4}{2\omega_e c^4 M}\times\left(\frac{1}{10}b^O_{J',J''}F^O_\gamma\gamma^2\right)(v''+1) && \mathrm{O}_\perp\\
\left.\frac{\delta\sigma}{\delta\Omega}\right|_{\substack{v''+1\leftarrow v''\\ J''\leftarrow J''}} &= \frac{\hbar\omega_S^4}{2\omega_e c^4 M}\times\left(\frac{1}{15}b^Q_{J',J''}F^Q_\gamma\gamma^2\right)(v''+1) && \mathrm{Q}_\perp\\
\left.\frac{\delta\sigma}{\delta\Omega}\right|_{\substack{v''+1\leftarrow v''\\ J''+2\leftarrow J''}} &= \frac{\hbar\omega_S^4}{2\omega_e c^4 M}\times\left(\frac{1}{10}b^S_{J',J''}F^S_\gamma\gamma^2\right)(v''+1) && \mathrm{S}_\perp
\end{aligned}
\tag{2.44}
$$

Here, $b_{J',J''}$ denote the branch-dependent Placzek-Teller coefficients given in Eq. (2.45) [91].

$$
\begin{aligned}
b^O_{J',J''} &= \frac{J''(J''-1)}{(2J''-1)(2J''+1)}\\
b^Q_{J',J''} &= \frac{J''(J''+1)}{(2J''-1)(2J''+3)}\\
b^S_{J',J''} &= \frac{(J''+1)(J''+2)}{(2J''+3)(2J''+1)}
\end{aligned}
\tag{2.45}
$$

Branch dependent vibration-rotation interaction is accounted for by the Hermann-Wallis factors in Eq. (2.46) [111].

$$
\begin{aligned}
F_\alpha\alpha^2 &= \langle v'',J''|\alpha|v',J'\rangle^2\\
F_\gamma\gamma^2 &= \langle v'',J''|\gamma|v',J'\rangle^2
\end{aligned}
\tag{2.46}
$$

For these, different models from the literature are implemented. For the O- and S-branch, the Buckingham-Model [26] expressed in Eq. (2.47) is used, where B_e and ω_e denote the rotational constant and the vibrational wavenumber, respectively, while r corresponds to the Bohr radius and γ and $\partial\gamma/\partial r$ the anisotropic part of the polarizability and its derivative in atomic units [120]. Values for N_2 are extracted from the molecular parameter file provided with CARSFT.

$$
\begin{aligned}
F^O &= \left(1+4\frac{B_e\gamma}{\omega_e\frac{\partial\gamma}{\partial r}r}\left(2J''+3\right)\right)^2\\
F^S &= \left(1-4\frac{B_e\gamma}{\omega_e\frac{\partial\gamma}{\partial r}r}\left(2J''-1\right)\right)^2
\end{aligned}
\tag{2.47}
$$

Originally, CARSFT uses the James-Klemperer-Model [91] for Q-branch transitions, however, recent publications indicate that the models developed by Bouanich et al. [21] or Tipping et al. [155] may be more appropriate [111]. The developed code includes all models given in Eq. (2.48) to allow a sensitivity analysis with respect to this choice. Within these equations the parameters for N_2 are $\eta = \frac{2B_e}{\omega_e}$, $a_1 = -2.7$, $(p_2/p_1)_{iso} = 0.31$ (isotropic) or $(p_2/p_1)_{aniso} = 0.31$ (anisotropic).

$$\begin{aligned} F^Q_{JK} &= 1 - 3\eta J''\left(J''+1\right)/2 && \text{James et al. [91]} \\ F^Q_{LBY} &= \left[1 - 3\eta^2\left(a_1+1\right)J''\left(J''+1\right)/4\right]^2 && \text{Bouanich et al. [21]} \\ F^Q_{TB} &= 1 - \left[3\left(a_1+1\right)/2 - 4p_2/p_1\right]\eta^2 J''\left(J''+1\right)/4]^2 && \text{Tipping et al. [155]} \\ \text{where } \eta &= \frac{2B_e}{\omega_e} \end{aligned} \tag{2.48}$$

With this information, the final equation for the amplitudes a_q is expressed by Eq. (2.49), where $\xi = \gamma/\alpha$, i.e. the ratio of the anisotropy of the polarizability derivative to the mean polarizability derivative and ζ is the mean polarizability derivative α divided by $\sqrt{2\pi c\omega_e M}$ [120].

$$a_q^{\parallel,\perp} = N\Delta_q(v+1)\frac{\zeta^2}{4\pi c}\begin{cases} \frac{2}{15}\xi^2 b^O_{J',J''}F^O_\gamma & \mathrm{O}_\parallel \\ \frac{3}{4}\mathrm{O}_\parallel & \mathrm{O}_\perp \\ \\ (1+\frac{4}{45}\xi^2 b^Q_{J',J''})F^Q & \mathrm{Q}_\parallel \\ \frac{1}{15}\xi^2 b^Q_{J',J''}F^Q & \mathrm{Q}_\perp \\ \\ \frac{2}{15}\xi^2 b^S_{J',J''}F^S_\gamma & \mathrm{S}_\parallel \\ \frac{3}{4}\mathrm{S}_\parallel & \mathrm{S}_\perp \end{cases} \tag{2.49}$$

When using non-parallel polarization of pump and probe beam with relative polarization angle ϕ and a polarizer in front of the spectrometer at an angle of θ (with respect to the pump beam polarization), the superimposed resulting amplitude may be expressed by equation (2.50).

$$a_q = \cos(\phi)\cos(\theta)a_q^\parallel + \sin(\phi)\sin(\theta)a_q^\perp \tag{2.50}$$

Fig. 2.26 shows an example calculation of J'' dependent amplitudes for a temperature of 2000 K.

Line widths and shape Transitional line widths are calculated using a modified exponential gap (MEG) law as proposed by Rahn et al [127]. Within this model, the transition rate γ_{ji} at a given pressure p from state J_i to J_j $(i < j)$ is given by Eq. (2.51).

$$\gamma_{ji} = \alpha p\frac{1-\exp(-m)}{1-\exp(-mT/T_0)}\left(\frac{T_0}{T}\right)^{0.5}\left(\frac{1+1.5E_i/kT\delta}{1+1.5E_i/kT}\right)^2\exp(-\beta\left|\Delta E_{ij}\right|/kT) \tag{2.51}$$

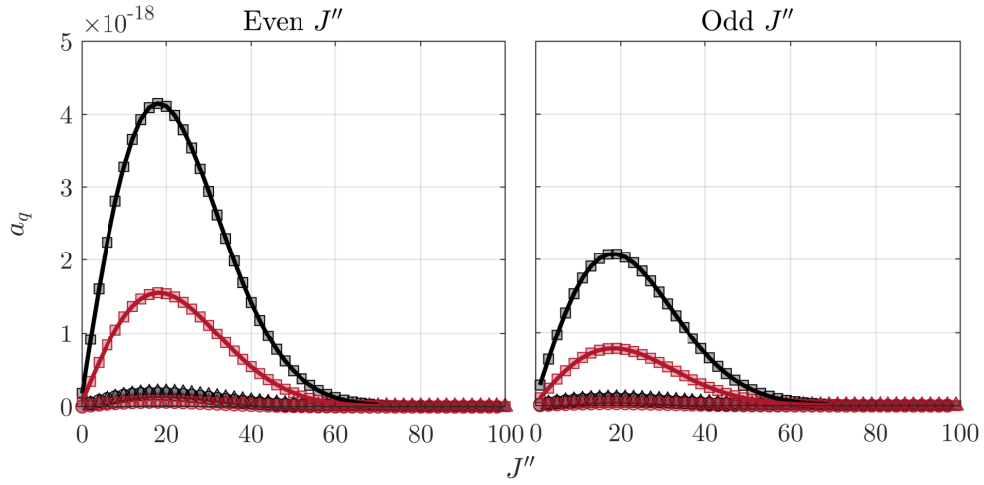

Figure 2.26: Amplitudes for even and odd J'' values as calculated from the present code (symbols) and CARSFT (solid lines) at a temperature of 2000 K. Coloring and symbols are consistent with Fig. 2.25. For comparison, CARSFT values have been divided by two. Apparently, CARSFT uses another definition of the squared susceptibility, where a factor of two is added to the denominator of Eq. (2.41) which effectively cancels this deviation [109].

The parameters $m = 0.1487$, $\alpha = 0.0231\,\mathrm{cm^{-1}atm^{-1}}$, $\beta = 1.67$ and $\delta = 1.21$ at a reference temperature of $T_0 = 295\,\mathrm{K}$ are obtained by a fit to experimental data. E_i corresponds to the rotational term energy in state i [127]. Transition rates γ_{ij} are determined by microscopic reversibility [99]:

$$\gamma_{ij} = \frac{2J_i + 1}{2J_j + 1}\gamma_{ji} \exp(\Delta E_{ij}/kT) \tag{2.52}$$

A priori, no information on the gas composition within the measurement volume is available. Consequently, foreign gas broadening induced by collisions with other species has to be approximated. Similar to the implementation in CARSFT, this is modelled by introducing a J-independent line width multiplier n that modifies the Lorentzian line width of every transition [120]. The collisional line widths Γ_j are then given by twice the sum of the off-diagonal matrix elements γ_{ij} times the line width multiplier n, see Eq. (2.53).

$$\Gamma_{J''} = 2n \sum_{i \neq j} \gamma_{ij} \tag{2.53}$$

Fig. 2.27 shows an example calculation of J'' dependent line widths for a temperature of 2000 K.

For the transitional line shape, three different models which are also available in CARSFT are implemented: (a) Isolated lines: here, every transition is modelled as a Lorentzian with line width Γ_j without contribution from Doppler broadening. (b) Voigt profile: before the summation over all transitions in Eq. (2.41), every transition is convolved with a Gaussian profile with appropriate Doppler width. (c) Rotational diffusion: for high pressure/low

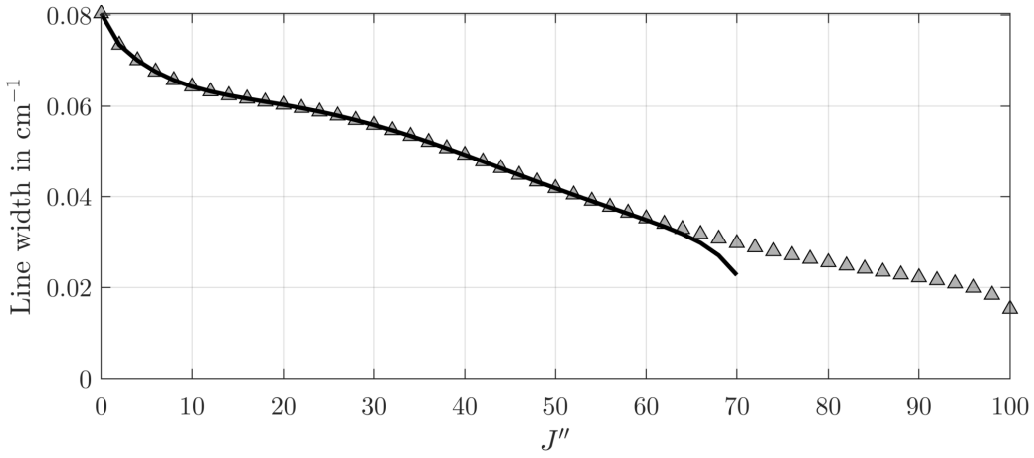

Figure 2.27: J'' dependent line widths as calculated from the presented code (triangles) and CARSFT (solid line) at a temperature of 2000 K and 2.5 bar. Minor deviations at high J'' values are observed when computed with CARSFT. It is assumed that this results from computational limitations in the FORTRAN code of CARSFT. However, as the respective amplitudes are comparably low for these J'' values, the impact on the final spectrum is assumed to be negligible.

temperature cases, collisional narrowing is modeled using the model proposed by Hall et al. [71].

Fig. 2.28 shows a comparison of the simulated theoretical susceptibility using Eq. (2.41) and CARSFT with and without convolution with a Gaussian apparatus function. The residual difference of the modulus of the theoretical susceptibility prior to convolution is $< 0.6\%$. After convolution with the apparatus function, the maximum deviation is $\approx 1{-}2\%$. This may result from different implementations of the convolution operation and is assumed to be negligible. In fact, if the spectrum created using the method described above is fitted using CARSFT, the resulting temperature difference is below 1 K, albeit at a slightly different value for instrumental line width.

2.2.2.3 Spectral Fit

Traditionally, the model described in the previous subsection is fitted to experimental data by means of a non-linear least squares fit. As one evaluation of the physical model is computationally quite expensive due to the high number of transitions involved, especially at higher temperatures, several strategies to improve the efficiency can be found in the literature. One notable approach is described by Cutler et al., where spectra are precomputed and stored in a sparse library for later interpolation [37]. One significant caveat is the fact, that a certain number of degrees of freedom of the physical model is already incorporated in the library and thus unavailable at runtime. In other words: reduced computational effort comes at the cost of reducing the generality of the physical model. Consequently, libraries have to be regenerated if one of the fixed parameters changes.

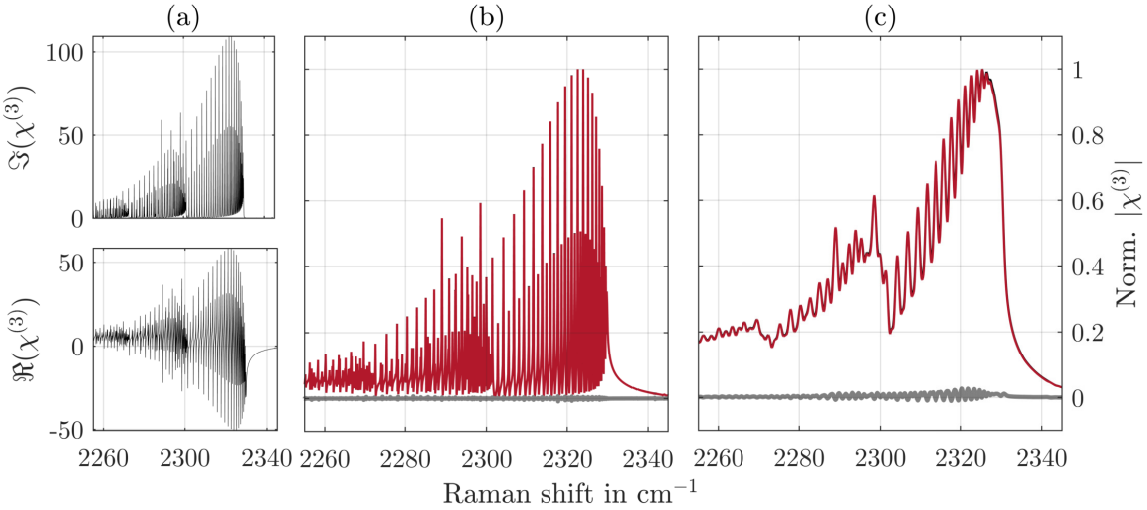

Figure 2.28: Comparison between simulated spectra using the proposed code and CARSFT at an N_2 mole fraction of 0.8 using the isolated lines model and the James-Klemperer Model for the Hermann-Wallis factors. Other conditions correspond to those of Fig. 2.25. Column (a) shows the real and imaginary component of the susceptibility as computed using Eq. (2.41). Additionally, comparisons of the peak-normalized modulus of $\chi^{(3)}$ (b) before and (c) after convolution with a Gaussian apparatus function (1 cm^{-1} FWHM). Black lines: this code, red lines: CARSFT. Grey lines indicate residual.

In addition to the physical degrees of freedom of the model, namely temperature T, resonant species' mole fraction X_R, line width multiplier n and the cumulative apparatus function G_i, a set of experimental degrees of freedom has to be introduced. These result from the necessity to interpolate the physical model onto the experimental wavenumber axis for calculation of the residual. To account for imperfect calibration of the spectrometer, a linear expansion of the wavenumber axis referred to as *wavenumber expansion* is introduced. In addition, beam-steering and realignment of the setup during the experiment may cause a shift of the wavenumber axis between measurements and calibration. This is accounted for by introducing a *wavenumber shift* during the interpolation. In the approach by Cutler et al., library spectra are calculated for every temperature and mole fraction with a given apparatus function and wavenumber expansion. Consequently, the user is left with temperature, mole fraction and wavenumber shift as fitting parameters [37].

The following describes a computationally efficient approach, that retains the number of degrees of fit at runtime by employing a novel loss-less library compression scheme by partly decoupling the physical parameters and a preconvolution step.

Eq. (2.41) may be rewritten to Eq. (2.54) by splitting the resonant and non-resonant contributions to the third order susceptibility. Quantities in brackets indicate the dependency of the individual contributions on the physical parameters.

$$I^*_{CARS} \propto G_i * |\chi^{(3)}_R(T,X_R,n) + \chi^{(3)}_{NR}(X_R)|^2 \tag{2.54}$$

The resonant contribution $\chi_R^{(3)}$ and the non-resonant contribution *of the resonant species* $\chi_{NR,R}^{(3)}$ scales with its mole fraction. To get the total non-resonant contribution, a reasonable assumption on the non-resonant signal of *all other species* within the measurement volume, i.e. the *buffer gas*, must be made, which is expressed by the term $\chi_{NR,buffer}^{(3)}$ in Eq. (2.55). Precise knowledge of the buffer gas non-resonant susceptibility is thus a stringent requirement for accurate mole fraction measurements with CARS. Within this work, only gas-phase temperature measurements are the quantity of interest such that this value can in principle be set to any arbitrary constant value > 0, as it only affects the derived mole fraction result of the probed species. For consistency with CARSFT, the default value of $8.5 \times 10^{-18}\,\mathrm{cm}^3/(\mathrm{erg\,amagat})$ is used.

$$\begin{aligned} \chi_R^{(3)}(T,X_R,n) &= X_R \hat{\chi}_R^{(3)}(T,n) \\ \chi_{NR}^{(3)}(X_R) &= X_R \hat{\chi}_{NR,R}^{(3)} + (1-X_R)\chi_{NR,buffer}^{(3)} \end{aligned} \tag{2.55}$$

Effectively, Eq. (2.55) decouples the mole fraction parameter from the other physical quantities. Decoupling the line width multiplier and temperature would result in a very large database, as every transition would have to be stored independently due to their respective contribution to the J'' dependent calculation of the line width $\Gamma_{J''}$. In principle, one could store the complex susceptibility $\hat{\chi}_R^{(3)}(T,n)$ in a library with those two parameters directly. However, as the wavenumber resolution has to be very fine due to the narrow transitions, this would result in a database with a size of $\approx 10^{11} - 10^{12}$ datapoints for 2000 temperature and 100 line width multiplier entries. RAM requirement for such a library is already in the order of 1 TB at single precision and as such practically not feasible. However, in the experiment, the final resolution is limited by the apparatus function. This fact is used for a loss-less compression scheme that is described in the following. Evaluating the squared modulus in Eq. (2.54) explicitly and inserting Eq. (2.55) yields Eq. (2.56):

$$I_{CARS}^* \propto G_i * \left(X_R^2 |\hat{\chi_R}^{(3)}(T,n)|^2 + 2X_R \Re(\hat{\chi_R}^{(3)}) \chi_{NR}^{(3)} + \left(\chi_{NR}^{(3)}\right)^2 \right) \tag{2.56}$$

Consider that the apparatus function G_i may be expressed as the convolution of two arbitrary functions which obey $G_i = G_1 * G_2$ and that convolution is distributive and associative. Additionally, G_i is normalized to unity area such that for any constant a:

$$G_i * a = \int_{-\infty}^{\infty} G_i(\hat{\omega}) \underbrace{a(\omega - \hat{\omega})}_{=\text{const.}} d\hat{\omega} = a \underbrace{\int_{-\infty}^{\infty} G_i(\hat{\omega}) d\hat{\omega}}_{=1} = a$$

With this, Eq. (2.56) may be rewritten to read:

$$I_{CARS}^* \propto G_1 * \left(X_R^2 G_2 * |\hat{\chi}_R^{(3)}|^2 + 2X_R \left(G_2 * \Re(\hat{\chi}_R^{(3)}) \right) \chi_{NR}^{(3)} + \left(\chi_{NR}^{(3)}\right)^2 \right) \tag{2.57}$$

Effectively, an arbitrary function G_2 with a width *narrower than the combined apparatus function* may be used to preconvolute the squared modulus and the real part of the resonant susceptibility independently without losing relevant spectral features. This allows to interpolate the spectra on a wavenumber grid with a manageable spacing prior to tabulation. Assuming a typical apparatus function with a width $> 1\,\mathrm{cm}^{-1}$, a preconvolution

with a $1\,\mathrm{cm}^{-1}$ wide (FWHM) Gaussian allows to reduce the memory requirement from $\approx 1\,\mathrm{TB}$ to $\approx 1\,\mathrm{GB}$ by means of interpolation to a coarser grid with a spacing of 0.1 times the FWHM of the preconvolution kernel.

The terms $G_2 * |\hat{\chi}_R^{(3)}|^2$ and $G_2 * \Re(\hat{\chi}_R^{(3)})$ are stored in the library at a selectable temperature and line width discretization, while the mole fraction X_R, the resulting non-resonant contribution $\chi_{NR}^{(3)}$ and the convolution with G_1 to the final apparatus function are computed at every function evaluation during the fit. Fig. 2.29 demonstrates the proposed library compression scheme. It is evident, that the results of Eq. (2.41) and Eq. (2.57) are indeed mathematically equivalent.

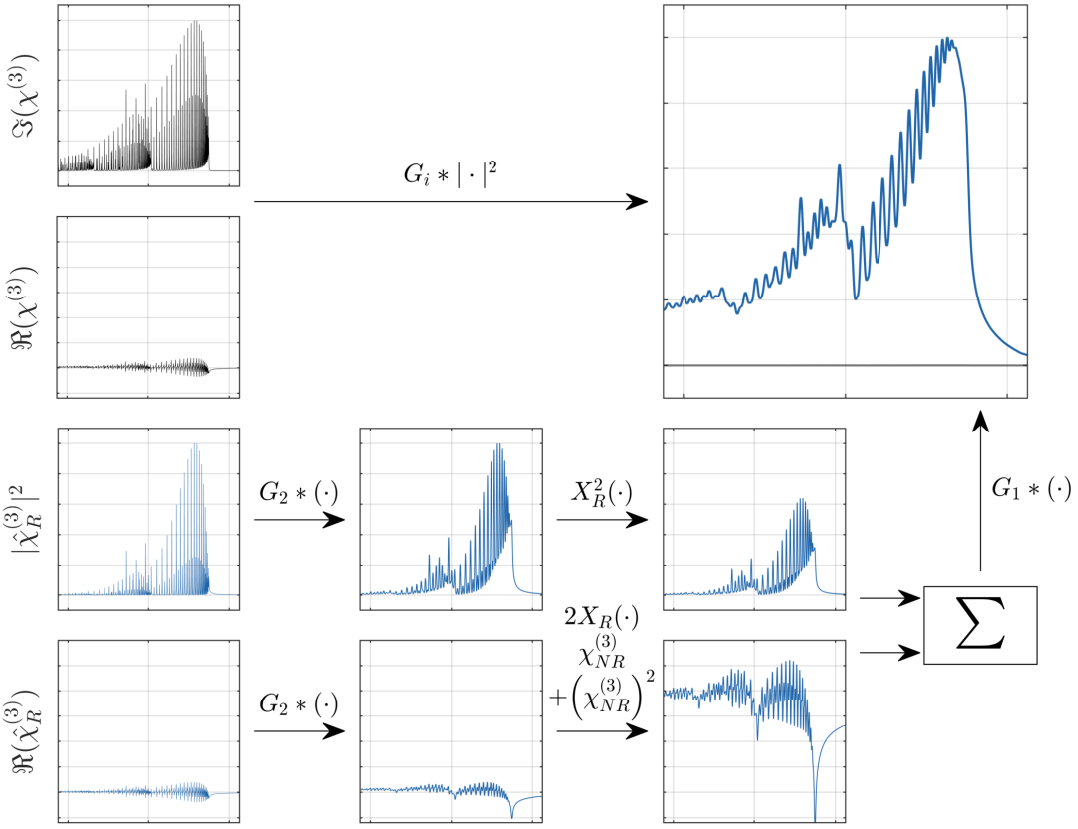

Figure 2.29: Demonstration of the loss-less library compression scheme. Top row: direct simulation of CARS signal using Eq. (2.41) (black). Bottom row: step-wise evaluation of Eq. (2.57) (blue). For this demonstration, a Gaussian preconvolution kernel G_2 with $0.5\,\mathrm{cm}^{-1}$ FWHM was used. To achieve convolution to the final Gaussian apparatus with $1\,\mathrm{cm}^{-1}$ FWHM, G_1 has an FWHM of $0.866\,\mathrm{cm}^{-1}$. Top right plot shows an overlay of the results and the residual in grey. Aside numerical error in the order of 1×10^{-4}, the residual vanishes. Axes labels omitted for clarity. Plots for a given row share a common scaling.

In principle, this compression scheme may now be used in any fitting algorithm. As temperature and line width multiplier are discretized in the library, any gradient based solver would require interpolation between spectra to achieve continuity and differentiabiliy of the objective function. To circumvent this, a mixed-integer genetic algorithm (MI-GA) is

used, as it allows to constrain a subset of the fitting parameters to integer values which in turn allows to treat temperature and line width by their library index only. As no gradients are computed, these parameters may even be discontinuous. This avoids costly interpolation between spectra at the cost of a denser library and reducing the precision in those parameters to the library discretization. Typically, the precision of temperature measurements using CARS is limited to a few K, such that this restriction is practically irrelevant. Due to the described compression scheme, a denser library is manageable which allows to focus on optimizing CPU time.

Typically, a genetic algorithm requires more function calls than a gradient based solver as it does not perform a directional search. To estimate the net computational benefit of the proposed method, a benchmark simulation is performed. The mean CPU time for direct simulation of a CARS spectrum, i.e. without a library, is in the order of $\approx 1\,\mathrm{s}$. This strongly depends on the temperature as it affects the number of transitions that have significant contribution to the signal as a result of the Boltzmann distribution. If a library is used in conjunction with a solver that requires interpolation between spectra, the average time to generate a spectra is $\approx 5\,\mathrm{ms}$ for linear interpolation. Higher order interpolation to reduce density in the library is in principle possible, however increases the computational cost as more library spectra have to be accessed. Due to tabulation, this does not depend on the simulated conditions. A direct library access as used in conjunction with the MI-GA requires $\leq 0.1\,\mathrm{ms}$ per spectrum. Basically, this is limited by memory bandwidth only. Without further investigation on the number of function calls for the MI-GA and a competitive gradient-based solver required to converge to a solution, it is not possible to determine which process is in the end faster. However, as the mean evaluation time for a set of 1000 spectra was in the order of 10 s using the MI-GA and thus sufficiently efficient, this comparative study was omitted.

Another benefit of the implemented MI-GA is the independence of the provided initial solution. This has been extensively shown and analyzed in [E6].

The code uses a modified chi-squared residual given in Eq. (2.58) as proposed in [37] to increase precision and accuracy when fitting noisy spectra. N_p denotes the number of pixels in the spectrum, $\nu = N_P - 1$ and σ_k^2 is a measure of the variance at pixel k.

$$R = \frac{1}{\nu} \sum_{k}^{N_p} \frac{(S_k - |\chi_k^{(3)}|)^2}{\sigma_k^2} \tag{2.58}$$

In contrast to [37], the square root of the squared modulus of $\chi_k^{(3)}$ is fitted to the square root of the signal intensity S_k as the obtained improvement in precision when fitting simulated noisy spectra was slightly better at high temperatures compared to fitting the squared modulus directly. Effectively, taking the square root of the signal leads to a higher relative weight during the fit to the $v = 1$ band for high temperature spectra. However, no systematic investigation was conducted to identify the gain in precision in a wide temperature range.

2.2.3 Imaging

This section describes the influence of the imaging system used for planar or line imaging of LIF signals within this work. At first, a general discussion on optical resolution is presented. The following subsections present the method how optical resolution is quantified within this work and how the effect of finite resolution on gradients is estimated.

2.2.3.1 Optical Resolution

Optical resolution is a matter frequently disregarded in imaging based laser diagnostics. A common misconception in digital imaging is that *optical resolution* refers to the number of pixels available per unit of length. In fact, this quantity represents the process of discretization due to usage of an array detector in the image plane. This is unquestionably an important number to report, as it provides the mapping between lab coordinates and pixel grid, but most often it is *not* the limiting factor for optical resolution. Wang et al. define the optical resolution as the *ability of the optical system to respond to spatial variations in the contrast of the object* [160]. Ultimately, the upper limit of optical resolution is determined by diffraction. However, imperfections in the optical system may lead to aberrations of different types which further degrade optical resolution, e.g. spherical aberration, coma, chromatic aberration, astigmatism, field curvature and - quite obviously - defocus. Many methods of characterizing the optical resolution are available in the literature. One of the common approaches is the concept of a point spread function (PSF), which describes the intensity distribution in the image plane after imaging an ideal point source. Consequently, finite size objects that are projected onto the image plane undergo a *convolution with the PSF* before the image is discretized using an array detector [160].

Due to the convolution, it becomes obvious that two closely spaced point sources are not individually resolved if their respective PSFs overlap too strongly. The threshold at which this limit is reached varies across methods. A quite common method is to define the distance between two point sources, where the intensity of the valley between overlapping PSFs is reduced to $8/\pi^2 \approx 81\%$. This corresponds to the well-known Rayleigh criterion [128]. Other criteria, such as Abbe's or Sparrow's work in a similar way, though the criteria are less stringent on the intensity minimum [80], leading to increased values for the reported optical resolution. All of the three methods have in common, that one has to obtain the PSF and subsequently has to choose a method to define the contrast threshold. However, without reporting the shape of the PSF itself, a single value for the resolution has only limited meaning for the ability of the imaging system to adequately represent gradients within the object plane.

An interesting notion of the PSF is that it is connected to the modulation transfer function (MTF) by Fourier transformation. The MTF is defined using the *image* contrast C_i normalized to the *object* contrast C_o of a sinusoidal pattern with spatial frequency s [160]. Using the definition of the Michelson contrast [17] in Eq. (2.59), one can obtain the MTF for a given spatial frequency of the pattern using Eq. (2.60).

$$C_{i,o} = \frac{I_{i,o,max} - I_{i,o,min}}{I_{i,o,max} + I_{i,o,min}} \tag{2.59}$$

$$MTF(s) = \frac{C_i}{C_o} \tag{2.60}$$

Disregarding the diffraction limit, an aberration free, perfect imaging system would have an $MTF(s) = 1$ for all spatial frequencies.

Commonly, targets with varying spatial frequencies are used to measure the MTF in wide frequency range. These targets may be linear or circular, such as the sector star target, also known as Siemens star. Unfortunately, manufacturing accurate sinusoidal patterns with high spatial frequencies is not as straightforward. Instead, bar patterns with a square wave intensity may be used to measure the *contrast transfer function* (CTF). While conceptually very similar, the CTF has - compared to the MTF - a larger magnitude across all spatial frequencies. MTF and CTF are related by Eq. (2.61) which allows to transform a measured CTF to an MTF curve and vice versa [160].

$$\begin{aligned} CTF(s) &= \frac{4}{\pi} \sum_{n=1}^{\infty} \frac{(-1)^n - 1}{2n-1} MTF\left[(2n-1)\, s\right] \\ MTF(s) &= \frac{\pi}{4} \sum_{n=1}^{\infty} \frac{A_{2n-1}}{2n-1} CTF\left[(2n-1)\, s\right] \\ \text{with } A_1 &= 1, A_3 = 1, A_5 = -1, \\ A_7 &= 1, A_9 = 0, A_{11} = 1, A_{13} = -1, ... \end{aligned} \tag{2.61}$$

Within this work, a square-wave type sector star target is used to measure the optical resolution of the imaging systems. The process of data evaluation is presented in the following subsection.

2.2.3.2 Sector Star Target Measurements

Fig. 2.30 shows an ideal representation of the sector star target with $n = 36$ line pairs used in this work.

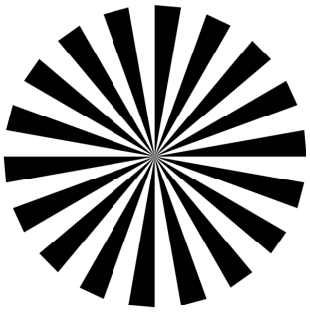

Figure 2.30: Siemens star with 36 line pairs used in this work to characterize optical resolution.

To derive the MTF from raw measurements, a code called YASSES[12] has been developed. The algorithm automatically detects the center and unwraps the sector star image by polar transformation. The unwrapped image is then split into n sectors and averaged over all sectors. This step partially eliminates uneven illumination of the target. In the next step, the contrast is calculated at every radial location using Eq. (2.59). Conversion from radius r in px to object-side spatial frequency s in lpmm is achieved using Eq. (2.62), where t is the physical size of a pixel in mm and M the magnification of the imaging system.

$$s = \frac{n}{2\pi r t / M} \tag{2.62}$$

As the limit of $s \to 0$ may not be available in the recorded image, the CTF is extrapolated to lower spatial frequencies. For extrapolation, different methods may be chosen within the code. These are linear extrapolation, extrapolation using a piece-wise cubic spline, nearest neighbor or by fitting a Gaussian to the CTF. After extrapolation, the result is again normalized to $CTF(0) \equiv 1$. The extracted CTF is subsequently transformed into an MTF using Eq. (2.61). Fig. 2.31 shows the implemented procedure step-by-step for a Siemens star measurement using a camera with $t = 6.5\,\mu\text{m}$ pixel size and 1:1 magnification, i.e. $M = 1$.

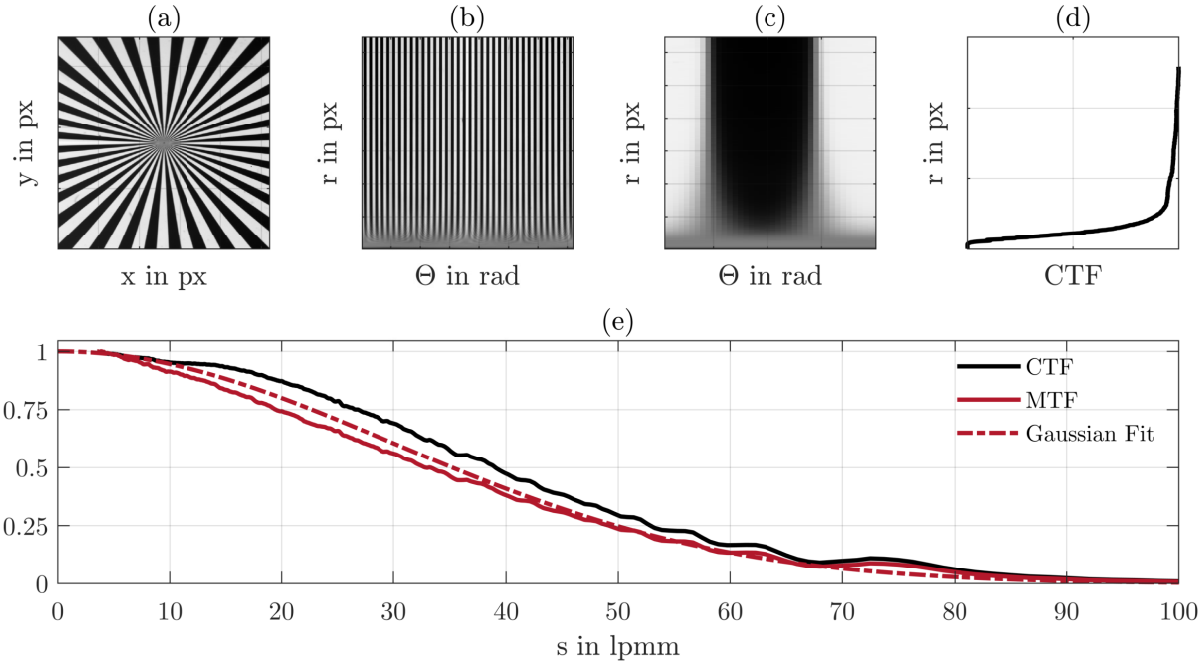

Figure 2.31: Evaluation of Siemens star images to extract MTF curves using YASSES. (a) Image of Siemens star. (b) Unwrapped image using polar transformation. (c) Mean sector for evaluation of Michelson contrast. (d) Extracted contrast for every radius. (e) Results for CTF and MTF and Gaussian fit to MTF.

To verify the implementation in YASSES, an artifical additional optical component with a Gaussian MTF with 50 lpmm FWHM is simulated. Combining MTFs is achieved by

[12]Yet Another Siemens Star Evaluation Script. Code available at https://github.com/tudarsm/yasses.

convolution of their respective PSFs and subsequent Fourier transform. By the convolution theorem, this is equivalent to a multiplication of the MTF curves. This allows to *predict* the total MTF and PSF of the artifical detection system. In theory, using the artifical PSF to convolve the Siemens star image in the above example should accurately retrieve the predicted MTF upon evaluation using YASSES. As shown in Fig. 2.32, the predicted

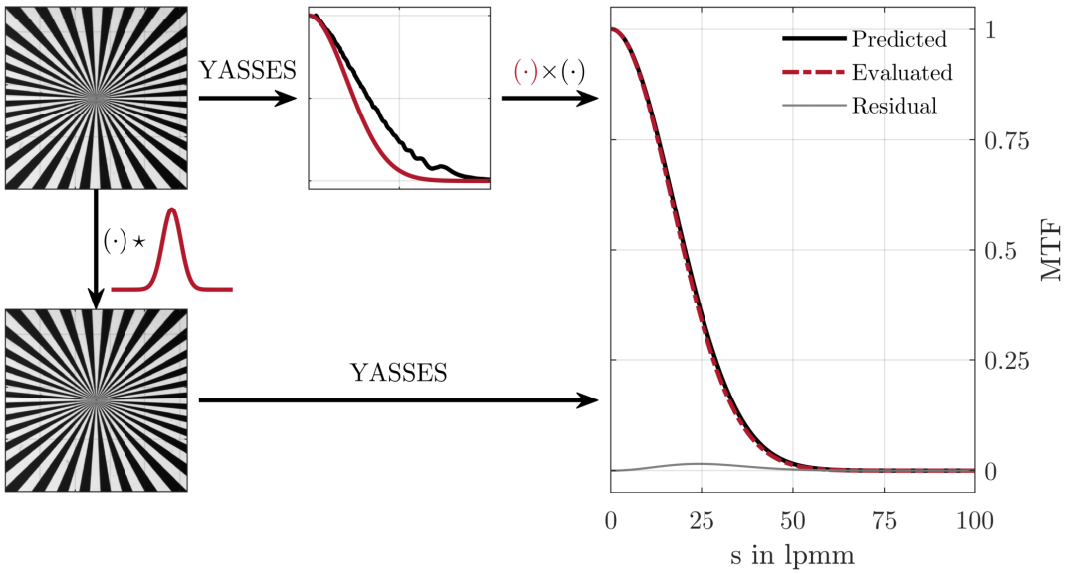

Figure 2.32: Verification of YASSES. Top row: Simulation of total MTF by evaluating the raw Siemens star image using YASSES (black MTF curve) and point-wise multiplication with artifical MTF (red curve) yielding the predicted curve in the right plot. Bottom row: Evaluation of the Siemens star image after convolution with the PSF of the additional simulated optical component.

and evaluated MTFs and PSFs match with a maximum deviation of 2%, indicating that the implementation returns physically accurate curves.

2.2.3.3 Common Imaging Systems

Within this work, imaging is used for LIF measurements. Typically, LIF signals are of weak intensity and have a temporal width corresponding to the lifetime of the upper state - convolved with the laser pulse width - in the order of $10-200\,\mathrm{ns}$. This requires detection systems that allow for fast gating to sufficiently suppress background signals arising from e.g. soot luminosity or chemiluminescence. For this reason, lens-coupled image intensifiers (LaVision, Low-Speed IRO) are used that allow gating in the nanosecond-range. These image intensifiers have an amplification stage that consists of a photocathode, which produces photo-electrons from incident photons. These electrons are accelerated by a high voltage potential across a micro channel plate, where secondary electrons are produced via collisions with the inner walls of the channels. These secondary electrons can in turn produce more secondary electrons, leading to a process commonly referred to as *avalanche process*. Fast switching of the high voltage enables the narrow gating of the intensifier. The magnitude of the potential allows to adapt the electron gain to the required level

to achieve sufficient signal for detection. A phosphor screen after the microchannel plate (MCP) converts the electrons back to photons which are then imaged onto an array detector (CCD or CMOS). Due to repulsive Coulomb forces between electrons, the MCP stage induces a degradation of optical resolution which is further affected by the lens system for imaging on the array detector. LaVision provides MTF measurements for every image intensifier separately.

Furthermore, some of the LIF signals - OH and NO - are in the UV spectral region and consequently, the lenses used for imaging the measurement plane onto the photocathode of the intensifiers have to be UV transmissive. As the market for this type of lenses is not very large, only a limited selection is available. At the RSM, two OUC3.60 (Bernd Halle Nachfl. GmbH), three Cerco 2178 (Sodern) and two UV Nikkor 105/4.5 (Nikon) are available. The Halle lenses have a focal length of 150 mm with a fixed f number of 2.5. The Cerco lens has a continously variable aperture between f/2.8 and f/8 at a focal length of 100 mm. The UV Nikkor lenses have a variable aperture ranging from f/4.5 to f/32 at 105 mm focal length. Halle and Cerco provide MTF measurements in their data sheets, unfortunately, such data is not available for the Nikon lenses. Fig. 2.33 shows MTF curves extracted from the data sheets of the lenses and image intensifiers for 1:1 imaging.[13] As

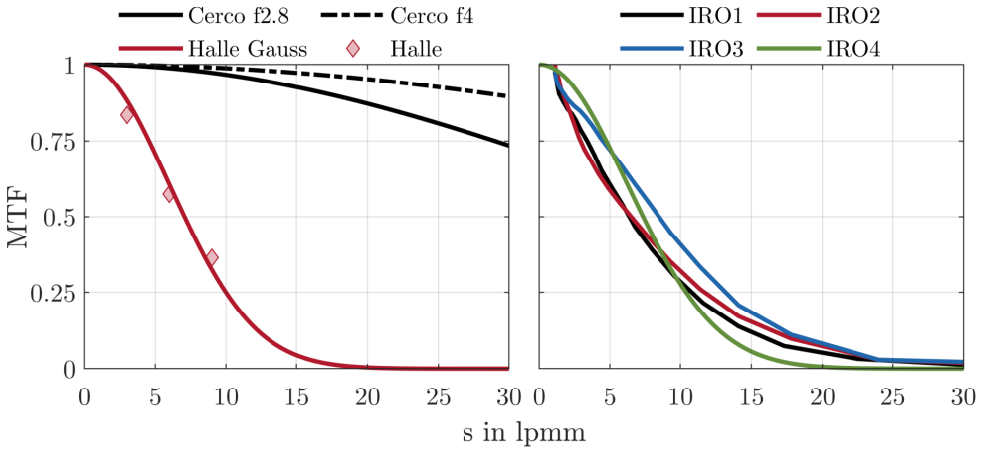

Figure 2.33: MTF curves for selected lenses (left) and image intensifiers (right) extracted from data sheets. Cerco provides a single MTF value of 30% at 60 lpmm (f2.8) or 100 lpmm (f4.0). Curve is assumed to be Gaussian. IRO1: VC17-0136, IRO2: VC15-0302, IRO3: VC18-0012, IRO4: VC19-0174 (Manufacturer serial numbers). IRO1-3 are measured using sector star targets and the data sheet reports raw data in tabular format. IRO4 is characterized by edge spread function measurements (ESF) and the FWHM of the ESF is reported. For this plot, it is assumed to be Gaussian and the PSF has the same FWHM which is converted to an MTF by Fourier transformation.

evident from the MTF curves of the Halle and Cerco lens, optical performance of these two lens types is very different. In fact, the Halle lens shows an MTF comparable to the raw MTF curves from the image intensifiers, which show a similar performance across

[13] In case of the intensifiers, this corresponds to 1:1 imaging onto the photocathode. Internally, the lens coupling has a magnification of 2.17:1 to image the active area of the phosphor screen onto the smaller CCD/CMOS sensors.

all variants. However, the MTF curves seem to be normalized to $MTF \equiv 1$ around $1 - 3\,\mathrm{lpmm}$ and show no inflection point when approaching low spatial frequencies. This may be an indication that the assumption of DC contrast at the lowest available spatial frequency within the image does not hold. This is visible in Fig. 2.34, where even the lowest spatial frequencies, located at the outer edge of the Siemens star, exhibit notable blur. Thus it is likely, that the actual performance of intensifiers IRO1-3 is overestimated

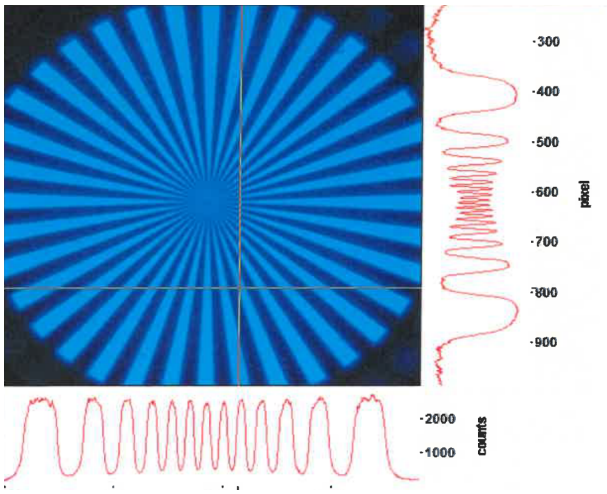

Figure 2.34: Siemens star measurement as provided by LaVision in data sheet of IRO1. Note the blur around the outer edges of the Siemens star which are used for normalization of the MTF.

by the provided MTF measurements.

To provide an estimate of the typically achievable optical resolutions, Fig. 2.35 shows simulated combined MTFs and the corresponding PSFs for two cases: (a) Halle + IRO4, (b) Cerco + IRO4. Additionally, the PSFs convolved with a step function are presented to indicate the minimally resolvable gradient measurable with such a configuration, assuming 1:1 imaging. For the combination with the Cerco lens, the MTF, PSF and Step response are dominated by the optical resolution of the intensifier whereas a notable difference in performance is observed for combination with the Halle lens. Application of the Rayleigh criterion yields a spatial resolution of $\approx 120\,\mu\mathrm{m}$ for the combination Halle+IRO4 and $\approx 90\,\mu\mathrm{m}$ for the combination Cerco+IRO4. The FWHM of their PSFs correspond to $\approx 85\,\mu\mathrm{m}$ and $\approx 60\,\mu\mathrm{m}$, respectively. The gradient of the inflection point of the step response amounts to $10.9\,\mathrm{mm}^{-1}$ and $15.5\,\mathrm{mm}^{-1}$.

In Sections 4-6, various lens and intensifier combinations are used at different magnifications which all affect the achieved spatial resolution. Thus, Siemens star measurements have been conducted for each detection system and individual MTF curves are reported in the respective sections. To avoid underestimating the spatial resolution due to chromatic aberration, the Siemens star is illuminated with a light source that matches the LIF emission in the respective filter pass bands.

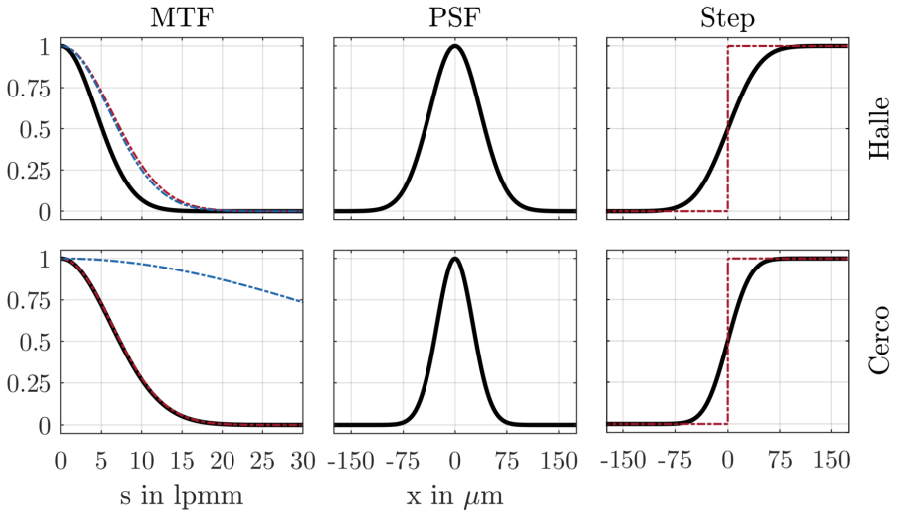

Figure 2.35: Effect of two different lens/intensifier combinations on measured spatial gradients. From left to right: MTF, PSF and Step response for Halle + IRO4 (top row) and Cerco + IRO4 (bottom row). For the MTF curves, dashed lines represent contribution from lens (blue) and intensifier (red). Black solid lines correspond MTF, PSF and Step response of the respective lens/intensifier combination.

Chapter 3

Single Sector Model Gas Turbine Combustor

This section describes the effusion cooled model single sector gas turbine combustion test rig used for the investigation of flame-cooling air interaction. The test rig was constructed by J. Hermann during his PhD studies at RSM [84]. At first, a brief overview of relevant parts of the rig is presented, followed by a description of the available instrumentation and the investigated operating conditions in Sect. 4-6.

3.1 Test Rig

Fig. 3.1 shows a color coded overview of the single sector combustor (SSC) with some of its most important peripherals.[14]

Air is supplied by two parallel scroll compressors (*Atlas Copco*) at ambient temperature and a subsequent refrigerant type dryer (*Hankinson*) providing up to 1 kg/s at 1.3 MPa of filtered dry air. Three individually controllable mass flows are drawn from this supply, namely oxidizer mass flow $\dot{m}_{\mathrm{ox}}$, effusion cooling mass flow $\dot{m}_{\mathrm{eff}}$ and pressure vessel cooling mass flow $\dot{m}_{\mathrm{cooling}}$. Oxidizer and effusion cooling mass flows are controlled using thermal mass flow controllers (MFC, *Bronkhorst*) and independently preheated using electrical inline heaters (Oxidizer: *Schniewind*, 80 kW; Effusion cooling: *OSRAM Sylvania*, 15 kW) to a maximum value of 773 K and 923 K at their respective inlet of the flame tube. The pressure vessel cooling air mass flow is determined by measuring the differential pressure across an orifice plate with a diameter of 17 mm and controlled using a pneumatic valve.

Natural gas is taken from the domestic pipeline, compressed (*Bauer*) to 28 MPa and stored in a bottle array with a total volume of 1 m^3. Two independent MFCs control the mass flows of the main stage $\dot{m}_{\mathrm{f,Main}}$ and the pilot stage $\dot{m}_{\mathrm{f,Pilot}}$, respectively.

Preheated air and main fuel are mixed via six uniformly distributed ports in a jet-in-a-crossflow configuration in the plenum before entering the test section through a movable-block swirler based on the well-known TECFLAM design [4, 81, 82, 92] shown in Fig. 3.2.

[14] The presented description of the test rig is taken from the *Flow, Turbulence and Combustion* paper [E9] with permission from *Springer* and the first author J. Hermann. A declaration on the author's contribution to the scientific publication may be found in the appendix.

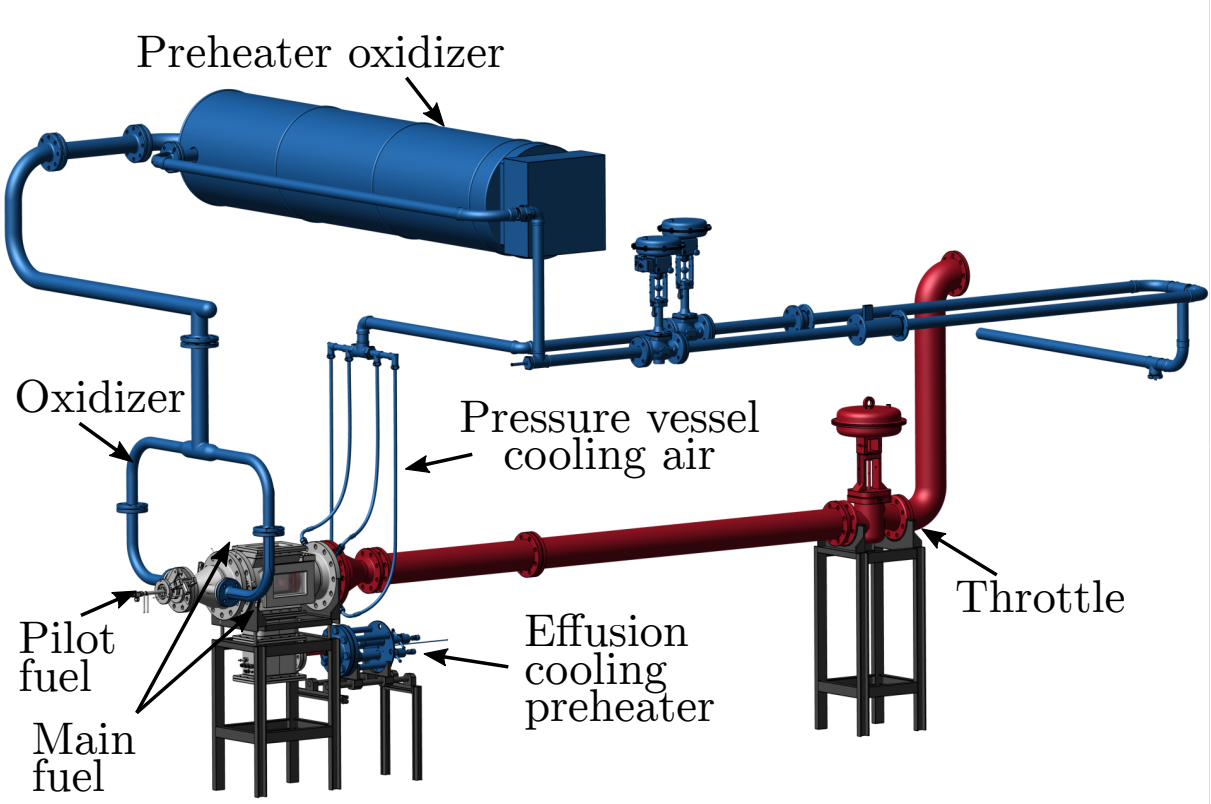

Figure 3.1: Overview of the test rig with its peripherals. Blue: air supply and preheating; Red: exhaust pipe and throttle; Gray: pressure vessel with flame tube [E9].

By rotating the movable block of the swirler, the geometrical swirl number as defined by Eq. (3.1) can be adjusted. The geometrical properties are listed in Tab. 3.1. To ensure accurate positioning, the stepper motor turning the movable block features an absolute rotary encoder.

$$S(\vartheta) = S_0 \frac{\sin(\beta)\cos(\beta)\left(1+\tan(\beta)\tan(\frac{\vartheta}{2})\right)\frac{\vartheta}{\vartheta_0}}{\left[1-\left[1-\cos(\beta)\left(1+\tan(\beta)\tan(\frac{\vartheta}{2})\right)\right]\frac{\vartheta}{\vartheta_0}\right]^2} \tag{3.1}$$

$$S_0 = \frac{\pi}{n\vartheta_0}\frac{R}{H}\left[1-\left(\frac{2r}{2R}\right)^2\right] \tag{3.2}$$

The premixed fuel-air stream enters the flame tube through a mixing pipe to further homogenize fuel distribution in the flow due to the highly turbulent flow in this region. A central bluff body is used for flame stabilization at low swirl-numbers. The bluff body has a central bore of 2 mm which serves as an optional fuel port for the pilot stage. To avoid large thermal stress on the material and uncontrolled preheating of the fuel supplied through this stage, the bluff body is constructed from coaxial pipes with internal water cooling.

$$SR = \frac{\dot{m}_{\mathrm{F,Pilot}}}{\dot{m}_{\mathrm{F,Pilot}} + \dot{m}_{\mathrm{F,Main}}} 100\,\% \tag{3.3}$$

The governing parameter for the fuel split is the *staging ratio* SR defined as the ratio of *pilot* stage fuel mass flow and *total* fuel mass flow, see Eq. (3.3), which can also be

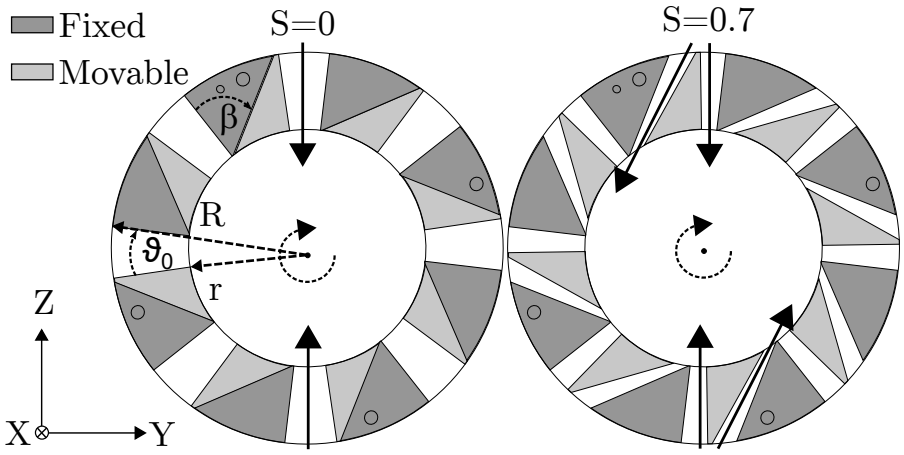

Figure 3.2: Cross-section of the movable block swirler. Left $S = 0$; right $S = 0.7$. Solid lines symbolize flow direction, dashed lines indicate dimensions and angles, see Tab. 3.1. Channel height H (not shown in figure) denotes extension in direction perpendicular to viewing plane (X) [E9].

Table 3.1: Geometrical properties of the swirler [E9].

Property	Symbol	Value	Unit
Number of channels	n	8	-
Tangential channel wall angle	β	60	°
Max. angle of rotation	ϑ_0	15	°
Channel height	H	24	mm
Inner radius	r	9.75	mm
Outer radius	R	17.25	mm

gradually varied between 0% and 100% during reacting operation. Fig. 3.3 shows two sectional views of the SSC. The flame tube has a rectangular cross section of 100 x 100 mm^2 and an axial length of 180 mm. Optical access is provided from three sides using fused silica windows (*Heraeus, SQ1*). The outer windows are designed to absorb the mechanical forces imposed by the increased pressure of the system while the liner windows enclose the flame tube, separating the hot zone within the combustor from pressure vessel cooling air. Additionally, a set of cooling air windows is placed 6 mm outwards of the liner windows providing a channel for the exiting pressure vessel cooling air which is mixed with the hot exhaust gases downstream of the flame tube. No additional window film-cooling is performed on the inside, i.e. all mass flows within the flame tube are well known.

The flow exits the flame tube through an internally water-cooled non-choking nozzle. The water cooling serves a two-fold purpose: firstly, the nozzle is manufactured from 1.4305 stainless steel by selective laser melting and needs to be cooled to withstand the high exhaust temperatures and secondly, the throttle downstream of the exhaust pipe, which is used to increase and control the system pressure, is designed for temperatures well below 650 K. Four pin jet nozzles are used to create a uniformly distributed cooling water spray, lowering the exhaust temperatures to a safe value (not shown in figure). To prevent

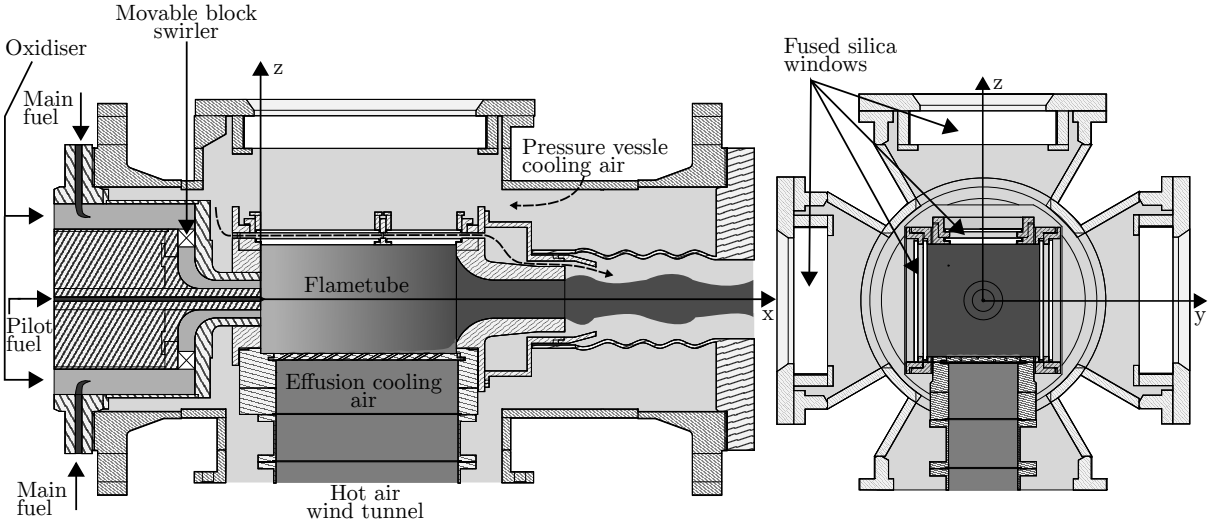

Figure 3.3: Longitudinal and cross section view of the SSC. The right handed coordinate system is anchored at the burner head along the central flame tube axis. The x-axis is defined normal on the burner head plate with the z-axis perpendicular to the effusion cooled liner [E9].

accumulation of sediments and calcification, water from the domestic supply is de-ionized and filtered.

A modular effusion cooling geometry can be mounted as a bottom wall segment of the flame tube to investigate different cooling schemes (e.g. effusion only, impingement only, effusion and impingement cooling). Cooling air is supplied through a dedicated hot air wind tunnel providing a top-hat like flow upstream of the effusion liner to ensure spatially homogeneous outflow of effusion cooling air, see Fig. 3.4. This is realized by a very compact arrangement of grid stages with different mesh sizes to homogenize the flow. Spatial homogeneity has been verified with particle image velocimetry measurements. Temperature and pressure of the effusion cooling air is measured $\approx 5\,\mathrm{mm}$ upstream of the liner. In all investigations reported in this article, an effusion cooling geometry with a regular hole pattern was used. The geometrical properties are listed in Tab. 3.2.

Table 3.2: Geometrical properties of the effusion cooled liner [E9].

Property	Symbol	Value	Unit
No. of holes	n	145	–
Angle	α	30	°
Hole diameter	d	2	mm
Intermittency	N	3	–
Axial distance	x/d	1,38	–
Lateral distance	y/d	2,5	–
Porosity	p	4	%
Material Number	-	2.4663	-

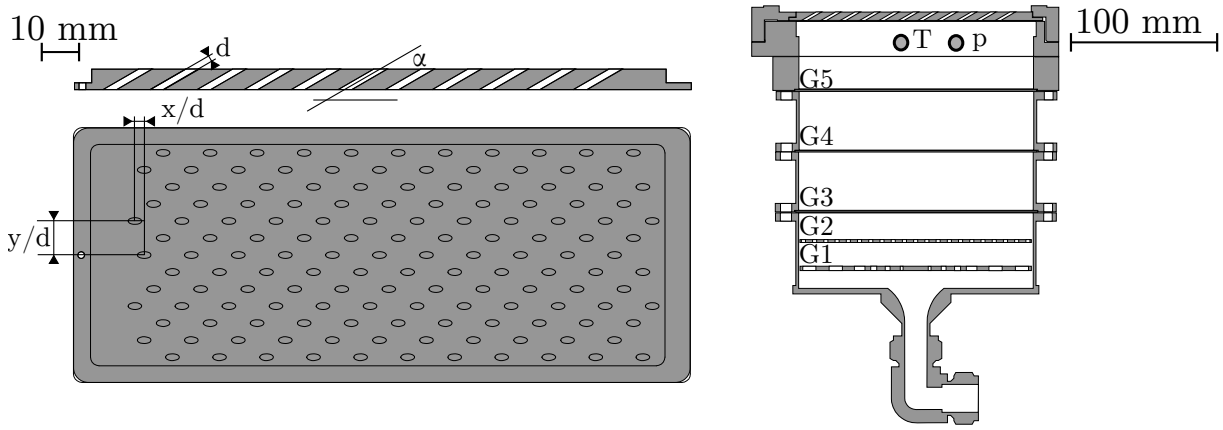

Figure 3.4: Left: Top down and section view of the effusion cooling plate used in this study. Holes are inclined 30° with respect to the horizontal axis. Right: Cross-section of the hot air wind tunnel supplying spatially homogeneous flow to the effusion cooled liner. Grids (G_i) with different mesh sizes are used to homogenize the flow. Temperature and pressure is measured $\approx 5\,\text{mm}$ upstream of the liner [E9].

3.2 Laminar Flame

For the investigations presented in Sections 4-6, it is helpful to be able to conduct measurements in a laminar adiabatic flame as a reference case and for calibration purpose.[15] The geometry of the combustor unfortunately prohibits to reduce the mass flows to such an extent that a laminar flame can be established. For this reason, a calibration burner was constructed that may be used as a replacement part for the bluff body of the swirler, which can be pulled out at the rear side of the test rig. This allows to (un-)mount the calibration burner without removing the pressure vessel windows, endangering the alignment of optical components close to the combustor. To establish a flame with a reaction zone far from the head-plate to ensure adiabaticity and avoidance of additional vignetting effects, a laminar V-flame was constructed as depicted in Fig. 3.5.

The calibration burner consists of two coaxial pipes. The central pipe with an inner diameter of 8 mm carries a premixed methane-air mixture. The outer pipe carries an N_2 co-flow with matched bulk-outlet velocity to minimize shear effects. A 1 mm steel-rod was welded to the outlet of the inner pipe, acting as a flame holder. The flame holder was intentionally welded a little below the xy-symmetry plane to achieve a longer upper branch. This led to an improved stability in terms of ignition as well as spatial stability of the reaction zone. Spark ignition was either realized by increasing the energy of the used diagnostics, e.g. the CARS lasers, above the breakdown threshold or by using a co-linearly mounted stainless steel welding rod with a ceramic insulation, connected to an ignition coil.

Compared to a Bunsen flame, this approach has the benefit that the established flame was nearly V-shaped, thus featuring a "flat" side that could be used for calibration without curvature effects. Due to the rise in flame speed when operating with preheated mixtures,

[15] This section is taken in part from the *Combustion and Flame* paper (pre-print, post-review) [E4] with permission from *Elsevier*.

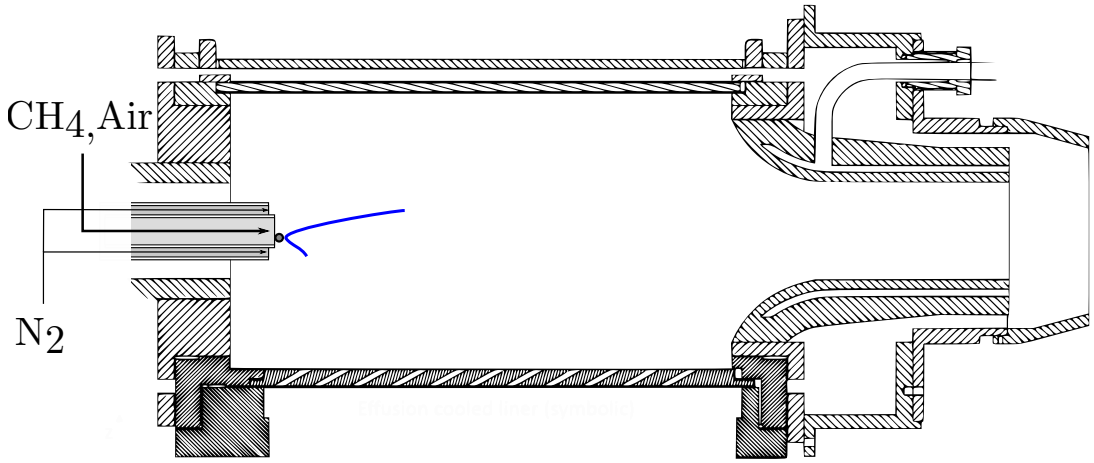

Figure 3.5: Sketch of the laminar calibration flame within the combustor.

a pressurized laminar flame at identical conditions of the combustor in terms of preheating and equivalence ratio could not be stabilized. The range of equivalence ratios for stable operation without preheating reaches from 0.65 to 1.4 at pressure levels from atmospheric to 4 bar. Mass flows for air, CH_4 and N_2 were controlled using individual MFCs for accurate control of the equivalence ratio and bulk outlet velocity.

3.3 Operating Conditions

To investigate flame-cooling air interaction, parametric variations of relevant parameters concerning combustion and cooling air are conducted.[16] The staging ratio SR, which is the proportion of pilot fuel mass flow to total fuel mass flow, is varied between 0% and 10%, i.e. the rig is either operating fully premixed (FP) or partially premixed (PP). The nominal equivalence ratio of $\Phi = 0.75$ is calculated with respect to the total amount of fuel, i.e. at fully premixed operation, the main stage burns at an equivalence ratio of 0.75, while at partially-premixed combustion, the actual equivalence ratio of the main stage is reduced to 0.675, as 10% of the total fuel mass flow is supplied via the non-premixed pilot. The geometric swirl S number is varied in three steps: $S = 0.7$ (low swirl; LS), $S = 1.0$ (intermediate swirl; IS) to $S = 1.3$ (high swirl; HS). Additionally, two different cooling air mass flows were used. The low cooling air mass flow (LC) with 7.5 g/s corresponds to a blowing ratio of 1.7 while the high cooling air mass flow setpoint (HC) corresponds to a blowing ratio of 3.5. Different operating conditions follow this nomenclature: Swirl-Cooling air mass flow-Staging, e.g. IS-HC-FP for the conditions with intermediate swirl, high cooling air mass flow set point and fully premixed operation. All other boundary conditions were kept constant, see Table 3.3 for a complete list. These

[16]The description of boundary conditions is taken from the *International Journal of Heat and Fluid flow* [E5] with permission from *Elsevier*.

are similar boundary conditions already used in previous publications, albeit with an increased nominal equivalence ratio from $\Phi = 0.65$ to $\Phi = 0.75$ [E8].

Table 3.3: Boundary conditions [E5].

Property	Symbol	Value	Unit
Oxidizer mass flow	$\dot{m}_{\mathrm{ox}}$	30	g/s
Oxidizer temperature	T_{ox}	623	K
Eff. cooling mass flow	$\dot{m}_{\mathrm{eff}}$	[LC: 7.5, HC: 15]	g/s
Eff. cooling temperature	T_{eff}	623	K
Equivalence ratio	Φ	0.75	–
Pressure	p	2.5	bar
Swirl	S	[LS: 0.7, IS: 1.0, HS: 1.3]	–
Staging	SR	[FP: 0, PP: 10]	%

Chapter 4

Mixing Processes

4.1 Aim of this Investigation

In this chapter, mixing processes between effusion cooling air and main flow are investigated. This is achieved by seeding the effusion cooling air with nitric oxide (NO) as an inert tracer which is used for planar imaging of laser induced fluorescence. Simultaneous quantitative OH-PLIF measurements are conducted to extract the instantaneous location of the flame front and to gain insights on the relative importance of mixing events *before*, *during* and *after* reaction in the primary zone of the combustor and in the FCAI region.[17]

4.2 Method

4.2.1 Optical Setup

Fig. 4.1 shows a sketch of the optical setup used for the investigation described in this chapter. A detailed explanation of the used components is given in the following subsections regarding the quantitative OH-PLIF and NO-PLIF measurements.

4.2.2 Quantitative OH Planar Laser-induced Fluorescence

For this investigation, OH-PLIF is used to extract local distributions of OH number densities. To compare results across all operating conditions and locations within the combustor, a quantification is necessary to avoid ambiguities in the interpretation arising from absorption effects:

(a) Absorption effects will vary with axial and radial coordinate due to the non-homogeneous OH distribution within the combustor and the different absorption lengths until reaching the region of interest.

(b) Different operating conditions will also result in different OH distributions.

[17] This chapter is taken in part from the *International Journal of Heat and Fluid flow* paper (pre-print, post-review) [E5] with permission from *Elsevier* licensed under CC BY-NC-ND 4.0 [2]. A declaration on the author's contribution to the scientific publication may be found in the appendix.

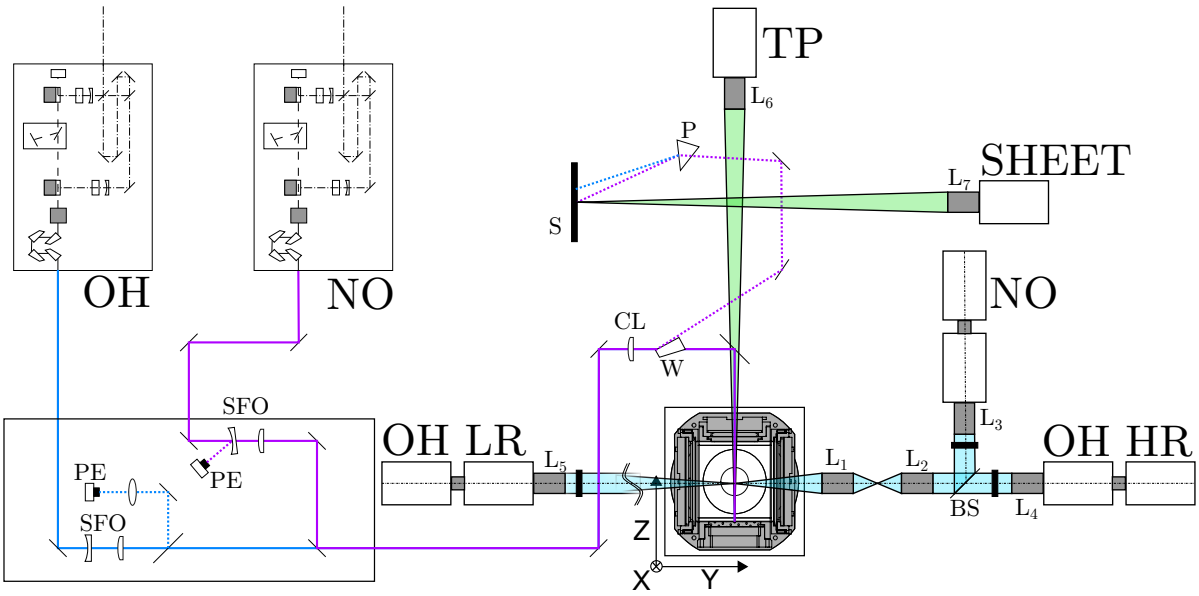

Figure 4.1: Optical setup. OH LR: Low-resolution OH detection system; OH HR: High-resolution OH detection system; SHEET: CCD camera capturing both laser sheet profiles within one frame; TP: CCD camera capturing phosphorescence signal on effusion cooled liner. To allow measurements at different locations, the laser beams are aligned to the axis of a traversing system. OH LR and TP are only moved in axial direction, all other systems can also be moved in radial direction. SFO: Sheet forming optics; PE: pyro-electric energy meter; CL: cylindrical focusing lens; W: wedged plate beamsplitter; P: Dispersing prism; L_{1-7}: Camera lenses; BS: Detection beamsplitter; S: YAG : Tb^{3+} coated fused silica substrate. Figure taken from [E5] with permission from Elsevier.

The quantification is achieved using a combined measurement of the line-of-sight integrated absorption and OH PLIF, a method described in [83] and [124]. The measured absorption is used initially to correct the qualitative OH-PLIF measurements for variations in local laser intensity and subsequently to calibrate the OH signal. The quantification of the LIF signal to local OH distribution [OH(x,z)] follows Equation (4.1) (adapted from [83]), where $I^*_{LIF}(x,z)$ denotes the measured LIF intensity after correcting for variations in local laser intensity and laser line overlap integral, $A(x)$ the measured line-of-sight integrated absorption, spatially resolved in axial direction, g_0 the line overlap integral, ν_{ji} the center frequency of the excitation laser, B_{ji} the Einstein-B-coefficient, D_i the degeneracy and f_i the temperature dependent Boltzmann factor of the selected transition.

$$[\mathrm{OH(x,z)}] = I^*_{LIF}(x,z)\frac{A(x)}{\int I_{LIF}(x,z)\mathrm{d}z}\frac{1}{g_0 h\nu_{ji}/c B_{ji} D_i f_i} \tag{4.1}$$

Due to the dependence on temperature and/or chemical composition of some of the spectroscopic quantities, see Sect. 2.2.1, a careful selection of the excitation wavelength has to be made. As in previous studies [E7, E8] the line pair $Q_1(9.5) + Q_2(7.5)$ in the OH $A^2\Sigma \leftarrow$ OH $X^2\Pi(\nu' = 1 \leftarrow \nu'' = 0)$ system at 35,210.42 cm^{-1} was selected as

it presents a proper choice due to its low variation in Boltzmann factor (10% between 1200 K and 2400 K) and the broad spectral structure when measuring under increased pressure, improving the accuracy of the line overlap integral g_0 calculation. Excitation of the selected transition was realized using the frequency doubled output from a dye laser (Sirah, Precision Scan), pumped by a frequency doubled Q-switched flash-lamp pumped Nd:YAG laser (Spectra Physics, PIV400) operating at 10 Hz.

The absorption is inferred from an energy reference before and after the test section, as discussed below. To account for non-resonant losses, e.g. on the optical access of the combustor, on-resonant and off-resonant measurements, where the laser was tuned away from any surrounding OH resonance, were measured with short time separation. The line-of-sight integrated absorption, spatially resolved in x direction, is computed using Eq. (4.2) (adapted from [E7]), where E denotes a linear reference to energy.

$$A(x) = 1 - \frac{E(x)_{\mathrm{on,out}}/E(x)_{\mathrm{on,in}}}{\overline{E(x)_{\mathrm{off,out}}}/\overline{E(x)_{\mathrm{off,in}}}} \tag{4.2}$$

Measuring the spatially resolved energy of the OH laser light sheet after the test section is challenging in wall-normal measurements for a number of reasons: (a) The beams are dumped on the wall, so the energy reference has to be measured *at the wall* of the combustor, (b) depending on the operating condition, the effusion cooled liner reaches temperatures ≥ 1200 K [E8], (c) the NO-PLIF measurements are conducted almost at the same time (temporal separation between laser pulses is 100 ns) and exactly at the same location, (d) for near-wall measurements, the intensity is very high due to the proximity to the focal line of the laser light sheet.

To address all issues, the effusion cooled liner was coated with a dispersion of a high temperature binder (Zyp, HPC binder) and YAG : Tb^{3+} (Merck, $d_{50} = 4\,\mu$m) using an airbrush. While this is commonly used for wall-temperature measurements, here the dependency of phosphorescence on the incident intensity is used. YAG : Tb^{3+} was chosen as it provides a strong signal even at high temperatures and its emission in the green spectral range, allowing a good spectral separation from flame and soot luminescence. Phosphorescence was captured using an uncooled CCD camera (Basler, piA2400-17gm), equipped with an 135 mm lens (L_6: Takumar) mounted with a 15 mm extension tube. A bandpass filter with a transmission range between 525 and 575 nm (Edmund Optics) was used to improve separation from flame luminosity and black body radiation of the hot effusion cooled liner. Spatial variations in wall-temperature significantly impact the intensity of the phosphorescence signal. However, the absorption measurement is unaffected as long as the temperature is constant *in time*, i.e. the wall is in thermal steady state and has no significant fluctuation. More problematic is the non-linear energy response due to the high irradiation by the OH laser light sheet. This is accounted for by measuring the energy dependence at every measurement location independently. As the effusion holes cause discontinuities in the signal, the absorption was measured $\Delta y = 2$ mm adjacent to the center line. During this calibration measurement, the NO laser was blocked to avoid interference. From these measurements, the term $A(x)/\int I_{LIF}(x,z)\mathrm{d}z$ from Eq. (4.1) is calculated, temporally averaged and transferred to a measurement at the center line, now in combination with NO-PLIF. This approach assumes, that the integral quantity

$A(x)/\int I_{LIF}(x,z)\mathrm{d}z$ is constant with respect to time. To further improve accuracy and spatial continuity, the evaluated absorption within all field of views (FOVs) from one operating condition were interpolated on a common grid and smoothed using a piecewise cubic spline fitted to the data.

As an energy reference before the test section, a portion of the laser beam was extracted using an uncoated wedged fused silica plate beamsplitter at Brewster's angle and guided to a fused silica substrate that was coated using the same method, see Fig. 4.1. This allows, after dispersing the overlapped light sheets for OH- and NO-LIF with a prism, to capture both sheet profiles with one camera (Basler, piA2400-17gm). As with the detection system for the energy reference on the effusion cooled liner, a bandpass filter with the same transmission range in front of the lens (L_7: Carl Zeiss, 100/f2) was used to spectrally separate the phosphorescence signal from ambient light. Unlike within the combustor, the phosphorescence response to incident energy was linear due to the low intensity of the beam extracted by the wedged beamsplitter (W). This was verified by simultaneous measurements with a pyro-electric energy meter. The beamsplitter was put into the beam-path after the common cylindrical focusing length (CL; $f = 600\,\mathrm{mm}$) at Brewster's angle to minimize extracted energy.

An implication of Eq. (4.1), due to the integral LIF signal in the denominator, is that the region of interest of the LIF detection system has to cover the entire test section, i.e. every OH molecule has to be within the field of view. Imaging the height of 100 mm onto the photocathode of the image intensifier (LaVision, IRO; L_5: Cerco 100/f2 UV lens) results in a magnification of ≈1:5. In order to increase optical resolution, a second OH-PLIF detection system was mounted on the opposite side of the combustor. A UV lens (L_1: Cerco 100/f2) with extension tubes was used to produce a $\approx 1:1.7$ intermediate image which is subsequently collimated by a doublet (L_2) of spherical plano-convex lenses with a net focal length of $\approx 60\,\mathrm{mm}$. The collimated light is focused onto the photocathodes of the image intensifiers with two UV lenses (L_{3-4}: UV Nikkor, 105/f4.5), imaging the intermediate image with a magnification of 1.75:1, resulting in a total magnification of $\approx 1:1$. To minimize influence from signal trapping a narrow bandpass filter transmitting only the (1,1) vibrational band between 312 and 320 nm is used in front of the lenses on the image intensifiers [135]. Laser energy was adjusted to $\approx 6\,\mathrm{mJ}$ within the measurement volume to avoid saturation effects. Linearity was verified by measurements with varying energy on a laminar adiabatic V-flame burner within the test section.

For the interpretation of measured OH number densities, it is helpful to consider certain aspects derived from laminar flame simulations shown in Fig. 4.2. For a laminar adiabatic premixed flame, the OH number density is non-monotonic with respect to temperature. A super-equilibrium zone is observed in the vicinity of the flame-front. This super-equilibrium reaches values of ≈ 3 times the equilibrium value. Under the given conditions, chemical relaxation to equilibrium occurs within $\approx 0.5\,\mathrm{ms}$. For an easier interpretation of the measured OH number density, unless otherwise noted, results are normalized to the equilibrium value of the simulated flamelet at combustor conditions ($\Phi = 0.75$, $T_u = 623\,\mathrm{K}$, $p = 2.5\,\mathrm{bar}$), i.e. a normalized [OH] value ≥ 1 indicates super-equilibrium. The correlation between [OH] and temperature in chemical equilibrium is nearly independent from equivalence ratio for lean flames [83]. This allows to extract

an unambiguous dependency of temperature on [OH] in equilibrium conditions, shown in Fig. 4.2, i.e. the local temperature field can be derived from the measured OH number density.

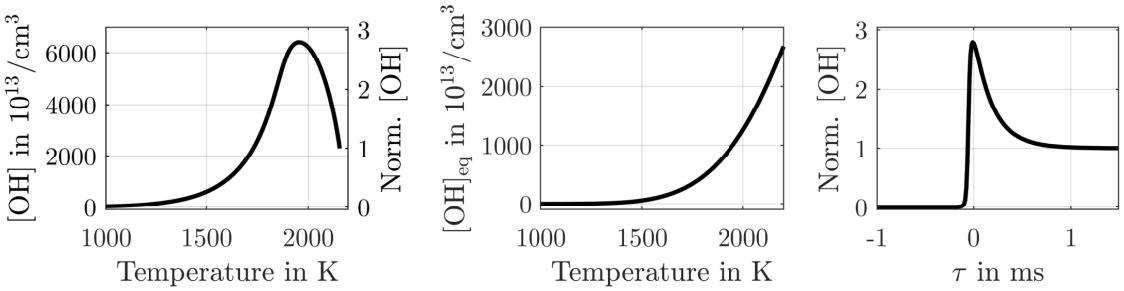

Figure 4.2: Top frame: [OH]-T curve from laminar adiabatic flame simulation at combustor conditions ($\Phi = 0.75$, $T_u = 623\,K$, $p = 2.5\,bar$). Middle frame: Extracted correlation between equilibrium temperature and OH number density. Bottom frame: OH number density normalized to equilibrium over simulated residence time. Residence time $\tau \equiv 0$ at peak [OH]. Figure adapted from [E5] with permission from Elsevier.

4.2.3 NO Planar Laser-induced Fluorescence

To investigate mixing between main flow and effusion cooling air, NO was seeded to the effusion cooling air. The choice of NO as a tracer was motivated due to its high thermal stability and relatively slow reaction kinetics [147], well-known spectroscopic properties and high signal-to-noise ratios (SNR) due to strong absorption [15, 121, 134]. Effusion air was seeded with 9000 ppm_V NO to prevent potential combustion generated NO to affect the measurements. Estimating the amount of combustion generated NO is challenging in this configuration, as it is mainly driven by long residence times at high temperatures [157]. As residence times vary strongly within the combustor due to high bulk outlet velocities

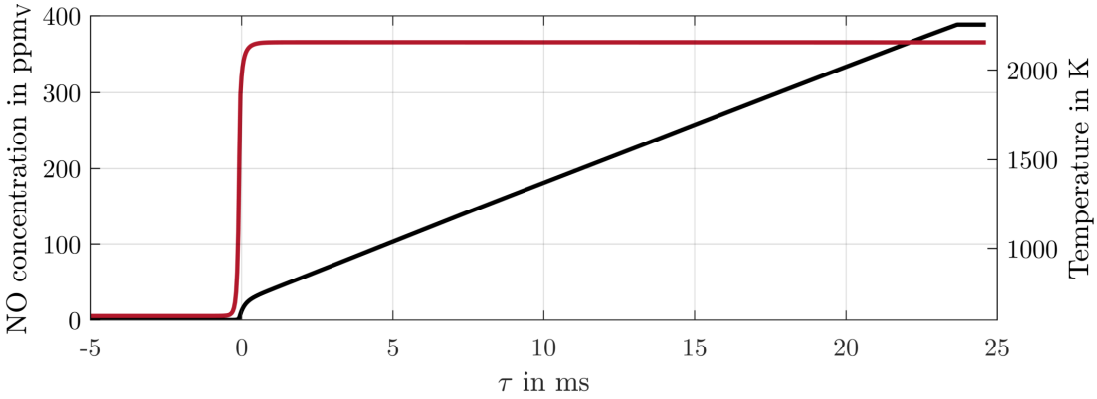

Figure 4.3: Combustion generated NO (black) and temperature profile (red) in a laminar flame simulation at combustor conditions with respect to residence time.

on the one hand and recirculation zones on the other hand. Plug-flow transit time, as

estimated from PIV measurements at similar operating conditions [E9], is in the order of 8 ms. Fig. 4.3 shows the simulated NO number density in ppm_V as a function of residence time for a freely propagating flame at combustor conditions. Even after 20 ms at *adiabatic flame temperature*, the combustion generated NO amounts to 300 ppm_V only, which is a factor of 30 below the amount of seeding used.

When investigating mixing processes of flows with different chemical compositions and temperatures, a proper selection of the excitation scheme is of great importance. To ensure proportionality of the measured spatially-resolved LIF intensity with the molar fraction X_e, i.e. the amount of cooling air divided by the total amount of cooling air and main flow, LIF signals were simulated using LIFSim [16] with quenching data from [144], as described in Sect. 2.2.1.3, under varying conditions. To evaluate the correlation between measured

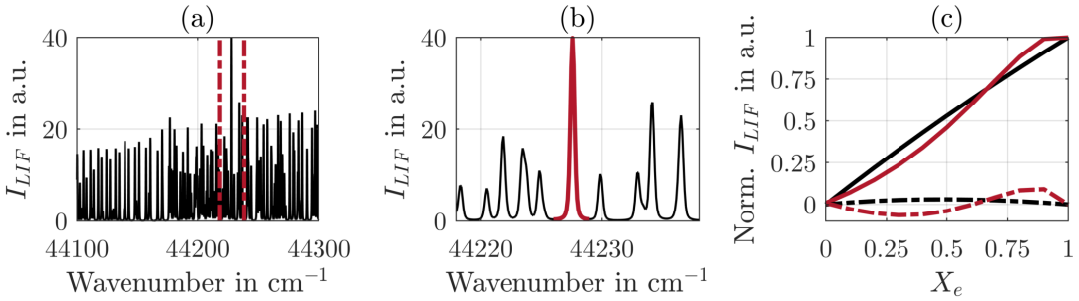

Figure 4.4: Selection of NO-PLIF excitation line. (a) Simulated excitation spectrum in the $44100 - 44300\,cm^{-1}$ range at equilibrium conditions of a $\Phi = 0.75$ methane-air flame with preheating to 623 K at 2.5 bar. (b) Zoomed in range with selected excitation line (red). (c) Correlation between normalized measured LIF signal and X_e. Solid lines represent correlation (Black: mixing before reaction; Red: mixing after reaction), dashed lines represent deviation from perfect linear relationship. Figure adapted from [E5] with permission from Elsevier.

LIF signal and X_e, one-dimensional laminar flame calculations at combustor conditions are used. The resulting gas compositions were subsequently mixed with varying fractions X_e of effusion cooling air. The derived chemical compositions and temperatures were fed into LIFSim to compute excitation spectra for every composition at various values of X_e. Fig. 4.4 shows a simulated excitation spectrum of NO at equilibrium conditions at the nominal equivalence ratio and preheating temperature of the combustor conditions and the resulting correlation between normalized LIF signal and X_e for the selected line. Although it appears as a single line in the simulated spectrum, there are actually 4 contributing transitions under the curve, namely $P_{21}(12.5)$, $Q_1(12.5)$, $Q_2(19.5)$ and $R_{12}(19.5)$ with major contributions from the Q-branch transitions. Due to the difference in rotational quantum number, the overlapping line-pair varies only slightly with temperature, allowing for good correlations for all expected mixing scenarios, i.e. mixing *before* reaction, mixing *during* reaction and mixing *after* reaction. The largest differences from perfect linear relationship between the measured LIF signal and X_e is represented by the red line in Fig. 4.4(c), where the deviation reaches values ≤ 0.08. For mixing before reaction, a maximum systematic error of 0.03 is estimated.

The excitation of the selected transition around $44227.6\,\mathrm{cm}^{-1}$ is realized using the frequency-tripled output of a dye laser (Sirah, Precision Scan), using Pyridine I as dye. The dye laser was pumped using a frequency-doubled pulsed Nd:YAG laser (Spectra Physics, GCR-4). The excitation beam is formed to a light sheet with a width of 20 mm and overlapped with the OH laser light sheet prior to the common cylindrical focusing lens, see Fig. 4.1. During the measurements, the fundamental wavelength of the dye laser was continuously monitored and controled using a wavemeter (HighFinesse, WS6) to avoid drift. LIF signals were captured using an image intensifier (LaVision, IRO) equipped with an uncooled CCD camera (Basler, Pilot). In order to record the same field of view as the high resolution OH-PLIF detection system, they share a common intermediate image, see Fig. 4.1. A dichroic longpass beam-splitter (Chroma, DCLP 270) was used to spectrally separate the NO-PLIF from the OH-PLIF signal. An additional longpass filter (Semrock, RazorEdge LP 224) in front of the lens on the intensifier (UV Nikkor 105/4.5) was used to suppress scattered radiation from the laser. Laser energy was attenuated to 1.6 mJ to stay within the linear regime. The latter was verified from measurements were the energy was varied between $0 - 8\,\mathrm{mJ}$ in an undisturbed jet-flow within the combustor.

4.2.4 Processing

4.2.4.1 Quantitative OH-PLIF

Quantification of the OH-PLIF signal for the low-resolution (LR) setup using Eq. (4.1) requires to correct the raw LIF signal for variations in local laser intensity and laser line overlap integral. Additionally, the absorption has to be inferred from phosphorescence measurements before and after the test section using Eq. (4.2). Furthermore, knowledge about the laser line overlap integral g_0 without modulation of the laser line shape has to be obtained. To extract the quantitative OH number density for the high-resolution (HR) setup, the HR FOV has to be found within the LR FOV in order to extract the local laser intensity for the HR FOV. These processing steps are described in the following.

Laser line overlap integral The laser line overlap integral g_0 is obtained from a non-linear least squares fit of experimental data to a simulated excitation spectrum using LIFBASE, see Sect. 2.2.1.4. The excitation scan was performed in the laminar V-flame at 2.5 bar and $\Phi = 1$ with an inlet temperature of 300 K, see Sect. 3, in the range $35205 - 35\,217.5\,\mathrm{cm}^{-1}$ in $0.05\,\mathrm{cm}^{-1}$ increments, covering the $Q_1(9.5) + Q_2(7.5)$ line pair as well as the $P_1(5.5)$ transition and minor contributions from the lines $P21(9.5)$, $Q21(17.5)$, $R12(7.5)$ and $R1(17.5)$. At every spectral position, 100 samples have been recorded for averaging out shot-to-shot variations in laser sheet profile and energy. From the images, a stationary region of interest (ROI) in the exhaust of the flame is extracted and spatially averaged to obtain the excitation scan. To avoid influence from residual non-resonant background signal, the extracted excitation scan is normalized to the interval [0,1] by subtracting the minimum far from a resonance at $35\,217.5\,\mathrm{cm}^{-1}$ and normalizing to the peak of the $Q_1(9.5) + Q_2(7.5)$ line pair. Instead of attempting to extract the laser line shape by deconvolution of the measured spectrum with the simulated spectrum, it is assumed that the laser line shape has a Voigt shape with unknown Gaussian and

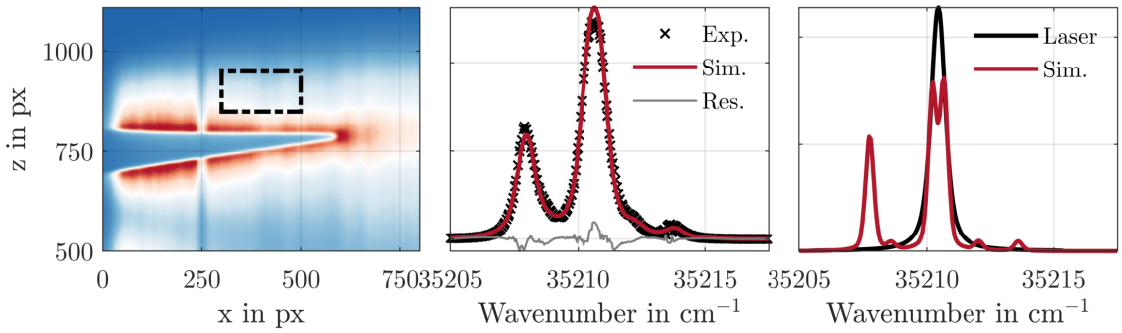

Figure 4.5: OH-LIF excitation scan in the spectral range 35205 – 35 217.5 cm^{-1} obtained from measurements in a stoichiometric laminar V-flame at 2.5 bar. Left: mean OH-PLIF signal. Inset rectangle shows ROI for spatial averaging; Middle: Extracted excitation scan (black symbols) with simulated spectrum after convolution with fitted laser line shape (red) and residual (gray); Right: extracted laser line shape (black) and simulated excitation spectrum from LIFBASE normalized to unity area for calculation of g_0.

Lorentzian contribution. In a non-linear least squares fit, these contributions are extracted by convolution of the excitation spectrum with different Voigt profiles until a best fit is obtained. Fig. 4.5 shows the procedure and the result of the fitting process. Best fit was obtained for a Voigt profile with 0.42 cm^{-1} Gaussian and 0.33 cm^{-1} Lorentzian contribution (all values FWHM). Evaluating Eq. (2.35) yields a value of 0.74 cm^{-1} for g_0.

As the laser line width is in the order of the transitional line width, variations in local laser line overlap at high integral absorption levels are expected. As described in Sect. 2.2.1.4, these variations are modeled using Eq. (2.37) by modulating the laser line shape by subtracting fractions of the absorption line. For an exact solution of the model, spatially

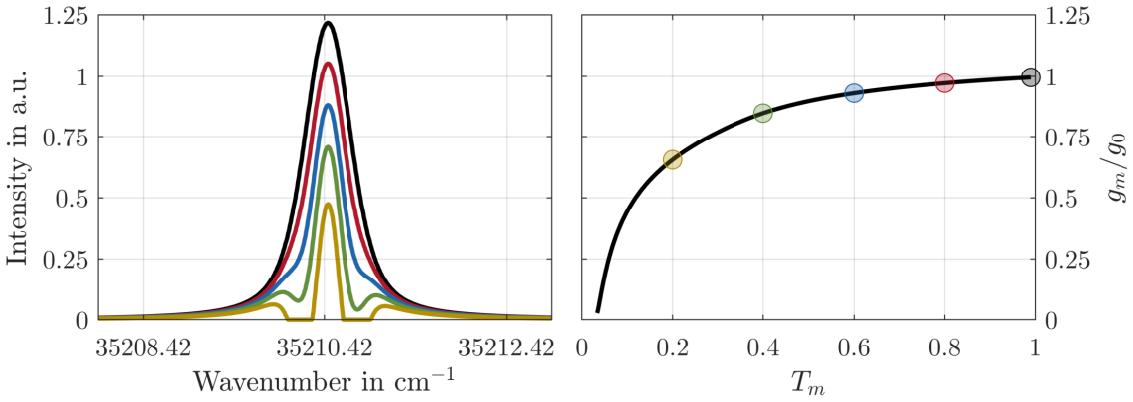

Figure 4.6: Modeled dependency of variation in local laser line overlap integral on local laser intensity. Left: Modulated laser line shapes at varying local laser intensity values. Right: Variation in local laser line overlap as a function of local laser intensity. Colors in the left plot indicate which laser line shape corresponds to a local laser line overlap integral value in the right plot.

resolved knowledge about the transitional line shape along the absorption path length is

required. This is a priori unknown. As a first order approximation, it is assumed that the transitional line shape does not vary strongly in the relevant temperature range and is properly represented by exhaust temperature and composition at combustor conditions. A benefit of this assumption is the implication that Eq. (2.37) may be evaluated ab initio, as it is then only dependent on local laser intensity T_m. This assumption is later addressed when discussing the uncertainty of the method. Fig. 4.6 shows the dependency of the resulting variation in local laser line overlap integral $g(x)$ on the local laser intensity for the given case. For visualization, $g(x)$ is normalized to g_0, i.e. to the overlap integral before any modulation of the laser line shape. For a local intensity of 0.2, i.e. 80% absorption, the spectral overlap integral is reduced by approximately 35% to 0.485 cm.

Absorption Spatially resolved absorption is inferred from phosphorescence measurements before and after the test section using Eq. (4.2). As discussed above, only the temporally averaged absorption is required for the calculation of $A(x)/\int I_{LIF}(x,z)\mathrm{d}z$. Before the absorption is calculated, the individual measurement systems have to be background corrected and matched to physical coordinates to allow mapping of the energy reference *before* and *after* the test section and subsequently derived integral absorption values to columns of the spatially resolved LIF signal. These processing steps are depicted in Fig. 4.7 and described in more detail in the following paragraph.

Background correction is done via subtraction of a mean image (100 samples), where the lasers were blocked. This eliminates influence from black body radiation from the effusion cooled liner and ambient light. Subsequently, the set of background corrected images is averaged over all acquired samples. For the phosphorescence measurement at the liner, a non-linearity correction is required as the intensity of the incident laser sheet exceeds the linear limit of phosphorescence of $YAG : Tb^{3+}$. This is achieved by continuously varying the laser energy by rotating a half-wave retardation plate before the BBO crystal for frequency doubling inside the laser used for OH-LIF excitation. This allows to vary the energy of the laser pulse without affecting polarization and sheet profile. Measurements of the total energy within the sheet using a pyro-electric energy meter are used as a linear reference for these measurements. These measurements have also been used to verify linearity of phosphorescence on the fused silica substrate coated with $YAG : Tb^{3+}$ used as reference for the incident laser sheet. To avoid resonant absorption within the FOV influencing the inferred linearity curve, these measurements have been conducted for the off-resonant case with 1000 samples per run. Spatial matching between the measurement systems is achieved by an additional measurement, where an irregular pattern was placed inside the beam path that allows to identify scaling and offset between the cameras in units of pixels. Matching to physical coordinates is performed by matching the resulting sets to the grid of the OH LR system after dewarping and mapping to physical coordinates as discussed in the next paragraph.

OH-PLIF Processing of OH-PLIF data is split up in three steps. These are a preprocessing step for both the low- and high-resolution detection system (LR/HR) that includes background subtraction, dewarping and mapping to physical coordinates as well

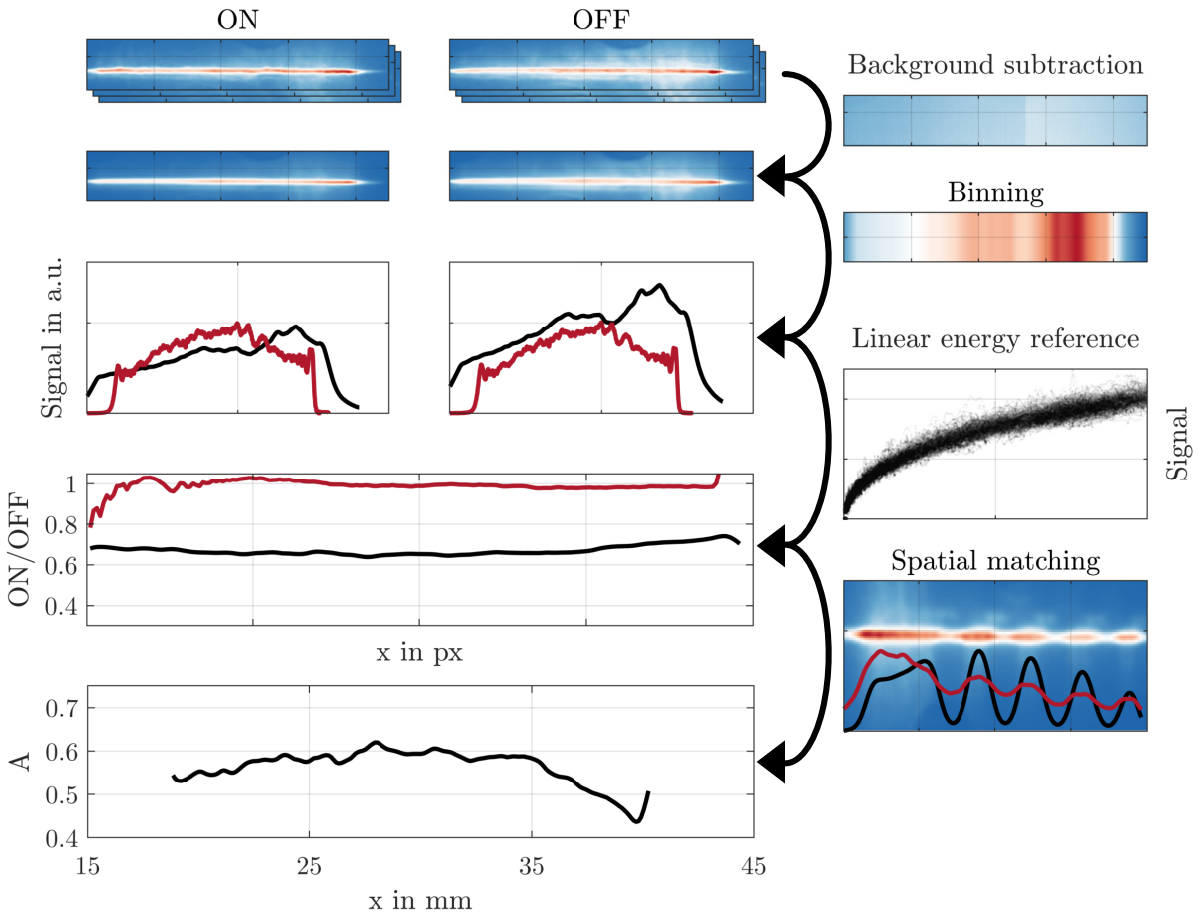

Figure 4.7: Processing steps to derive spatially resolved absorption from phosphorescence measurements. Figure shows processing of FOV3 at LS-HC-FP condition. Images in the first two rows show phosphorescence signal at the effusion cooled liner as an example. The same processing has been used for the measurement before the test section. Line plots show binned signals and ratios between on- and off-resonant measurements (black: ratio at effusion cooled liner after non-linearity correction displayed as scatter plot on the right side; red: before test section, no non-linearity correction necessary). From these ratios, the absorption A shown in the bottom plot is inferred using Eq. (4.2) after spatially matching the profiles to the OH LR detection system using an irregular pattern in the beam path.

as flat-field and vignetting correction. After preprocessing, the OH LR images are quantified according to Eq. (4.1) by correcting the signal for variations in local laser intensity and spectral overlap and subsequent calibration using spectroscopic constants from LIFBASE. In a last step, quantification of OH HR data is performed. This involves finding the HR region of interest within the LR FOV to repeat the calibration procedure for the HR system.

Preprocessing In a first step, OH PLIF images are background corrected by subtracting the mean off-resonant signal from the entire dataset. Subsequently, dewarping

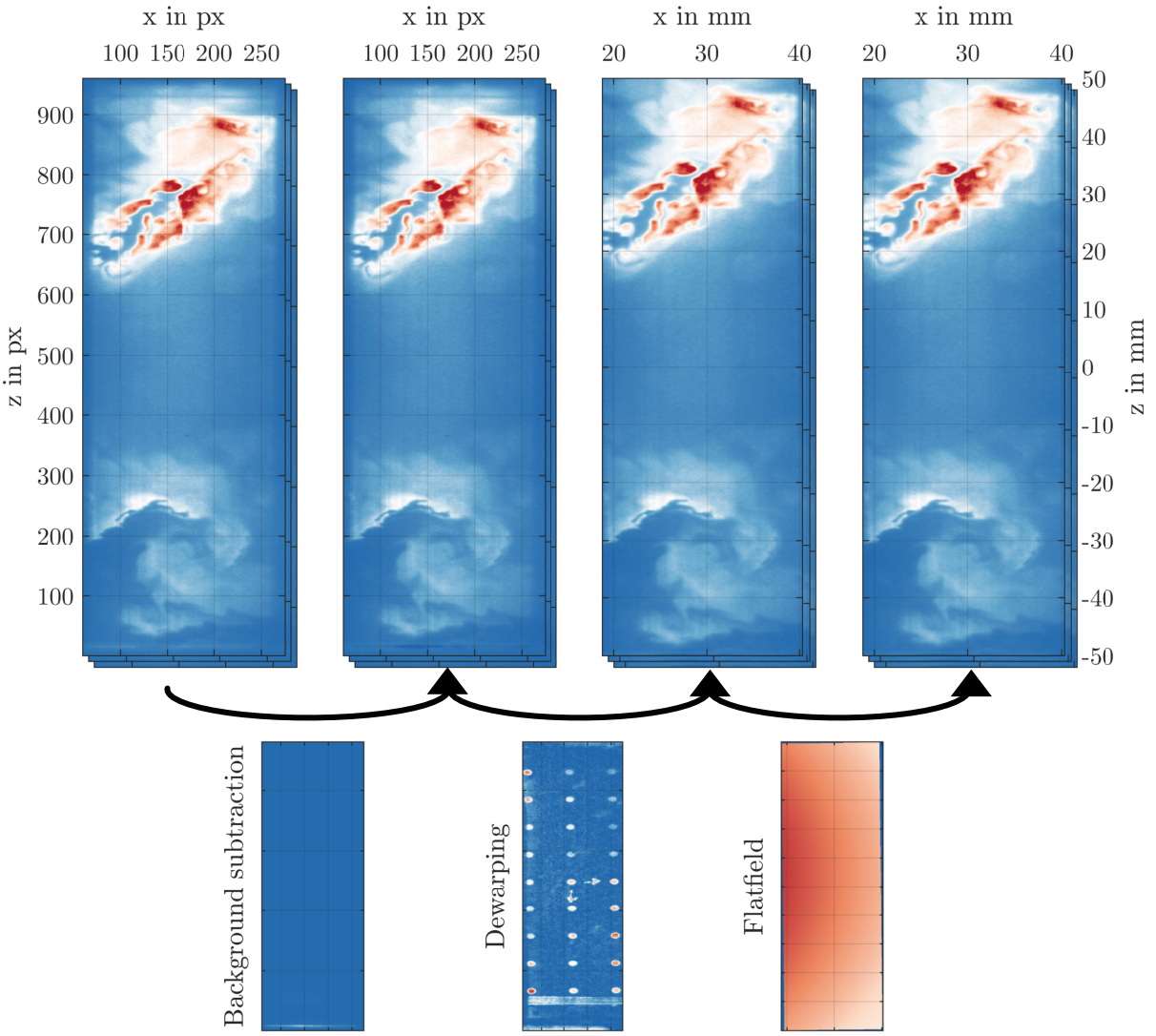

Figure 4.8: Preprocessing of OH-PLIF data: Background subtraction, dewarping and mapping to physical coordinates using a dot pattern target, flatfield correction.

and mapping to physical coordinates is achieved using a dot pattern target. A commercial software (LaVision, Davis) is used to fit a third-order polynomial surface to the dot pattern which is used as an interpolation grid. To account for non-uniform intensity distribution due to vignetting, an electroluminescent panel (Zigan, EL-1010) has been used to acquire a flat-field image. These panels have the advantage of being very thin ($\leq 0.4\,\mathrm{mm}$) and they can be cut to size at the opposite end of their electrical connector. This allows to achieve a nearly borderless flat field within the combustor to account for additional vignetting by the combustor geometry. The panel has been glued onto a precision milled block of aluminum for rigidity. This block was then placed in the object plane to acquire flat-field images for every FOV individually. Deviation from uniformity, as measured with a 1 mm aperture in front of a photodiode, was $\leq 10\%$ across the entire panel. These preprocessing steps are used for the LR and HR detection system.

Calibration After preprocessing, the OH PLIF data has to be corrected for variations in local laser intensity and laser line overlap integral. The local laser intensity is derived from the spatially resolved absorption measurement as shown in Fig. 4.7 and the OH PLIF signal *integrated in z-direction*, i.e. along the absorption path length.

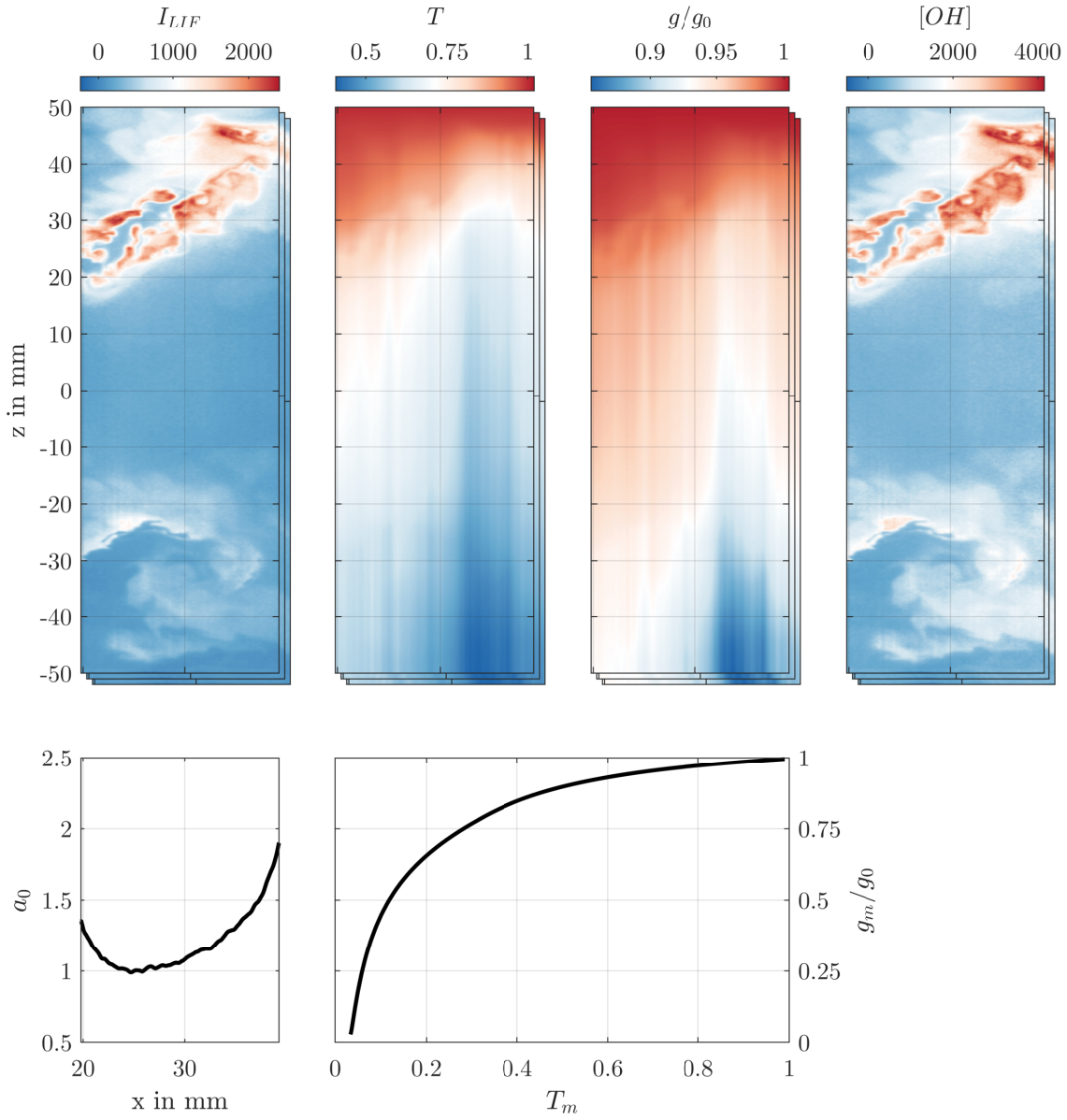

Figure 4.9: Calibration of OH-PLIF data. Top row, from left to right: Preprocessed LIF images, reconstructed local laser intensity, variations in laser liner overlap integral and calibrated OH number density in $10^{13}\mathrm{cm}^{-3}$. Bottom row shows a_0 and dependency of variation in laser line overlap integral with local laser intensity. Figure shows processing of OH LR data acquired in FOV3 at LS-HC-FP condition as an example.

The reduction of laser intensity at a given pixel m along the absorption path z is proportional to the local absorption coefficient. Although it cannot be measured directly, this

absorption coefficient can be approximated using the LIF signal itself as the LIF *image* is proportional to the derivative of the local laser intensity, assuming a constant fluorescence quantum yield along a given column in the PLIF image [83]. The assumption of a constant fluorescence quantum yield is further addressed when discussing the uncertainty of the method. This allows to iteratively reconstruct the local laser intensity T_{m+1} from the local laser intensity T_m, measured integral absorption $A(x)$ and the local LIF intensity $I_m(x)$ at a given pixel m along z using Eq. (4.3), where $T_1(x) \equiv 1$.

$$T_{m+1}(x) = T_m(x) - a_0 I_m(x) \tag{4.3a}$$

$$a_0 = \frac{A(x)}{\sum_m I_m(x)} \tag{4.3b}$$

The variation of the laser line overlap integral is inferred from the reconstructed local laser intensity by simply interpolating the entire field using the modeled dependency as shown in Fig. 4.6. After correcting the preprocessed LIF images by point-wise division with T and g/g_0, final calibration to [OH] is performed using Eq. (4.1). For the Einstein-B coefficient, a value of $B_{ij} = 2.955\,\mathrm{m^3\,J^{-1}\,s^2}$ is used, which corresponds to the mean of the $Q_1(9.5) + Q_2(7.5)$ line pair. As the temperature field is a priori unknown, the mean Boltzmann fraction of the line pair at 1800 K is used for evaluation which amounts to $f_i = 0.0384$. Fig. 4.9 shows the entire calibration procedure on an exemplary dataset.

Matching OH HR In principle, the evaluation of PLIF data acquired with the high-resolution detection system follows the same steps as the low-resolution system. For the calibration of HR data, the local laser intensity reconstructed for the LR system is used to derive the integral absorption within the HR FOV. This requires precise knowledge of the location of the HR region of interest (ROI) inside the LR FOV. This is determined by downsampling the HR data onto the grid of the LR system after dewarping and subsequently finding the location by cross-correlation on a single-shot basis. The detected ROI is then used to extract the ensemble averaged local laser intensity profiles at the boundaries. Subsequently, these profiles are upsampled to the original HR resolution and used to derive a local laser intensity field in the HR FOV. Fig. 4.10 shows the implemented procedure. Evaluation of the OH number density is then performed using the steps described above.

4.2.4.2 NO-PLIF

In this section, the processing steps necessary to derive the quantitative effusion air mole fraction X_e from NO-PLIF images are described. This is split up in the steps preprocessing and calibration.

Preprocessing The preprocessing of NO-PLIF images basically follows the same scheme as for OH-PLIF as depicted in Fig. 4.8, i.e. it involves background and flatfield correction, dewarping and mapping to physical coordinates. Additionally, to improve SNR while preserving spatial gradients, block-matching 3D filtering (BM3D) [39] was

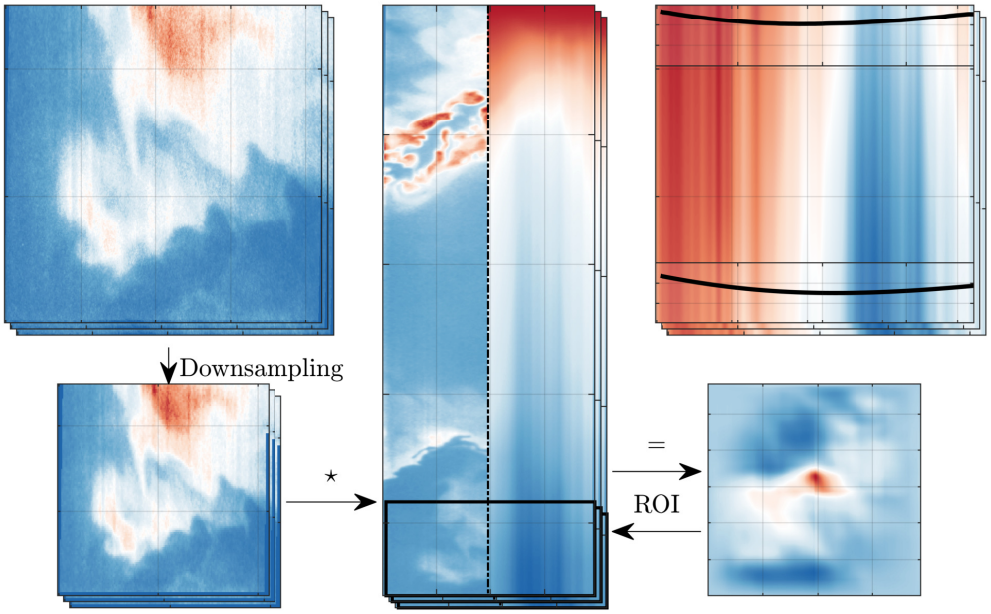

Figure 4.10: Matching of high- and low-resolution OH PLIF data. Upper left: OH HR dataset prior to downsampling. Middle: corresponding OH-LR data and local laser intensity. Inset rectangle shows boundary of HR ROI inside LR FOV as evaluated from 2D cross-correlation (bottom right). Upper right plot shows reconstructed local laser intensity of the HR FOV as calculated using Eq. (4.3) with the ensemble averaged incident and exiting intensity profiles as insets extracted at the boundaries of the HR ROI.

used. Subsequently, the images are corrected for shot-to-shot variations in the laser sheet profile using the phosphorescence measurement at the fused silica substrate before the beams enter the combustor.

Calibration For near-wall measurements, where the effusion holes are within the FOV, the NO LIF signal is calibrated using the mean signal in the core of the effusion jet. The core of the jet is automatically identified by the location of the lowest relative standard deviation above the hole. For some cases, especially at LC condition, the PDF of the LIF signal at this location is bi-modal due to locally disturbed outflow. For these cases, the peak at high LIF signals, corresponding to samples that have sufficient outflow, is used for calibration. Fig. 4.11 shows the calibration procedure. For FOVs further away from the wall, where no location with $X_e = 1$ is within the FOV that could be used for calibration, results are only analyzed qualitatively.

Absorption effects, e.g. from hot CO_2 are neglected [140]. As the calibration is performed at a location where the beam has already passed $\geq 98\%$ of the combustor's height, this influence is assumed to be negligible. However, this possibly leads to an overestimation of X_e with increasing wall-distance inside the FOV. As a last step, the calibrated NO-PLIF images are interpolated onto the OH HR grid to simplify further evaluation.

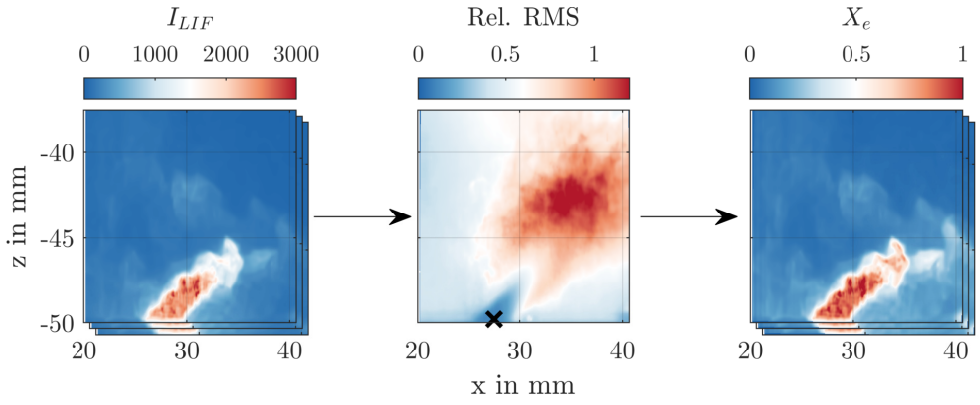

Figure 4.11: Derivation of quantitative effusion air mole fraction X_e from preprocessed NO-PLIF images. From left to right: preprocessed NO-PLIF images, relative standard deviation of ensemble with identified minimum shown as black X, calibrated effusion air mole fraction X_e.

4.2.5 Resolution

Fig. 4.12 shows object side MTF measurements as obtained using a Siemens star evaluated with YASSES, see Sect. 2.2.3, for all detection systems used in the experiment. As evident

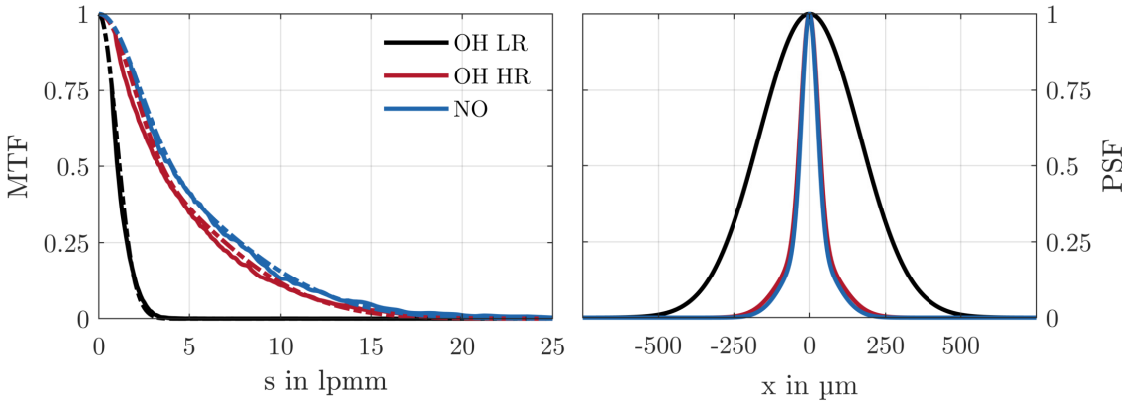

Figure 4.12: MTF and PSF of OH LR (black), OH HR (red) and NO (blue) detection system as obtained from Siemens star measurements evaluated using YASSES. Solid lines represent measured values, dashed lines represent fits with a Gaussian (OH LR) or sum of two Gaussian (OH HR, NO) form functions.

from the figure, the detection system for OH LR has the lowest resolution with an MTF that is well approximated with a Gaussian PSF of $\approx 390\,\mu m$ FWHM. For the OH HR and NO detection system, a better fit to the measured MTF curve was obtained with a PSF consisting of the sum of two Gaussians. The widths of the PSFs are $\approx 76\,\mu m$ and $\approx 68\,\mu m$ FWHM, respectively. Focal line thickness of the laser sheets are $\approx 120\,\mu m$ for NO and $\approx 150\,\mu m$ for OH, respectively.

4.2.6 Uncertainty

4.2.6.1 Quantitative OH-PLIF

As the derivation of quantitative OH number densities from combined absorption and PLIF measurements involves a comparably complex evaluation procedure, estimating the uncertainty is rather challenging due to the many correlated influencing parameters. Additionally, assumptions such as constant Boltzmann fraction, constant fluorescence quantum yield along the absorption path and uncertainties in the variation of laser line overlap integral may lead to additional errors which heavily depend on the local temperature and species composition. For this reason, a Monte-Carlo simulation is performed to estimate the net measurement uncertainty. For every uncertain parameter within the simulation, a normal distribution with given mean and standard deviation is assumed. A flow-chart of the simulation with all involved modules, which are discussed below, is depicted in Fig. 4.13.

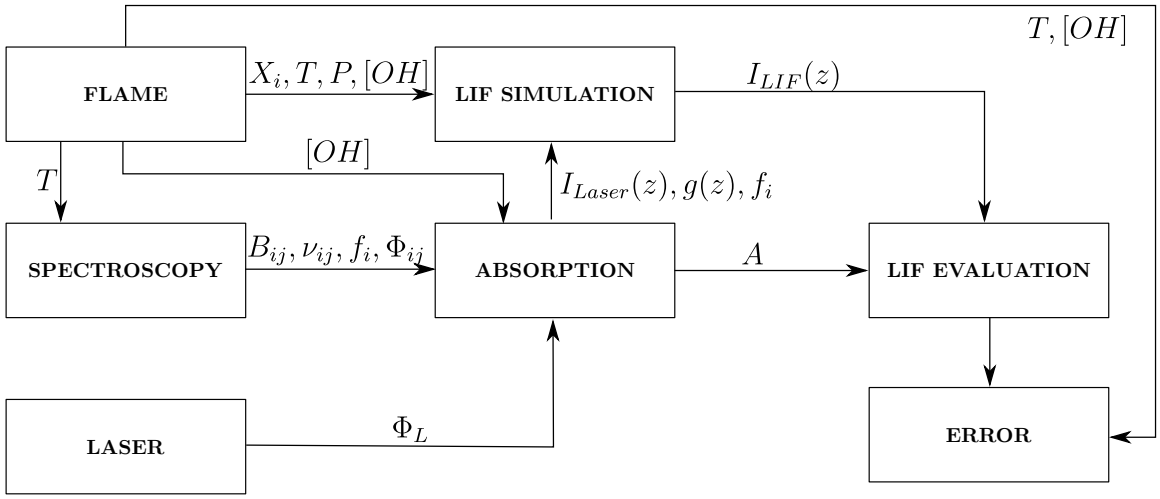

Figure 4.13: Flow-chart of Monte-Carlo simulation for uncertainty estimation of quantitative OH measurements.

Flame module In this module, non-adiabatic laminar flame calculations at $P = 2.5\,\text{bar}$, $T_u = 623\,\text{K}$ and $\Phi = 0.75$ with varying heat loss, simulated using the *Universal Flame Solver* (ULF[18]) [170], are used to mimic typical radial profiles in the primary zone of the combustor. Four of these simulations are combined to establish a profile with 100 mm length that resembles the presence of two outer recirculation zones, the two lobes of the main stage and an inner recirculation zone, see Fig. 4.14. The amount of heat loss in the inner recirculation zone is chosen to approximate the measured mean temperature in this area, see Sect. 5. For the outer recirculation zones, different levels of heat loss are simulated to expand the temperature range to lower values. This approach has been

[18]Thanks to Dr. Arne Scholtissek for providing the non-adiabatic laminar flame simulations.

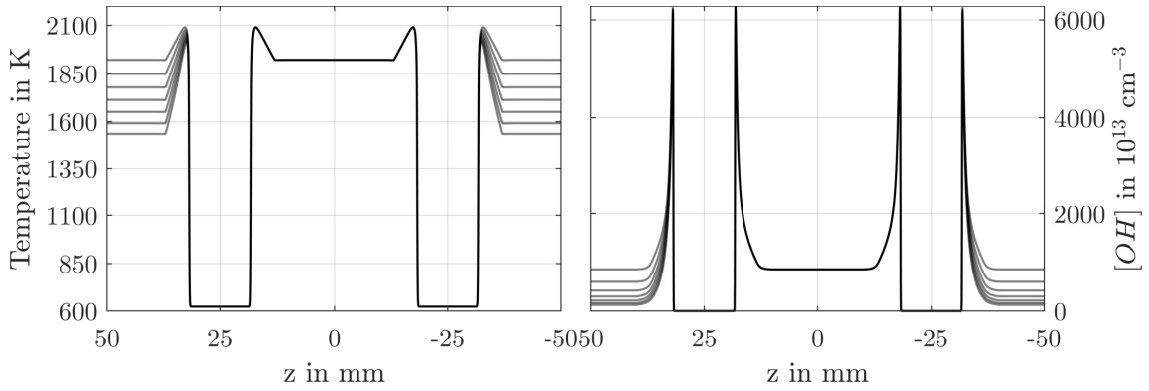

Figure 4.14: Non-adiabatic flame simulation used for Monte-Carlo simulation. Left: temperature profile, Right: OH number density profile.

chosen to cover a temperature range where OH number densities are significant to properly represent variations in Boltzmann fraction, quenching and transitional line shapes. To simplify parts of the computation, the profiles are symmetrical, i.e. both outer recirculation zones are taken from the same non-adiabatic laminar flame simulation. This neglects asymmetrical influences such as effusion cooling. However, for the estimation of uncertainty, it is only required to ensure representative variations in temperature and species concentrations in the simulated profiles.

This module provides temperature and species concentration profiles required for the other modules.

Spectroscopy module In this module, the transitional line shape of the overlapping $Q_1(9.5) + Q_2(7.5)$ line pair is simulated. The line shape is modeled with contributions from Doppler and collisional broadening as described in Sect. 2.2.1.4. Within this module, uncertainty of seven parameters are accounted for as summarized in Tab. 4.1. These are the Einstein-B coefficients and the center frequencies for both transitions as well as factors affecting collisional broadening. Fig. 4.15 shows 250 randomly selected realizations of the transitional line shapes within the Monte-Carlo simulation within the IRZ at $z = 50\,\mathrm{mm}$, the ORZ at $z = 10\,\mathrm{mm}$ and the peaks of the inner and outer reaction zone near $z = 70\,\mathrm{mm}$ and $z = 80\,\mathrm{mm}$, respectively. Note that the FWHM of Doppler broadening is approximately twice the value of collisional broadening. Consequently, variations of the latter do not affect the spectrum to a large extent.

This module returns the transitional line shape Φ_{ij}, the Boltzmann fraction f_i as well as the Einstein-B coefficients and the center frequencies ν_{ij}.

Laser module The laser line shape is modeled as a Voigt profile with uncertain Gaussian ($\Delta\nu_G$) and Lorentzian ($\Delta\nu_G$) contributions. This is to account for uncertainties in the line scan measurement. In addition, the laser center frequency is assumed to be uncertain due to limited accuracy of the wavemeter measurement and repeatability due to

Table 4.1: Spectroscopic uncertainties.

Parameter	Mean	RMS	Comment
p	2.5 bar	±0.1 bar	Estimated uncertainty of combustor operating pressure.
T_{ref}	2000 K	±8%	Variation in reported values in [11].
n	0.66	±0.2	Broad range because reported value of 0.66 in [129] is only valid for (0,0) transitions.
$\nu_{Q_1(9.5)}$	$35\,210.64\,\mathrm{cm}^{-1}$	±0.05%	Uncertainty from HITRAN [64]
$\nu_{Q_2(7.5)}$	$35\,210.20\,\mathrm{cm}^{-1}$	±0.05%	See comment above.
$B_{Q_1(9.5)}$	$2.988 \times 10^{17}\,\mathrm{m}^3\,\mathrm{J}^{-1}\,\mathrm{s}^2$	±5%	Taken from Heinze et al. [83]
$B_{Q_2(7.5)}$	$2.923 \times 10^{17}\,\mathrm{m}^3\,\mathrm{J}^{-1}\,\mathrm{s}^2$	±5%	See comment above.

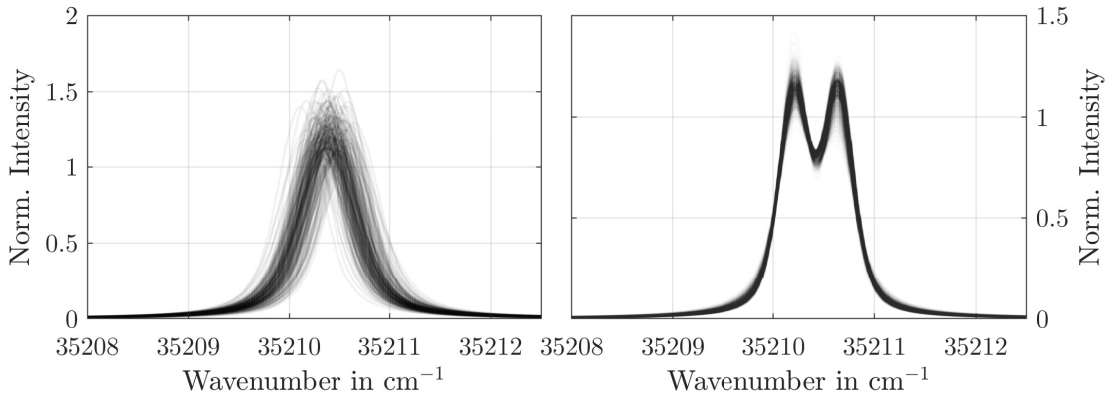

Figure 4.15: Variations of laser line (left) and transitional line shapes (right) in Monte-Carlo simulation. Shown are 250 randomly selected area normalized line shapes.

frequent changing between off- and on-resonant measurements. Uncertainties accounted for in this module are given in Tab. 4.2. 250 randomly selected realizations of the laser line shapes within the Monte-Carlo simulation are shown in Fig. 4.15.

Table 4.2: Laser uncertainties.

Parameter	Mean	RMS	Comment
ν_0	$35\,210.4\,\mathrm{cm}^{-1}$	$\pm 0.15\,\mathrm{cm}^{-1}$	Variation in measured center frequency across all measurements
$\Delta\nu_L$	$0.42\,\mathrm{cm}^{-1}$	±5%	Estimated from line scan measurement.
$\Delta\nu_G$	$0.33\,\mathrm{cm}^{-1}$	±5%	Variations in this range correspond to 10% increased residuals.

This module returns the laser line shape Φ_L required for calculation of the laser line overlap integral.

Absorption module In this module, information from flame simulations, spectroscopy and laser line shape are used to calculate the local laser intensity $I_{Laser}(z)$, local laser line

overlap g and line-of-sight integrated absorption A. Local laser intensity is calculated using the discrete linearized form of Beer's law of absorption given in Eq. (2.36). The local laser line overlap integral is calculated using Eq. (2.35) including modulation of the laser line shape using Eq. (2.37), accounting for the entire *history* of transitional line shapes. Fig. 4.16 shows the variation of the local laser intensity and overlap integral within the Monte-Carlo simulation.

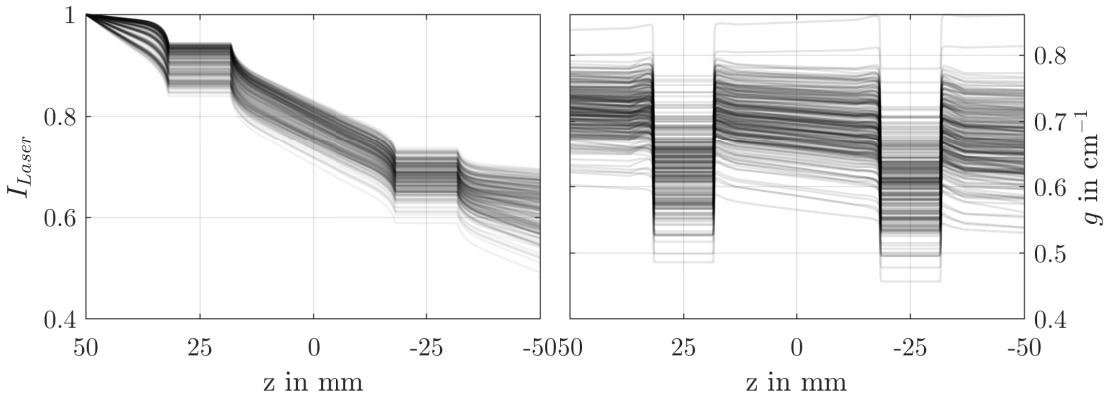

Figure 4.16: Calculated local laser intensities (left) and laser line overlap integrals (right) within the Monte-Carlo simulation. Shown are 250 randomly selected samples.

This module returns the local laser intensity, local overlap integral and Boltzmann fraction for the LIF signal simulation as well as the line-of-sight integrated absorption for the LIF evaluation.

LIF simulation module In this module, the 1D OH-LIF signal is simulated according to Eq. (2.26). Quenching rates are calculated using the chemical composition, temperature and pressure from the flame module. In addition to accounting for local laser intensity, Boltzmann fraction, quenching, spectral overlap integral, Einstein-B coefficient and OH number density, this module simulates the dual-resolution detection system. This is achieved by convolving the simulated LIF signal with the PSFs for the LR and HR detection system prior to interpolating the signals on a uniform pixel grid to mimic the behavior of the array detector. Just as in the experiment, the LR detection system covers the entire width of the flame while the HR system covers a width of 15 mm at the end of the absorption path. This simulates measurements near the effusion cooled liner, see Sect. 4.2.7. To account for the precision of the LIF measurement, Poisson distributed noise is added to the simulation. Commonly, the intensifier gain in the experiment is adjusted to maximize the dynamic range. Consequently, both simulated LIF signals are normalized in a way that the peak within the FOV corresponds to 4000 counts. Additionally, an artificial residual background is added to the signal to account for imperfect background subtraction commonly observed when using image intensifiers for detection. Fig. 4.17 shows 250 randomly selected LIF signal simulations used in the Monte-Carlo simulation. Uncertainties within this module are summarized in Tab. 4.3.

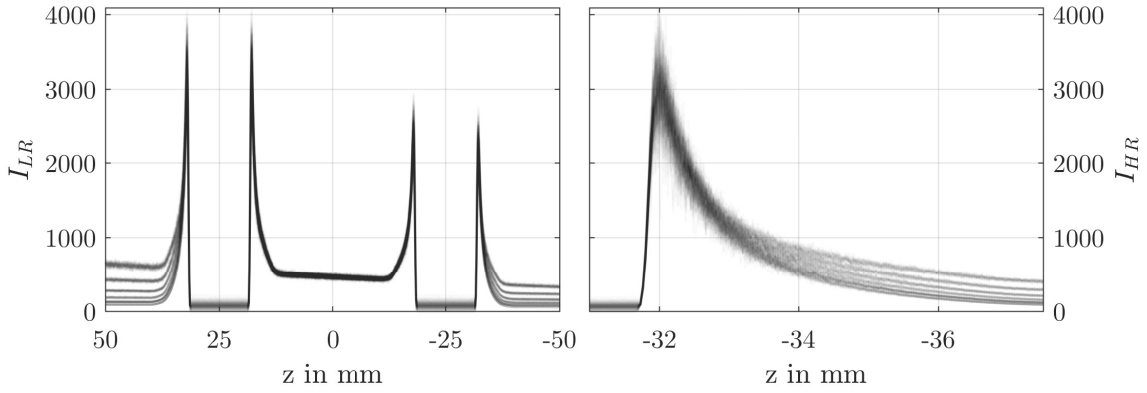

Figure 4.17: Simulated LR (left) and HR LIF signals within Monte-Carlo simulation. Note the asymmetry of the profile induced by absorption. Laser enters from the left side at $z = 50\,\text{mm}$. HR signal zoomed in to reaction zone between $-30\,\text{mm}$ and $-37\,\text{mm}$, actual HR window extends to $-50\,\text{mm}$. Shown are 250 randomly selected samples.

Table 4.3: LIF measurement uncertainties.

Parameter	Mean	RMS	Comment
SNR	30	-	Estimated from measurements in laminar flame.
Residual background	100	±50	Estimated from signal in fresh gas in combustor.

LIF evaluation module In this module, the simulated LIF signal and the absorption A is used to feed the evaluation algorithm described in Sect. 4.2.4.1. To account for uncertainty of the absorption measurement, the absorption is imposed with an uncertainty of 10%. This uncertainty is estimated by repetition measurements within the combustion chamber. Fig. 4.18 shows the evaluated OH number density for the 250 samples shown in Fig. 4.17.

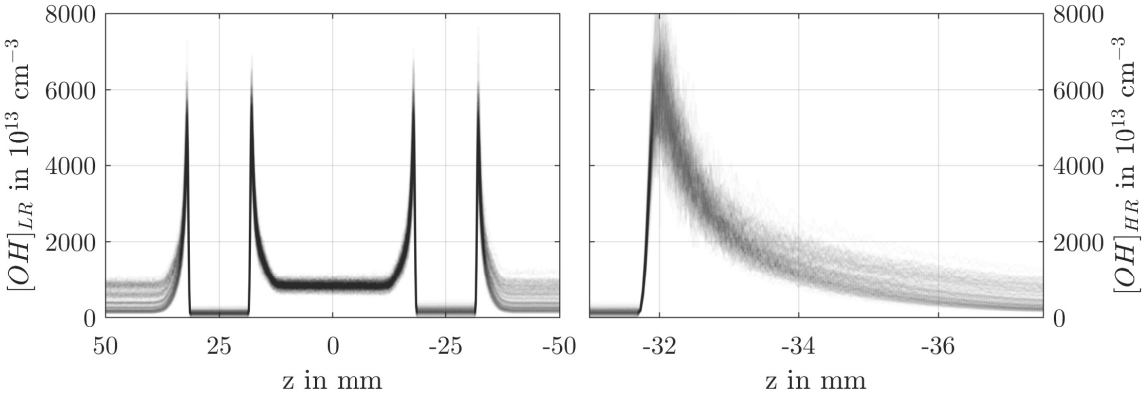

Figure 4.18: Evaluated LR (left) and HR LIF signals within Monte-Carlo simulation. Shown are the same 250 samples used in Fig. 4.17.

In addition to the evaluated number density for the LR and HR measurements, this module returns the temperature estimated from OH number density using the [OH]-T correlation presented in Fig. 4.2.

Error module In this module, the relative error of the measurement with respect to the underlying simulation is evaluated for every iteration of the Monte-Carlo simulation. As the LR system is mainly used to derive the local laser intensity at the boundaries of the HR FOV, the error is defined only for the HR system, see Eq. (4.4), where ϵ_N and ϵ_T represent the relative error of the number density and temperature, respectively.

$$\begin{aligned} \epsilon_N(z) &= \frac{[OH]_{sim}(z) - [OH]_{eval}(z)}{[OH]_{sim}(z)} \\ \epsilon_T(z) &= \frac{T_{sim}(z) - T_{eval}(z)}{T_{sim}(z)} \end{aligned} \tag{4.4}$$

Fig. 4.19 shows the evaluated OH number density and temperature in comparison to the exact solution for an exemplary flame configuration within the simulation. Quite notable is the large deviation in the temperature evaluation in regions where the equilibrium assumption is not met, i.e. close to the reaction zone for $z \leq 84\,\mathrm{mm}$, where the temperature is overestimated by approximately 500 K. This is expected as only the *equilibrium* OH number density has a reasonable correlation with the local temperature. For $z > 84\,\mathrm{mm}$, the relative error is drastically reduced. Due to the near-exponential dependency of the equilibrium OH number density on temperature, the precision of temperature measurements is much higher compared to the evaluation of the OH number density itself, as visible by the lower spreading of the profiles shown in Fig. 4.19. For areas before the reaction zone, the error in [OH] and temperature increase drastically, mainly due to the simulated residual background which limits the dynamic range of the method. The impact of limited optical resolution is visible near the [OH] peak of the reaction zone, where measured values are shifted further to the right as a result of the convolution with the PSF which affects the steep spatial gradient encountered during OH production.

Results of Monte-Carlo simulation Fig. 4.20 shows the resulting 2σ range around the mean relative error for temperature and [OH] evaluation. Due to finite resolution effects, OH number densities near the simulated peak are systematically underestimated by 50%, followed by declining over-estimation of post reaction zone [OH] with a peak of around 5%. For $z > 84\,\mathrm{mm}$, OH number densities are in average underestimated up to 9%, which is a result of the assumption of constant Boltzmann fraction and fluorescence quantum yield along the absorption path length. As finite optical resolution causes the OH peak to shift to higher temperatures (in this case, higher z-coordinates), the high degree of underestimation somewhat exaggerates the actual error when comparing at fixed spatial locations. If instead the *peak* simulated OH number density is compared to the peak evaluated number density, the underestimation is reduced to 9%. The standard deviation of the relative error has a maximum value of 18% near $z = 82\,\mathrm{mm}$ and reduces to values $\leq 13\%$ for $z > 84\,\mathrm{mm}$. Thus, for quantitative [OH] measurements, a conservative

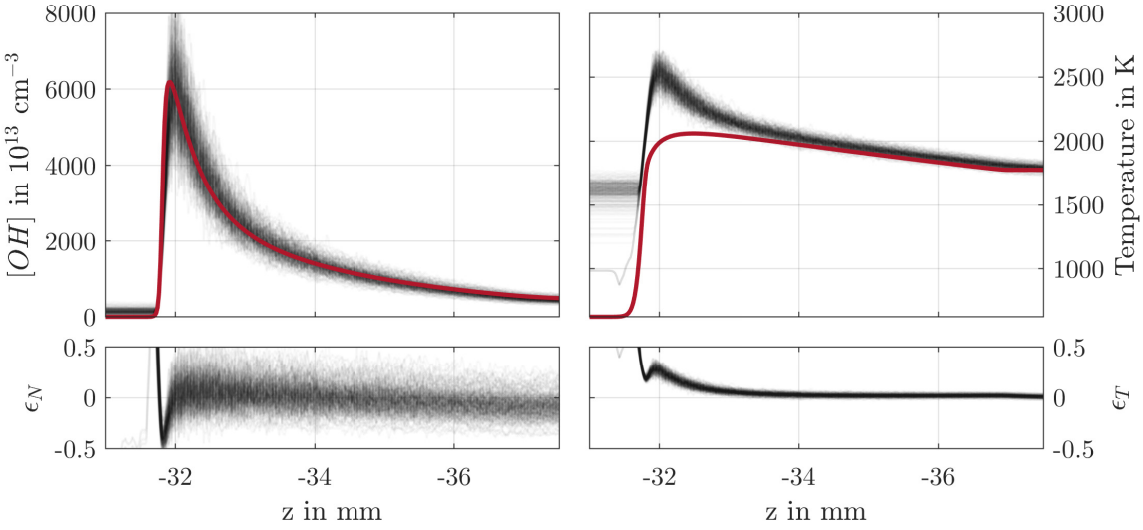

Figure 4.19: Comparison between simulated (red) and evaluated (black) [OH] (left) and temperature (right) with relative errors ϵ_N and ϵ_T in the bottom row for the HR simulation. Shown are 250 randomly selected results for an intermediate heat loss in the ORZ, where the temperature in chemical equilibrium corresponds to $\approx 1750\,\mathrm{K}$.

estimate for the accuracy and precision with values of 15% and 20%, respectively, is reported. For derivation of a temperature field in chemical equilibrium, in this simulation for $z \geq 84\,\mathrm{mm}$, an accuracy of $\leq 2\%$ and a precision of $\leq 3\%$ of the measured value is reported. For a temperature of 2000 K, this corresponds to 40 K and 60 K, respectively.

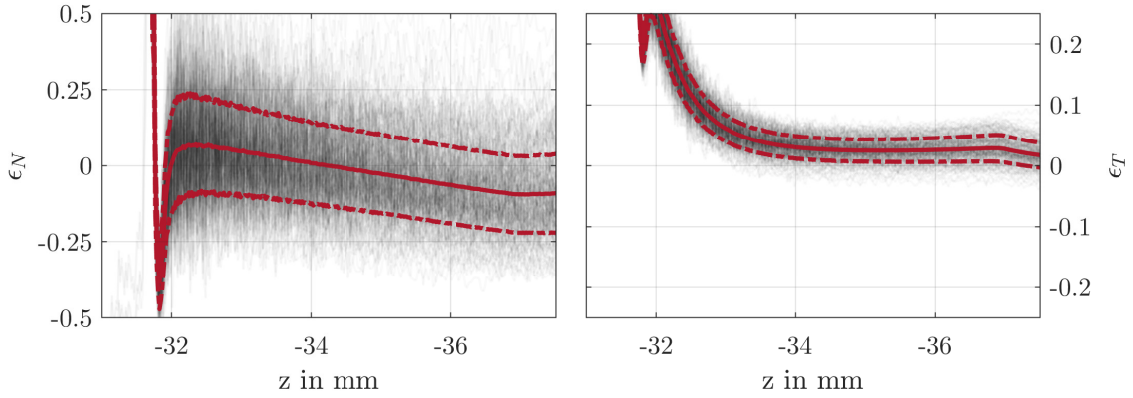

Figure 4.20: Mean (solid red lines) and 2σ range (dashed red lines) of relative errors ϵ_N and ϵ_T of all 10.000 Monte-Carlo iterations over 250 randomly selected realizations (black).

To further assess the accuracy of the quantitative OH-PLIF measurements, a comparison to gas-phase temperatures, cf. Sect. 5, is performed at the outlet, see Fig. 4.21. As the typical chemical relaxation time is much faster than the estimated residence time in the combustor[19], the equilibrium assumption is met in this region. The mean derived gas-

[19]Plug-flow transit time is $\approx 8\,\mathrm{ms}$, estimated from bulk outlet velocity and length of combustor.

phase temperature from [OH] measurements deviate by less than 30 K in a temperature range $\geq$ 1600 K which is close to the uncertainty of the presented CARS measurements. Deviations increase when approaching lower temperatures due to the limited dynamic range of the method and the fact that temperatures can only be measured in regions with sufficient OH signal. The lower temperature limit corresponds to approx 1400 K. As the deviation from mean temperature and the detectable temperature limit, which is $\approx$ 200 K below the simulated detection limit shown in Fig. 4.19, it is assumed that the Monte-Carlo simulation provides a valid conservative estimate of the measurement uncertainty.

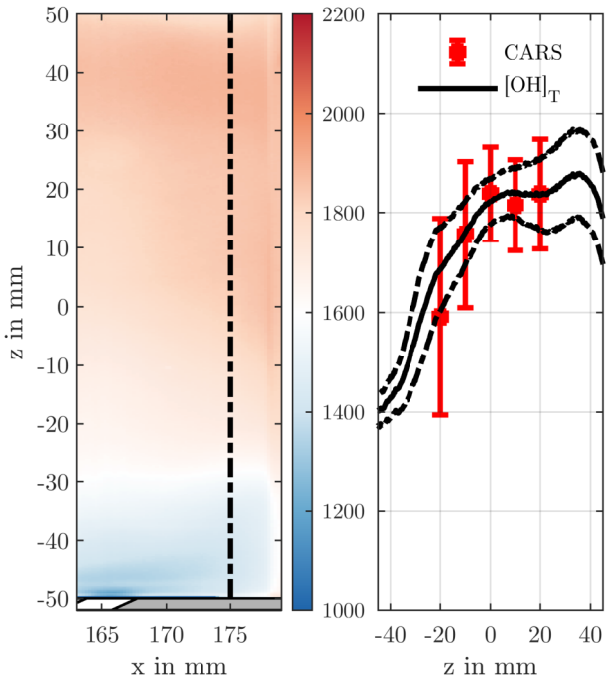

Figure 4.21: Verification of quantitative OH measurements by comparing the temperature field derived from equilibrium assumption to CARS measurements at the same conditions. Left plot shows spatially resolved temperature field as calculated from [OH] low-resolution measurements. Line plots at $x = 175$ mm are extracted for the right plot. Errorbars and dash-dotted lines show a 2σ range around the mean temperature (1000 samples) measured by CARS and [OH], respectively. Figure taken from [E5] with permission from Elsevier.

4.2.6.2 NO-PLIF

The estimation of precision for NO-PLIF measurements is based on the relative standard deviation in the core of the effusion jets which amounts to approximately 10%, corresponding to an SNR of 10 as defined by the reciprocal coefficient of variation. In areas with lower X_e values, the SNR is assumed to degrade according to Poisson statistics, i.e. the SNR is proportional to the square root of the local signal intensity. With this assumption, the estimated detection limit at SNR = 1 corresponds to $X_e = 0.01$. The observed value in reaction zones far from the effusion cooled liner within FOV3, where

only minor contribution from effusion cooling air is expected, amounts to ≈ 0.02, indicating that either the SNR is slightly overestimated or these reaction zones indeed contain measurable (with SNR = $\sqrt{2} \approx 1.414$) amounts of effusion cooling air.

The accuracy reported for X_e measurements corresponds to deviation from linearity of the effusion air mole fraction with the measured LIF signal as shown in Fig. 4.4 and amounts to 0.03 and 0.08 for areas with fresh-gas mixing and mixing with reaction zones, respectively.

4.2.7 Parameter Space and Measurement Locations

Fig. 4.22 shows an overview of the investigated FOVs in the primary zone and the FCAI region. FOV1 is centered at the nozzle, FOV2 is located within the flame brush in the inner shear layer (ISL). FOV3-5 are measured above the first three effusion holes on the center line of the combustor. As can be seen in the figure, the three effusion holes interact with different parts of the flame. The upstream located FOV3 covers parts of the outer recirculation zone (ORZ) and the outer shear layer (OSL). In FOV4, the tip of the flamebrush approaches the wall. FOV5 is located in the exhaust region of the ISL. One additional FOV was measured near the outlet of the combustor (not shown in Fig. 4.22).

Measurements have been conducted for all parametric variations, i.e. three levels of swirl (LS, IS, HS) as well as two levels of cooling air mass flow (LC, HC) and staging (FP,PP), respectively, which results in 12 operating conditions total.

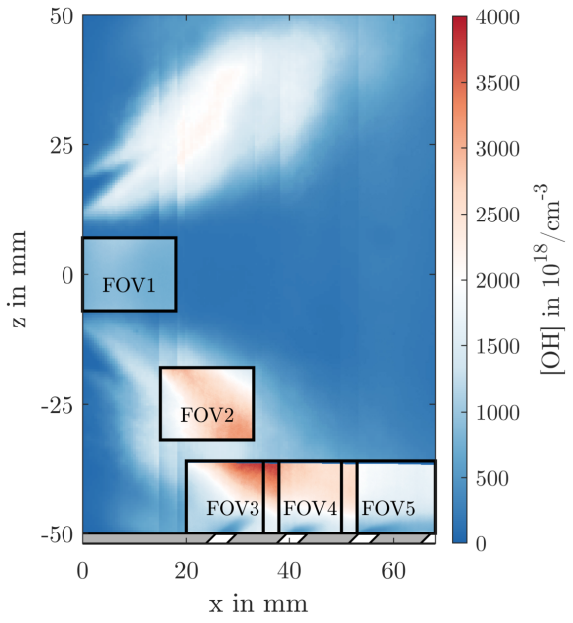

Figure 4.22: Overview of the high-resolution FOVs investigated in this chapter marked by inset rectangles showing mean OH number density. Background image represents standard deviation of the underlying low-resolution FOVs. Figure taken from [E5] with permission from Elsevier.

4.3 Results

This section presents the results obtained from combined quantitative OH-PLIF/NO-PLIF measurements to estimate relative occurrence of mixing *before* reaction, mixing *during* reaction and mixing *after* reaction in the primary zone, i.e. close to the inlet nozzle, and in the FCAI region near the effusion cooled liner.

4.3.1 Primary Zone

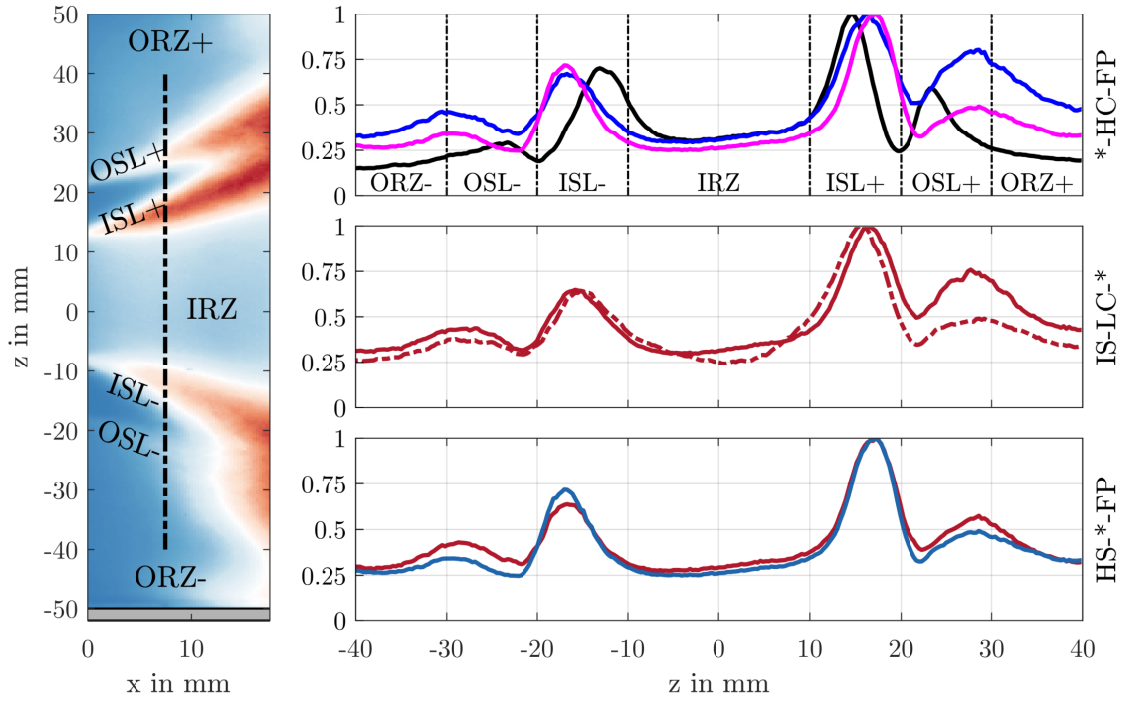

Figure 4.23: Mean [OH] distribution (1000 samples) near the inlet of the combustor. Radial profiles shown in the right half of the figure are extracted at $x = 7.5$mm. All lines have been normalized to the peak in the inner shear layer at positive z coordinates for comparison. Top frame: swirl study. Black: LS-HC-FP, Blue: IS-HC-FP, Magenta: HS-HC-FP. Middle frame: Staging study. Dashed lines represent partially premixed operation (PP), solid lines correspond to fully premixed operation (FP). Bottom row: Effusion cooling study: Red coloring indicates LC, blue coloring indicates HC effusion air set point. Figure adapted from [E5] with permission from Elsevier.

In this section, the influence of effusion cooling air within the primary zone is investigated. Figure 4.23 shows extracted radial profiles at $x = 7.5$mm for all operating conditions, normalized to their respective peak OH number density in the upper inner shear layer for comparison. The profiles resemble typical swirl-stabilized flame features, such as the presence of an inner and outer recirculation zones (IRZ, ORZ) and an inner and outer shear layer (ISL, OSL), where the flame stabilizes. Postscript minus and plus signs indicate the respective region in the lower or upper half of the combustor. It is evident, that the local OH number density is strongly asymmetrical with respect to the central

axis. Local OH number density in the lower (-) half of the combustor are systematically lower than in the upper half (+). Region ISL- shows a $\approx 25\%$ reduction in OH number density compared to the upper ISL+. This trend is even stronger for the OSL, where OSL- assumes a reduction of $\approx 50\%$ compared to OSL+. Increasing swirl increases the radial extension of the IRZ, pushing the shear layers more outwards in the direction of the combustor liner. The asymmetry of the shear layers is mostly independent from swirl for this axial location. It has to be noted that due to comparably strong change in flow field, the swirl dependency cannot be clearly identified with radial profiles, as the general behavior is similar albeit at different axial locations.

Staging influence is observed in the central region and the outer shear layers, where locally reduced OH number densities compared to the ISL+ peak are observed. It has to be noted that the penetration depth of the pilot strongly depends on the swirl, where higher swirl numbers lead to a more rapid mixing for lower axial distances and thus to lower penetration depths of unburned fuel. Regardless of the penetration depth, partially premixed operation increases [OH] in the ISL and reduces it in the OSL. Effectively, the main stage operates leaner for partially premixed combustion, reducing the equilibrium OH number density in areas with less pilot, i.e. the OSL. On the other hand, increased equivalence ratios within the ISL due to mixing with the pilot leads to increased number densities.

For constant swirl and staging, influence of the effusion cooling air is mostly confined to the ORZ and OSL with still some measurable impact on ISL-. Quite interestingly, a reduction in OH number density for case HC is observed within OSL+, indicating that effusion air actually impacts the primary zone *above the center line*. Reduced OH number densities in the OSL- and ISL- but constant number density within the ORZ- indicate possible dilution of fresh gas with effusion cooling air.

To further investigate this effect, an analysis was carried out to identify mixing *prior to combustion* in the flame brush. Fig. 4.24 shows two representative samples from measurements in FOV2. In a first step, quantitative [OH] data was binarized using a threshold value of 65% of the equilibrium number density of a freely propagating flame at $\Phi = 0.75$ and an unburnt gas temperature of $T_u = 623\,K$ at 2.5bar. This effectively separates *hot* from *cold* regions. In a subsequent step, based on the mean of the NO-PLIF signal *within the identified cold regions*, a threshold for the binarization of NO-PLIF images is derived to extract areas with significant signal arising from effusion cooling air within the FOV. This allows to approximately identify parts of the *cold* region without significant effusion cooling air content as *unburnt fresh gas*. The binarized NO-PLIF images are then expanded by 1 pixel towards the *hot* region. This allows to identify samples,where cooling air and fresh gas overlap and *are not separated by a reaction zone* by simply intersecting the identified binarized fresh gas region and expanded binarized NO-PLIF images, which represent areas containing effusion air. For cases where identified fresh gas areas are separated from areas with significant amounts of effusion air by zones of high OH number density, i.e. *no mixing before reaction is observed*, the intersection returns an empty set. For cases, where no separation is present, i.e. *mixing before reaction*, the intersection yields a line with a width of 1 pixel. Effectively, the length Λ of this boundary line is a measure of the intensity for fresh gas mixing with effusion air within the FOV.

The given examples in Fig. 4.24 are chosen to demonstrate the applied algorithm for a case, where (a) no significant dilution was found and (b) significant influence of cooling air is indicated.

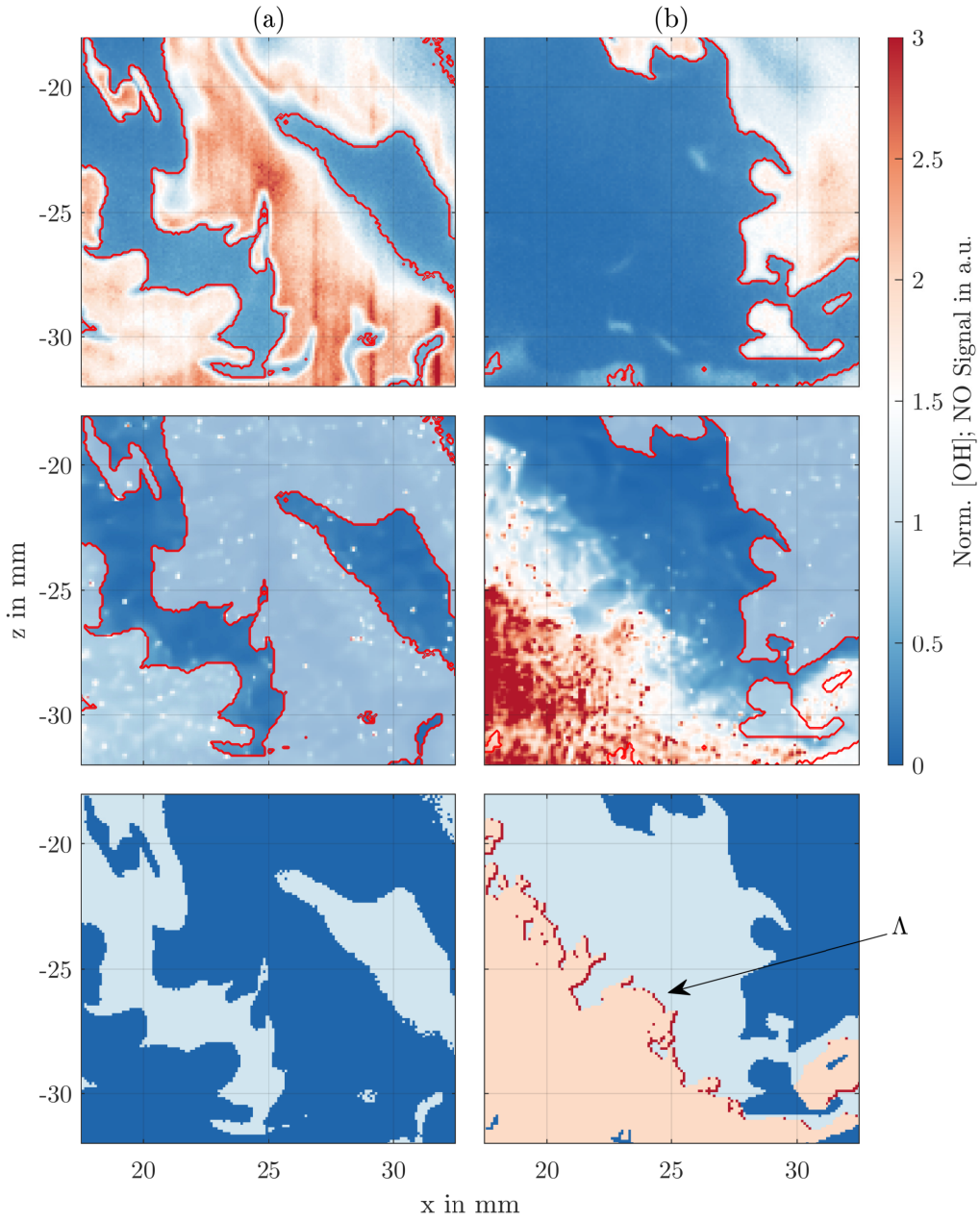

Figure 4.24: Two representative samples within the flamebrush in FOV2 (a) with no effusion air within unburnt gas and (b) with significant effusion air dilution before combustion. Top row shows OH images with extracted boundary between cold and hot gases. Middle row shows qualitative NO-PLIF images with extracted boundary from top row. Bottom row: Identified fresh gas region (light blue) and cold gas containing effusion air (orange). Connected boundary with length Λ shown in red. OH number density normalized to theoretical equilibrium value at combustor conditions. Shown case: LS-LC-FP. Figure adapted from [E5] with permission from Elsevier.

Fig. 4.25 shows a scatter plot of the spatial mean of [OH] in the extracted hot region, i.e. the reaction zone and post-flame OH number density for a given sample, over the extracted length of the boundary Λ. Although there is a strong scatter of OH number densities, it is evident, that a higher boundary length correlates with decreased post-flame and reaction zone OH number densities, indicating a strong local disturbance by dilution and partly explaining the observed asymmetry shown in Fig. 4.23. The scatter of [OH] number densities with respect to boundary length is - in part - a result of the limited size of the FOV. If large parts of the FOV are covered by hot gases, the spatial mean of [OH] is likely to exhibit smaller values because it is more likely to measure equilibrium OH as opposed to super-equilibrium, which is more likely to occur if large parts of the image are *cold* and a reaction zone is at the edge of an image. There, the spatial mean of [OH] is most likely to be near super-equilibrium. On the other hand, the boundary can only be *long* if most of the OH image is *cold*. This influence arising from spatial intermittency is not straight-forward to quantify. Additionally, as there is no calibration point with $X_e = 1$ within FOV2, the boundary length strongly depends on the chosen threshold for NO-PLIF images for every operating condition. As a consequence, only trends may be described. In temporal average, the extracted boundary is most likely localized at z coordinates below the peak standard deviation of [OH], see right frame in Fig. 4.25. This indicates that the influence of effusion cooling air is more prominent in the OSL-.

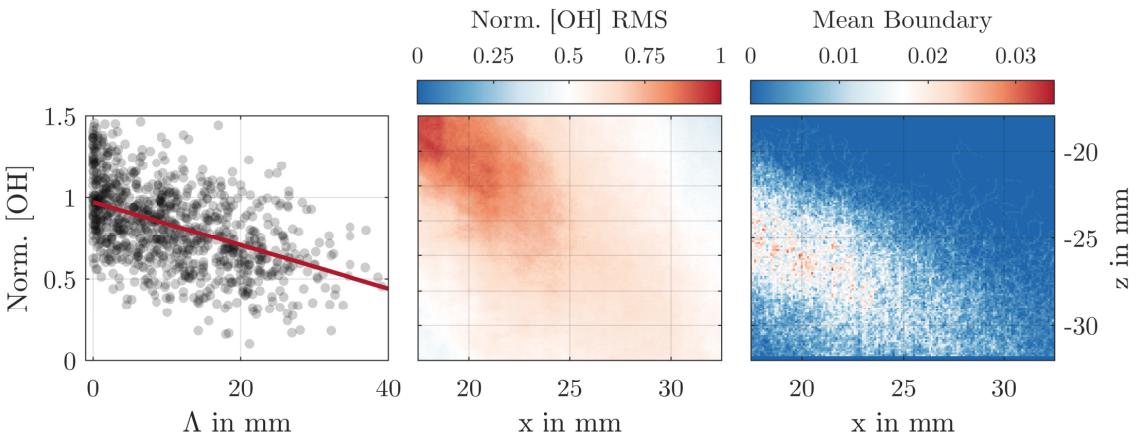

Figure 4.25: Left: Correlation between boundary length and mean post-flame OH number density. Red solid line shows linear fit. Middle: Local standard deviation of normalized [OH]. Right: Local average of extracted boundary. 1000 samples were included in the calculation of mean and standard deviation. Shown case: LS-LC-FP. Figure adapted from [E5] with permission from Elsevier.

Fig. 4.26 shows the results of the parametric study within FOV2. Here, $|\nabla[\mathrm{OH}]|$ describes the magnitude of the gradient of the linear fit seen in Fig. 4.25. It describes the amount of reduction of spatially averaged post-flame and reaction zone OH number density per mm boundary length. From the parametric studies, the following conclusions can be drawn: (a) Increasing swirl increases both the mean boundary length $\overline{\Lambda}$ and its fluctuation Λ'. However, the effect on the gradient of post-flame OH with respect to boundary length is reduced. This is most likely a result of parts of the IRZ entering the FOV from the upper

right corner at higher swirl numbers, reducing the derived post-flame OH number density. This effect is hard to separate as the location of the IRZ cannot be inferred on a single-shot basis with enough confidence due to the high turbulence intensities and associated spatial fluctuations. (b) Increasing cooling air has no significant impact on boundary length and intermittency. This is expected, as the derived boundary length does not reflect the higher effusion air concentration due to case dependent thresholding. The increased gradient of post flame and reaction zone OH number density with respect to boundary length for the higher cooling air mass flow indicates higher local concentrations of effusion air for case HC. In other words: mixing events are observed with a similar frequency for case LC and HC, albeit with a stronger effect for HC due to increased local X_e. (c) Mean and standard deviation of boundary length are increased for partially premixed combustion. The reduction in post flame OH number density is stronger for case FP. Most likely, this is due to the fact that the main stage operates at a lower equivalence ratio for case PP, reducing the expected post flame [OH] levels to begin with such that dilution effects are less prominent.

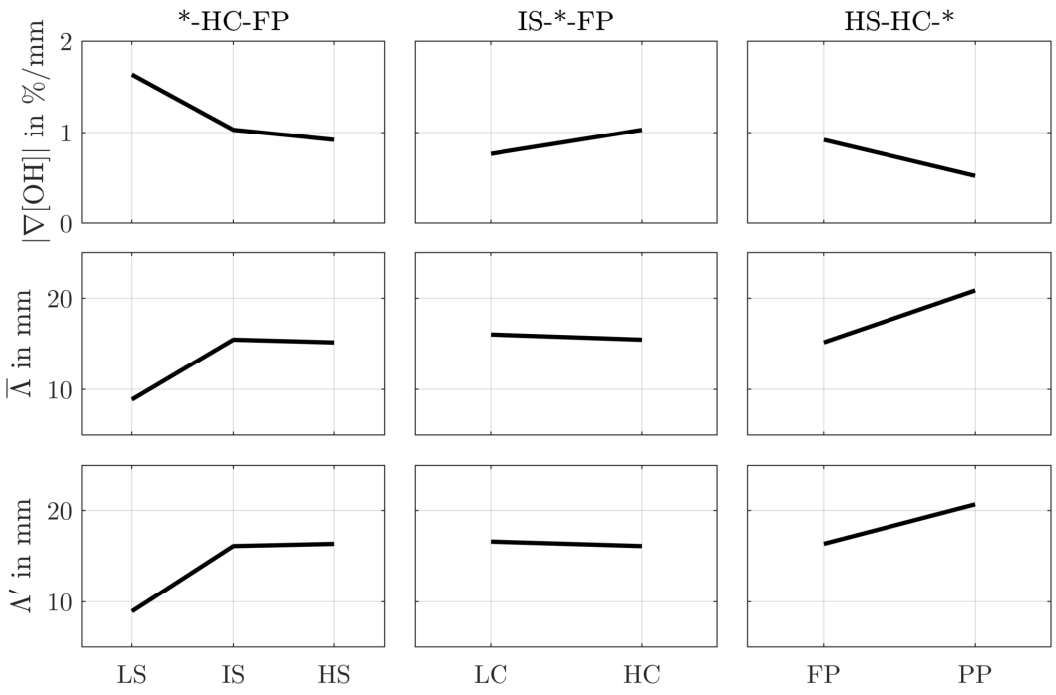

Figure 4.26: Top row: dependence of the magnitude of the OH gradient with respect to boundary length. Middle row: Mean boundary length. Bottom row: Standard deviation of boundary length. Left column: Swirl study. Central column: Cooling air mass flow study. Right column: Staging study. Figure adapted from [E5] with permission from Elsevier.

4.3.2 Near-wall Zone

Fig. 4.27 shows the dependency of the cooling air jet penetration depth of the first three holes on the center line (FOV3-5) together with an overview of the local standard

deviation of [OH]. The penetration depth is defined by the radial distance from the effusion cooled liner, where the effusion air mole fraction X_e is reduced to a value of 0.5. As expected, the mean penetration depth z_p is significantly reduced for case LC compared to case HC. Staging has no significant influence on penetration depth. Increasing swirl systematically reduces z_p due to the previously described expansion of the IRZ, resulting in a steeper angle at which the main stage approaches the wall. Influence of swirl is reduced

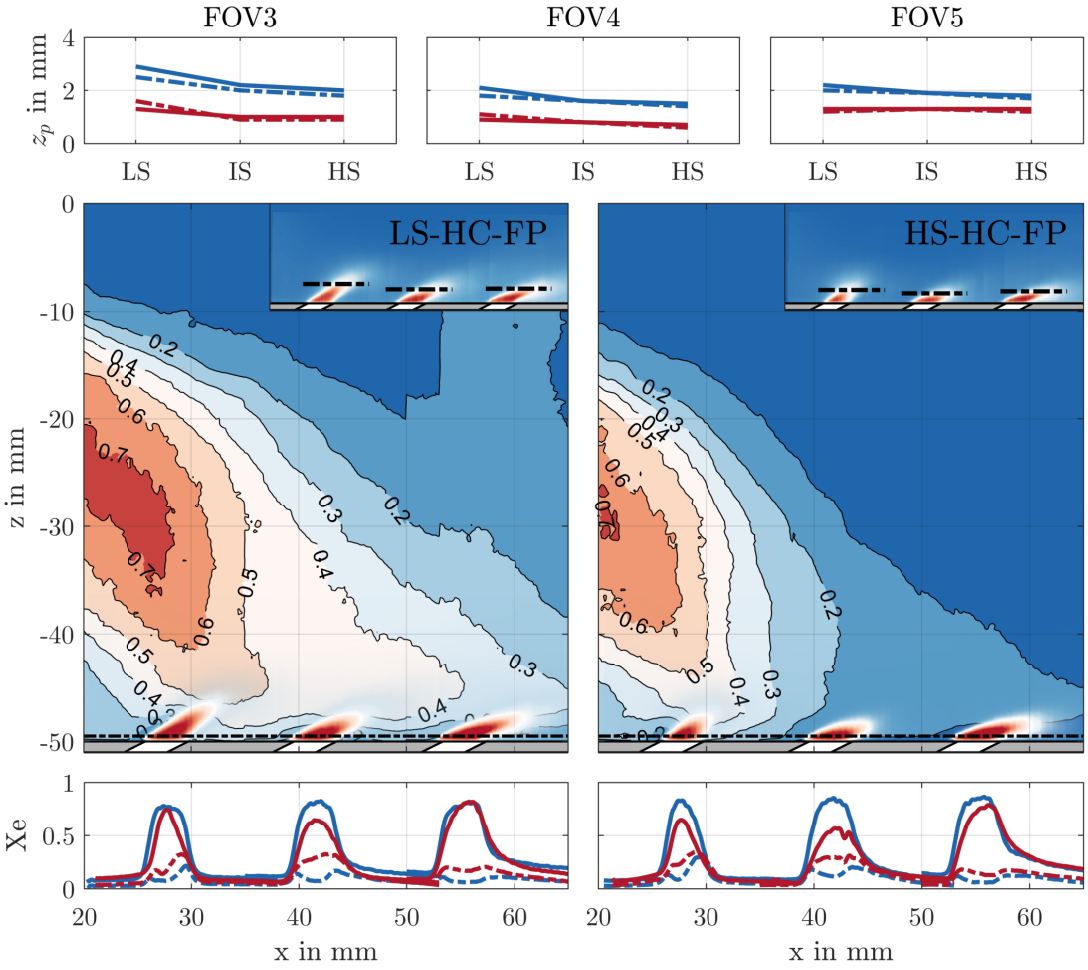

Figure 4.27: Line plots on top: Mean penetration depth of effusion air jets depending on operating condition (Red: LC; Blue: HC; Solid: FP; Dashed: PP). Images (middle) show local standard deviation of OH number density normalized to theoretical equilibrium overlayed with mean X_e images from FOV3-5. Insets show mean X_e and the derived penetration depth at $X_e = 0.5$. Bottom line plots show mean (solid line) and RMS (dashed line) X_e profiles extracted at the black dashed line 0.5 mm above the effusion cooled liner (Red: LC; Blue: HC). 1000 samples used for calculation of average and standard deviation. Figure adapted from [E5] with permission from Elsevier.

with increasing axial location. Increased local standard deviation of [OH] for lower axial coordinates suggest that this is caused by the location of the flame brush. Previous flow field measurements at similar conditions indicate that stream-lines originating from the primary zone approach the wall in a region between the first and second effusion hole and

are mostly parallel close to the wall for locations further downstream [E8]. Mean and RMS profiles of X_e extracted 0.5 mm above the effusion cooled liner in Fig. 4.27 show increased intermittency for all three holes and reduced mean values at the second hole for case LC. This is consistend with previous investigations, were a local rupture of cooling film and partially impaired outflow above the second hole on the centerline for similar operating conditions using OH-PLIF data was derived [E8]. Mean and RMS profiles are not significantly affected by staging. Another observation that can be drawn from Fig. 4.27 is that the investigated effusion cooling holes interact with different areas of the main stage. The first center line effusion hole interacts with the edge of ORZ- and the OSL-, while the second and third hole interact with hot products from the ISL- and upstream effusion air. Due to the proximity to the highest fluctuations in [OH], the first effusion hole is expected to disturb local reaction in the near wall region of OSL-.

To gain first insights on the interaction mechanisms close to the effusion cooled liner, Fig. 4.28 shows two exemplary samples of X_e overlayed with [OH] and the averaged overlay for all near-wall FOVs at LS-HC-FP condition. Additionally, the spatially resolved product of X_e and [OH] is shown. The product $[\mathrm{OH}]\cdot X_e$ features large values in areas with substantial amounts of cooling air in direct contact with regions of high OH number densities. Thus, it indicates where the probability of interaction between super-equilibrium and post-flame [OH] from the flame and cooling air is increased. Within FOV3, the OSL- from the main stage approaches the wall. When comparing realizations (a) and (b) from FOV3, a strong spatial intermittency in [OH] is observed. Sample (a) shows cold areas, i.e. with low [OH], that are not explained by present cooling air, i.e. low X_e values. Thus, this area is assumed to be fresh gas.

The fresh gas area and the cooling air jet are not separated by a zone of increased [OH], indicating that effusion air mixes prior to combustion. Sample (b) shows normalized [OH] number densities ≥ 1, i.e. super-equilibrium [OH] in the direct vicinity of significant amounts of cooling air. This causes the product $[\mathrm{OH}]\cdot X_e$ to increase. In temporal average, the location of highest $[\mathrm{OH}]\cdot X_e$ values is downstream at the tip of the effusion jet. In FOV4, mixing with fresh gas is less likely. Instead, (super-)equilibrium [OH] from the ISL- and OSL- reaches the effusion cooled liner and is mixed with effusion air. Consequently, compared to FOV3, $[\mathrm{OH}]\cdot X_e$ is increased at the left side of the effusion air jet, where [OH] is more likely to be high. In FOV5, relaxation to chemical equilibrium, mixing with upstream effusion air and heat-losses cause a reduction in [OH] number density. Thus, in average, $[\mathrm{OH}]\cdot X_e$ is reduced compared to FOV3 and FOV4. In this area, the flow field shows stream lines which are nearly parallel to the wall [E8], leading to a lower penetration angle of the effusion air jet. Unlike in FOV3, cold areas as indicated by low [OH], are explained by the presence of significant amounts of cooling air.

As the spatial location of mixing phenomena is intermittent, further analysis is conducted in state space. Presence of super-equilibrium [OH] in the near-wall region and limited optical resolution of the intensifier cause a detection limit in this area of $\approx 0.2 \cdot [\mathrm{OH}]_{\mathrm{eq}}$. This is estimated from the measured mean OH number density at locations where X_e approaches 1. For the following analysis, this detection limit is subtracted from the data, such that the conditional mean of [OH] with respect to X_e approaches zero at $X_e = 1$. To avoid confusion, the OH number density after subtraction is denoted as $\{\mathrm{OH}\}$. This

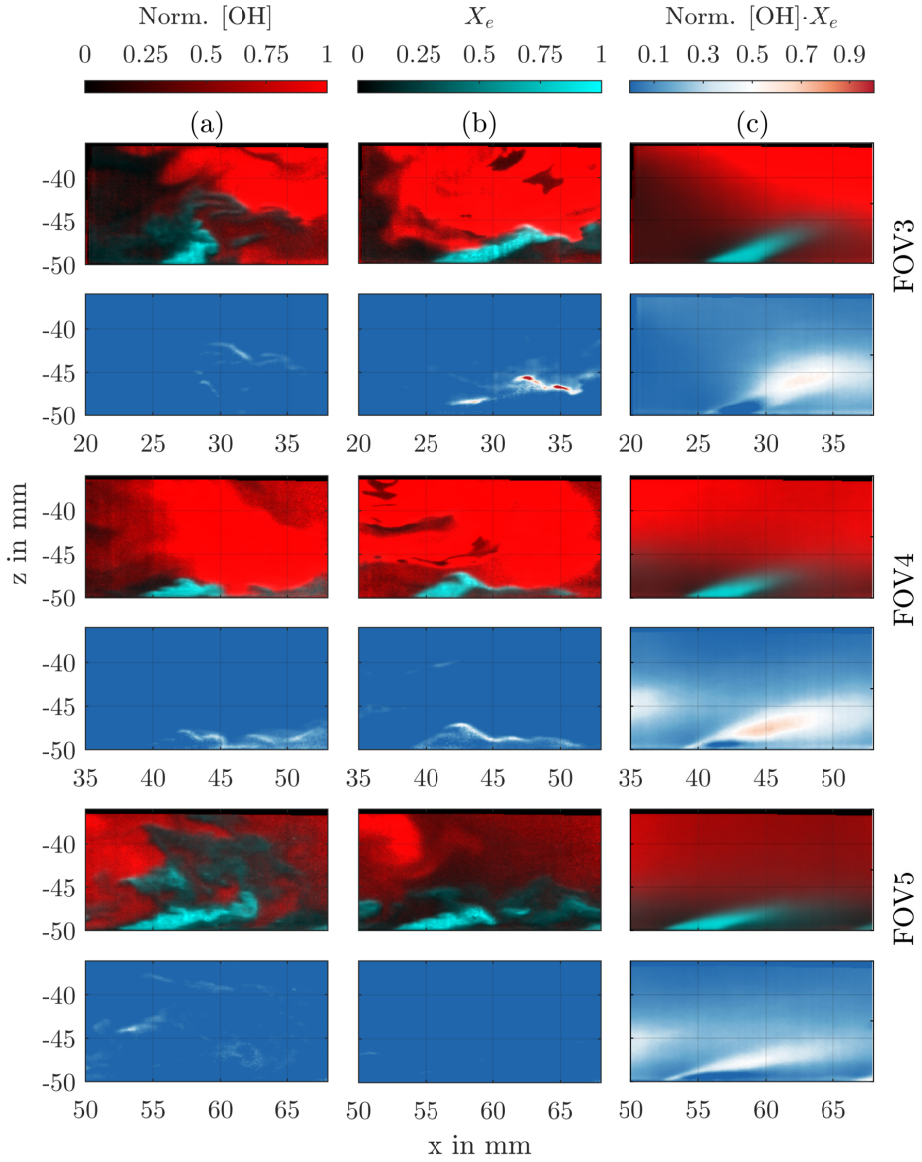

Figure 4.28: Rows 1,3,5: Qualitative overlay of X_e (cyan) and [OH] (red); Rows 2,4,6: product of [OH] and X_e. Column (a) and (b) show two example single realizations, column (c) shows the average of 1000 samples. Condition: LS-HC-FP. Colorbar for [OH]·X_e ranges from 0.05 to 0.7. Ensemble average (1000 samples) multiplied by a factor of 4 to fit on the same colorscale. Figure adapted from [E5] with permission from Elsevier.

correction causes {OH} to possibly exhibit negative values at low number densities due to noise. As the subtracted detection limit is estimated in an area with nearby spatial gradients due to the cold effusion air jet, i.e. is affected by the optical resolution of the intensifier more intensely, larger cold areas such as fresh gas are overcompensated, driving {OH} further towards negative values.

Fig. 4.29 shows the results of the conducted analysis in state-space based on bivariate PDFs of X_e and {OH}. As staging shows no measurable influence within the near-wall studies, this analysis is limited to fully-premixed combustion (FP). The extraction of events that represent mixing *prior to*, mixing *during* and mixing *after* reaction is challenging, as the processes are not strictly separated from one another and multiple processes may happen within the same single-shot. To deduce tendencies, the following assumptions are made:

(I) OH number density instantly follows temperature. As the temperature is nearly linearly dependent on X_e, OH has a nearly exponential dependency, see Fig. 4.2. As a consequence, interaction between [OH] and X_e can only be observed where there is enough [OH] to detect. Due to the strong sensitivity, this is limited to approximately $X_e \leq 0.4$.

(II) Even with strong dilution prior to combustion, local super-equilibrium of the diluted reaction zone is $\geq [OH]_{eq}$ at combustor conditions ($\Phi = 0.75$, $T_u = 623\,K$, $p = 2.5\,bar$). This is verfied by laminar flame simulations. Even a flamelet with a complete mixture of fresh-gas from the main stage and effusion cooling at HC condition, the peak OH number density is $\approx 5\%$ larger than the equilibrium value at nominal combustor conditions.

(III) Areas with X_e below the lower detection limit represent undisturbed reaction zones.

(IV) Areas with low [OH] and low X_e above the lower detection limit represent areas, where fresh-gas is diluted by effusion cooling air.

(V) As a consequence of (I), local OH number density is reduced by any heat-loss mechanism, i.e. *not exclusively* by mixing.

With these assumptions, the bivariate PDFs can be separated in four regions, see upper left plot in Fig. 4.29:

(a) Undisturbed reaction zones. In this region, no significant amount of cooling air is present. The measured OH number densities reach from 0 to values slightly above the expected peak super-equilibrium value of $\approx 2.7 \cdot [OH]_{eq}$ due to noise.

(b) Mixing of super-equilibrium [OH] of local, i.e. possibly diluted, reaction zones with effusion cooling air.

(c) Mixing of post-flame [OH], i.e. sub-equilibrium, with effusion cooling air.

(d) Fresh gas with measurable amounts of effusion cooling air mixed prior to combustion.

The bottom three rows in Fig. 4.29 summarize the results for all relevant operating conditions and FOVs. Probabilities to measure a sample within a certain region are extracted by integrating the PDF within the boundaries of the entire region. Note that the sum of probabilities across all regions is not equal to 1, as this analysis is limited to regions with measurable [OH]. Aside some samples that lie above the boundary of region (b) due to noise, the vast majority of remaining samples correspond to $X_e \geq 0.4$.

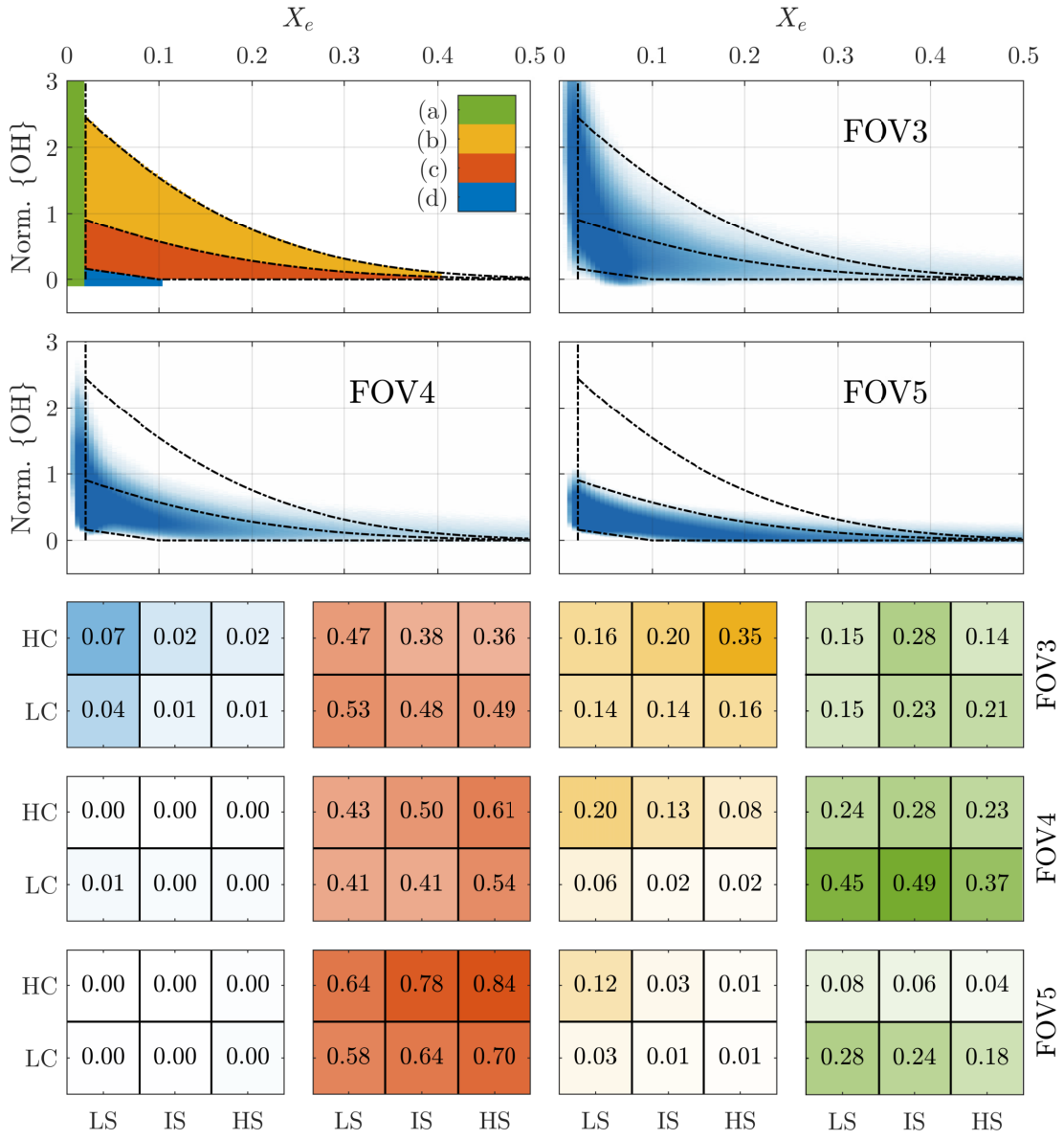

Figure 4.29: Top two rows: Scatter plots of {OH} over X_e within FOV3-5 for HS-HC-FP condition and segmentation in zones: (a) Undisturbed reaction zones, (b) Super-equilibrium region, (c) Sub-Equilibrium region, (d) Fresh-gas mixed with effusion air. Boxes in the three bottom rows show the probability to measure a sample in region (a)-(d) as value and color coded for every operating condition and FOV. Colors represent regions (a)-(d), saturation of color is scaled according to the probability value to indicate the relative occurrence. Figure taken from [E5] with permission from Elsevier.

Independent from swirl and effusion cooling air mass flow, chances of encountering mixing events with fresh-gas in region (d) are substantially reduced with increasing axial distance, i.e. from FOV3-5. This is expected from the location of the flamebrush, see Fig. 4.27. At the same time, frequency of events in the sub-equilibrium region (c) increases,

accompanied by decrease in super-equilibrium region (b). Additionally, all regions within a given FOV show a dependency on swirl and effusion cooling air mass flow.

Occurrence of mixing events with fresh gas in FOV3 are more likely to be observed for lower swirl and higher effusion cooling mass flow. Additionally, increasing swirl at HC condition reduces sub-equilibrium mixing (c) and increases super-equilibrium mixing (b). This is most likely caused by the increased penetration depth at lower swirl numbers and the higher impulse ratio at HC condition, making it more likely that effusion air either reaches pockets of fresh-gas from the main stage or reaction zones which are located further away from the effusion cooled liner. In comparison to FOV3, region (b) and (c) for FOV4 and FOV5 show a reversed trend for increasing swirl. Most likely, this is a result of the changed flow-pattern. As the radial extension of the IRZ increases, the flame brush approaches the effusion cooled liner at a steeper angle, moving the spatial location of peak [OH] further upstream, thus making mixing with post-flame OH more likely in the downstream FOVs.

Within region (a), represented by the probability to measure a sample with X_e below the detection limit, i.e. undisturbed flow from the main stage, a non-monotonic dependency on swirl is observed. For FOV3 and FOV4, the intermediate swirl causes the highest probability, while for FOV5, cases with low swirl show increased values. Additionally, it is more likely for case HC to measure samples in region (d) within FOV3, while the opposite is true for the downstream FOVs 4 and 5. With the exception of FOV3 at intermediate swirl, increased cooling air mass flow leads to lower probabilities in region (a). This is expected as less area within the FOV contains measurable amounts of X_e for LC cases. Unlike in the other regions, extracted integrated probabilities are very sensitive to the definition of the detection limit of X_e and are thus less reliable.

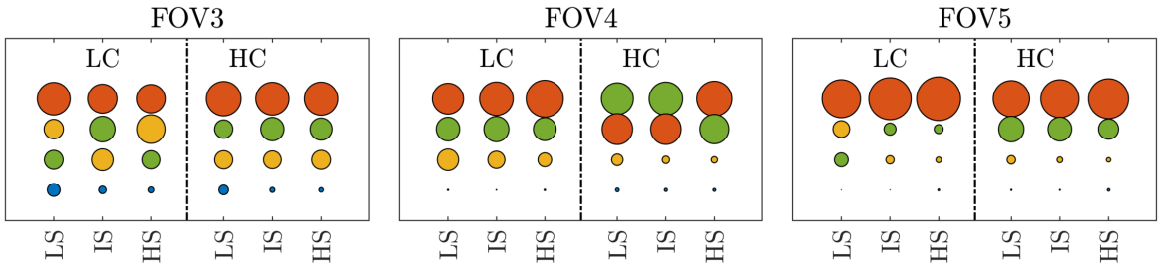

Figure 4.30: Visualization of the dominant mixing processes for all FP operating conditions. Color coding refers to zones, size of circle represents integrated probability within zone. Circles are vertically sorted by their probability value. Vertical dashed lines splits operating conditions within each plot into LC and HC condition. Figure adapted from [E5] with permission from Elsevier.

Fig. 4.30 shows which of the identified mixing processes are dominant in each FOV for all operating conditions. Except within FOV4 for conditions LS-LC-FP and IS-LC-FP, mixing processes of sub-equilibrium [OH] and effusion air is dominant. For these cases, the observation of undisturbed main flow is approximately equally likely. With the exception in FOV3 for lower swirl numbers, mixing with fresh-gas has a negligible occurrence. Within FOV3, interaction between cooling air and super-equilibrium [OH]

is approximately equal in their relative importance. Further downstream, where [OH] is reduced from relaxation to chemical equilibrium and potential heat-loss, mixing with super-equilibrium has a lower significance.

4.4 Summary

In this chapter on mixing phenomena inside an effusion cooled pressurized single sector gas turbine combustor, quantitative OH number density measurements simultaneously with measurements of effusion air mole fraction using NO-PLIF were presented. Within the primary zone close to the nozzle, a significant case dependent asymmetry of OH number density was observed. Reaction zones at the side of the flame brush facing the effusion cooled liner are severly impaired by effusion cooling air. This asymmetry is partly explained by investigations in the lower flame brush, where more intense mixing of effusion cooling air and fresh gas was observed. Post-flame OH number densities are reduced for events with significant dilution.

Mixing events *before*, *during* and *after* reaction were identified in a state-space analysis in the near wall region. Bivariate PDFs of OH number density and effusion air mole fraction were separated in four regions: a) undisturbed reaction zones, b) interaction with reaction zones, c) interaction with post-flame zones, d) interaction with fresh gas. The relative importance of all regions depend on operating condition and axial location. Across all conditions, adiabatic mixing with post-flame OH and undisturbed reaction zones are the dominant processes. A notable influence of fresh gas mixing with effusion air is observed for upstream locations at low swirl numbers only, were a higher effusion cooling air mass flow leads to significant dilution prior to reaction.

Chapter 5

Thermochemical State

5.1 Aim of this Investigation

Within this chapter, quantitative CO mole fraction and gas-phase temperature measurements are conducted to investigate the influence of cooling air on the thermochemical state within the combustor. This is achieved by a combination of point-wise ro-vibrational coherent anti-Stokes Raman Spectroscopy (CARS) with N_2 as a resonant species in combination with CO-LIF.[20]

5.2 Method

5.2.1 Coherent anti-Stokes Raman Spectroscopy

Gas-phase temperatures were measured using nanosecond ro-vibrational N_2 CARS. A frequency-doubled, flashlamp pumped Nd:YAG laser (Spectra Physics, PIV400) operating at 10 Hz was used as a source for the pump and probe beam. Additionally, a portion of the output was used as a pump source for a custom-built modeless dye laser generating radiation with a bandwidth of $\approx 100\,\mathrm{cm}^{-1}$ at around 607 nm for the Stokes beam. The beams were focused through a common achromatic lens (f = 250 mm) in a planar BOX-CARS configuration to form the measurement volume. The pulse energy was adjusted using pairs of half-wave retardation plates and polarizing beam splitter cubes to avoid pump-induced population changes [60]. The generated CARS signal at around 473 nm was collected using a second achromatic lens (f = 250 mm) and focused onto the slit of a Czerny-Turner type spectrometer (McPhearson, Model 209) using a spherical lens (f = 100 mm). A notch-filter in front of the focusing lens eliminated residual radiation at 532 nm. Spectra were recorded using a backlight-illuminated CCD camera (Princeton Instruments, PIXIS 400B) with on-chip binning operating at twice the repetition rate of the lasers to record a background spectrum in between every CARS spectrum. The principal axis of the CARS system was aligned with the y axis of the combustor, i.e. parallel to the head plate and the effusion cooled liner. To enable measurements close to

[20] This chapter is taken in part from the *Combustion and Flame* paper (pre-print, post-review) [E4] with permission from *Elsevier*. A declaration on the author's contribution to the scientific publication may be found in the appendix.

the head plate and close to the effusion cooled liner, the beam arrangement was rotated 90° between measurement days.

5.2.2 CO Two-photon Laser-induced Fluorescence

CO-LIF was excited in the Hopfield-Birge system $B^1\Sigma^+(v' = 0) \leftarrow\leftarrow X^1\Sigma^+(v'' = 0)$ with two photons in the band head at around 230.1 nm. The required UV laser beam was generated by third-harmonic generation of a narrow-band dye laser (Sirah, Precision Scan) using Pyridine I as a dye. The dye laser was pumped using a commercial frequency-doubled pulsed Nd:YAG laser (Spectra Physics, GCR-4). To avoid long-term drift, the fundamental wavelength was measured and controlled using a wave meter (High Finesse, WS6). A spherical lens (f = 300 mm) focused the beam into the measurement volume. The pulse energy within the measurement volume was kept constant at 2 mJ. To align the beam co-axially with the optical axis of the achromatic lenses used for CARS, a 10 mm hole was drilled into these lenses to allow the UV beam to pass. The resulting fluorescence signal was detected using a photomultiplier tube (PMT; Hamamatsu, H11901-01), connected to a high-speed transimpedance amplifier (Femto, DHPCA-100). A narrow bandpass filter around 485 nm (10 nm FWHM) was used to separate the LIF signal of the (0,1) vibrational transitions in the Ångström band from ambient light and scattered laser radiation. The resulting amplified voltage signal was temporally sampled and recorded using a digital phosphor oscilloscope (Tektronix TDS5032B). To increase the dynamic range, three channels with different sensitivities were used simultaneously to record the data.

A common problem when using PMTs as point-wise detectors is the uncertainty of the measurement volume location. For the combined CARS/CO-LIF approach, it is of great importance to only measure the LIF signal in the same volume where the CARS signal is generated, otherwise the information may be uncorrelated in a turbulent environment. In lateral direction, this was achieved by overlapping all lasers through a pinhole with a diameter of 100 µm. To ensure that all lasers passed the pinhole without cropping, this was done at full energy to increase the precision of the overlap. In beam-wise direction (in this case y), the CARS measurement volume was found by creating a non-resonant signal in a thin glass plate (100 µm thickness). Figure 5.1 shows a sketch of the detection system, consisting of an achromatic lens (L_1; f = 360 mm) and a 135 mm camera lens at $f/2$ (Canon, EF 135/2,0 L USM) set to infinity, which were used to generate an intermediate image within the housing of the PMT. This intermediate image was cropped using an adjustable slit (S) oriented orthogonally to the beam-wise direction. This image was again collimated and directed to the PMT to illuminate the entire active area of the photocathode. A rotatable mirror in front of the PMT allowed to extract the collimated beam and redirect it to a CMOS camera with a lens L_2 adjusted to infinity. Effectively, this imaged the intermediate image in the slit plane onto the CMOS camera for adjustment purposes. During measurements, the mirror was rotated out of the signal beam path to allow capturing the LIF signal with the PMT. The entire detection assembly could be translated in all three dimensions until a) the image was in focus, b) the glass plate was centered in the slit with respect to the y-axis and c) the scattered light from all lasers on the glass plate was clearly visible, ensuring that the measurement volume is centered

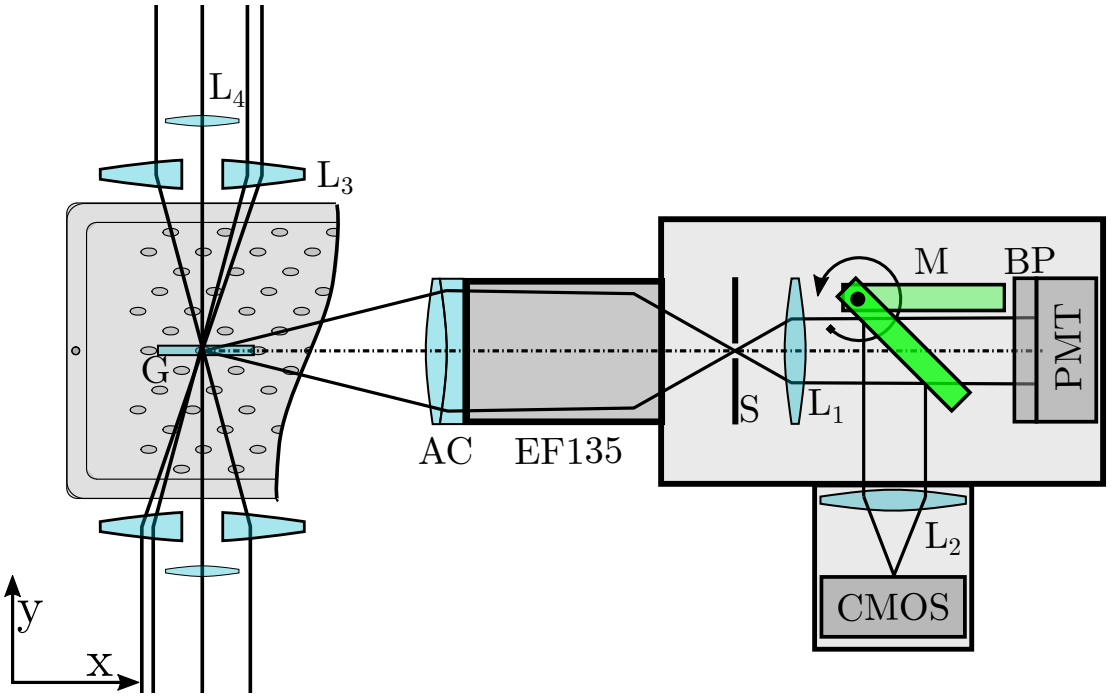

Figure 5.1: Sketch of the PMT based detection system for CO-LIF and beam alignment near measurement volume in horizontal configuration for measurements near effusion cooled liner. AC: Achromatic lens, EF135: camera lens at infinity, S: adjustable slit, L_1: aspheric collimation lens, L_2 spherical focusing lens for CMOS camera, M: rotatable mirror, BP: Bandpass filter, G: Glass plate for non-resonant CARS signal, L_{3-4}: focusing lenses for CO-LIF/CARS. Drawing not to scale. PMT drawn in xy-plane for clarity, actual detection along z-direction from top of combustor. Figure taken from [E4] with permission from Elsevier.

in the slit in x-direction. The width of the slit was adjusted such that $\approx 0.4\,\text{mm}$ were integrated in beam-wise direction to ensure coincident acquisition of temperature and CO information. Two beam monitoring cameras at separate locations for each laser each were used to monitor the stability of the focal position during measurements.

5.2.3 Optical Setup

Fig. 5.2 shows a simplified sketch of the optical setup for the combined CARS/CO-LIF measurements. All laser beam paths feature spherical telescopes with a small magnification ratio of $\approx 1:1.2$ to adjust their respective divergence such that the focal points overlap within the measurement volume. As the test rig and all used lasers were stationary in space, a traversing unit was constructed that allowed to move the entire detection assembly and the measurement volume in all directions. This is achieved by aligning all four lasers beams used for CARS and CO-LIF to be parallel on a stationary optical table. This set of parallel beams is then aligned to the axes of the traversing unit by means of mirrors that are reflective for all involved wavelengths. The PMT detection system and the focusing lenses are mounted on a common structure, ensuring that the relative position of these elements - and consequently the location of the measurement volume

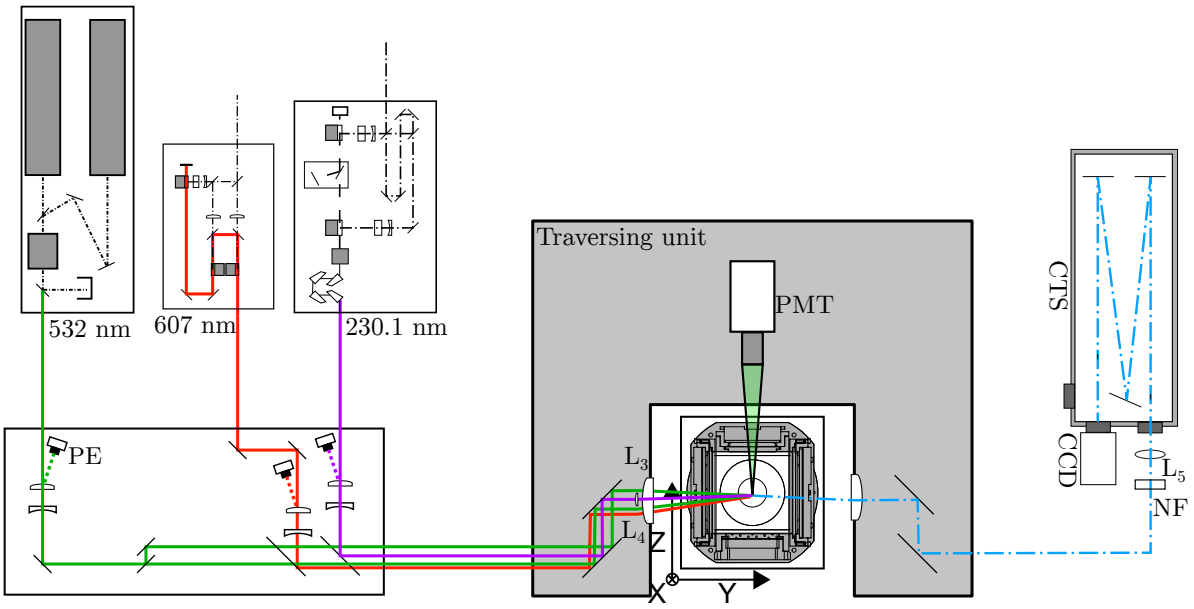

Figure 5.2: Optical setup used for CARS/CO-LIF measurements. Shown is the vertical BOXCARS arrangement to allow measurements close to the head plate. L_{3-4}: focusing lenses for CO-LIF/CARS. L_5: Focusing lens for spectrometer (CTS). NF: Notch filter. PE: Pyroelectric energy meter.

with respect to the detection area of the PMT - is fixed. To test the spatial stability of the overlap, the entire assembly including the glass plate was traversed to all accessible locations within the combustor. Even during travel at $2\,\mathrm{m\,min^{-1}}$, the overlap was ensured, mainly verifying that all beams were indeed aligned to the axis of the traversing unit with sufficient accuracy and vibrations from the system were not affecting the overlap. Additionally, the overlap was verified at the end of each measurement day.

5.2.4 Processing

Processing of CARS spectra In a preprocessing step, acquired CARS signals are corrected using background-subtraction and normalization to a non-resonant signal acquired in pure methane to compensate the uneven spectral profile of the Stokes laser. Fig. 5.3 shows an example set of acquired CARS spectra, background and non-resonant signals.

These preprocessed spectra were subsequently fitted using MARSFT as described in Sect. 2.2.2 to derive the temperature from a single-shot spectrum. The required library used a Gaussian preconvolution kernel with $0.8\,\mathrm{cm^{-1}}$ FWHM. Temperature is discretized in $\Delta T = 1\,\mathrm{K}$ increments in the range $250 - 2500\,\mathrm{K}$. The included range of line width multiplier is $1 - 3$ in $\Delta n = 0.08$ steps. Single shot CARS spectra are fitted in the Raman shift range $2270 - 2340\,\mathrm{cm^{-1}}$ with the parameters summarized in Tab. 5.1. As the experimental degrees of freedom *wavenumber expansion* and *wavenumber shift* pose challenges to the fitting routine due to their non-orthogonality, the wavenumber shift was fitted on a mean high temperature CARS spectrum directly after calibrating the spectrometer using a Xenon lamp (LOT Oriel, LSP033) and set as constant throughout

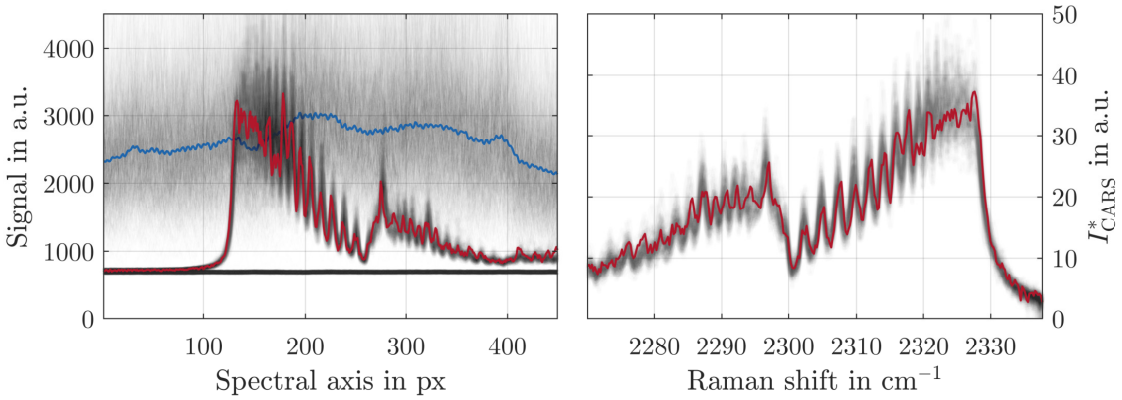

Figure 5.3: Preprocessing of CARS spectra. Example shows measurements in exhaust of adiabatic laminar flame at $\Phi = 1$ and 2.5 bar. Left: Raw single-shot CARS spectrum (red), mean background (black straight line) and non-resonant signal acquired in CH_4 (blue). 1000 single shots for CARS spectra and NR signals as black semi-transparent lines in the background to indicate variance. Right: preprocessed CARS spectrum after subtraction of mean background, normalization to non-resonant signal and taking the square root.

the entire investigation. This is justified as the wavenumber expansion parameter adjusts the linear mapping of Raman shift to the pixel grid which is only affected when rotating the grating of the spectrometer. The wavenumber shift on the other hand depends on the alignment and potential beam-steering effects that cause spatial fluctuations within the entrance slit of the spectrometer and is thus fitted for every single shot spectrum. To reduce computational cost of the fit, the intensity expansion was fixed to unity as no influence on the extracted mean and standard deviation of temperatures was encountered.

Table 5.1: Fit parameter range for evaluation of CARS spectra.

Parameter	Initial solution	Lower bound	Upper bound	Unit
Wavenumber shift	0	-5	5	cm^{-1}
Wavenumber expansion	-0.6868	–	–	cm^{-1}
Instrumental linewidth	1	0.9	1.5	cm^{-1}
Intensity expansion	1	–	–	–
N_2 mole fraction	0.7	0.5	0.8	–
Temperature	1200	280	2500	K
Line width multiplier	1	1	3	–

For the spectral fit, a noise model with contributions from dark noise, shot noise and dye laser noise was used to improve precision and accuracy. Contributions from dark noise were estimated using the standard deviation from the background signal. Shot noise is assumed to be Poisson-distributed, i.e. it is proportional to the square root of the signal itself. Dye laser noise was extracted from the relative standard deviation of the non-resonant signal and is linearly dependent on the signal. The noise model along with an example fit result is presented in Fig. 5.4. As evident from the noise model, spectral noise

of the dye laser and shot-noise have an equal contribution to total noise at ≈ 200 counts and dye laser noise becomes dominant for signals with ≥ 1000 counts.

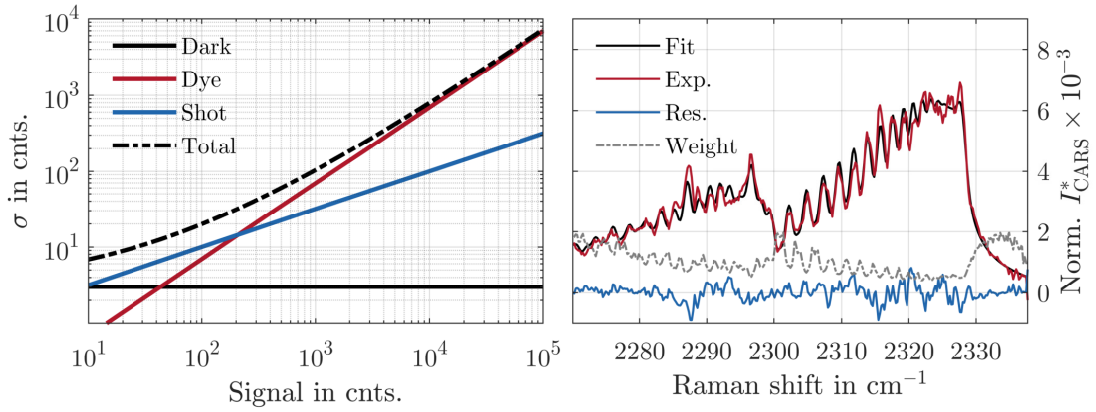

Figure 5.4: Noise-model with individual contributions from dark, shot and dye laser noise used for fitting of CARS spectra (left) and example fit of a spectrum acquired in the exhaust of the laminar flame (right). In addition to the best fit, data and residual, the right plot shows the weight used for fitting based on the noise-model (gray dashed line) scaled to fit the same y-axis.

Processing of CO-LIF signals Fig. 5.5 shows the processing of CO-LIF signals as acquired with the oscilloscope from raw time traces to preprocessed results. As a first step of the evaluation, the oscilloscope channel was selected dynamically depending on the signal strength, i.e. the channel with the highest signal amplitude without saturation was selected. The resulting signal was background-corrected by fitting a baseline to the temporally resolved signal before integration in a 100 ns window around the LIF signal. From a meta analysis, where all signals that have been acquired during the entire investigation have been compared, it is ensured that the channels have an equal sensitivity. In this meta analysis, all samples have been extracted where the signal is within the dynamic range of two respective channels and the area integrated signal is compared. Equivalence between Ch. 1 and Ch. 2 as well as between Ch.2 and Ch.3 is within 99.5%.

Due to the nature of a two-photon process, the LIF signal has a non-linear dependence on the incident intensity. While absorption from the electronic ground state to the B state has a quadratic dependence, photoionization reduces the exponent depending on the local intensity. This effectively reduces the intensity exponent. The power law fitted to the experimentally obtained energy scan shown in Fig. 5.5 in the exhaust of the calibration flame yields a net exponent of 1.3.

The final step of preprocessing is the density correction, where the CO-LIF signal after energy correction is multiplied by the ratio T/T_{ref}, where T refers to the corresponding gas-phase temperature as measured with CARS and $T_{ref} = 300\,\mathrm{K}$ is an arbitrary constant reference temperature. These preprocessed CO-LIF samples are then calibrated using the procedure described in the following paragraph.

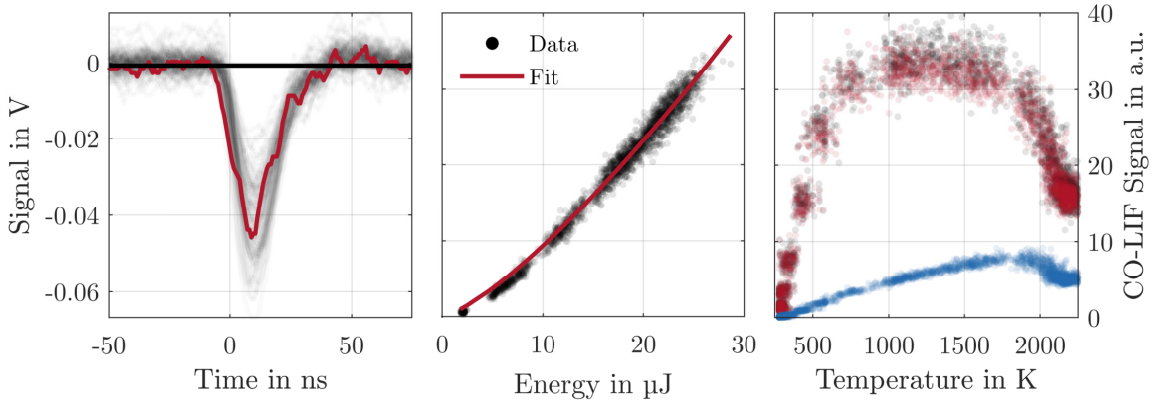

Figure 5.5: Preprocessing of CO-LIF signals. Left: Example raw signal as acquired with the scope (red) of a measurement near the reaction zone of the laminar flame. Black solid line represents fitted baseline, grey shaded lines indicate variance of signal induced by noise as well as minor fluctuations of the spatial position of the reaction zone. Middle: Non-linear energy dependence of the LIF signal used for correction. Right: CO signal as obtained from integration of signal shown in the left plot. Dots represent raw CO signal (black), after energy correction (red) and subsequent density correction (blue).

When measuring close to the head-plate of the burner, parts of the signal were subject to vignetting from the combustor walls. This was accounted for by geometrically modeling the effective collection cone depending on the measurement location within the combustor based on a CAD model of the test rig and the detection system. Measurements with axial locations $x \geq 5\,\mathrm{mm}$ were not affected by vignetting.

Calibration In previous publications, a heated jet with a calibration gas with known CO concentration was used to calibrate the LIF signal in a temperature range up to 1000 K. The temperature range for calibration was expanded by measuring in the exhaust of an adiabatic laminar flame operating at the same equivalence ratio as the burner of interest. From these measurements and a comparison to a laminar adiabatic flame simulation, a temperature dependent calibration polynomial was derived [90, 97].

For the given circumstances, this was impractical due to the preheating temperature of the combustor to $T_\mathrm{u} = 623\,\mathrm{K}$. The temperature range accessible with electrical inline heating is only approximately 350 K above the inlet temperature. In practice, this was even lower due to heat losses in the inlet duct for the calibration gas that was necessary to deliver the heated mixture into the combustor. Instead, the laminar calibration burner was used as a source for calibration data, see Sect. 3.2. Calibration measurements were taken in the longer branch, approximately 4 mm downstream of the flame holder. To extend the calibration to the high temperature range of the preheated flame in the combustor, the equivalence ratio was increased to $\Phi = 1$. The operating pressure of the laminar flame corresponds to the operating pressure at investigated combustor conditions, i.e. $p = 2.5\,\mathrm{bar}$. The influence arising from the different chemical compositions was estimated using the CO-LIF signal simulation as described in Sect. 2.2.1.2. As shown in Fig. 5.6, the influence of the different chemical composition on the fluorescence quantum

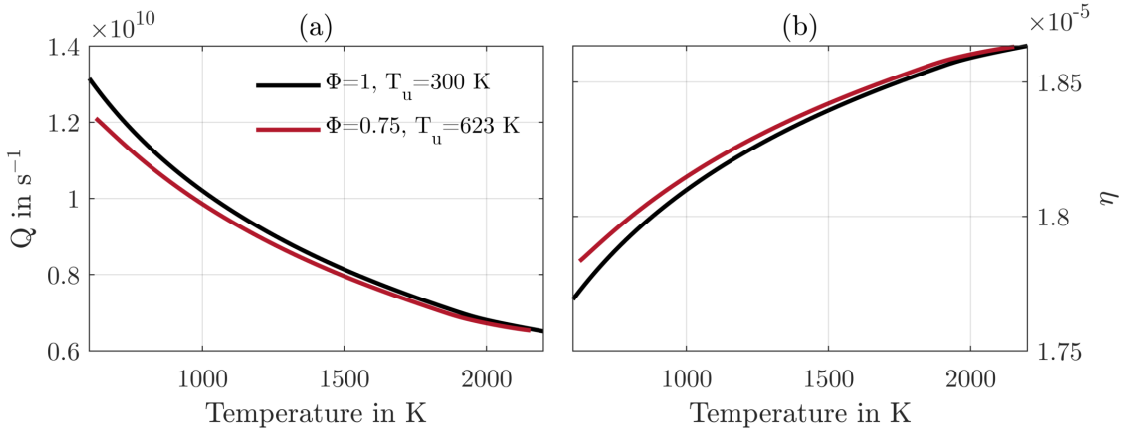

Figure 5.6: Influence of difference in chemical composition between calibration flame at $\Phi = 1$ and $T_\mathrm{u} = 300\,\mathrm{K}$ inlet temperature and operating conditions of combustor at $\Phi = 0.75$ and inlet temperature of $T_\mathrm{u} = 623\,\mathrm{K}$. $p = 2.5\,\mathrm{bar}$ for both cases. (a) simulated quenching rate Q. (b) Fluorescence quantum yield η. Figure adapted from [E4] with permission from Elsevier.

yield η is well below 1% and is thus neglected. This is a result of the high ionization rate R_i compared to quenching rate Q and Einstein-A coefficient. Under the given circumstances, the ionization rate amounts to $\approx 1.2 \times 10^{11}\,\mathrm{s}^{-1}$ (with an ionization cross-section of $1 \times 10^{17}\,\mathrm{cm}^{-2}$ which is approximately one order of magnitude larger than Q and about 4 orders of magnitude larger than the combined Einstein-A coefficients for all vibrational bands for $B - A$ fluorescence which amounts to $A = 3.35 \times 10^7\,\mathrm{s}^{-1}$.

The calibration curve was extracted by fitting a temperature dependent piece-wise cubic spline to the measured LIF signal after preprocessing and subsequent division of this spline by the simulated $X_{CO}(T)$ curve. Figure 5.7 shows an examplary calibration.

One additional influence that has to be addressed is the difference in photolytic production of CO by CO_2 photodissociation [118] between the calibration flame at $\Phi = 1$ and $T_\mathrm{u} = 300\,\mathrm{K}$ and the combustor conditions at $\Phi = 0.75$ and $T_\mathrm{u} = 623\,\mathrm{K}$. To estimate this effect, the measured CO-LIF data from the calibration measurement is compared to a simulated LIF signal under the same conditions, see Fig. 5.8. In the temperature range $1200\,\mathrm{K} \leq T \leq 1800\,\mathrm{K}$, the deviation ε, i.e. the ratio between the *simulated* and *measured* LIF signal, is $< 2\%$, indicating that the simulation of the LIF signal and the spatial overlap of the CO and temperature measurement is sufficiently accurate. For temperatures $\leq 1200\,\mathrm{K}$, the experimentally obtained profile exhibits larger values than the simulation with increased differences up to 10%. Most likely, this deviation is a result of inaccuracies in the LIF simulation at lower temperatures. However, it cannot be completely excluded that beam-steering effects cause the overlap between the measurement volumes to diverge slightly as the four laser beams enter the combustor at different angles and thus exhibit different deflections due to variations in the local index of refraction. For higher temperatures, the simulation predicts lower LIF signals than encountered during the experiment. The curves start to diverge, where the ratio ζ between CO_2 and CO mole fraction increases, which indicates that a significant portion of the measured CO signal arises from photolytic

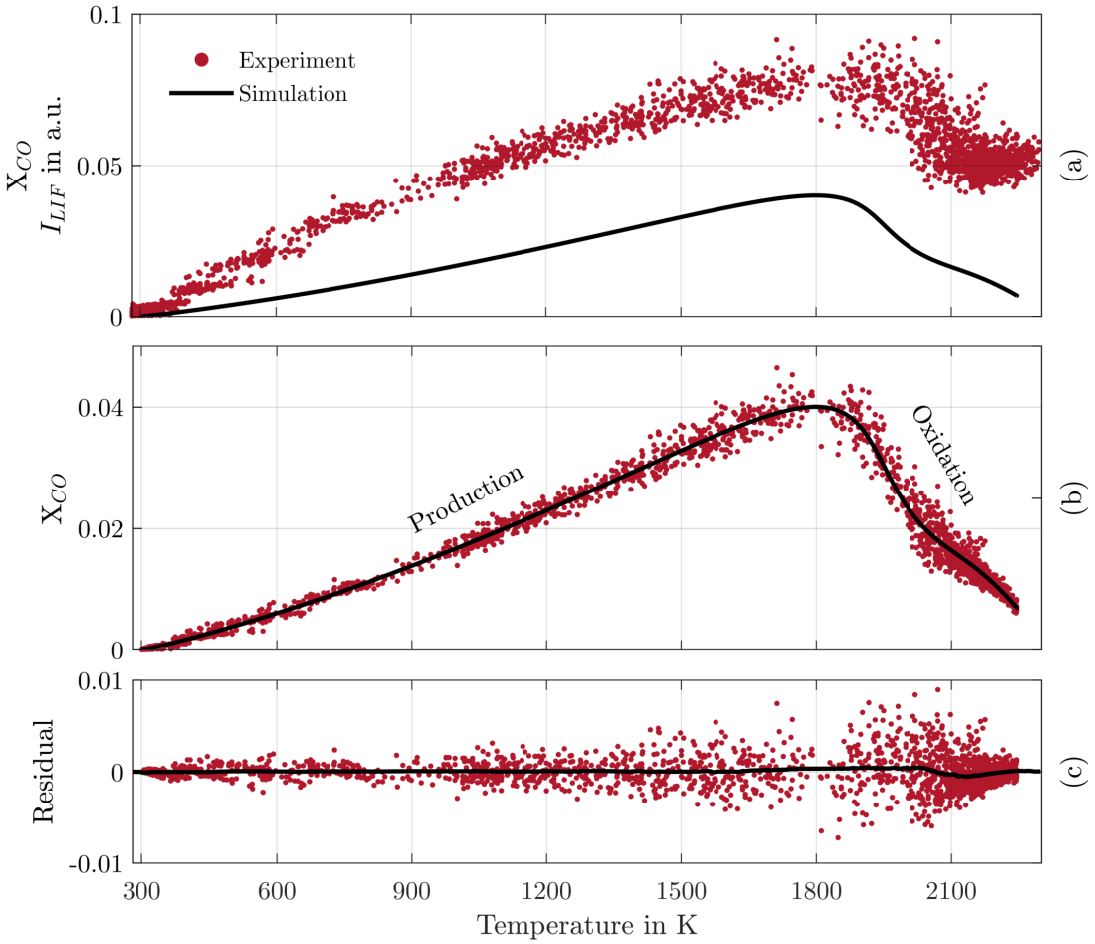

Figure 5.7: Calibration procedure. (a) Preprocessed CO-LIF data from measurements in the calibration flame scattered over measured temperature in comparison to laminar flame simulation. (b) Calibrated CO-LIF results. (c) Residual between measured and simulated CO mole fraction. Red line shows a moving average (bin width $\approx 300\,\mathrm{K}$) through the residual to provide an estimation of the calibration accuracy. Temperature from simultaneous CARS measurements. Figure adapted from [E4] with permission from Elsevier.

production. For the calibration flame, the CO_2/CO equilibrium ratio is $\zeta_{\Phi=1,Eq.} \approx 5.8$. At this condition, the measured LIF signal is 1.6 times higher as predicted by the simulation. As can be seen in the second frame of Fig. 5.8, ε is nearly proportional to the ratio $\zeta_{\Phi=1}$. This fact is now used to calculate the deviation δ shown in the third frame, i.e. the relative error after calibrating a $\Phi = 0.75, T_\mathrm{u} = 623\,\mathrm{K}$ flame with a calibration taken at $\Phi = 1, T_\mathrm{u} = 300\,\mathrm{K}$ due to different proportion of *actual* and *photolytically produced* CO mole fraction. Due to the linear dependence of ε to $\zeta_{\Phi=1}$, the proportion of photolytically produced CO *unaccounted for by the calibration* can be expressed by the ratio $\zeta_{\Phi=0.75}/\zeta_{\Phi=1}$. The bottom right plot in Fig. 5.8 shows this influence mapped on the temperature scale of the laminar adiabatic flame simulations. This influence could not be corrected in the

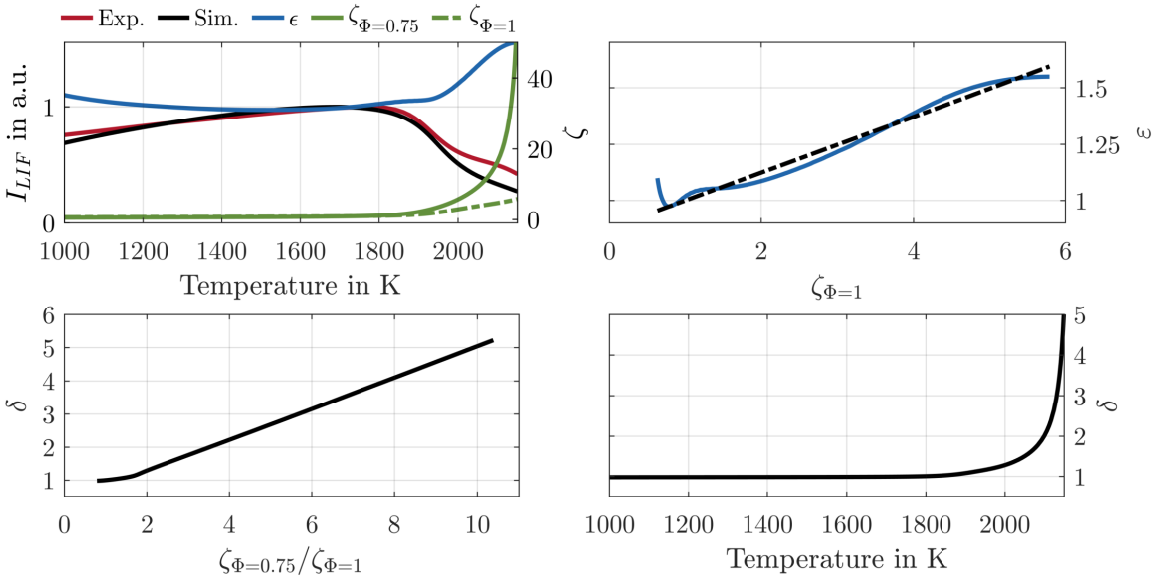

Figure 5.8: Effect of CO photolysis on the calibration accuracy. Top left: comparison between measured and simulated CO-T profile of the calibration flame at $\Phi = 1$ and $T = 300\,\mathrm{K}$. The blue line represents the ratio ε between the measured and simulated LIF signal as a function of temperature. The upper right frame shows a linear fit through ε as a function of $\zeta_{\Phi=1} = X_{CO_2}/X_{CO}$. The deviation δ represents the amount of CO_2 dissociation unaccounted for during calibration. This quantity is plotted in the bottom two frames over the ratio $\zeta_{\Phi=0.75}/\zeta_{\Phi=1}$ and over temperature. Figure adapted from [E4] with permission from Elsevier.

current setup as the CO_2 mole fraction was not measured. Instead, this systematic error is included in the discussion on accuracy and precision.

Time-scale considerations One aspect to consider when interpreting CO-T diagrams is the different time scales of the production and oxidation branch, see Fig. 5.9. The timescale τ is derived from laminar flame simulations using the local flow velocity. The instant where the peak CO mole fraction is reached is defined as $\tau = 0$, i.e. negative values indicate time scales of the production branch while positive values represent time scales of the oxidation branch. The time needed to produce 95% of the CO peak amounts to $\approx 0.15\,\mathrm{ms}$, consuming the same amount takes $\approx 0.5\,\mathrm{ms}$, i.e. about 3 times longer. Around 50% of peak CO mole fraction, production and oxidation are nearly symmetrical. Consequently, the oxidation branch is further separated into an *early* and *late* section at 1980 K, corresponding to the temperature at 50% of the CO mole fraction peak.

5.2.5 Resolution

For the combined CARS/CO-LIF technique, the beam geometry near the focal point limits the spatial resolution of the measurement. For CARS, the measurement volume was reconstructed by traversing a beam profiling camera through the measurement volume

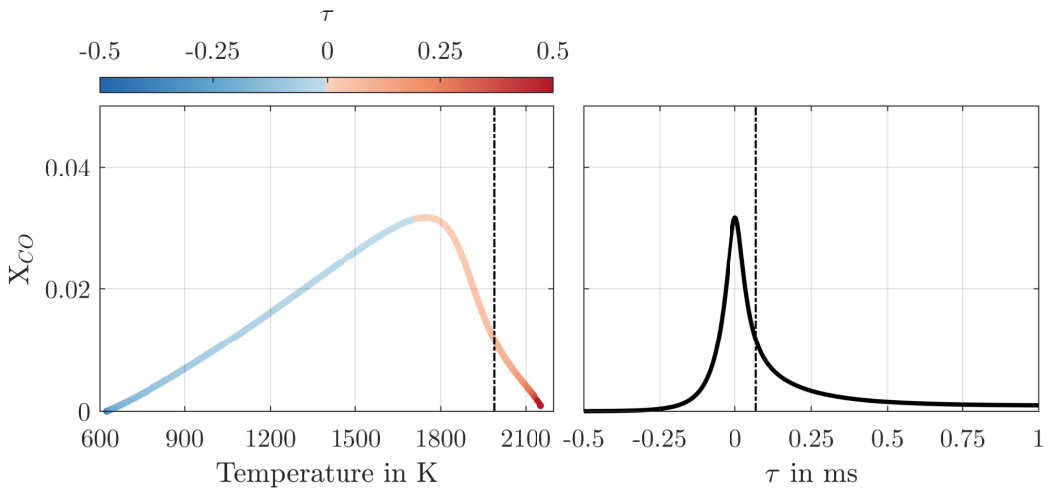

Figure 5.9: Time scales of CO chemistry. Left: CO-T diagram color coded with time scale τ. Right: CO mole fraction over τ. Dashed line separates *early* and *late* stages in the oxidation branch. Simulated conditions: $\Phi = 0.75$, $T_u = 623\,K$, $p = 2.5\,bar$. Figure adapted from [E4] with permission from Elsevier.

along its length (i.e. the principal direction) in increments of 50 µm. At every increment, the local intensity profile of each beam was measured individually with the same set of neutral density filters placed in the respective beam paths to allow the lasers to run at the same pulse energy used in the experiment. As the CARS signal is proportional to the product of the intensity of all involved lasers beams, the measurement volume is reconstructed by point-wise multiplication of the intensity images at every spatial increment. The length of the measurement volume is extracted at the isocontour at 90% peak intensity. The beam waist had a lateral extension of $\approx 50\,\mu m$ (FWHM) and the measurement volume length was measured to be $\approx 0.5\,mm$. This value was confirmed by additional measurements of a non-resonant signal when traversing the measurement volume through a thin glass plate with 100 µm thickness.

For CO-LIF, the transversal beam profile at the focal point was measured to be $\approx 60\,\mu m$ (FWHM). The width of the slit that is used to crop the intermediate image within the PMT assembly was adjusted such that $\approx 0.4\,mm$ were integrated in beam-wise direction to ensure coincident acquisition of temperature and CO information. The slit width was reduced by 100 µm compared to the CARS measurement volume length to account for the unknown PSF of the lens system (AC+EF135+L_1) used for detection which might otherwise lead to collection of LIF signal outside of the CARS measurement volume.

5.2.6 Uncertainty

Due to the nature of the method, uncertainties in the gas-phase temperature measurement directly affect the uncertainty of the measured CO mole fraction. The precision of CARS is estimated by the standard deviation of the exhaust temperature of the calibration flame, which is assumed to be constant. This standard deviation amounts to $\approx 40\,K$.

As the intensity of the CARS signal scales with the total number density squared, this represents an upper bound of the precision as lower temperatures yield higher signal strengths, leading to improved precision. This improvement over previous measurements (e.g. in [E8], where 60 K were reported) is mainly attributed to the new evaluation algorithm that uses appropriate variance weighting and global fitting, see Sect. 2.2.2. The deviation from adiabatic flame temperature of the calibration flame is $\approx 10\,\mathrm{K}$, indicating a high accuracy.

As a measure of precision for the quantitative CO measurements, the standard deviation of the calibration residual in Fig. 5.7 is reported, which amounts to 1.7×10^{-3}. This corresponds to a relative precision of $\approx 4\%$ at peak CO mole fraction and $\approx 25\%$ at the exhaust CO mole fraction $X_{CO} = 6.9 \times 10^{-3}$. The accuracy of calibration, i.e. the systematic deviation, is estimated by low-pass filtering the residual with a moving average filter to eliminate noise. The mean absolute error amounts to 2×10^{-4}. This calibration error does not yet include the influence of different photolytic production of CO due to the different equivalence ratio between combustor operating condition and calibration. For measurements in a hypothetical laminar adiabatic flame at $\Phi = 0.75$ and $T_\mathrm{u} = 623\,\mathrm{K}$ at 2.5 bar, i.e. known correlation between ζ and temperature, the deviation δ in the CO production branch for temperatures $T \leq 1800\,\mathrm{K}$ is $\leq 1\%$. The oxidation branch is increasingly affected with increasing temperature where the resulting error might be as large as 500% for adiabatic equilibrium conditions, see bottom right frame in Fig. 5.8. Additionally, if heat losses or mixing with effusion cooling air occurs, i.e. chemical composition and temperature are not represented by the simulated flamelet, this error is further increased due to the strong sensitivity of δ at high temperatures. Thus an absolute accuracy for our quantitative CO measurements of 2×10^{-4} in the production branch and $\approx 1 \times 10^{-3}$ for the oxidation branch and areas with significant heat loss is reported.

During operation of the combustor, the measurement volumes of CARS and CO-LIF may misalign due to beam-steering effects. As the individual beams are entering the combustor at different angles, they are differently affected by local variations of the index of refraction. The amount of misalignment cannot be quantified easily and add additional uncertainty to the measurement.

5.2.7 Parameter Space and Measurement Locations

Due to the time-consuming and thus expensive nature of point-wise measurements, the amount of parametric variations had to be reduced. As the main goal of this investigation is the influence of effusion cooling air on the thermochemical state in various areas of the combustor, the parameter space is limited to the variation of the effusion cooling air mass flow at low swirl (LS) and fully premixed (FP) condition. For easier readability, abbreviations LS and FP are omitted within this chapter and operating conditions are only referred to as LC and HC for the low and high effusion cooling air mass flow setpoint, respectively.

Fig. 5.10 shows the measurement locations superimposed on a mean OH-PLIF image at HC condition for orientation. Abbreviations indicate specific regions typical for a swirl-

stabilized flame: These are the inner and outer recirculation zones (IRZ/ORZ) and the inner and outer shear layer (ISL/OSL), where the flame is stabilized.

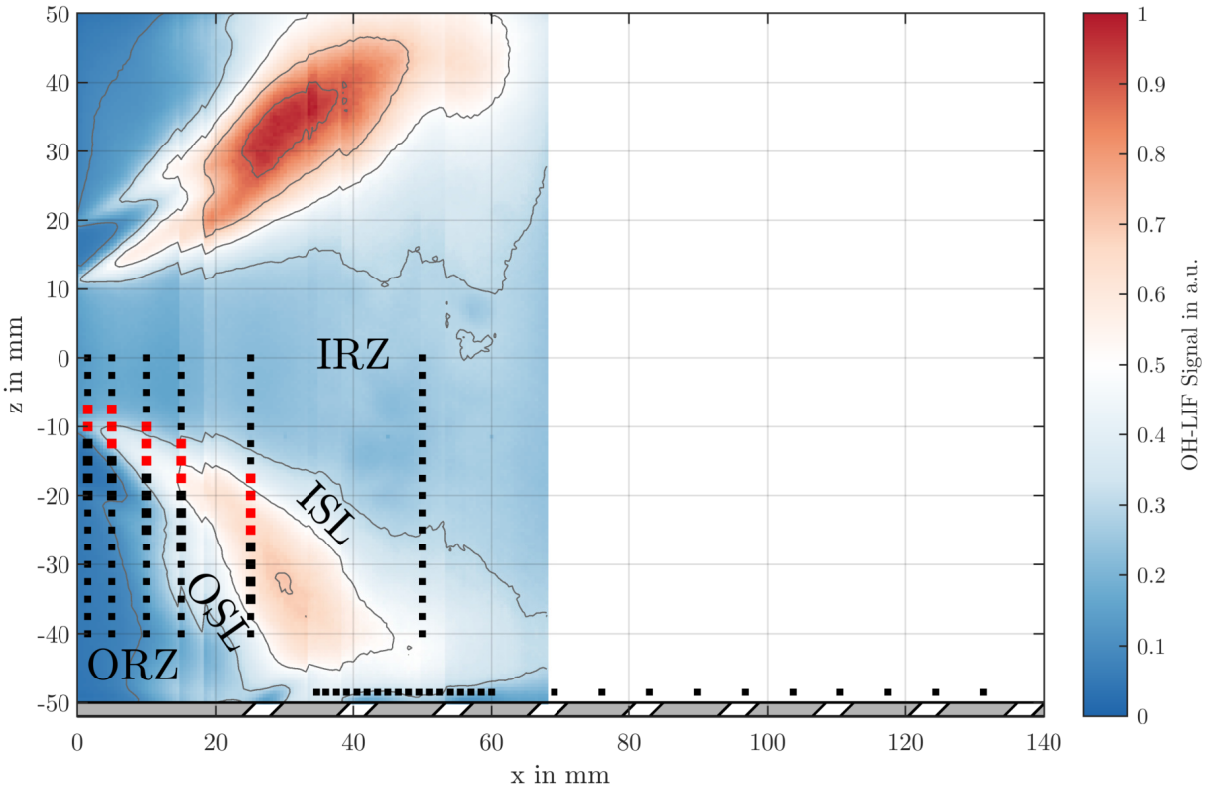

Figure 5.10: Overview of selected measurement locations indicated by dots superimposed on a mean OH-PLIF image at HC condition. Large dots indicate measurements within the inner shear layer (red) and outer shear layer (black). IRZ: Inner recirculation zone; ORZ: Outer recirculation zone; ISL: Inner shear layer; OSL: Outer shear layer. Figure taken from [E4] with permission from Elsevier.

5.3 Results

5.3.1 Primary Zone

Radial profiles of temperature and CO mole fraction Radial profiles of mean temperature and CO mole fraction are presented in Fig. 5.11. Mean temperature profiles for both operating conditions show typical features of a swirl-stabilized flame. Near the main outlet at $x = 1.5\,\text{mm}$ and $z = -15\,\text{mm}$, fresh gas is entering the combustor at the inlet temperature of 623 K. The flame is stabilized in the ISL and OSL, identified by the radial temperature gradients in Fig. 5.11. The shear layers are surrounded by high gas phase temperatures of recirculated exhaust in the IRZ and ORZ. The radial extension of the IRZ increases with axial distance from the head-plate, which can also be seen in the mean OH-PLIF data shown in Fig. 5.10. Due to heat losses, the ORZ consistently shows lower mean temperatures than the IRZ which seem to be - at least for the first two radial profiles at $x = 1.5\,\text{mm}$ and $5\,\text{mm}$ - dominated by conduction to the head-plate rather

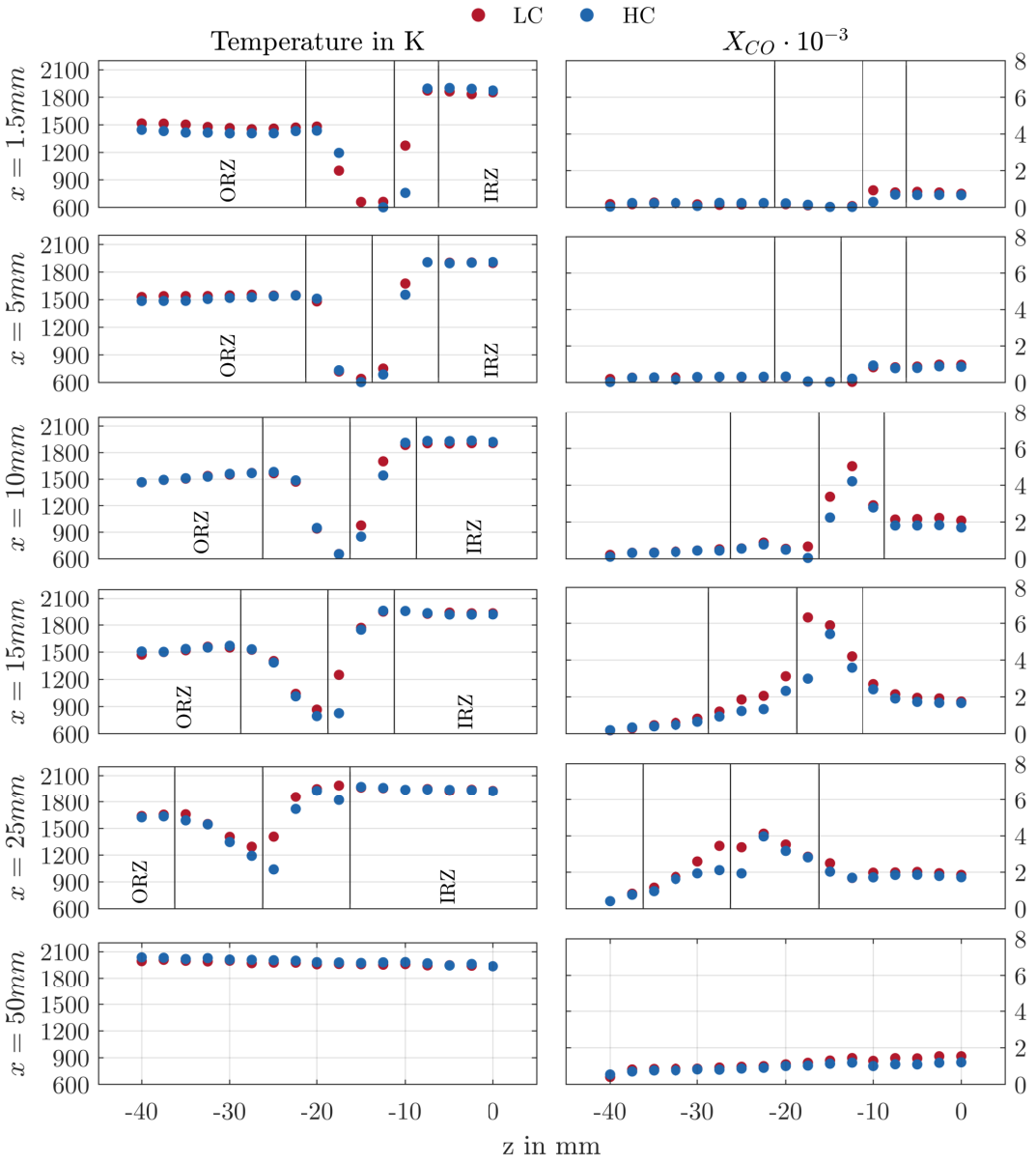

Figure 5.11: Radial profiles of mean tempererature and CO mole fraction. Red dots indicate low cooling air mass flow (L), blue dots indicate high cooling air mass flow (H). This coloring scheme is carried out through all following plots. Grid lines in the upper row show the segmentation in ORZ/OSL/ISL/IRZ. Measurements of both conditions conducted on the same day to avoid influence of uncertainty of calibration for comparison. With 1000 samples per datapoint, statistical uncertainty of the mean value is below the marker size. Absolute uncertainty of X_{CO} for both cases $\leq 1 \times 10^{-3}$, i.e. half the vertical grid spacing. Figure taken from [E4] with permission from Elsevier.

than mixing with effusion air as the temperature profiles are only slightly dependent on effusion cooling mass flow and there is almost no perceivable mean temperature gradient $\delta T/\delta z$. Mean CO mole fraction profiles are consistent with the temperature profiles. Locations with high probability of encountering reaction zones (ISL/OSL) are identified

by increased CO mole fraction compared to the recirculation zones. The ORZ and the OSL show systematically reduced CO mole fractions compared to the ISL and IRZ. This indicates either (a) a more advanced reaction process due to the longer residence times expected in the ORZ, or (b) possible disturbances in reaction rates for CO chemistry for the side of the flame brush facing the effusion cooled liner. This aspect will be further discussed in the next subsection.

Only minor differences between operating conditions are observed in the radial temperature profiles. Generally speaking, the difference decreases with increasing distance from the effusion cooled liner and the head plate. For profiles with an axial location $x \geq 10\,\mathrm{mm}$, mean temperatures are identical within the precision and accuracy of the measurement. A notable difference can be observed in the first two radial profiles in the ORZ, where the higher effusion cooling mass flow leads to a temperature lowered by $\approx 100\,\mathrm{K}$ which indicates that a significant amount of cooling air from the first holes on the liner entrain the ORZ. The highest measured mean temperature of 2050 K is in the post flame region around $x = 50\,\mathrm{mm}$ and $z = -40\,\mathrm{mm}$. Mean temperatures decrease to 1975 K towards the center line, i.e. within the inner recirculation zone. This behaviour is consistent with previous investigations at similar conditions [E8, E9].

Similar to the temperature profiles, the mean CO mole fraction results show only minor differences. There is a trend to higher CO concentrations with less cooling air for locations closer to the center line within the internal recirculation zone, which indicates that a fraction of effusion cooling air is entrained in the inner recirculation zone and is thus convected upstream.

Influence on thermochemical state To investigate the thermochemical state in areas with a high probability to observe reaction zones, Fig. 5.12 shows CO-T scatter plots from measurements in ISL and OSL for axial coordinates between $x = 1.5\,\mathrm{mm}$ and $x = 25\,\mathrm{mm}$ and at the location of peak CO mole fraction at $x = 15\,\mathrm{mm}, z = -15\,\mathrm{mm}$.

A first observation is that - opposed to the laminar flame calibration in Fig. 5.7 - the area under the flamelet is filled with datapoints. Partly, this arises from the limited spatial resolution of the detection system as it is simply very unlikely to measure a flame front which is exactly parallel to the elongated measurement volume. As a consequence, multiple states are integrated within the probe volume. Additionally, beam-steering, recirculation and mixing as well as the precision of the measurement itself are represented in an increased spreading of values. As a consequence, only trends can be described.

Compared to the ISL, higher heat losses are observed in the OSL as indicated by the shift to higher probabilities to measure samples at intermediate temperatures and low CO mole fractions. Additionally, nearly all measured samples fall below the dashed line, indicating that compared to the ISL, reaction rates are indeed severly impaired from heat losses and mixing with effusion cooling air. The lowered CO mole fraction is caused, in part, by longer residence times and associated later stages of the CO oxidation branch. This reduction is less pronounced in the ISL, where the measured samples fill the entire area under the limit defined by the laminar flame calculation, proving that the calibration procedure at a different equivalent ratio does not significantly impair the derived CO mole

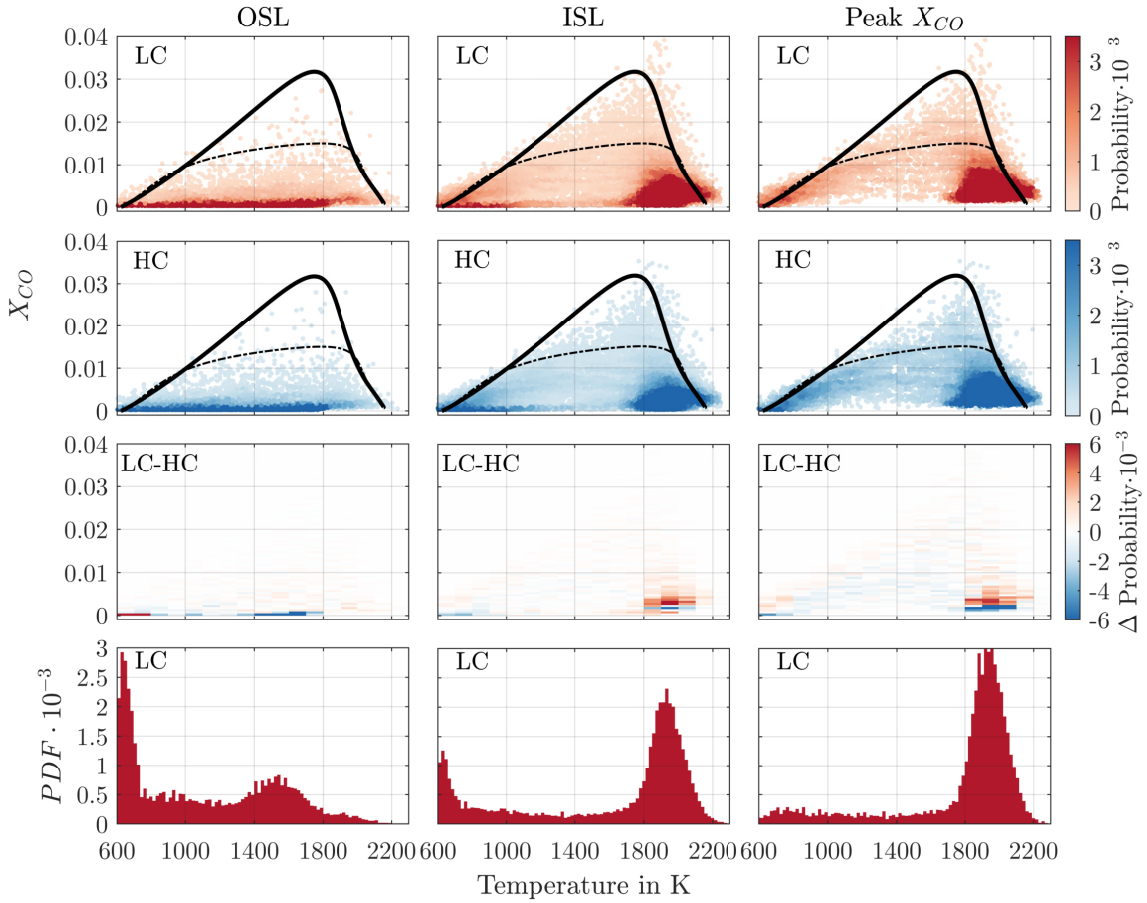

Figure 5.12: CO-T scatter plot of selected areas in primary zone. Left column represents the outer shear layer (OSL), middle column inner shear layer (ISL) and right column measurements with highest measured mean CO mole fraction ($[x,z] = [15, -15]$). First and second row show scatter plots of measured CO mole fractions over temperature for LC and HC condition. Color coded is the probability to measure a sample within a bin with a width of $\Delta T = 100\,\mathrm{K}$ and a height of $\Delta X_{CO} = 5 \times 10^{-4}$. The colorscaling is intentionally cropped at 3×10^{-3} to emphasize areas with low probability. Black solid lines represent laminar adiabatic flame simulations at combustor conditions. The dashed line represents the simulation after filtering it with the spatial resolution of the measurement. The third row shows the difference in bivariate CO-T PDFs between operating conditions (LC-HC) to visualize influence of cooling air in the state-space diagram. Bottom row shows temperature PDFs for case LC. Case HC is omitted as there is no significant difference observed. Figure taken from [E4] with permission from Elsevier.

fraction in the production and early oxidation branch. Temperature PDFs show a typical bi-modality found in premixed flames due to the thin flame fronts. The scatter plot at peak mean CO mole fraction, which is the spatially central point of the measurements within the ISL, is characterized by the lowest disturbance of CO chemistry. The mean temperature of the peak in the temperature PDF amounts to 1940 K which is approximately 100 K below the highest observed mean temperature of 2050 K observed in the post-flame zone

at $x = 50\,\text{mm}, z = -40\,\text{mm}$, indicating that even this point is affected by significant heat loss and/or mixing.

Differences between operating conditions LC and HC are observed in all selected areas of the primary zone. For measurements in the OSL, the difference in bivariate CO-T PDFs, see third row in Fig. 5.12, in the temperature range between 1000 and 1800 K indicates a more dominant mixing with effusion cooling air for the higher effusion cooling air mass flow (HC). As the area of increased probability is confined to a small range of X_{CO} values and strongly elongated in temperature direction, it is assumed that this is mostly caused by mixing of exhaust gases with effusion cooling air in the outer recirculation zone. For the ISL and peak CO location, significant differences can only be observed at high temperatures near chemical equilibrium, where the higher cooling air mass flow leads to lowered CO concentrations.

5.3.2 Near-wall Zone

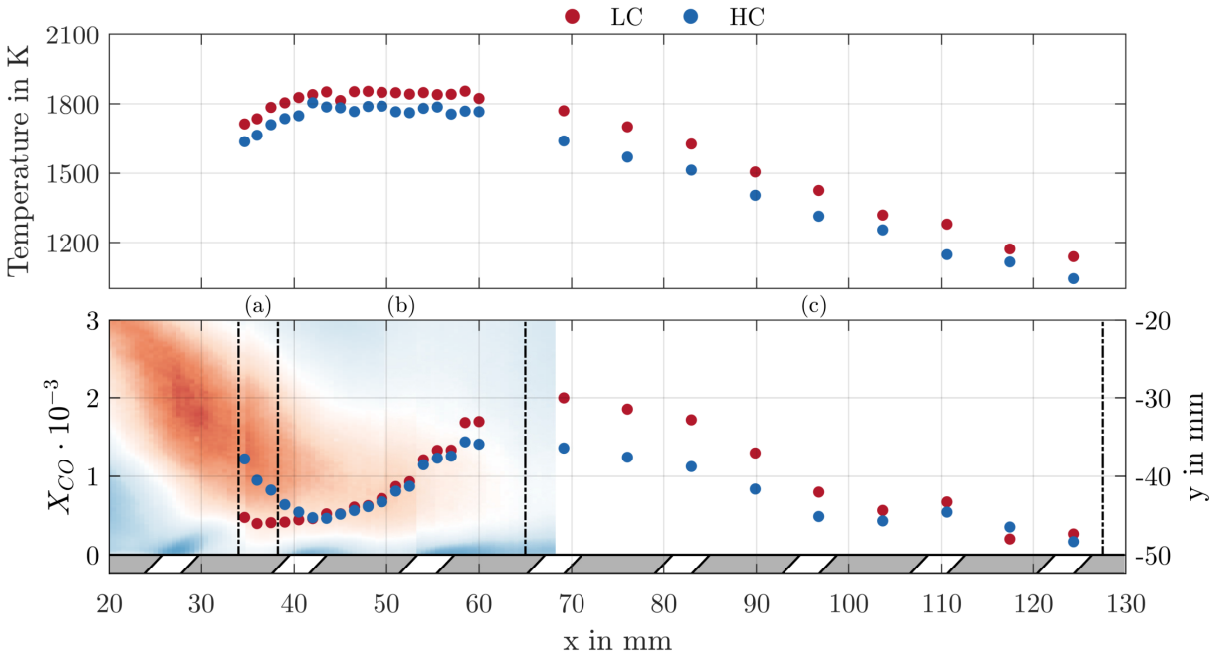

Figure 5.13: Mean temperature and CO mole fraction profiles 1.5 mm above the effusion cooled liner. Inset image shows mean OH-PLIF data for orientation. Measurements of both conditions conducted on the same day to avoid influence of uncertainty of calibration for comparison. With 1000 samples per datapoint, statistical uncertainty of the mean value is below the marker size. Absolute uncertainty of X_{CO} for both cases $\leq 10^{-3}$, i.e. the vertical grid spacing. Figure taken from [E4] with permission from Elsevier.

Axial profile of temperature and CO mole fraction As expected, a significant influence of cooling air mass flow close to the effusion cooled liner is observed, see Fig. 5.13. Mean gas phase temperatures are systematically lower with increasing cooling air. Mean CO mole fractions on the other hand show an unexpected behavior. Three regions of interest can be identified: Region (a), just upstream the second effusion hole on the

center line, where the mean measured CO mole fraction of case HC is *larger* than for case LC. This behavior indicates possible interactions between flame and cooling air within the production and/or oxidation branch of CO beyond adiabatic mixing processes. Locations further upstream were impossible to reach due to partial clipping of the horizontally aligned CARS setup. The intermediate region (b) between the second and third effusion hole, where the mean CO mole fractions reaches a local minimum, appears to be *independent* from cooling air mass flow setting. This region is dominated by exhaust from the primary combustion zone approaching the wall, see Fig. 5.10. The CO concentration convected from the ISL is systematically higher than from the OSL, see Fig. 5.11, consequently resulting in a rise in CO concentration with axial coordinate which reaches a peak at $x \approx 70\,\text{mm}$. The third region (c) shows an increased CO mole fraction for case LC, which indicates that adiabatic mixing is dominant in the post-flame area. CO mole fraction declines for axial locations $x \geq 70\,\text{mm}$ due to mixing with increasing number of effusion holes.

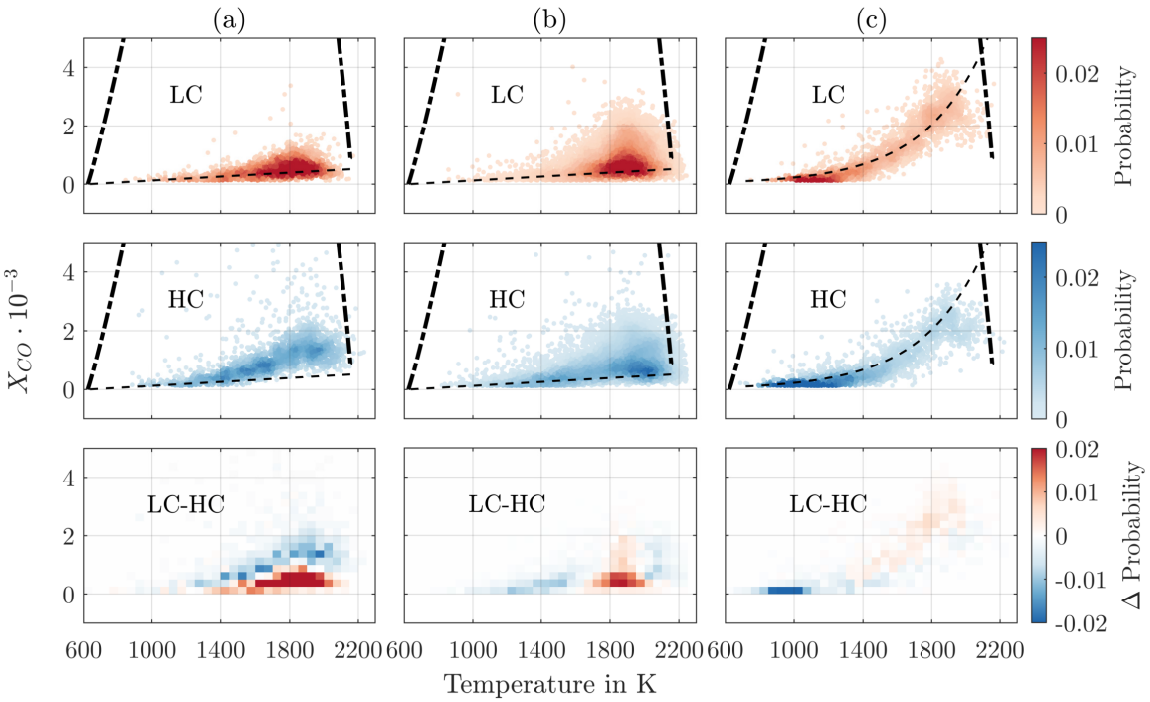

Figure 5.14: CO-T scatter plot of selected regions near the effusion cooled liner. Dashed lines in region (a) and (b) show theoretic decline in CO concentration and temperature based on mixing of adiabatic equilibrium conditions and effusion cooling air. Dashed line in region (c) shows an exponential fit through the measured data. Dash-dotted lines in all regions represent laminar flame calculations. The third row shows the difference in bivariate CO-T PDFs between operating conditions (LC-HC) to visualize influence of cooling air in the state-space diagram. Bin width equal to those used for Fig. 5.12. Figure taken from [E4] with permission from Elsevier.

Influence on thermochemical state Figure 5.14 shows CO-T scatter plots of the data presented in Fig. 5.13. All three areas are strongly affected by heat losses and as

such suffer from degraded accuracy due to CO_2 photolysis, see previous section. The data is thus only interpreted semi-quantitatively, i.e. by comparing the two measured conditions HC and LC which were measured on the same day and as such underwent the same calibration.

In region (a), the mean CO mole fraction is about twice as high for case HC as it is for case LC in the temperature range $1400 - 2000\,\mathrm{K}$, see third row in Fig. 5.14. Additionally, the gradient of CO values with respect to temperature is higher for case HC, indicating that there is an increased chemical interaction between cooling air and the late CO oxidation branch. Measurements for LC condition fall quite precisely on the dashed line representing adiabatic mixing between equilibrium condition and cooling air. Measurements for HC condition deviate from that line for temperatures $\geq 1400\,\mathrm{K}$. One possible explanation is that the increased penetration depth of the single effusion jets due to the increased mass flow leads to a higher chance of mixing of effusion cooling air with earlier states of the CO oxidation branch. For case LC, local rupture of effusion cooling air jets, cf. [E8], effectively prevents this interaction, leading to a higher probability to measure samples that originate from equilibrium conditions after enthalpy loss to the cooled liner.

In region (b), i.e. between the second and third effusion cooling air holes, mean CO concentration increases with axial distance, see Fig. 5.13. As stated earlier, this is most likely due to increasing convective transport of exhaust gases from the ISL, where CO concentrations are generally higher as in the OSL, approaching the effusion cooled liner. Quite notably, the measured CO concentration is independent from the cooling air mass flow setting. Apparently, mixing between the upstream located region (a), where the CO mole fraction is *increased* for case HC, and exhaust CO from the shear layers, which are in average *lower* in concentration for case HC, balances in region (b).

In region (c), the measured CO mole fraction reaches its peak at around $x = 70\,\mathrm{mm}$ and starts to decline again, see Fig. 5.13. With increasing probability, samples originating from the ISL are measured, leading to increased CO concentrations. The roll-off of CO mole fraction towards lower temperatures resembles findings from atmospheric flame-wall-interaction investigations [90, 97]. The intersection between the exponential fit reaches a CO mole fraction of approximately 4×10^{-3} which corresponds to measured levels in the ISL, see Fig. 5.11, further assisting the interpretation that the rise in mean CO mole fraction is dominated by convection of exhaust gas from the ISL. Further downstream, the stream lines are nearly parallel to the wall. This leads to a decline in CO concentration due to mixing with cooling air from an increasing number of effusion holes, explaining why the measured mean CO concentration is again lower for case HC compared to case LC.

5.4 Summary

In this study on thermochemical states due to interaction of flame and cooling air, instantaneous quantitative CO mole fraction measurements and gas-phase temperature measurements were presented in a combined approach of advanced laser diagnostics. Temperature was measured using ro-vibrational coherent anti-Stokes Raman spectroscopy with

N_2 as a resonant species. Quantitative CO mole fractions were derived from CO-LIF measurements and temperature dependent calibration based on laminar flame measurements. Two different operating conditions with varying effusion cooling air mass flow were investigated.

Within the primary combustion zone, different thermochemical states for the inner and outer shear layer were observed. In the outer shear layer, increased heat loss by conduction to the head-plate and mixing with effusion cooling air leads to significant disturbance in CO chemistry indicated by reduced CO mole fractions and temperatures across the entire CO-T state-space. Probabilities to measure low temperature and low CO concentrations increases with effusion cooling air mass flow, indicating that the primary zone is indeed affected by the effusion cooling air at wall distances $\geq 25\,\mathrm{mm}$. In the inner shear layer, decreased effusion cooling air mass flow leads to higher exhaust CO concentrations at high temperatures.

Close to the effusion cooled liner, three regions could be identified which vary in their cooling air mass flow dependence. In the outer recirculation zone, a higher effusion mass flow leads to *increased* CO mole fractions due to chemical quenching of reaction zones in the outer shear layer of the primary combustion zone. For the low effusion cooling mass flow, local rupture of the cooling film, as discussed in [E8], effectively prevents this effect. Further downstream, hot exhaust products from the inner shear layer of the main stage near equilibrium condition are convected towards the effusion cooled liner, leading to an increase in CO mole fraction. Within this region, it is assumed that upstream chemical quenching and mixing with exhaust from the shear layers compensates for the high effusion cooling mass flow set point, such that the measured mean CO concentration is independent from effusion cooling mass flow. Downstream of this region, the processes are dominated by dilution with increasing amounts of effusion cooling air, leading to again decreasing CO mole fractions and temperature with axial distance.

Chapter 6

Reaction and Heat Release Rate Imaging

6.1 Aim of this Investigation

Within this investigation, a combination of OH-PLIF and CO-LIF is used in combination to infer the influence of effusion cooling air on the oxidation reaction of CO:

$$\mathrm{CO} + \mathrm{OH} \rightarrow \mathrm{CO_2} + \mathrm{H} \tag{6.1}$$

While the investigation presented in Sect. 5 focused on the inference of the local thermochemical state with high precision, it was not able to identify *why* a given sample is in a given CO-T state as no information on the reaction progress was available. This is predominantly important for the measurements in the primary zone, where a strong scattering of results in the area under the laminar flame simulation was observed, as it could not be identified if the origin of the state was caused by dilution before reaction - which lowers both temperature and peak CO mole fraction due to the dependence on equivalence ratio - or if the state was caused by mixing or heat loss in the early oxidation branch - which also lowers temperature and CO mole fraction, leading to a similar state albeit with a different *history*.

Within the investigation presented in this chapter, [OH][CO] reaction rate (RR) measurements are combined with CH_2O-LIF to acquire a spatially and temporally resolved indicator for low-temperature chemistry. As the location of peak formaldehyde number density resides within the production branch of CO, this allows to separate samples into the production and oxidation branch of CO and consequently allows to gain further insight on the local thermochemical state. Furthermore, the combined evaluation of CH_2O-LIF and OH-LIF allows to extract information on the heat release rate, as the forward reaction rate of the reaction

$$\mathrm{CH_2O} + \mathrm{OH} \rightarrow \mathrm{HCO} + \mathrm{H_2O} \tag{6.2}$$

is the major contribution to HCO production which is an excellent marker for heat release rate. HCO plays a key role in the dominant pathway of CO production and many of the elementary reactions with large contributions to heat release follow this pathway [12,123].

Fig. 6.1 shows laminar adiabatic flame simulations at three different equivalence ratios. While $\Phi = 0.75$ represents the nominal equivalence ratio of the fully premixed main stage,

the other two correspond to hypothetical cases, where the effusion air mixes completely prior to combustion. Diluting the main stage with $7.5\,\mathrm{g\,s^{-1}}$ (LC condition) leads to an equivalence ratio of $\Phi = 0.6$, diluting with $15\,\mathrm{g\,s^{-1}}$ (HC condition) corresponds to $\Phi = 0.5$. The variation of equivalence ratio strongly affects the number density profiles of OH and CO and consequently the forward reaction rate of the oxidation reaction (6.1) (RR) and the heat release rate (HRR). With increasing Φ, profiles show a narrower appearance and increased peak values. For [OH] and [CO], the number density at $\Phi = 0.75$ compared to $\Phi = 0.5$ is increased by a factor of 2.65 and 1.75, respectively. [CH_2O] on the other hand is significantly less sensitive to changes in equivalence ratio, where the increase amounts to 20% only. This justifies to treat [CH_2O] as a marker for low-temperature chemistry which is - as a first order approximation - *independent of mixing with effusion cooling air.*

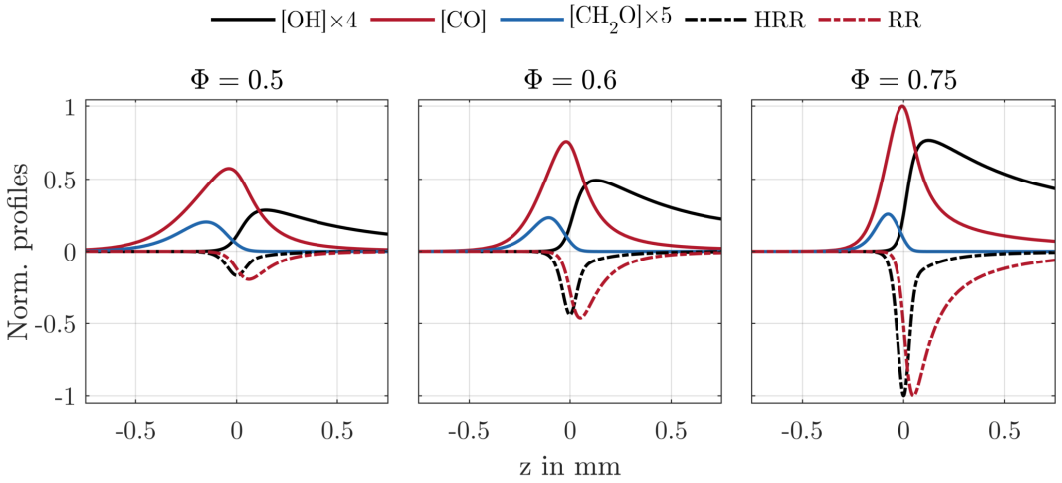

Figure 6.1: Laminar flame simulations at $T_u = 623\,\mathrm{K}$ and 2.5 bar at varying equivalence ratio Φ. Number density represented by solid lines, and inverse heat release rate (HRR) and reaction rate of [CO][OH] (RR) shown as dashed lines. All profiles normalized to the peak value at $\Phi = 0.75$. [OH] and [CH_2O] multiplied by 4 and 5, respectively, to fit a common y-axis with [CO].

This allows to define four different cases that can be identified using this technique:

Exhaust region: RR ↓ [CH_2O] ↓ [OH] ↑
This region is characterized by low reaction rate, no significant low temperature chemistry and high OH concentration. This is identified as the region downstream of the main reaction zone when the reaction progress approaches equilibrium. The level of [OH] gives an indication of the temperature, see Sect. 4, but does not allow to identify the mechanism of potential heat-loss, i.e. it may be due to mixing with effusion air, radiative or conductive.

Unburnt region: RR ↓ [CH_2O] ↓ [OH] ↓
Just as in the exhaust region, no significant reaction rate or low-temperature chemistry is

observed. As [OH] is also low, this can be identified as either fresh gas of the main stage or effusion cooling air or an unknown mixture of both.

Production branch CO: RR $\rightarrow$ [CH_2O] $\uparrow$ [OH] $\downarrow$
This region is characterized by significant low-temperature chemistry as indicated by high [CH_2O]. This coincides with intermediate levels of RR at its rising edge and the production branch of CO. As peak [CH_2O] is in comparison to RR less sensitive to equivalence ratio, the measured level of reaction rate gives an indication if the mixture has been diluted prior to onset of reaction.

Oxidation branch CO: RR $\uparrow$ [CH_2O] $\downarrow$ [OH] $\uparrow$
In the oxidation branch of CO, [CH_2O] already declined significantly and the peak RR is observed near the intersection of [CO] and [OH]. Comparing different operating conditions in this area, the peak RR allows to estimate the influence of cooling air on the local reaction rate.

While measuring the forward reaction rates for the reactions (6.1) and (6.2) directly is not straightforward, the combination of LIF techniques with carefully selected excitation and detection schemes allows to derive the reaction rate from the pixel-by-pixel product of the involved LIF signals. This is further discussed in the following section.

6.2 Method

The forward reaction rate for (6.1) and (6.1) may be expressed by Eq. (2.8), where the forward reaction rate RR is proportional to the product of the rate constant $k(T)$ as calculated from the Arrhenius law in Eq. (2.9) and the reactants' number densities. As any LIF signal is proportional to the number density of the molecule of interest, one has to make sure that the *combined temperature dependency* of the LIF techniques is proportional to the rate constant $k(T)$ to successfully derive the forward reaction rate from the pixel-by-pixel product of the signals. This is commonly achieved by the usage of simulated signals to obtain the correlation between the product of LIF signals with the forward reaction rate of interest. This approach has been successfully demonstrated in numerous publications investigating [CO][OH] [5, 12, 57] and [CH2O][OH] reaction rates for estimation of the local heat release rate [36, 98, 126] in atmospheric flames but has - to the best knowledge of the author - not yet been attempted to pressurized flames.

While the expected path integrated number densities for CO and CH_2O and consequently absorption effects are negligible - especially for the case of CO, as the two-photon absorption cross-section is small, this is not true for OH measurements as evident from the investigations presented in Sect. 4. Thus, it is again required to correct for absorption effects using the quantification approach described therein. For this reason, it is favorable to use the same excitation/detection scheme for OH-PLIF, i.e. excitation of the overlapping line pair $Q_1(9.5) + Q_2(7.5)$ with fluorescence detection of the (1,1) vibrational band to avoid influence from signal trapping. Consequently, a matching choice for the

excitation schemes for CO and CH_2O has to be made. In contrast to the investigations in Sect. 4, where wall-normal measurements where conducted, the orientation of measurements for combined reaction and heat release rate imaging have to be executed in a wall-parallel configuration due to the high laser intensities required for CO-LIF excitation which would cause local breakdowns at the effusion cooled liner when the high laser intensity is deposited on the wall.

6.2.1 OH-PLIF

As mentioned above, the excitation and detection scheme from the investigation of mixing processes has also been used for this investigation to allow reusing the quantitative evaluation procedure for OH-PLIF measurements. In principle, as CO-LIF is limited to 1D measurements, OH-PLIF could as well be reduced to 1D. However, as wall-parallel measurements of quantitative OH alone have not been conducted in this test rig, the measurements were conducted with a planar sheet. Changing the orientation to wall-parallel has some practical implications that have to be considered. The absorption measurement is greatly simplified, as the laser light sheet is not deposited on the wall and exits the combustor. This allows to use a dye cell filled with a fluorescent dye dissolved in ethanol for the energy reference before and after the test section instead of coating the effusion cooled liner with YAG : Tb^{3+}, which avoids non-linearity correction of the energy reference when using an extracted portion of the laser light sheet which decreases the uncertainty in the evaluation of the path integrated absorption. For this purpose, Coumarin 307 was dissolved in spectroscopy grade ethanol. Using spectroscopy grade ethanol greatly increases long term stability in contrast to denaturated ethanol containing methyl ethyl ketone.

For increased spatial resolution, the dual resolution approach for OH detection is also employed for this investigation. In a wall-parallel configuration, the high resolution (HR) detection system has to be mounted above the combustor as close to the upper pressure vessel window as possible. This leaves only the side-windows for the low resolution (LR) detection system. Inevitably, this requires to use a Scheimpflug arrangement for detection to ensure imaging the entire test section with reasonable optical resolution. Details on the optical setup and the detection systems are reported in subsection 6.2.4

6.2.2 CO-LIF

The setup for CO-LIF measurements largely follows the setup described in Sect. 5, i.e. excitation of a two-photon transition at around 230.1 nm with subsequent detection in the Ångström band. The reason for limiting CO-LIF measurements to point-wise detection in Sect. 5 was the simultaneous acquisition of CARS spectra. As for this investigation only other LIF techniques are used in combination, the detection system is replaced with an intensified camera to allow one-dimensional measurements of CO-LIF within the Rayleigh length near the focal point. For a reasonable detection efficiency in the visible wavelength region, an intensifier with a Gallium arsenide phosphide (GaAsP) photocathode was used (LaVision, IRO X), which has a quantum efficiency of $\geq 40\%$ in the wavelength region $450 - 600\,\text{nm}$. This is an improvement of approximately a factor of 3-4 compared to the

S20 photocathode optimized for detection in the UV. However, this increase in detection efficiency does not fully compensate the SNR reduction caused by increased spatial resolution in comparison to PMT measurements. Thus, a broadband detection scheme is employed, where the fluorescence of the vibrational bands (0,1)-(0,4) is captured to maximize the signal yield. No significant interference from C_2-LIF, see Sect. 2.2.1.2, was observed during a verification measurement in a lean laminar flame at $\Phi = 0.75$ and 2.5 bar, where the laser was tuned away from Q-branch CO resonances. Details on the optical setup and the detection system are reported in subsection 6.2.4

Following the common approach in the literature, selection of the transition used for CO excitation is based on LIF signal simulations as described in Sect. 2.2.1.2 and 2.2.1.4 in conjunction with the laminar adiabatic flame simulations. For a good SNR, it is desirable to excite CO near the band head. Thus, only the first 31 rotational lines are considered in the signal simulation. Fig. 6.2 shows the performed simulation. Although the individual

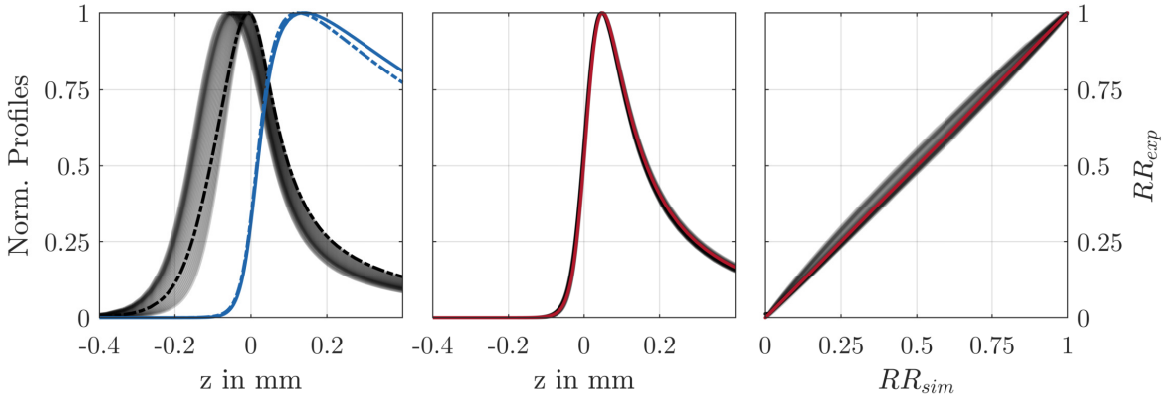

Figure 6.2: Simulated CO- and OH-LIF signals in comparison to simulated RR. Left: Black and blue curves represent number density (dashed lines) and simulated LIF signals (solid lines) for CO and OH, respectively. Shown are 31 simulated CO-LIF signal for excitation of $J'' = 0 - 30$. Middle: comparison of peak normalized RR from adiabatic flame calculation at $\Phi = 0.75$ (red) and peak normalized product of CO- and OH-LIF simulated signals for all J''. Right: Correlation between RR from adiabatic flame simulation and simulated experimental RR. Red solid line shows ideal case of perfect proportionality.

simulations of CO-LIF profiles shows a significant deviation from the underlying number density and a notable spatial variance which depends on the selected rotational line for excitation, the peak normalized product of the simulated CO and OH signals correlates well with the peak normalized forward reaction rate as calculated from laminar flame simulations. A slight hysteresis is observed, as excitation of lower J'' transitions tend to shift the signal to lower temperatures. Consequently, the simulated experimental RR rises and declines prematurely in comparison to the actual RR. Exciting rotational lines with higher J'' leads to an inverse behavior. The lowest deviation from perfect proportionality is obtained for $J'' = 24$, where the maximum deviation is in the order of 0.01, located near $RR_{sim} = 0.5$. However, as shown in Fig. 6.3, the signal magnitude when exciting the $J'' = 8$ transition is approximately a factor of two higher. For this excitation, the

deviation from linearity is increased to 0.04 near $RR_{sim} = 0.5$, corresponding to $\leq 10\%$, which is a reasonable trade off for improving the SNR by $\sqrt{2} \approx 1.4$.

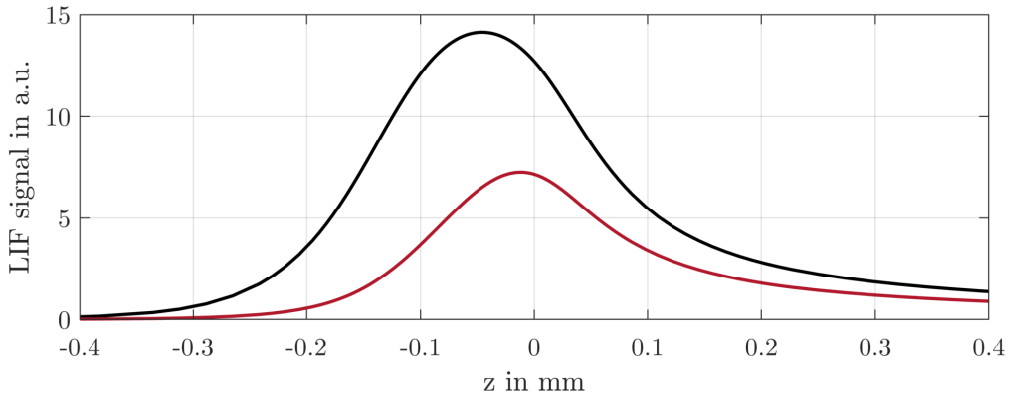

Figure 6.3: Comparison of signal magnitude for two different excitation schemes for CO-LIF. Black: $J'' = 8$. Red: $J'' = 24$.

6.2.3 CH_2O-LIF

CH_2O-LIF was excited in the overlapping $2_0^1 4_0^1 + 4_0^2 6_0^1$ band of the $\tilde{A}^1A_2 \leftarrow \tilde{X}^1A_1$ system using the frequency doubled output of a dye laser (Sirah, Precision Scan) which was optically pumped using a solid-state Q-switched Nd:YAG laser (Spectra Physics, PIV400) to produce UV radiation at around 339 nm. The achieved pulse energy was maximized to 24 mJ by using both cavities of the PIV laser simultaneously. Within the probe volume, approximately 15 mJ were available. Linearity of the LIF signal with respect to pulse energy was verified by measurements in the laminar calibration flame. For this purpose, a half-wave retardation plate was mounted before the frequency doubling crystal within the dye laser to vary the energy without affecting polarization. As the formaldehyde concentration for methane-air combustion is comparably low, measurements are limited to 1D. Fluorescence was captured in a broad range within the visible wavelength region between $350 - 470$ nm to maximize the signal yield. Details on the optical setup and the detection system are reported in subsection 6.2.4

Proper correlation between the product of OH- and CH_2O-LIF signals to the heat release rate are derived in a similar way as described above for the forward reaction rate of CO oxidation. In contrast to CO-LIF simulation, the simulation of formaldehyde LIF signals is subject to larger uncertainties as described in Sect. 2.2.1.5. Fig. 6.4 shows the impact of the uncertainty on the derived HRR from the product of OH and CH2O signals. In this figure, the uncertainty as estimated by the Monte-Carlo simulation in Sect. 2.2.1.5 is represented by the overlaid black curves. It is evident, that independent from the uncertainties, peak normalized HRR as calculated from laminar adiabatic flame simulations correlates reasonably with the peak normalized product of CH2O- and OH-LIF signals, albeit with a more prominent hysteresis due to the systematic shift of the CH2O-LIF signal towards higher temperatures due to the assumed $T^{-0.5}$ dependence of

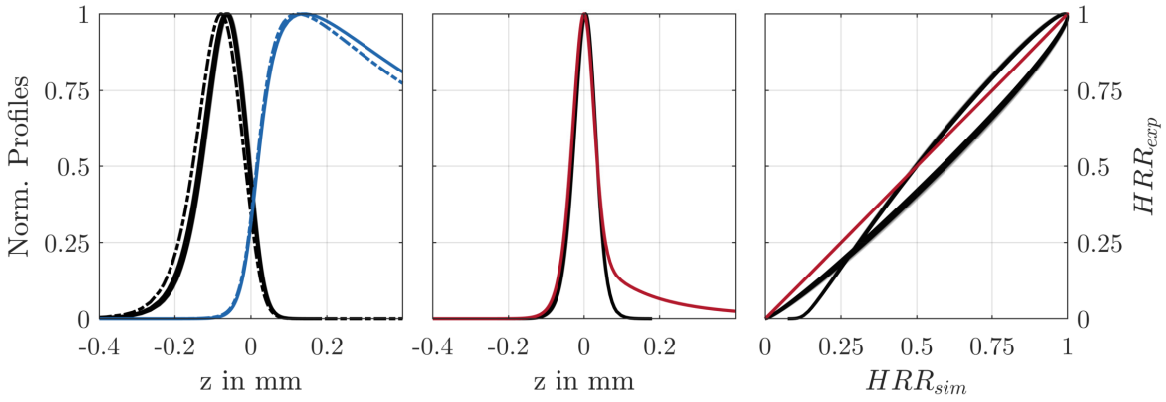

Figure 6.4: Simulated CH2O- and OH-LIF signals in comparison to simulated HRR. Left: Black and blue curves represent number density (dashed lines) and simulated LIF signals (solid lines) for CH2O and OH, respectively. Middle: comparison of peak normalized HRR from adiabatic flame calculation at $\Phi = 0.75$ (red) and peak normalized product of CH2O- and OH-LIF simulated signals. Right: Correlation between HRR from adiabatic flame simulation and simulated experimental HRR. Red solid line shows ideal case of perfect proportionality.

the quenching rate Q. Additionally, the actual HRR is asymmetric, with a longer tail on the high temperature side, while the LIF signal product is nearly symmetrical. This leads to a significant underestimation of HRR on the high temperature side. Deviation from perfect proportionality across the entire range of normalized HRR is within 15%.

6.2.4 Optical Setup

An overview of the optical setup used for this investigation is shown in Fig. 6.5. Fig. 6.6 shows a more detailed view of the setup near the test rig.

Beam alignment The laser beams for CO- and CH_2O-LIF feature a telescope consisting of a spherical convex and a spherical concave lens to match their divergences to ensure that the focal point within the combustor overlaps. Magnification of the telescopes is $\approx 1:1.2$. Partial reflections of the spherical convex lenses are used to monitor the pulse energy using individual pyroelectric energy meters. UV radiation at 339 nm and 230.1 nm is overlapped using a wavelength beam splitter (LEO optics, T339 + R230). Sheet forming optics (SFO) for OH-PLIF consists of a cylindrical concave lens and a cylindrical convex lens with a magnification of $\approx 5:1$. A rectangular aperture after the SFO was used to extract a laser light sheet with 20 mm height. Just as in the other experiments, the beams and the sheet are aligned to the axes of the traversing unit to allow to translate the measurement volume within the combustor. Combining a planar and a linear measurement requires that their respective beams enter the test section from opposite sides as otherwise the OH-PLIF laser light sheet would have to pass the focusing lens L_1

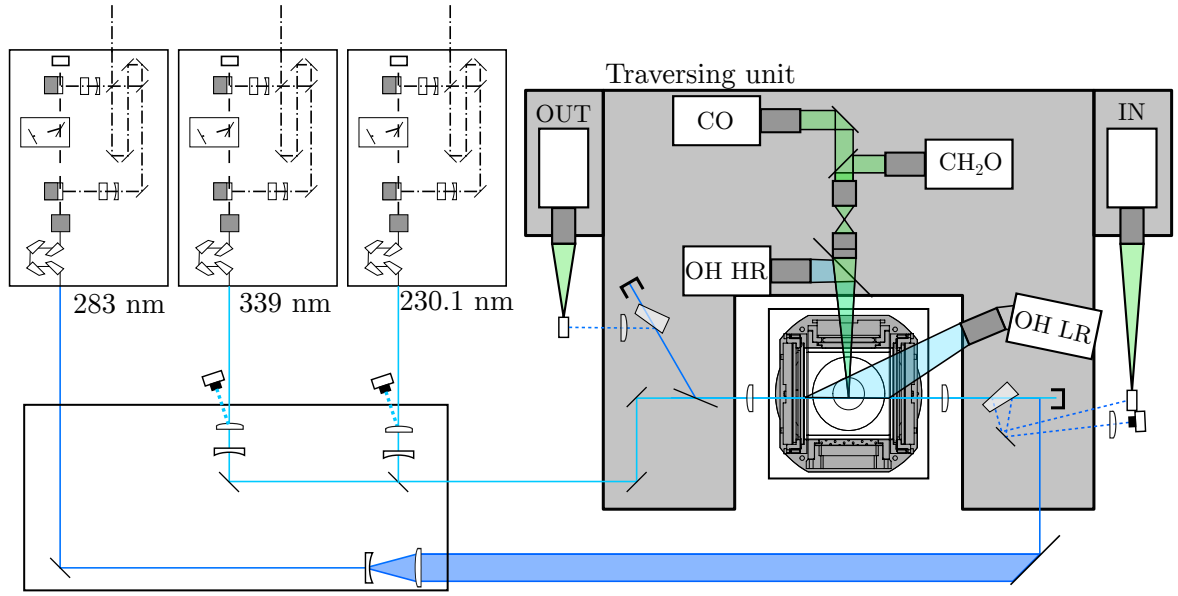

Figure 6.5: Overview of optical setup for combined reaction and heat release rate imaging. IN/OUT: Detection system for energy reference before and after test section. CO, CH_2O, OH HR, OH LR: Detection systems for LIF.

($f = 300\,\text{mm}$) for CO/CH_2O-LIF which would lead to undesired convergence of the laser light sheet.[21]

The overlapped CO/CH_2O-LIF laser beams are entering the combustor from the left while the OH laser light sheet is guided into the test section from the right as shown in Fig. 6.6. A wedged beam splitter is used to extract two partial reflections from the incident OH laser light sheet which are guided to a reference dye cell and a pyroelectric energy monitor (PE), respectively. A cylindrical focusing lens in front of the PE is used to fit the entire sheet onto the active area to ensure that the total pulse energy is accounted for. The theoretical focal point of the lens is behind the PE to stay within the tolerable intensity limits. The laser light sheet is then focused into the measurement volume using a cylindrical convex lens (L_2) with a focal length of 500 mm. As the exiting OH laser light sheet inevitably has to pass lens L_1 which produces an undesired focus approximately 300 mm behind the lens, a mirror reflective for 283 nm (M) is placed behind the lens to locate the focal point between the mirror and another wedged beam splitter. To minimize reflection losses at 339 nm and 230.1 nm, this mirror is placed at Brewster's angle. The transmitted beam of the splitter is guided into a beam dump to safely deposit the majority of the energy. One of the partial reflections is used for the required energy reference after the test section. As the beam is at this point divergent due to passing lens L_1, another lens L_3 with a focal length of 300 mm is placed into the beam path. Effectively, the lens system consisting of L_1 and L_3 form a 1:1 relay optic that images the central area of the

[21] Obviously this could be circumvented by placing the sheet forming optics for OH onto the traversing unit and using only a concave cylindrical lens to expand the OH beam with subsequent height collimation and width focusing through the spherical lens L_1. However, space constraints prevented this approach. Additionally, usage of a 300 mm lens for focusing the OH beam might lead to partial saturation of the LIF signal.

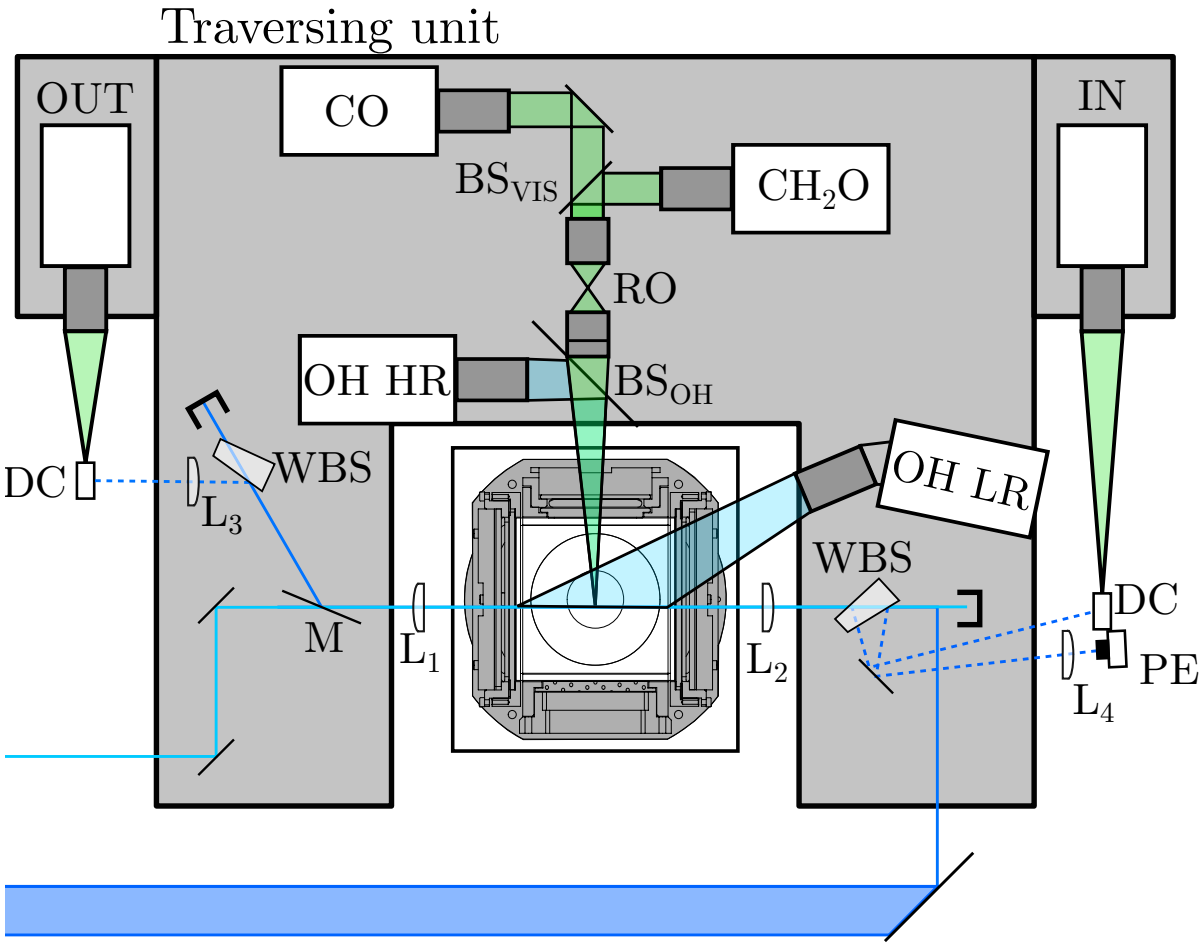

Figure 6.6: Details of optical setup near combustor for combined reaction and heat release rate imaging. DC: Dye cell for energy references. WBS: Wedged beam splitter. BS_{OH}: Beam splitter for separation of OH-PLIF signal from CO-LIF and CH_2O-LIF. BS_{VIS}: Beam splitter for separation of CO and CH_2O signal. RO: Relay optics. PE: Pyroelectric energy meter. L_1: Spherical focusing lens for CO/CH_2O-LIF. L_2: Cylindrical focusing lens for OH-PLIF. L_3: Spherical collimation lens for energy reference after test section. L_4: Cylindrical focusing lens for partial reflection of incident light sheet. M: Mirror to extract OH laser light sheet at exiting side.

combustor onto the exiting side reference dye cell which greatly minimizes beam steering effects caused by variations in refractive index due to temperature gradients in the test section.

Detection systems Coumarin fluorescence for energy reference before and after the test section was detected using two uncooled CCD cameras (Basler, piA2400-17gm) equipped with commercial objective lenses (IN: Nikon Micro-NIKKOR 60 mm 1:2.8G ED,

OUT: Computar V1228-MPY 12 mm C-Mount lens with continuously variable aperture). To improve separation from ambient light, a narrow bandpass filter (532 ± 10 nm) in front of the lenses was used.

The low-resolution detection system for OH (OH LR) consisted of a narrow bandpass filter, transmitting the (1,1) vibrational band between 312 and 320 nm, a 100 mm UV-transmissive lens at f/8 (Sodern, Cerco 2178) and an intensified CMOS camera (LaVision, IRO + M-Lite) in a Scheimpflug arrangement. To capture the entire length of the combustor, as required for the absorption based quantification approach, without significant vignetting from the combustor geometry, a fairly high Scheimpflug angle was required. The lens has an angle of $\approx 20°$ with respect to the horizontal axis.

Detection systems for high-resolution OH (OH HR), CO and CH_2O are mounted above the combustor as close as possible to the top pressure vessel window. Fluorescence from all three species is separated using two imaging beam splitters. BS_{OH} is a high pass filter with an edge wavelength of 350 nm with physical dimension of 120 mm × 80 mm (Laseroptik Garbsen, custom optic) to prevent reduction of the effective aperture of the 150 mm lens at f/2.5 (B. Halle Nachflg. GmbH, OUC 3.60). Despite its significantly worse optical performance compared to the Cerco lens, the Halle lens was selected due to the higher focal length, allowing a larger magnification ratio of 1 : 1.6 onto the photocathode of the intensifier. An additional narrow bandpass filter (not shown in figure) with a transmission range between 312 and 320 nm was mounted directly in front of the lens. The backside of the beam splitter featured an anti-reflective coating with $\leq 1\%$ residual reflection in the wavelength range $350 - 650$ nm to prevent ghosting effects.

To optimize magnification ratio for CO-/CH_2O-LIF detection despite the increasing object distance, a relay imaging system was used. This system consisted of a 250 mm achromatic lens in combination with a 135 mm lens (Canon EF135 f/2.0 L USM) to produce an intermediate image with a magnification ratio of 1 : 1.85. This intermediate image is then imaged onto the photocathodes of the respective image intensifiers using a combination of a 85 mm lens (Canon EF85 f/1.2 L II USM) and two 180 mm lenses (Sigma 180 mm f2.8 EX DG OS) with a magnification of 2.1 : 1, resulting in a total magnification of 1.14 : 1. Spectral separation of LIF signals is achieved by placing a longpass beam splitter (BS_{VIS}; Chroma, T470 LPXR) with an edge wavelength of 470 nm in the collimated beam path between the intensifiers.

6.2.5 Processing

Quantitative OH PLIF Aside omitting the non-linearity correction that was required for phosphorescence measurements, processing of quantitative OH-PLIF follows exactly the routine presented in Sect. 4.2.4.1, thus a redundant explanation is omitted here.

CO-/CH_2O-LIF As processing of CO- and CH_2O-LIF follow essentially an identical procedure, the discussion of the evaluation is combined in this section. In a first step, LIF signals are dewarped and mapped to physical coordinates using a dot-pattern target. This corrects for image distortion and provides an initial guess for the spatial matching of

all involved signals which is described in the following paragraph discussing the derivation of reaction and heat release rates. Subsequently, the images are corrected for shot-to-shot pulse energy fluctuations as obtained from the pyroelectric energy meters. For the case of CO-LIF, a non-linear energy correction was performed based on measurements in the exhaust of the calibration flame as described in Sect. 5. As CH_2O-LIF is a one photon process, a linear correction was used. Residual background from scattered laser radiation and luminosity was extracted in a region adjacent to the signal on a single-shot basis. In a final step, the images are binned in lateral direction to obtain a line measurement which is then cropped in a central region to the Rayleigh length.

Spatial matching of LIF detection systems For the evaluation of [OH][CO] reaction rates (RR) and heat release rate (HRR), it is of great importance to accurately match the spatial positions of the respective LIF measurements prior to interpolation on a common grid to allow pixel-by-pixel multiplication. To avoid cross-talk of the LIF signals of the respective species during actual measurements, the laser pulses are temporally separated. The OH laser pulse arrives at $t = t_0$ at the combustor, while the CO and the CH_2O laser pulses are delayed to arrive at $t = t_0 + 150\,\text{ns}$ and $t = t_0 + 300\,\text{ns}$, respectively. However, for best possible matching of the spatial location, *cross-talk* measurements are conducted, where the intensifier gate used for OH detection was temporally adjusted to record either a portion of the CO- or the CH_2O-LIF signal allowing to match these signals on the pixel grid of the OH camera. To detect the signal, the gain of the intensifier was increased to the maximum value due to the low intensity of the signal which arises from a partial reflection of BS_{OH} transmitted through the narrow bandpass filter for OH detection. Consequently, the SNR of these cross-talk measurements is fairly low, requiring 250 samples for averaging to recover the position of the 1D signals *on the OH HR camera*. This allows to extract a one dimensional OH-LIF signal coincident with the signal of the other species by finding the displacement in beam-wise and lateral direction using a 2D cross-correlation after interpolating the images for CO- and CH_2O-LIF onto the OH HR grid. After matching, RR and HRR are extracted by point-wise-multiplication and subsequent peak-normalization. Fig. 6.7 shows the result of this matching procedure on measurements in the laminar flame.

For measurements in the turbulent flame, this procedure is slightly modified due to the required averaging which prevents accurate matching in beam-wise direction. Only the lateral position of the 1D signal is extracted from the cross-talk measurements and the matching for the beam-wise direction is taken from measurements in the laminar flame acquired on the same measurement day.

6.2.6 Resolution

Fig. 6.8 shows object side MTF measurements as obtained using a Siemens star evaluated with YASSES, see Sect. 2.2.3, for the high resolution OH detection system as well as the systems used for CO- and CH_2O-LIF detection. Evaluation of the low-resolution detection system is omitted as the LR system is only used to provide the local laser intensity for the HR measurements. As verified by repeating the Monte-Carlo simulation described in Sect.

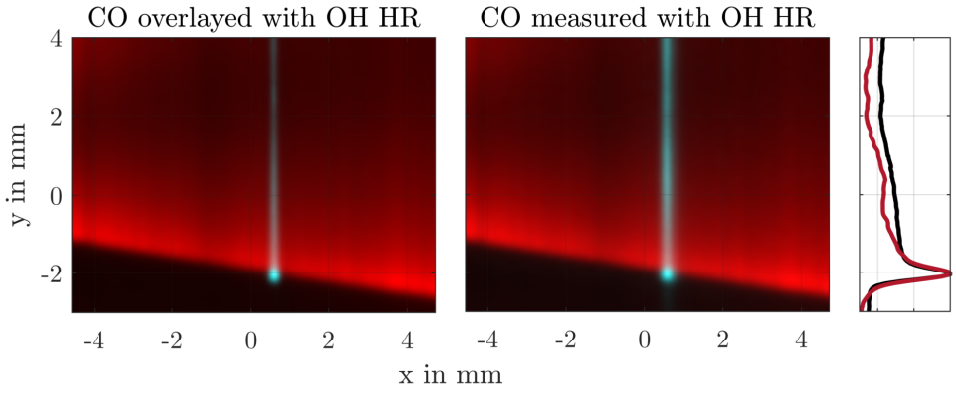

Figure 6.7: Spatial matching of 1D signals with OH HR camera. Example shows result from matching procedure using cross-talk measurements of CO on OH HR camera. Left: CO as *measured with the CO detection system* (cyan) overlayed with OH HR data (red) in comparison to Middle: CO as *measured with the OH HR detection system* (cyan) overlayed with the same OH HR data (red). Plot on the right shows horizontal sum of the CO profiles of both measurements to visualize quality of matching.

4.2.6.1, even a PSF with 2 mm FWHM has no significant influence to the uncertainty. The OH HR detection system has the lowest optical performance with a PSF that is

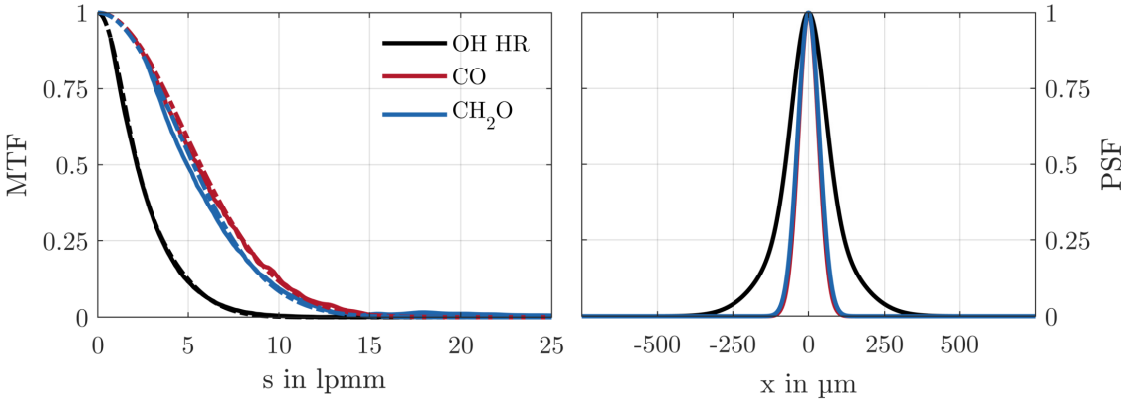

Figure 6.8: MTF and PSF of OH HR (black), CO (red) and CH_2O (blue) detection systems as obtained from Siemens star measurements evaluated using YASSES. Solid lines represent measured values, dashed lines represent fits.

well described by the sum of two Gaussians which have a combined FWHM of 150 µm. However, in comparison to a single Gaussian PSF, the longer tails results in a poorer performance when representing steep gradients. For the CO and CH_2O detection system, optical performance is nearly identical. The PSF is well described using a Gaussian form function with a combined FWHM of 80 µm. The effect of optical resolutions on the measurement of reaction and heat release rates will be discussed in Sect. 6.2.7. Focal line thickness of the OH laser sheet is ≈ 110 µm (FWHM) as measured with a beam profiling camera. The focal diameter for CO and CH_2O is ≤ 60 µm (FWHM) with a Rayleigh length in the order of $4 - 5$ mm.

6.2.7 Uncertainty

Quantitative OH-PLIF Uncertainty for quantitative OH-PLIF measurements is estimated in the same way as described in Sect. 4.2.6.1, accounting for the change in resolution and slightly decreased uncertainty in the absorption measurement. From repetition measurements at the same conditions, the latter corresponds to approximately 8% of the measured value in contrast to the 10% reported for the previous investigation. Fig. 6.9 shows the resulting relative errors ϵ_N and ϵ_T analog to Fig. 4.20. As the resulting

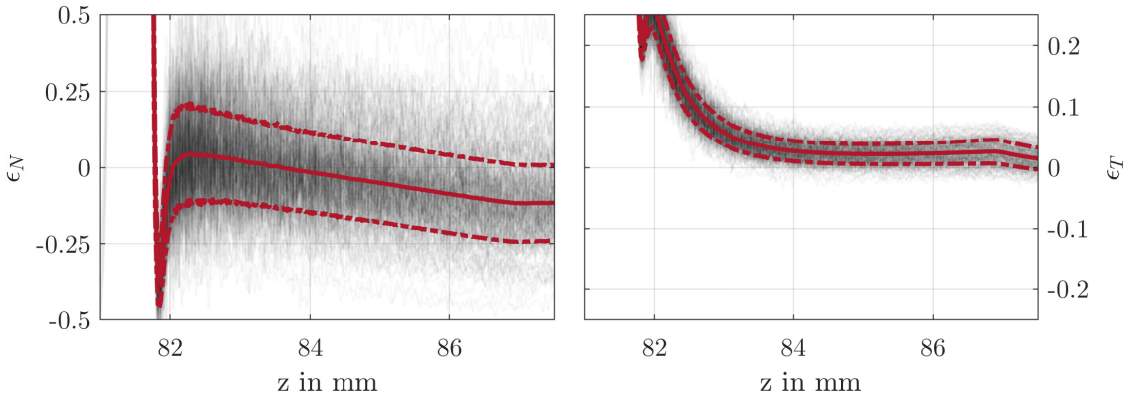

Figure 6.9: Mean (solid red lines) and 2σ range (dashed red lines) of relative errors ϵ_N and ϵ_T of all 10.000 Monte-Carlo iterations over 250 randomly selected realizations (black).

uncertainty is nearly unaffected, the same values as for the previous investigation are reported which are 15% for the accuracy and 20% for the precision of the measurement.

CO-LIF/CH2O-LIF The precision for CO- and CH_2O-LIF measurements is estimated based on the relative standard deviation in laminar flame measurements shown in Fig. 6.10. For these measurements, the laminar flame was operated at 2.5 bar with an equivalence ratio of $\Phi = 1$. For both measurements, the relative standard deviation amounts to $\leq 8\%$, corresponding to a single-shot SNR of ≥ 12.5 defined by the coefficient of variation.

Reaction and Heat Release Rate The proposed method for measuring the reaction and heat release rate relies on accurate representation of gradients as the product of two LIF signal profiles peaks at their intersection. Representation of spatial gradients is affected by the in-plane resolution from the detection systems as well as the out-of-plane resolution which is dominated by the thickness of the sheet for OH and the focal diameter for CO and CH_2O, respectively. Additionally, the magnitude of the gradient that has to be resolved depends on the orientation and curvature of the reaction zone with respect to the measurement axis, both of which are unknown within the combustor. As a first order approximation, the following discussion is limited to *planar reaction zones*, i.e. curvature effects are neglected.

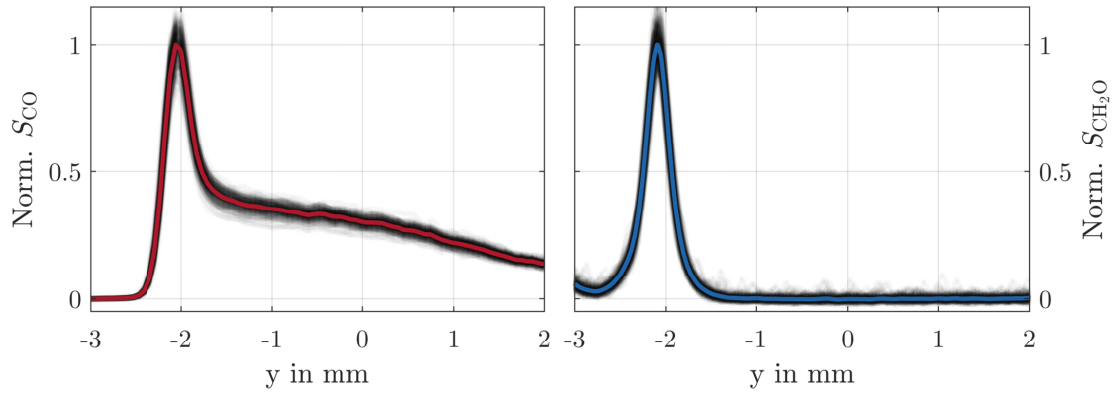

Figure 6.10: Precision of CO- and CH_2O-LIF signals based on measurements in a laminar flame. Shown are the mean profiles after peak normalization in color overlaid on 250 samples in semi-transparent black to indicate variance.

Consider the example shown in Fig. 6.7, where the local reaction zone is rotated *in-plane* by about $\theta = 20°$ with respect to the linear axis of the shown CO measurement. The measurement was conducted with an *out-of-plane angle* of $\phi = 0°$, i.e. the planar reaction zone of the calibration flame is perpendicular to the shown xy-plane. As the laminar flame calculations are - by definition - along the flame front normal, the simulation has to be projected onto the y axis. For the projected laminar flame simulation, LIF signals are simulated and convolved with the optical resolution. Sheet thickness and focal diameter are modeled with a Gaussian form function with the measured FHWM values, scaled with $\sin(\phi)$, i.e. an effect is only visible for reaction zones that are not perpendicular to the xy-plane and consequently show an actual spatial variation of species and/or temperature in the direction of sheet thickness. Fig. 6.11 shows a comparison between simulated LIF signals excluding and including finite resolution effects with measured profiles in a laminar flame. For comparison, the spatial axis of the projected simulation and the experiment have been matched using the peak [OH][CO] reaction rate, i.e. the profiles are not matched individually.

For the case of OH measurements, finite resolution effects cause a shift of the peak towards the high temperature side of the flame and a significant under representation of the gradient. The measured optical performance seems to approximate the actual resolution very well, as the LIF signal simulation including finite resolution closely matches the measured profile. For CO, the impact on the gradient at the rising edge of the profile is not as pronounced as for OH, as (a) the gradient itself has a lower magnitude and (b) the PSF of the detection system is about half as wide. The rising edge of the measured and simulated profiles including finite resolution effects match well, however, there is a notable over estimation at the high temperature side, which is most likely caused by CO_2 photolysis, see Sect. 5.2.6. A significant deviation between measured and simulated LIF signals is observed for CH_2O. This is most likely a result of over estimating the spatial resolution due to extrapolating the MTF to low spatial frequencies, see Sect. 2.2.3.

Fig. 6.12 shows the impact for the given example on the derivation of local reaction and heat release rates. While the derived reaction rate calculated from simulated and

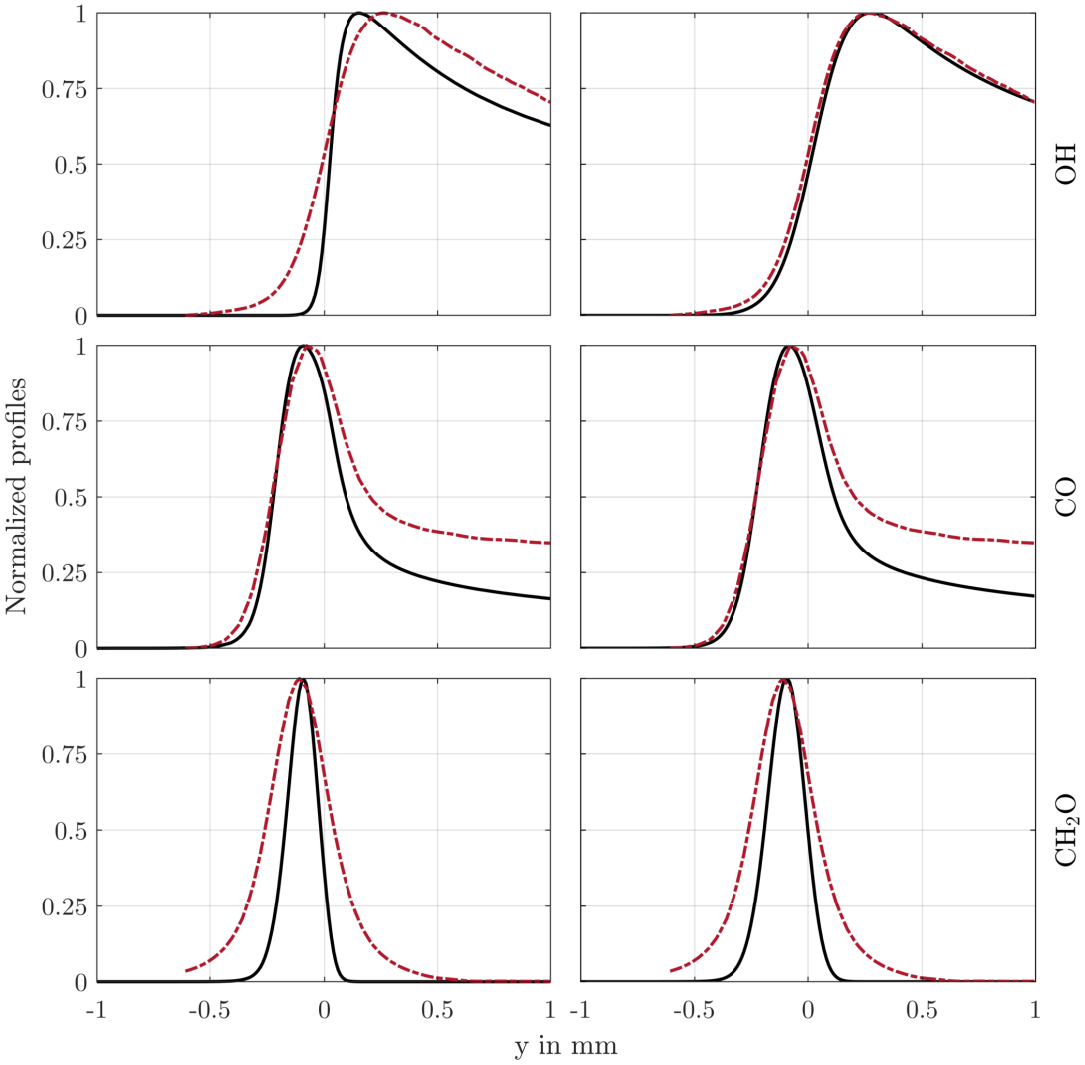

Figure 6.11: Effect of spatial resolution on LIF measurements of OH, CO and CH_2O. Solid lines represent simulated LIF signals excluding (left column) and including finite resolution effects (right column). Dashed red lines correspond to measured profiles in a laminar flame shown in Fig. 6.7.

measured LIF signals match very well on the rising edge, the impact of increased CO signal in the post flame zone due to CO_2 photolysis is evident by increased apparent reaction rates. In general - even without photolysis - correlation with derived reaction rates and the underlying actual reaction rate is severely degraded due to broadening the apparent reaction rate. There is a notable hysteresis, where the rising edge of reaction rates shows an even worse correlation compared to the falling edge due to its steeper gradient. For the heat release rate, experimentally derived heat release rate shows even less sensitivity to the simulated HRR in the laminar flame due to the strong broadening observed for the CH_2O-LIF signal.

Although the LIF simulation does not capture effects such as photolysis and underestimates the width of the measured CH_2O profile, it has the benefit of allowing to derive

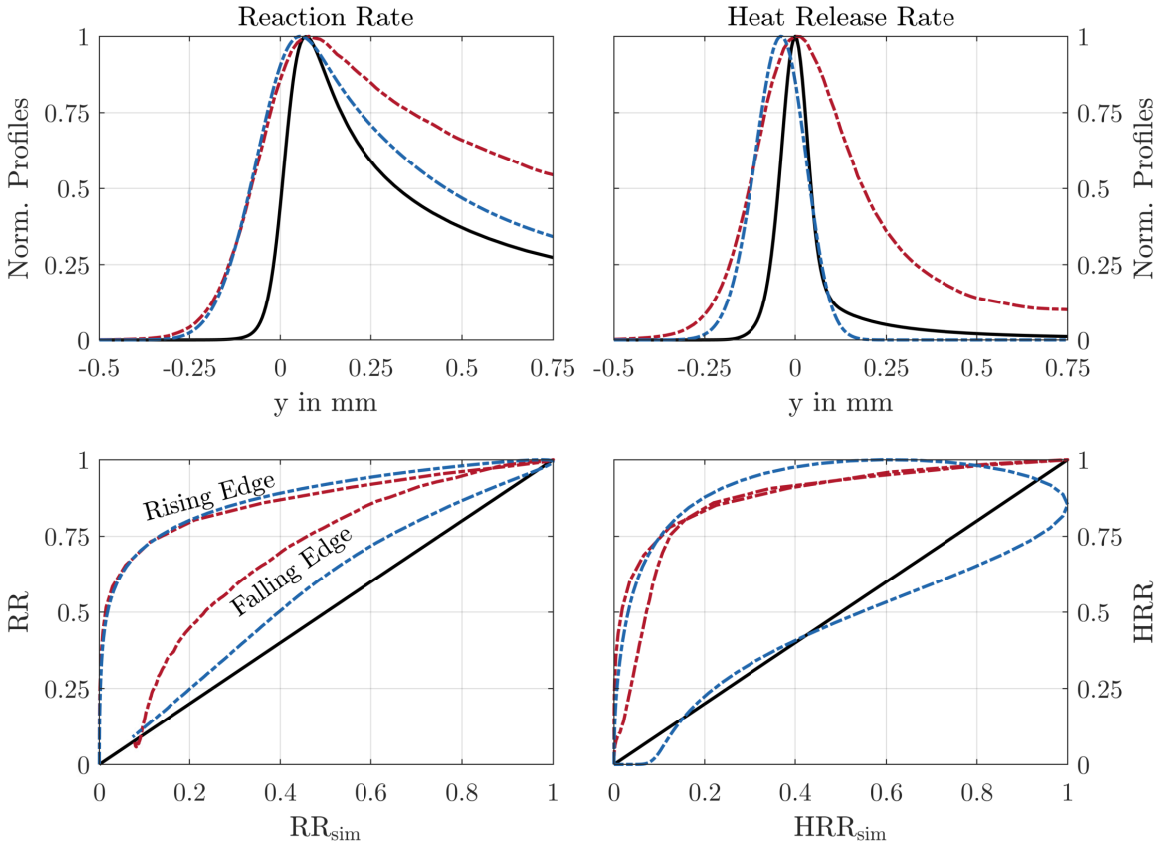

Figure 6.12: Effect of spatial resolution on measured reaction (left column) and heat release rates (right column). Top row: Spatial profiles, bottom row: Correlations of reaction and heat release rates based on LIF signals with actual rates from laminar flame simulation. Black: adiabatic flame simulation, projected on y axis. Blue: Simulated LIF signal including finite resolution effects. Red: Measurement in laminar flame.

the dependency of the flame front orientation as an additional source of uncertainty. Fig. 6.13 shows the angle dependency of the correlation between derived rates based on simulated LIF signals including finite resolution effects and the actual rates from laminar flame calculations. For increasing values of θ, an improved correlation for both reaction and heat release rate is obtained with minor variations observed for different angles ϕ. However, as the instantaneous orientation of the flame front surface cannot be derived from the available data, this has to be considered as an additional uncertainty. For instance, if a measured reaction rate amounts to 0.5, the actual underlying reaction rate might be anything between 0.5 and close to zero. A measured value of 0.75 corresponds to a range of $0.1 - 0.75$. As the location of peak heat release rate is accurately captured, uncertainties decrease again for reaction rates ≥ 0.95. Curvature effects might further aggravate this uncertainty.

Additionally, an uncertainty arises from the peak normalization of measured RR and HRR distributions. For the shown case, the peak is normalized to the peak of the mean profile which resides in the flame front. While this is easy to achieve in an undisturbed laminar

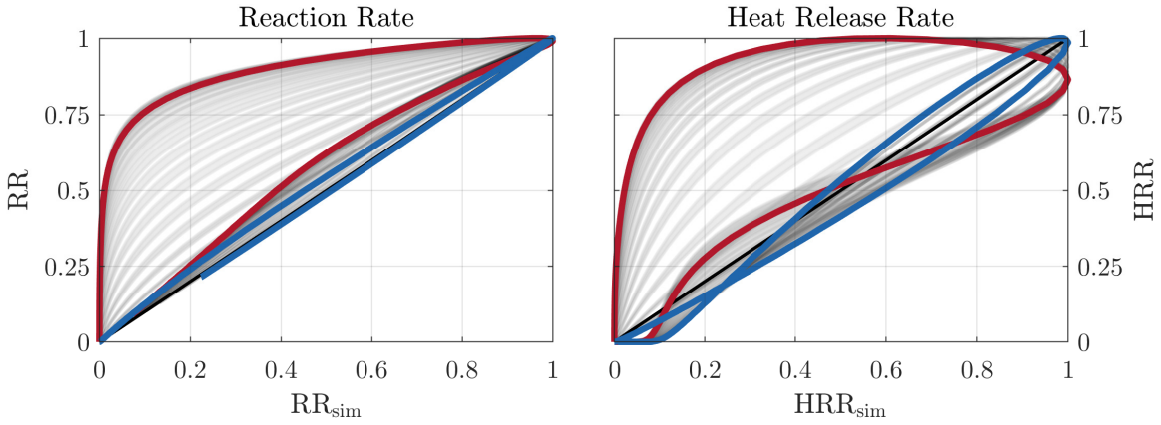

Figure 6.13: Angle dependency of the correlation between derived rates based on simulated LIF signals including finite resolution effects and the actual rates from laminar flame calculations. Shown are simulations in the range from $0° - 85°$ for angles ϕ and θ as semi-transparent black lines. Red and blue lines show the worst ($\phi = 90°, \theta = 0°$) and best case scenario ($\phi = 0°, \theta = 90°$), respectively.

flame, this normalization step is not straightforward for the turbulent case, where it is not guaranteed that an *undisturbed* flame front is observed within a given sample.

6.2.8 Parameter Space and Measurement Locations

Within the combustor, six different fields of view (FOVs) were investigated as shown in Fig. 6.14. One FOV is located in the flame brush at $x = 25\,\text{mm}$ and $z = -25\,\text{mm}$.[22] Measurements in the post-flame zone are conducted at $x = 75\,\text{mm}$ at the center line, i.e. $z = 0\,\text{mm}$. Near the effusion cooled liner, the first two center line holes where investigated with three FOVs each, located 1.5 mm above the effusion cooled liner. The axial locations for these FOVs is chosen based on the standard deviation of the effusion air mole fraction X_e as known from the investigations presented in Sect. 4. The first FOV per hole is located directly upstream of the hole, where no significant influence of the effusion air jet is expected. The threshold for this location is 10% of the peak standard deviation. The second FOV is coincident with the local peak in X_e standard deviation to capture the highest level of intermittency. The third hole is located downstream of the hole, where the X_e standard deviation is again declined to the same value as for the upstream location. As the highest intermittency is expected within the flame brush, 5000 statistically independent samples have been acquired for this FOV. All other FOVs have a sample size of 1000.

Due to potential interference with C_2-LIF for the CO-LIF measurements at partially premixed condition, the investigations presented in this chapter are limited to the swirl and

[22] At the stage of conducting this experiment, the detailed evaluation of the thermochemical state was not yet available. From the findings presented in Chapt. 5, it is known that the OSL exhibits greatly different thermochemical states as the ISL. If this had been known at this stage, another measurement location within the OSL would have been selected.

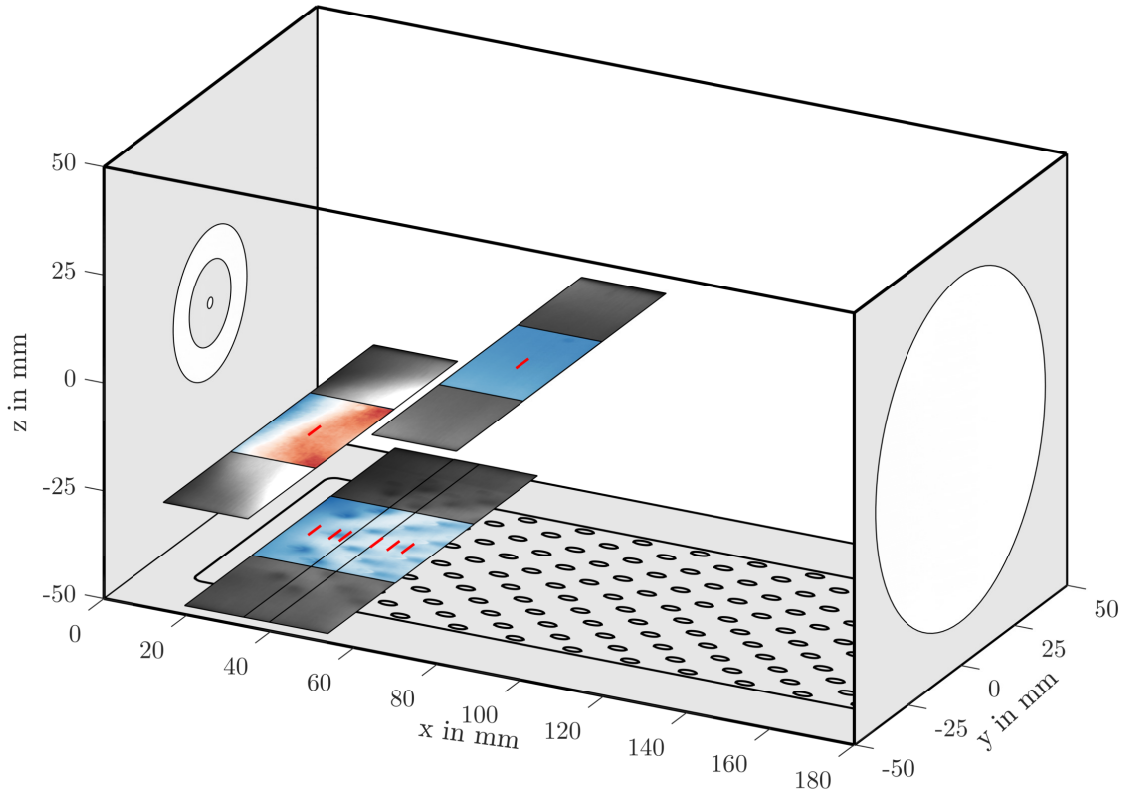

Figure 6.14: Investigated fields of view (FOVs) within the combustor for reaction rate and heat release rate investigation. Red lines indicate location of 1D measurements of CO- and CH_2O-LIF, superimposed on OH HR (color) and OH LR (gray) ensemble averaged data.

effusion cooling air mass flow variation. The suffix -FP in operating condition nomenclature is omitted for improved readability.

6.3 Results

6.3.1 Primary zone

Within this section, results from combined reaction and heat release rate measurements within the FOV at $x = 25\,\text{mm}$ and $z = -25\,\text{mm}$ are presented. For the presentation of results, a normalization of the LIF signals for all species has to be conducted. While this is easy to achieve in a laminar flame, where it may be ensured that the peak signal is (a) always in the field of view and (b) noise may be eliminated by temporal averaging, this is not straightforward in the turbulent environment of the combustor. If one were to normalize the LIF signals simply by dividing by the global maximum, the result is susceptible to outliers. This may be improved by normalizing to the ensemble average

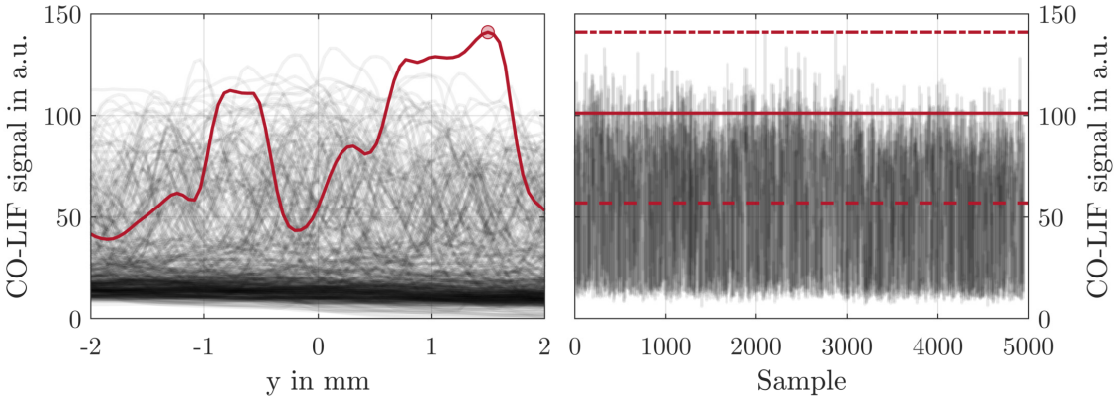

Figure 6.15: Normalization of LIF signals. Left: CO-LIF line measurements in the primary zone at LS-HC condition. Shown are 250 random samples in black along with the profile containing the global maximum. Right: Peak values for all 5000 samples at this condition (black). Horizontal red lines show different levels that may be used for normalization: global maximum (dash-dotted), ensemble mean of peaks (dashed) and the proposed method (solid).

of the peak signal within every measured profile. However, this implicitly assumes that every measured profile shows a peak of an *undisturbed* reaction zone which is most likely to be inaccurate as known from the investigations of mixing processes in Sect. 4 and thermochemical states in Sect. 5, where it has been shown that a notable influence from mixing with effusion cooling air also affects reaction zones in the primary zone. A more reasonable assumption, arising from the fact that within the ISL the CO-T diagram shows values close to the limit of the laminar adiabatic flame, that *some* of the samples show unaffected flame fronts. Thus, within the normalization procedure, the peaks from every species within every measured profile are extracted and the ensemble average mean of the top 90-95% values are selected. The 5% highest samples are disregarded to remove potential outliers from the dataset. The procedure is shown in Fig. 6.15 in comparison to taking the global maximum or the ensemble averaged peak value of all profiles using the example of CO. This normalization approach does not necessarily normalize the signals to unity but it does cancel out most of the noise, enabling a comparison between operating conditions.

Furthermore, it is required to normalize the pixel-by-pixel product to derive reaction and heat release rates. To avoid increasing the ambiguities, this is achieved by normalizing the product to the one obtained in measurements of the laminar flame as shown in Fig. 6.16. For the reaction rate to have a value of 1 at the peak, the obtained pixel-by-pixel

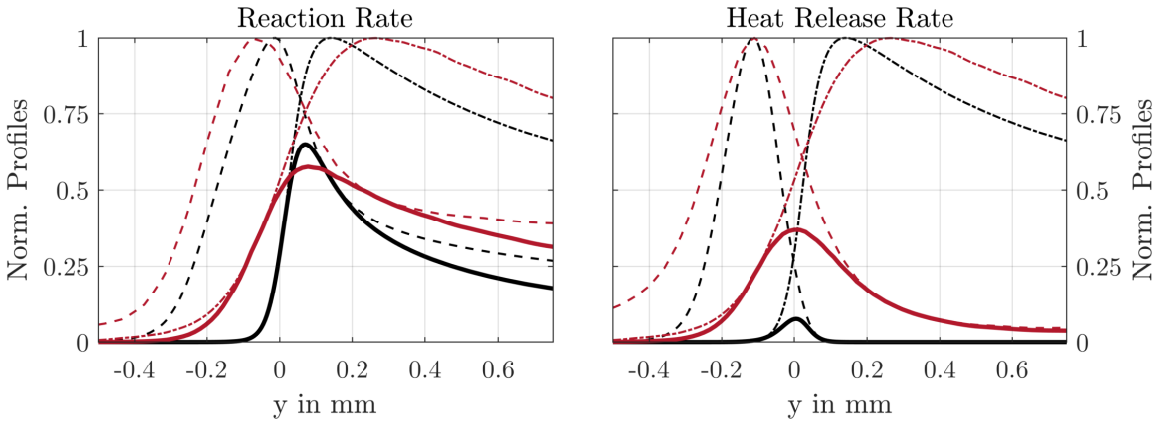

Figure 6.16: Normalization of measured reaction (left) and heat release rates (right). Black lines show LIF simulations and their pixel-by-pixel product excluding finite resolution effects. Red lines show corresponding measurements in the calibration flame as already shown in Fig. 6.11. Dashed: CO-LIF/CH_2O-LIF, dash-dotted: OH-LIF, solid: product of LIF signals.

product of CO-LIF and OH-LIF has to be divided by 0.57. For the heat release rate, the normalization value is 0.37 as obtained from the product of CH_2O- and OH-LIF signals.

For the interpretation of results, it is helpful to reconsider the theoretical limit from an adiabatic laminar flame and effects from limited optical resolution. Fig. 6.17 shows the measured levels of CO and CH_2O over OH from LIF signal predictions of laminar flame simulations and measurements in the laminar flame at the same conditions ($\Phi = 1$, $T_u = 623\,\mathrm{K}$, $p = 2.5\,\mathrm{bar}$). The state-space diagrams of CO over OH and CH_2O over OH show a nearly triangular shape where the production and oxidation phases of CO and CH_2O are identified by the rising edge at low OH and the falling edge towards the OH peak, respectively. Finite resolution effects cause an apparent rotation around the origin and a rounder transition near the edges. Additionally, overestimated CO-LIF signal due to CO_2 photolysis may lead to an increase of apparent CO values during the oxidation phase, depending on the local X_{CO_2}/X_{CO} ratio, see Sect. 5.2.6.

Fig. 6.18 shows a scatter plot of CO over OH, color coded with CH_2O after normalization for all investigated operating conditions. For this visualization, the samples have been sorted by increasing CH_2O signal, emphasizing the CO production branch. Qualitatively, they all exhibit a similar distribution. Just as for measurements of the thermochemical state using combined CARS/CO-LIF measurements presented in Sect. 5, the state space diagram is filled with data points within the limits of the laminar flame. Again, this is not only due to the states being occupied due to mixing and heat loss, but in part also caused by precision of the measurement and limited optical resolution. The normalization procedure yields reasonable results, as the state space is mostly occupied within the limit

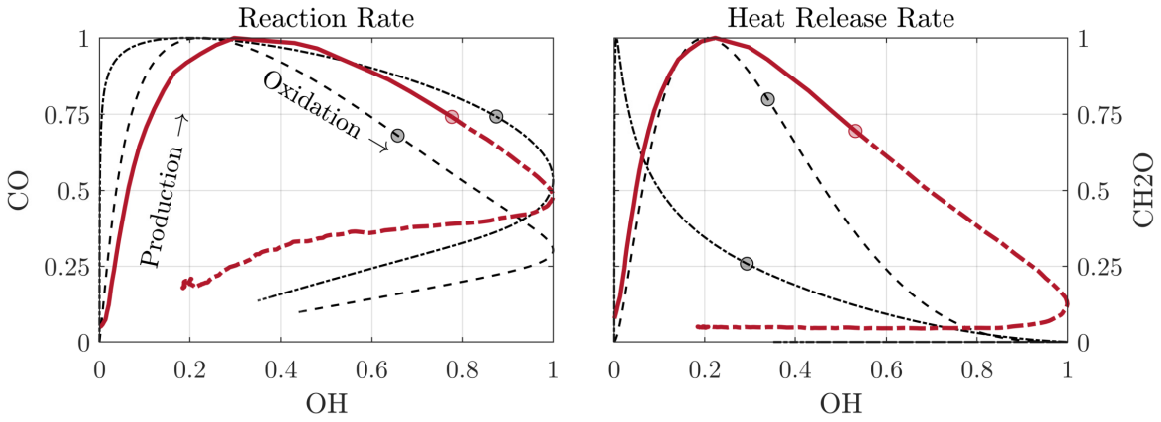

Figure 6.17: Comparison between number densities from laminar flame simulations (black, dash-dotted), corresponding LIF signal prediction accounting for finite resolution effects with $\phi = 25°$, $\theta = 0°$ (black, dashed) and measured profiles in laminar flame (red). Red line split into rising (solid) and falling (dashed) edge of reaction and heat release rate at their respective peaks, shown as circles.

of the expected results from LIF signal predictions with various reaction zone orientations. A first dependence on swirl is already visible in this diagram. For higher swirl, it is less likely to encounter fresh gas as seen in the bottom left edge of the plot, highlighted with a black circle at HS-HC condition. This is caused by the inner shear layer moving out of the measurement area with increasing swirl. Note that the scatter plot gives no indication on the probability to measure a sample in a given region as the point density is very much different which leads to visually overestimate the importance of states which actually are quite rare.

In contrast to the thermochemical state measurements, where no marker for low temperature chemical activity was measured simultaneously, the acquisition of CH_2O-LIF allows a separation into four phases as discussed in the introduction of this chapter and shown in Fig. 6.19. The *unburnt* region is characterized by all LIF signals being below the detection limit. The detection limit for LIF measurements is mainly caused by limited optical resolution of the used image intensifiers, as the long trailing edges of the MTF always cause a positive bias in areas, where no signal is expected. Additionally, the normalization procedure introduces an uncertainty of the threshold that is used to define that region. Empirically, a value of 0.075 for the normalized LIF signals was chosen. The *production* phase of CO, which coincides with the rising edge of the CH_2O-LIF signal, is identified by a combination of CH_2O above the detection limit and simultaneously OH values below ≈ 0.5 for the predicted LIF signals based on laminar adiabatic flame simulations. However, heat loss and mixing effects in the combustor may lead to lower levels of OH which complicates the definition of a hard threshold, as a mere definition using OH ≤ 0.5 would also include samples in the exhaust phase. Instead, the used OH threshold is adaptively chosen depending on the measured levels of CO and CH_2O for measurements in the combustor. The lower limit of the CO production phase is identified by regions with significant low-temperature chemistry and significant CO values, i.e.

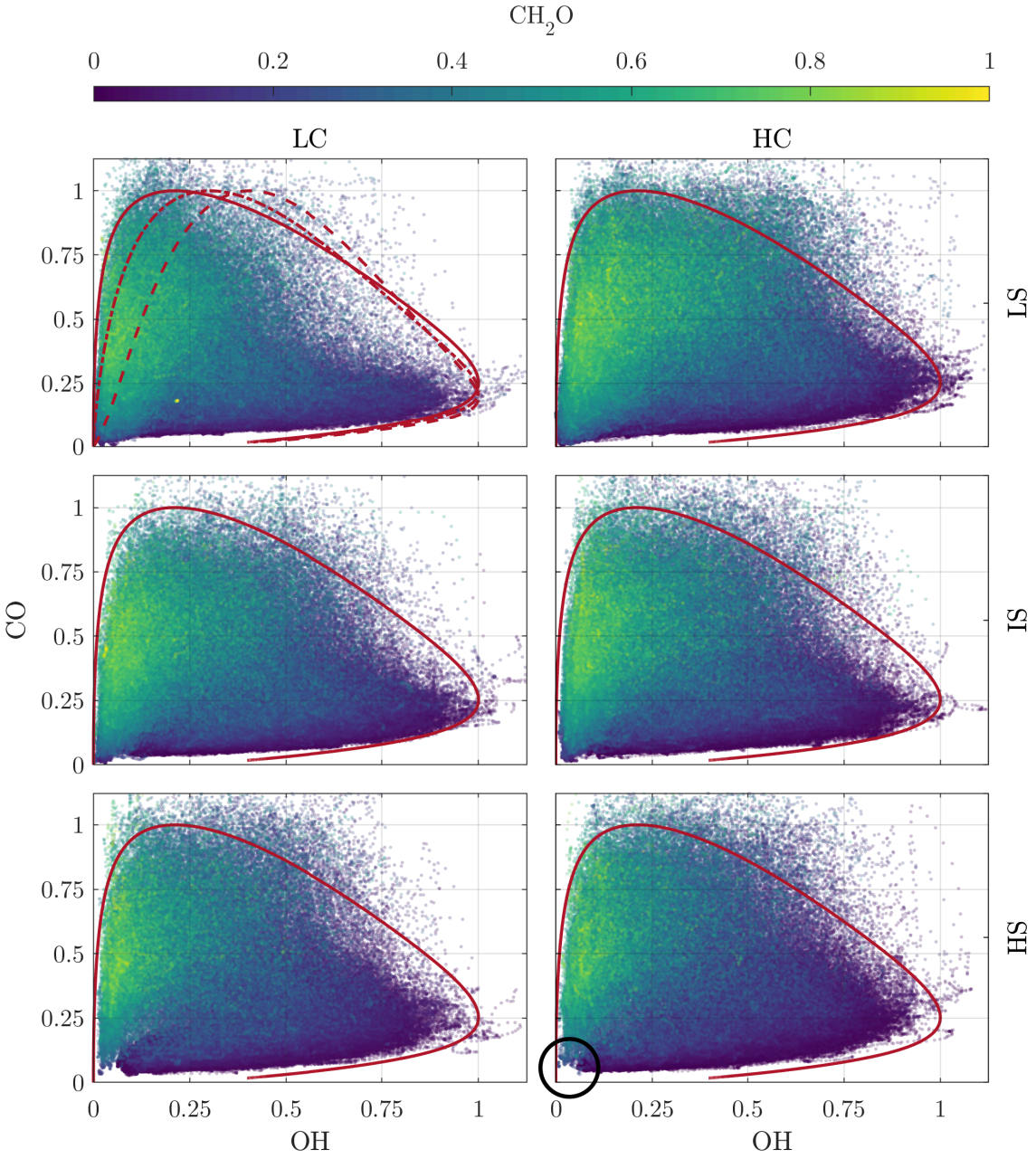

Figure 6.18: Scatter plots of normalized CO-LIF signal over normalized OH-LIF signal with color indicating normalized CH_2O-LIF signal in the primary zone. Per plot, 650.000 samples are shown. Red lines indicate LIF signal predictions including finite resolution effects from laminar adiabatic flame simulations at combustor conditions ($\Phi = 0.75$, $T_u = 623\,\mathrm{K}$, $p = 2.5\,\mathrm{bar}$) with varying orientation of hypothetical planar reaction zones: Solid: $\phi = 60°$, $\theta = 0°$, dash-dotted: $\phi = 45°$, $\theta = 45°$, dashed: $\phi = 0°$, $\theta = 90°$. Circle in bottom left corner at HS-HC condition highlights unburnt region.

CH_2O and CO above the detection limit, and simultaneously low OH levels (OH$\leq$ 0.1). The upper limit of the later production phase is limited by $CH_2O = 0.25$ at OH $\geq$ 0.3. The *exhaust* is characterized by samples with no significant CH_2O signal and OH $\geq$ 0.1.

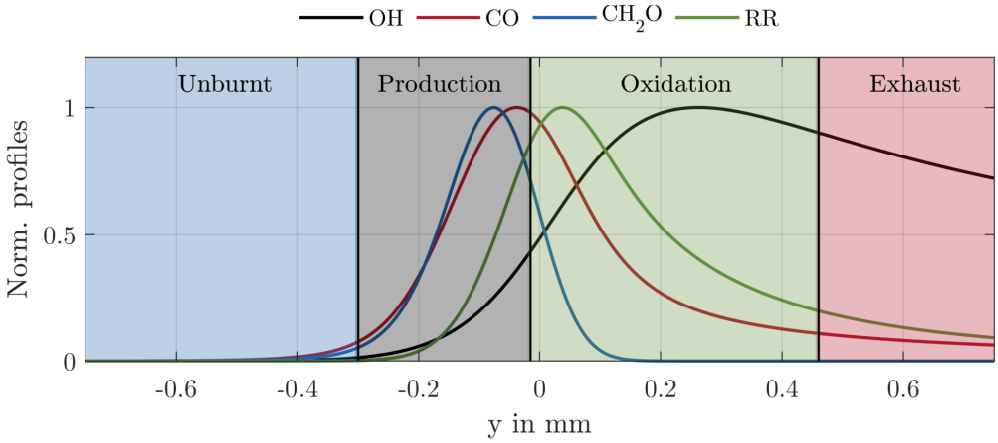

Figure 6.19: Separation into regions of unburnt fresh gas, CO production, CO oxidation and exhaust shown for LIF signal predictions of an adiabatic laminar flame at combustor conditions.

The remaining samples are associated to the *oxidation* branch of CO. Fig. 6.20 shows the result of the separation procedure for the LS-HC operating condition.

Obviously, the separation based on thresholds is susceptible to numerous uncertainties, such as finite resolution effects, orientation of the reaction zone with respect to the measurement axis, noise and residual background. For example the unburnt region has a fairly high leakage into the production phase mainly due to the OH measurements being planar and as such are most susceptible to false light. The separation between the production and oxidation phase using mainly formaldehyde for conditioning seems to include parts of the oxidation phase, where for some reason the apparent chemical activity based on CH_2O is large in areas with high OH values. Identifying the exhaust region, where OH approaches equilibrium and is then further reduced due to heat loss, works reasonably well, with some minor contribution from points that seem to be more likely to belong to the CO oxidation phase, as CO values are above the expected level. However, as mentioned above, when interpreting these scatter plots, which contain 100.000-200.000 data points for the production, oxidation and exhaust region, respectively, rare events are visually exaggerated with respect to their relative occurrence. For this reason, influence of swirl and effusion cooling on reaction and heat release rates is further discussed based on bivariate PDFs in the following.

Effusion air influence To isolate the influence of effusion air independently from swirl, Fig. 6.21 shows bivariate CO-OH-PDFs where the measurements at different swirl levels have been combined for both effusion air mass flow setpoints LC and HC. To ensure that every swirl set point is accounted for with the same statistical weight, the measurements have been equalized by randomly removing samples such that LS, IS and HS measurements effectively have the same sample count within every phase. This strategy has been chosen to increase the number of samples available for the comparison between LC and HC cases, such that the uncertainties from flame front orientation and normalization are reduced.

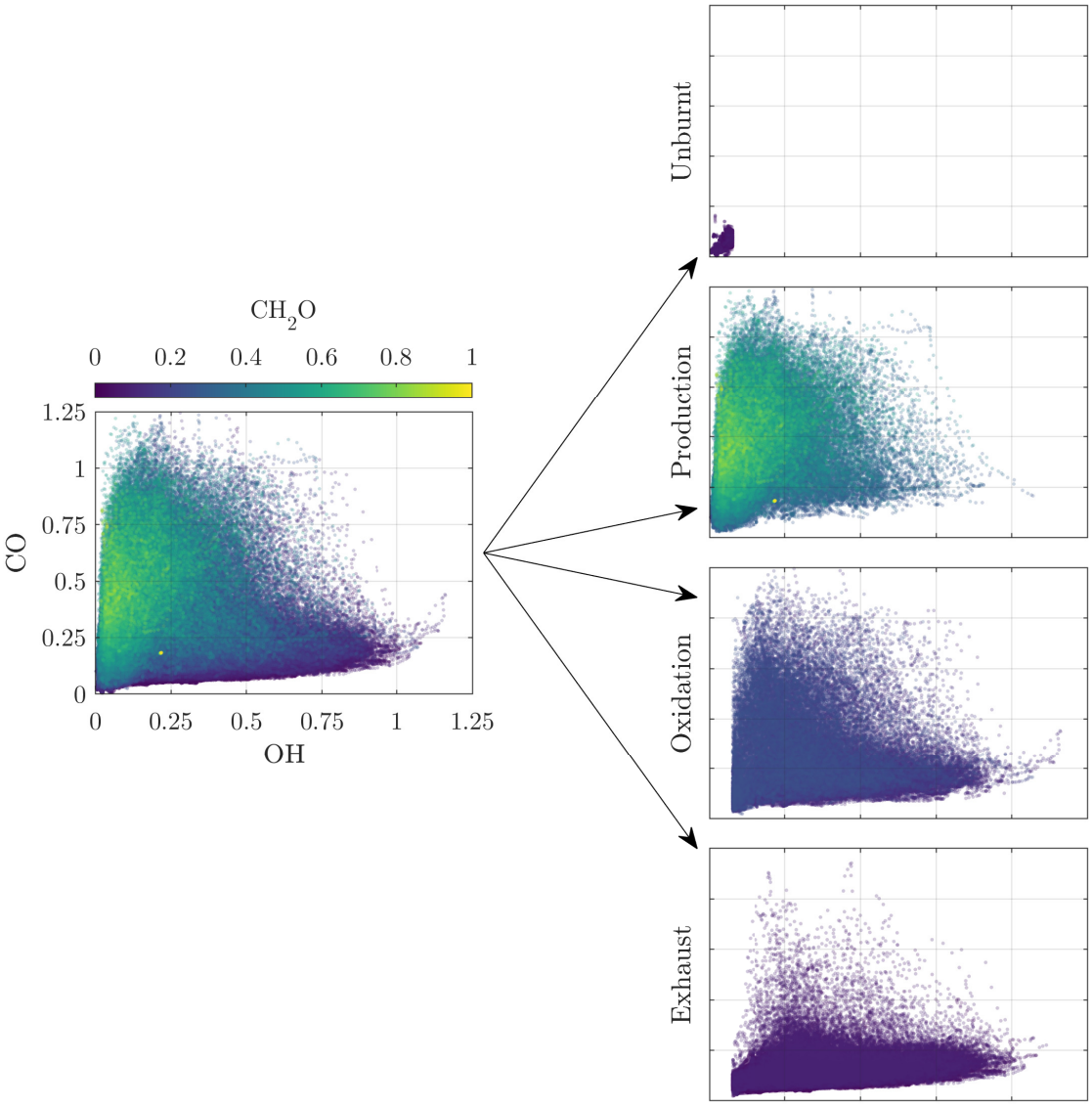

Figure 6.20: Example of data separation into regions (LS-HC).

During the production phase, it is more likely to measure samples with higher CO values at lower OH values for condition HC in comparison to condition LC. To test for statistical significance of this result, a χ^2 test was performed as given in Eq. (6.3) [133]. Here, h_i denotes the absolute number of samples within a specific CO-OH bin i at a given condition LC or HC and $n\hat{\pi}_i$ is the product of the total sample count at the respective condition with the probability to measure a sample in a specific bin for the combined distribution of HC and LC, i.e. this approach tests, if the respective condition deviate *significantly* from the combined distribution regardless of cooling air mass flow.

$$\chi^2 = \sum_i \frac{(h_i - n\hat{\pi}_i)^2}{n\hat{\pi}_i} \tag{6.3}$$

For both conditions, a statistical significance with $\alpha \leq 0.01$ was obtained by comparison to the tabulated values for $\chi^2_{1-\alpha}(k)$, where k is the number of degrees of freedom which is conservatively estimated as the total number of bins.

Even though the observed difference between operating conditions is statistically significant, the interpretation of this observation is somewhat ambiguous as the boundary between the late production phase and the early oxidation phase is not sharply defined. One possible explanation is, as the onset of OH production is very sensitive to temperature, that CO oxidation during late production and early oxidation is hindered due to reduced OH at HC condition, increasing the probability of high CO concentrations to prevail for a *longer duration*. If this is true, it may also explain why during the oxidation phase condition HC shows more samples at high CO and low OH values, indicating that CO oxidation is indeed more complete if less cooling air is supplied. Even though the *mechanism* remains unclear, the presented data conclusively shows that there is a change in the structure of the premixed flame depending on the cooling air condition in an area that is 25 mm away from the wall, which corresponds to ≈ 10 times the penetration depth as derived from NO-PLIF measurements in Sect. 4.

The largest differences are encountered in the exhaust phase, which seems to be dominated by dilution as at HC condition, it is significantly more likely to measure a sample with low OH - which is near its equilibrium effectively a marker for the local temperature - and low CO. This is consistent with the thermochemical state investigations in Sect. 5. Note that the isolines of the forward reaction rate for this PDFs in the exhaust are shown for orientation only. As the thermochemical state approaches equilibrium, the forward and reverse reaction rates start to balance in that area such that there is no net change in CO.

Fig. 6.22 shows bivariate CH_2O-OH-PDFs for the same conditions. As evident from the shown difference in probability, no significant difference is found in regions above the 0.2 isocontour of heat release rate within the uncertainties of the measurement.

Swirl influence In this evaluation, the cooling air mass flows at common swirl set point are combined to isolate the impact of varying swirl number. Fig. 6.23 shows the bivariate CO-OH-PDFs for increasing swirl number and the differences between IS and HS with respect to LS. Within the production phase, it is more likely to measure samples at later stages of CO production. This most likely caused by a change in the flow field, as the increasing expansion of the IRZ causes the ISL to change its location with respect to the measurement axis. This simply makes it less probable to catch the early production phase. Within the uncertainty of the measurement, the oxidation phase is entirely unaffected by a change in swirl. A notable influence is observed in the exhaust, where increased swirl seems to promote a better mixing with effusion air, leading to lowered CO values.

The change in flow pattern is as well visible in the analysis of the swirl dependency of heat release rates shown in Fig. 6.24. With increasing swirl, it is more likely to measure samples in the exhaust, explaining why the PDFs shift towards higher OH and reduced CH_2O values. The region where both have a significant contribution, i.e. the estimated

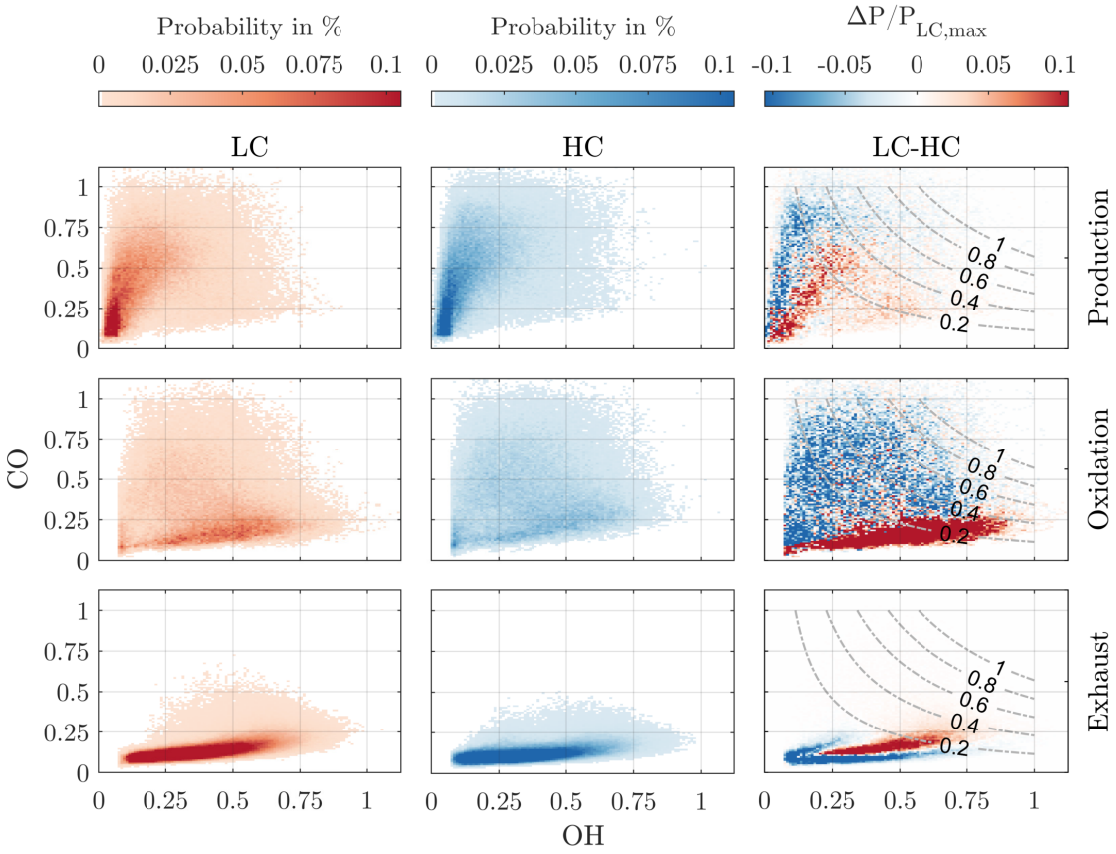

Figure 6.21: Bivariate PDFs of all samples at LC and HC conditions within CO production (top row), CO oxidation (middle row) and exhaust region (bottom row). Right column shows difference between bivariate PDFs for LC and HC condition together with isocontours of the reaction rate. PDF differences have been normalized to the respective peak probability at LC condition to account for the strong variations in broadness of the underlying PDFs, such that all cases fit on the same colorscale.

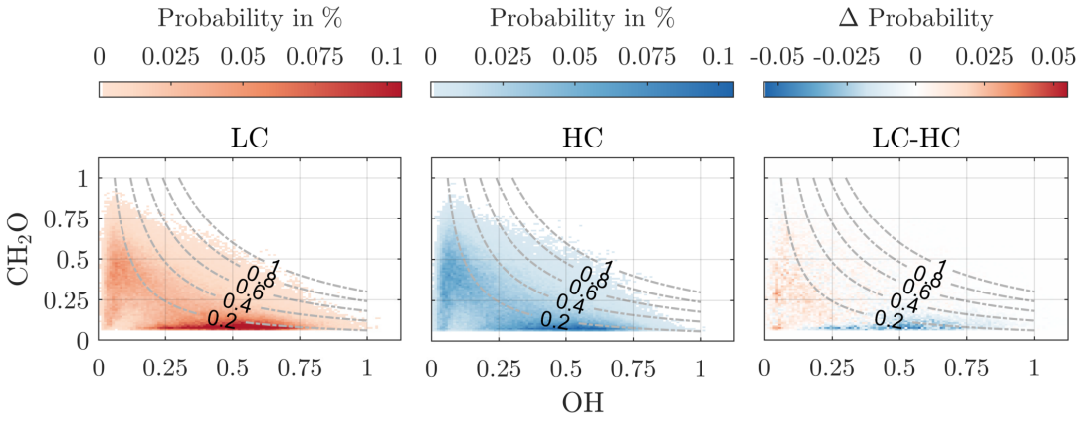

Figure 6.22: Bivariate CH_2O-OH-PDFs of all samples at LC and HC conditions together with isocontours of heat release rate.

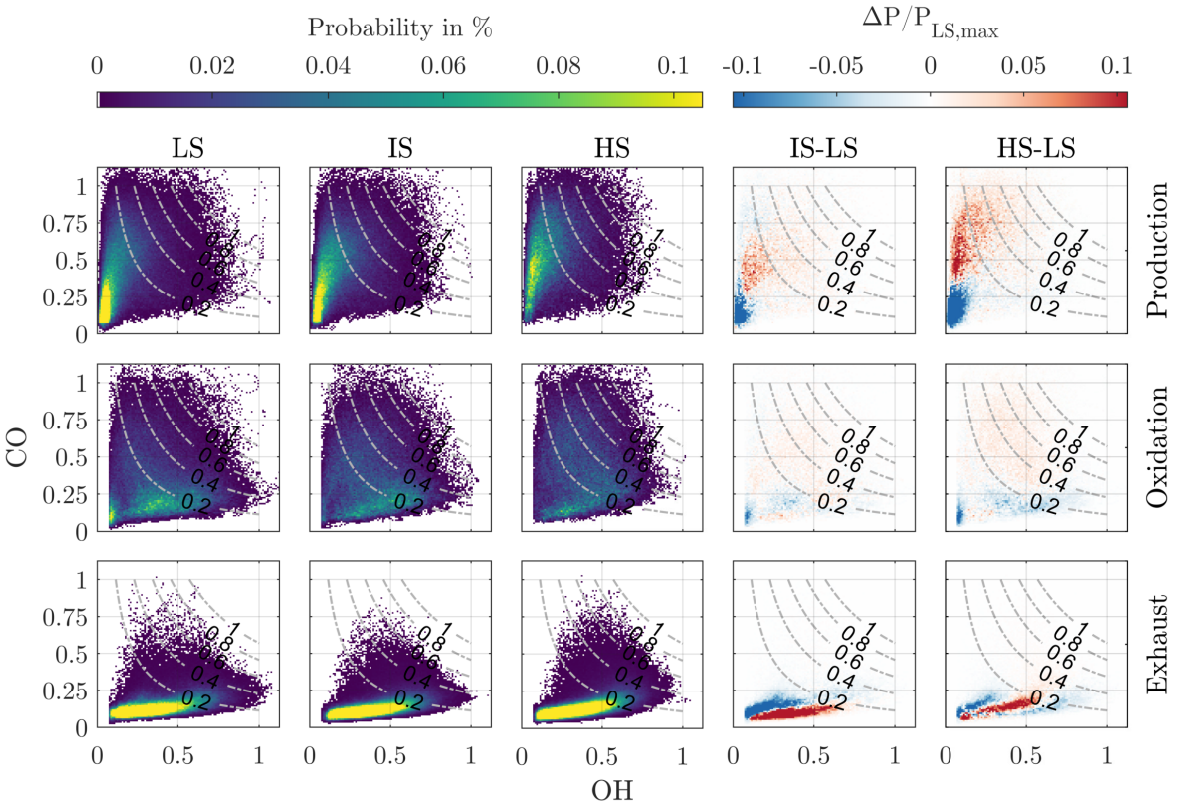

Figure 6.23: Bivariate CO-OH-PDFs of all samples at LS, IS and HS conditions within CO production (top row), CO oxidation (middle row) and exhaust region (bottom row). Differences between conditions are referenced to LS and scaled to the peak probability at LS condition such that all cases fit on the same colorscale.

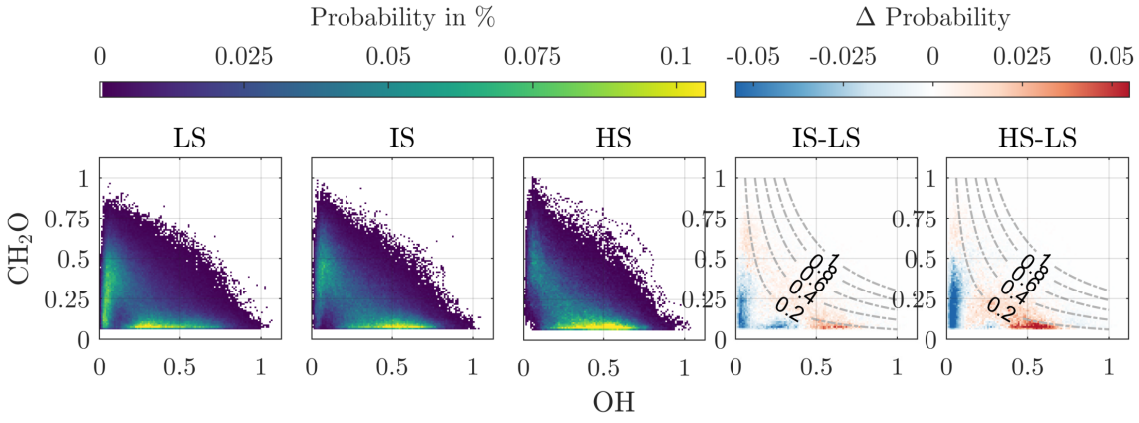

Figure 6.24: Bivariate CH_2O-OH-PDFs of all samples at LS, IS and HS conditions.

heat release is above the 0.2 isocontour, shows no significant difference between different swirl numbers.

6.3.2 Near-wall zone

Within this section, measurements in FOVs near the effusion cooled liner are presented. LIF signals are normalized with the constants derived in the flame brush to ensure that states are mapped to the same scale. This is possible as all measurements have been conducted at the same intensifier gain settings such that it can be assumed that the sensitivity of signal counts with respect to local LIF signal is constant.

A first observation from CH_2O measurements is that there are nearly no events, where low temperature chemistry plays a significant role. This is seen in the histograms of CH_2O-

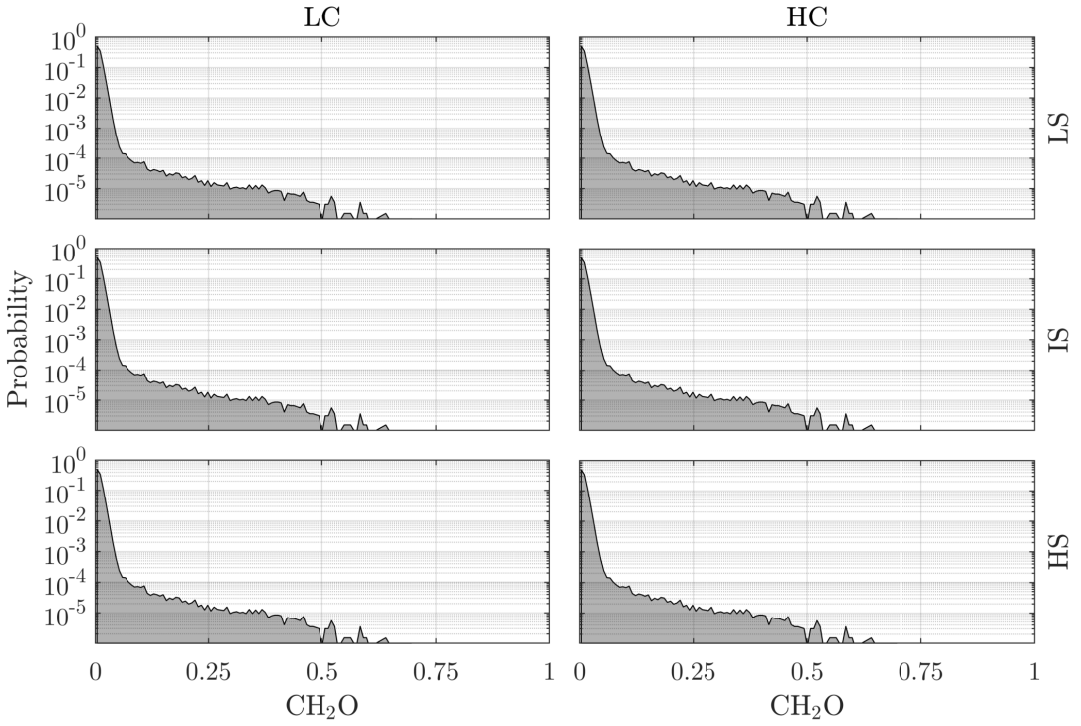

Figure 6.25: Histograms of CH_2O-LIF signal within FOVs near the effusion cooled liner for all operating conditions on a logarithmic scale. Bin width 0.1.

LIF measurements for all operating conditions shown in Fig. 6.25. For these histograms, measurements from all six spatial locations have been included. Measuring a formaldehyde signal ≥ 0.1 has a probability which is in the order of 0.15% for all operating conditions. This effectively means - without requiring knowledge of the other measured quantities - that there is no significant heat release and no significant CO production in this area of the combustor. It is thus expected that all bivariate CO-OH PDFs show only a significant number of samples in the late oxidation and exhaust phase. This is consistent with the thermochemical state measurements shown in Sect. 5. As a consequence, a separation into the phases as conducted for the presentation of results in the primary zone is not executed. Instead, bivariate CO-OH PDFs without any segregation are used to highlight the influence of swirl and effusion cooling air mass flow on the local states. Additionally, as the thermochemical state approaches equilibrium, the measured OH concentration is effectively a marker for the local temperature with a great sensitivity in the region between

$\approx 1400 - 2200\,\mathrm{K}$. For temperatures $\lessapprox 1400 - 1500\,\mathrm{K}$, the OH concentration is below the detection threshold which is dominated by residual background as discussed in Sect. 4.2.6.1. Essentially, this reduces the proposed method to a repetition of measurements of the thermochemical state as represented by CO and temperature, however, without the possibility to quantify the CO mole fraction due to missing calibration and an inferior temperature measurement. However, as the swirl variation was not conducted for the measurements presented in Sect. 5, the presented data may be used to investigate the sensitivity of increased CO mole fraction in the vicinity of the first center line effusion hole at HC condition to swirl.

Fig. 6.26 shows bivariate CO-OH-PDFs at LS-LC and LS-HC condition and the difference between them. These are the operating conditions that were also investigated in Sect. 5. As evident from the increased probability to measure a higher CO signal at every level of OH at condition HC, the finding that a *higher* effusion air mass flow leads to a *higher* local CO concentration in this area of the combustor is confirmed.

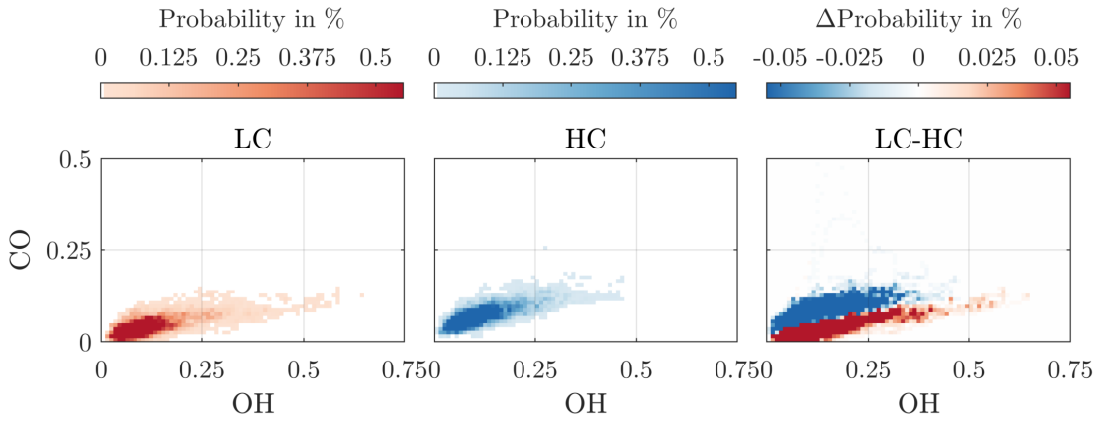

Figure 6.26: Dependency of bivariate CO-OH-PDFs on cooling air mass flow at LS condition.

To investigate the swirl dependency, the difference of the PDFs induced by cooling air is shown in Fig. 6.27 for all investigated swirl set points. As the shape and magnitude of observed differences is mostly insensitive to changes in swirl number, it can be concluded that this effect occurs at every investigated operating condition.

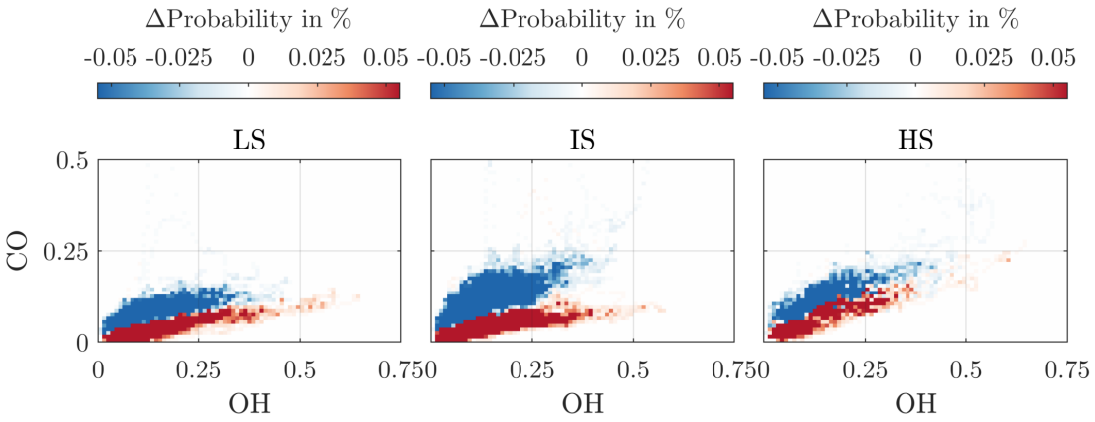

Figure 6.27: Dependency of the LC-HC difference in bivariate CO-OH-PDFs on swirl condition.

6.4 Summary

Within this investigation, local [CO][OH] reaction rates and heat release rates were measured by means of combined OH-, CO- and CH_2O-LIF. It was shown that for this application, finite resolution effects add significant uncertainties to the derived reaction rates from pixel-by-pixel products of the underlying LIF signals and the distribution of reaction zone orientations has a strong impact on the correlation between measured and predicted reaction rates in a laminar premixed flame at elevated pressure.

Regardless of the numerous uncertainties, an influence of effusion cooling air mass flow was observed in the primary zone within the oxidation, production and exhaust phase of the CO reaction chain. While in the exhaust phase dilution effects seem to dominate, as a higher effusion cooling air mass flow systematically lowers both measured OH and CO signals, the exhibits during CO production and early oxidation shows an opposite behavior. In these phases, a higher effusion air mass flow leads to a higher probability to measure increased levels of CO at a given level of OH. It is assumed that this is - in part - caused by the strong sensitivity of OH concentrations with respect to temperature in the preheating zone of the flame, slowing down low temperature chemistry which leads to incomplete CO oxidation at later stages of the reaction chain, depending on the reaction progress at which mixing with effusion air occurs. From the strong scatter of data points in CO production, it is assumed that mixing is not a binary event that occurs either *before* or *after* reaction but indeed occurs as well *during* reaction.

In the zone near the effusion cooled liner, no low-temperature chemistry as indicated by significant formaldehyde signal was observed. This allows to conclude, that there is neither significant heat release nor CO production in this area of the combustor and all interactions with effusion cooling air are in the late oxidation and exhaust phase. Effectively, nothing new is to be learned from this investigation, as the absence of low-temperature chemistry reduces the measurement to an inferior version of the measurements on the local thermochemical state presented in Sect. 5. However, the data was used to verify the finding that a higher effusion cooling air mass flow leads to an increase in local

CO concentration in the vicinity of the first center line effusion hole and the conducted swirl study confirmed, that this behavior is persistent across all investigated operating conditions.

Chapter 7

Conclusion and Outlook

7.1 Conclusion

Within this work, extensive experimental investigations in an effusion cooled single sector model gas turbine combustor were conducted using advanced laser diagnostics with parametric variations of important boundary conditions concerning the flow field, fuel supply and effusion cooling. In three measurement campaigns, the influence on mixing processes, thermochemical states and important reaction rates was analyzed, that allow to test the working hypotheses defined in Sect. 1.2, repeated here for convenience:

1. The interaction of effusion cooling air and main flow locally influences the structure of premixed flames across the preheating zone, reaction zone and post-flame zone.
2. Spatially, the interaction is not limited to an area close to the effusion cooled liner, but extends into the primary zone through recirculation.

Consistently, all three measurement campaigns lead to the conclusion that there is indeed an interaction between flame and cooling air in all stages of premixed combustion in the primary zone. In the investigation of mixing processes, it was found that effusion air penetrates the lower lobe of the main stage through the outer recirculation zone, diluting the fresh gas in this area which in turn leads to a reduction in reaction zone and post-flame OH concentrations, causing a strong asymmetry of the OH distribution with respect to the center line. This is supported by findings from reaction rate measurements, where a significant impact on CO production within the inner shear layer (ISL) was observed in areas where low-temperature chemistry is dominant. In these areas, a higher effusion air mass flow leads to a higher probability to measure higher CO concentrations at simultaneously reduced levels of OH. Furthermore, measurements of the thermochemical state, represented by local CO mole fraction and temperature, revealed major differences between reaction zones in the inner and outer shear layer (OSL), where CO mole fractions are significantly lowered within the OSL. Within the inner recirculation zone (IRZ), a trend to lowered CO mole fractions with increasing effusion air mass flow was observed, which suggests that parts of the effusion air are entraining the IRZ and are thus convected upstream.

Spatially, the interaction processes vary quite strongly, as for the given geometry and operating conditions, the reaction progress close to the wall is near to chemical equilibrium as shown by CH_2O-LIF measurements, where nearly no events were observed that show

significant low-temperature chemistry. Thermochemical state measurements in this area showed an axial dependence of the observed phenomena, where CO mole fractions were increased for a *higher* effusion cooling air mass flow in areas close to the outer recirculation zone due to chemical quenching of the late oxidation phase of CO. This conclusion is further supported by the investigations of reaction rates which additionally showed that this is mostly independent of the swirl condition. For the region where the flame impinges on the wall, CO mole fractions where found to be independent of the cooling air mass flow. This is most likely due to mixing of post-flame CO mole fractions from the ISL, where the CO mole fraction is systematically lower at HC condition, with the flow upstream where the opposite is true due to chemical quenching. Further downstream, the thermochemical state is dominated by dilution, where the CO mole fraction is lowered when more effusion cooling air is supplied. These findings are consistent with observations from the investigations of near wall mixing processes. For the first effusion hole on the center line, a notable influence of effusion cooling air within the unburnt region and reaction zones was found for the low swirl condition. Increasing swirl significantly decreases the penetration depth of the individual effusion air jets, which affects the mixing processes near the effusion cooled liner. For the first effusion hole, the probability to encounter mixing with fresh gas is drastically reduced in favor of mixing with later stages of the reaction where OH is above equilibrium. For locations further downstream, mixing with zones containing sub-equilibrium OH is dominant across all conditions. No significant difference was found for a variation in fuel staging.

Summarizing the presented findings, the following flame-cooling air interaction mechanisms are identified:

1. A fraction of effusion cooling air originating from the first rows penetrates the outer recirculation zone and affects chemical reactions in the primary zone, mainly in the outer shear layer.

2. Effusion air penetrates the inner recirculation zone, most likely after mixing with the exhaust of the lower lobe of the main stage at an axial location after the flame impinges on the wall.

3. A change in swirl causes the inner recirculation zone to expand which in turn reduces the penetration depth of the effusion air jets.

7.1.1 Transferability of Results

In this section, the transferability of the presented findings to a real aero engine gas turbine combustor is discussed. As unscaled measurement data from real engines is unfortunately unavailable due to IPR restrictions, a direct comparison of quantities such as the flow- and temperature fields, is not possible. Instead, a qualitative comparison to measurements conducted at the German Aerospace Center (DLR) in their BOSS rig (Big Optical Single Sector) is made [77,165], [E7]. In these publications, investigations regarding the flow and temperature field in a single sector configuration equipped with a commercial Rolls-Royce Lean Direct Injection (LDI) injector are reported.

Flow and temperature field Fig. 7.1 shows the flow field of the test rig used in this thesis at similar operating conditions [E9] and the flow field of the BOSS rig investigated by Hassa et al. [77], both measured by means of PIV. While Hassa et al. report the velocity magnitude normalized to the peak and the geometry axes normalized to the combustor height, major differences can still be identified. The size of the injector, compared to the

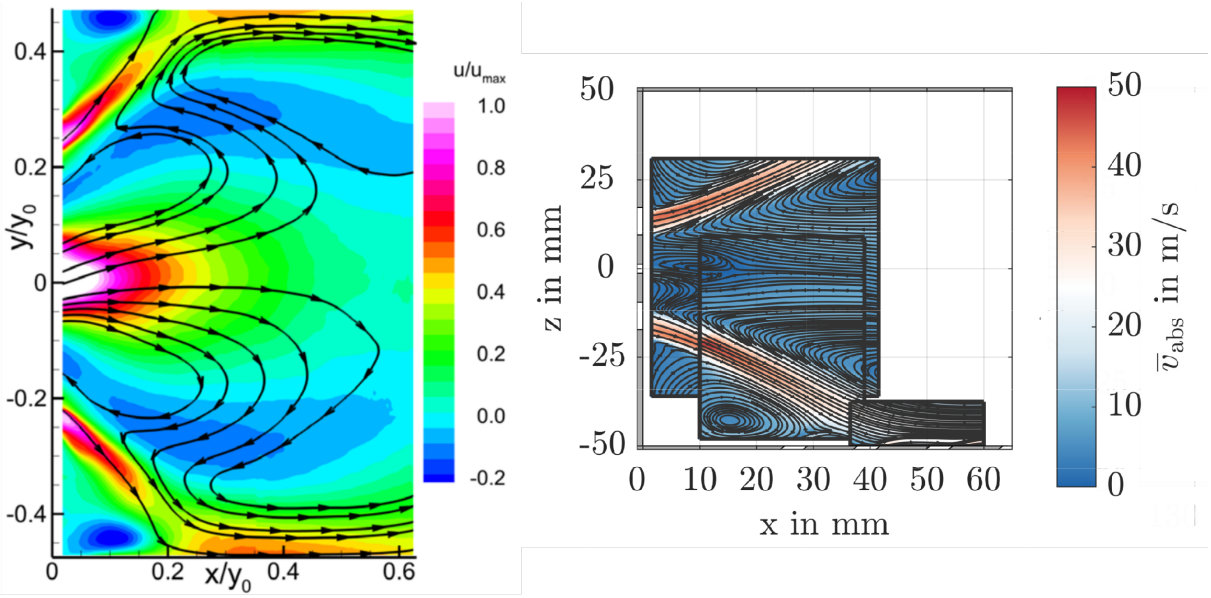

Figure 7.1: Comparison of the flow field of the test rig used in this thesis at similar operating conditions (right, Fig. taken from [E9] with permission from Elsevier.) with measurements in the BOSS rig (left, Fig. taken from *Investigation of the Reacting Flow Field of a Lean Burn Injector With Varying Degree of Swirl at Elevated Pressure Condition* by Christoph Hassa, Ulrich Meier, Johannes Heinze, Eggert Magens, Michael Schroll, I. Bagchi, Paper No: GT2017-64280 [77], with permission from *ASME*).

height of the combustor, is significantly larger. The annulus of the main stage extends from approximately $y/y_0 = 0.2 - 0.3$ in the BOSS rig, while in the present configuration the corresponding range is $z/z_0 = 0.1 - 0.175$. Within the BOSS rig, the lower lobe of the main stage impinges at the wall at significantly lower axial distances ($x/y_0 \approx 0.2$ compared to $x/z_0 \approx 0.4$), consequently, the angle with which the flame approaches the wall is significantly steeper. As the velocity measurements reported by Hassa et al. are normalized, the order of magnitude has to be estimated. In [E7], cross-correlations of OH* chemiluminescence and high-repetition rate temperature measurements in the exhaust revealed an estimate of 4 ms for the residence time within the BOSS rig, which is approximately half of the estimated plug flow transit time of the test rig used in this work as estimated from bulk outlet velocity and the combustor length. The height of the combustors is comparable to within 30%. The ratio between the combustor height and length until the converging section of the BOSS rig is estimated to be ≈ 0.75 from a figure published in [165], which is approximately a factor of 2.4 smaller than for the test rig used in this work. Unfortunately, due to IPR restrictions, the exact size of the combustor may not be published. As the difference in residence times is mostly explained by the shorter combustor length of the BOSS rig, it is assumed that the overall velocity

magnitude is comparable. These considerations lead to the estimation that the *time of flight* of the flow emerging the main stage until it reaches the liner is ≥ 1.5 times shorter within the BOSS rig.

Unfortunately, no unscaled temperature measurements of the temperature field within the primary zone are published for the BOSS rig. However, as measurements at the exhaust section presented in [E7] revealed a comparable temperature level[23], it is assumed that the temperature field is at least comparable to within $100 - 150\,\mathrm{K}$.

Chemical timescales To provide an estimate whether the identified interaction mechanisms within this thesis are relevant to more realistic configurations, the difference in flow time scales has to be put into perspective by additionally considering potential differences in chemical timescales. The possibly most obvious difference between the generic configuration used in this work and a real engine is the significantly lower pressure ratio and the fact that natural gas instead of kerosene is used as a fuel. To estimate the impact of this, a comparison of CO reaction timescales based on laminar flame simulations[24] under various conditions is presented in Fig. 7.2. Kerosene-air flames are simulated using ULF [170] in conjunction with a reaction mechanism for Jet A fuel [161, 168]. For comparison, two pressure levels, associated to two different inlet temperatures calculated by isentropic compression as given in Eq. (7.1) [25], at two representative air-to-fuel ratios (AFR) are shown. In this equation, $\kappa = c_p/c_v$ is the ratio of heat capacities at constant pressure and at constant volume, respectively.

$$\frac{T_2}{T_1} = \frac{p_2}{p_1}^{(1-1/\kappa)} \tag{7.1}$$

For the equivalence ratios, a range of 0.45-0.6, corresponding to an AFR of $\approx 32 - 25$, is considered, which according to Heinze et al. lies within the relevant range for a lean-premixed prevaporized injector [83]. As expected, there is a strong sensitivity of the chemical time scales with respect to the boundary conditions. Depending on the case, which approximates different load cases, chemical time scales may be shorter or longer when comparing the kerosene-air simulations with the simulations at conditions representing the combustor used in this work.

Cooling parameters As discussed in Sect. 2.1.4, the range of blowing, momentum and density ratios is reasonable in comparison to other studies and within the relevant range, which leads to the assumption that the penetration depth and the tendency of the cooling air jets to lift off from the wall is representative. However, with 2 mm, the diameter of the holes is considerably larger than for real effusion geometries with hole diameters in the sub-mm range [104]. This leads to a lower relative pressure loss across the effusion cooling plate and as such may partly explain the strong impact of the swirl on the penetration depth of the effusion air jets and why at the condition with lower effusion cooling air mass flow, the outflow in the area where the flame impinges at the wall is strongly disturbed.

[23] In that publication, temperature is reported in normalized units due to IPR restrictions.
[24] Thanks to Dr. Arne Scholtissek for simulating the kerosene flames.

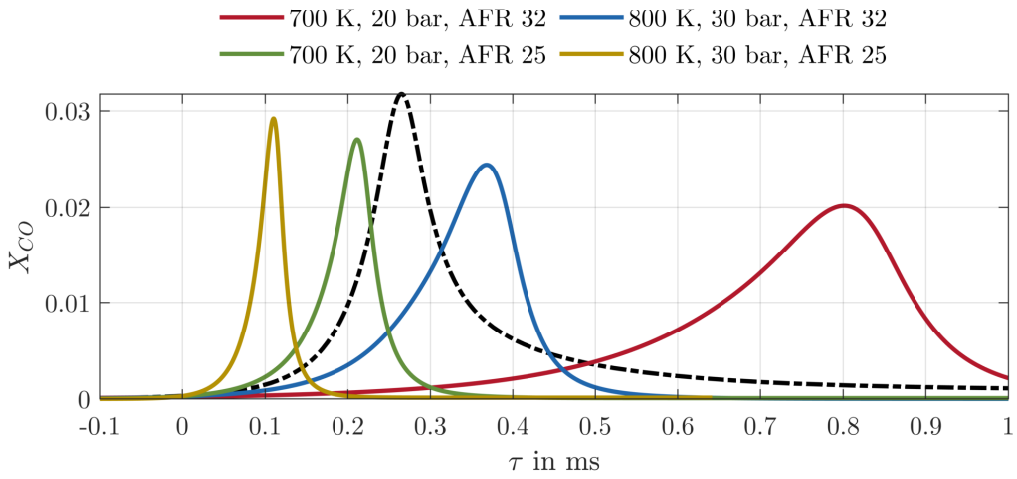

Figure 7.2: CO mole fraction X_{CO} over residence time τ for discussion of chemical timescales. Black dashed line represents laminar flame simulation at conditions of the combustor used in this work ($p = 2.5\,\text{bar}$, $T_u = 623\,\text{K}$, $\Phi = 0.75$, methane). Colored lines show results from kerosene-air flame simulations at various conditions. Stoichiometric AFR is 14.7. $\tau \equiv 0$ at 1% of the peak concentration.

Conclusion Whether the presented findings are of relevance to more realistic configurations is challenging to estimate. A potential interaction such as e.g. the increase in local CO mole fraction at higher effusion cooling air mass flow due to chemical quenching in the vicinity of the liner depends not only on the flow but also on chemical time scales which in turn highly depend on the current operating condition. For the presented comparison, the reacting main stage appears to reach the area of interest significantly faster in the BOSS rig, mainly because the injector used is larger with respect to the combustor height. At which progress of the CO reaction chain the interaction with effusion cooling air is taking place is additionally depending on the current pressure and AFR. Obviously, the flow field also depends on AFR and fuel staging, further increasing uncertainties in the comparison as the AFR at which the flow fields were acquired by Hassa et al. [77] is unknown. It is expected, that the findings presented are relevant for real engine under certain circumstances: It is more likely to encounter an interaction, when chemical time scales are comparably long. This is the case, when the engine is in lower load conditions, i.e. higher AFRs. Additionally, it is more likely to encounter the observed phenomena for conditions, where the majority of the fuel is supplied via the main stage rather than the pilot, as this increases the fuel conversion rate in direct vicinity of the liner.

7.2 Outlook

The current configuration is in its nature very complex and processes are highly coupled. For example, the increase of the inner recirculation zone volume with increasing swirl causes the observed phenomena to shift spatially in addition to potential impact on mixing processes as well as variations of the thermochemical state. Without precise knowledge of the flow field for every operating condition, this influence always causes the ambiguity

in interpretation if the *physics* changed or the same phenomena are merely at a *different location*. Furthermore, heat losses via convection or conduction are not straightforward to separate from mixing with effusion cooling air. For this reason, it would be beneficial to redesign the combustor core to accommodate a simpler flame stabilization mechanism to avoid the recirculation zones, e.g. by stabilizing the flame at a backward-facing step or a ceramic rod. Additionally, the number of holes could be drastically reduced and only placed on the center line to better isolate the interaction mechanisms as the emerging cooling air jets would in this configuration only interact with a single reaction zone.

Further improvement is as well indicated on the diagnostics side. The established method for quantitative OH measurements using combined LIF and absorption measurements could be used as an additional technique to Raman/Rayleigh measurements to improve gradient-free regime identification approach as developed by Hartl et al., where the inclusion of OH leads to improved results of the chemical mode profiles and heat release rate [76]. The developed code base may be used to optimize a scheme to allow investigations also at atmospheric conditions. As the spectral line shape becomes narrower due to decreased collisional broadening, inaccuracies arising from variations in the laser line overlap integral may further increase. The implemented Monte-Carlo simulation to assess these uncertainties may be used to identify transitions which are most insensitive to this effect. Additionally, the model allows to estimate the integral absorption and simulate OH-LIF signals for the given configuration which tremendously aids the design of the experiment.

Measurements of the thermochemical state should be extended by simultaneous probing of CO_2 with CARS in a dual-pump approach. For this, the spectral fitting code has to be extended with a model for CO_2 spectra, e.g. using the approach described by Hall and Stufflebeam [72], which seems to yield accurate results, as it is also successfully used by Cutler et al. [37]. To the best knowledge of the author, this would be the first example of a library based evaluation algorithm for CARS spectra, where the library size scales only *linearly with* - as opposed to *with the power of* - the number of probed species because the mole fraction is *not* tabulated. Aside the obvious benefit that an additional scalar leads to a better understanding of the local thermochemical state, quantitative measurements of the CO_2 mole fraction would allow to drastically improve single-shot uncertainty of CO mole fraction measurements by including a model for photolytic production of CO by dissociation of CO_2. If measurements at higher pressures are to be conducted, the CO-LIF simulation code should be extended to use a Lindholm line shape [106] for the homogeneous line profiles to account for increased asymmetry under low temperature-high pressure conditions [31, 159].

The presented method of combined reaction rate and heat release imaging has proven to be a valuable technique to gain further insight in the CO chemistry by using CH_2O- and OH-LIF signals for conditioning that allow to separate the CO production from the oxidation even under conditions with significant heat loss. However, the uncertainty of the method was shown to be dominated by finite resolution effects which require further optimization of the detection system. It would be beneficial to use a single UV transmissive achromatic collection lens, after which the signals are spectrally separated. This would allow a) to omit the Halle lens which has a tremendously lower optical performance compared to the

Cerco lens and b) the collection optics could be moved much closer to the measurement volume, further increasing magnification and thus improving object-side optical resolution and signal yield due to a larger collection angle.

Appendix A

A.1 Declarations on the contribution to the scientific publications

Declaration on the contribution to the scientific publication

Erklärung zum Eigenanteil der wissenschaftlichen Veröffentlichung

Ph.D. candidate, Max Greifenstein, M.Sc.

M. Greifenstein and A. Dreizler. MARSFT: Efficient Fitting of CARS Spectra Using a Library Based Genetic Algorithm. *Journal of Raman Spectroscopy*, pages 1–9, 2021.

Co-Authors:	Andreas Dreizler, Prof. Dr. habil.
Scientific contribution of the Ph.D. candidate Max Greifenstein:	Implementation of the spectral simulation for nitrogen coherent anti-Stokes Raman spectra based on available literature in a modern programming language (MATLAB). Development of a loss-less compression scheme for library-based fitting using a mixed-integer genetic algorithm for increased computational performance that is independent of the provided starting solution and achieves a higher precision and accuracy compared to a selected benchmark code. The code is published under CC-BY 4.0.
Entire contribution:	Conceptualization and development of the entire code as well as the characterization and benchmark against a widely used traditional fitting code. Writing of the initial manuscript and coordinating the review and publication process.

The publication is not subject of any further ongoing or completed dissertation.

(Max Greifenstein)

(Andreas Dreizler)

Declaration on the contribution to the scientific publication

Erklärung zum Eigenanteil der wissenschaftlichen Veröffentlichung

Ph.D. candidate, Max Greifenstein, M.Sc.

Paper: J. Hermann, **M. Greifenstein**, B. Boehm, and A. Dreizler. Experimental Investigation of Global Combustion Characteristics in an Effusion Cooled Single Sector Model Gas Turbine Combustor. *Flow, Turbulence and Combustion*, 102(4):1025–1052, 2019.

Co-Authors:

Jens Hermann, Dr.-Ing.
Benjamin Böhm, Dr.-Ing.
Andreas Dreizler, Prof. Dr. habil.

Scientific contribution of the Ph.D. candidate Max Greifenstein:

Assisted in the planning and conduction stage of the experiments designed by Dr. Jens Hermann during his time as a PhD candidate.

Development of a 3D-traversable CARS measurement system for application at the pressurized combustor test rig.

Developed processing code for evaluation of Acetone PLIF data to derive the fuel mole fraction from raw data.

Assisted the code development and processing for all other measurement data published.

Writing of the initial manuscript as well as responsibility for correction and revision in the peer review process of the respective journals.

Entire contribution:

Assistance in conducting the experiments, assisted in code development for CARS, PIV and OH-PLIF data, leading role in data analysis for acetone LIF data and manuscript writing.

The work originated from the Ph.D. project of my predecessor Dr. Jens Hermann, who designed and set up the combustor test rig. Refinement of the processing methods, the final data analysis, and paper manuscript were completed during the Ph.D. of Max Greifenstein. The publication itself is not the subject of any further ongoing or completed dissertation, although the content, i.e. the description of the test rig, has in part already been used in the Ph.D. thesis of Dr. Jens Hermann.

(Jens Hermann)

(Max Greifenstein)

(Benjamin Böhm)

(Andreas Dreizler)

Declaration on the contribution to the scientific publication

Erklärung zum Eigenanteil der wissenschaftlichen Veröffentlichung

Ph.D. candidate, Max Greifenstein, M.Sc.

M. Greifenstein and A. Dreizler. Influence of Effusion Cooling Air on the Thermochemical State of Combustion in a Pressurized Model Single Sector Gas Turbine Combustor. *Combustion and Flame*, 226:455–466, Apr. 2021.

M. Greifenstein and A. Dreizler. Investigation of Mixing Processes of Effusion Cooling Air and Main Flow in a Single Sector Model Gas Turbine Combustor at Elevated Pressure. *International Journal of Heat and Fluid Flow*, 88:108768, Apr. 2021.

Co-Authors:	Andreas Dreizler, Prof. Dr. habil.
Scientific contribution of the Ph.D. candidate Max Greifenstein:	Development and/or refinement of the required measurement techniques for application in a pressurized combustor test rig. Application of the refined methods to the combustor test rig. Development of the required code to process and visualize the data. Writing of the initial manuscript as well as responsibility for correction and revision in the peer review process of the respective journals.
Entire contribution:	Planned, designed and conducted all experiments, data analysis and writing of the manuscript.

This declaration refers to both publications as mentioned above because the scientific contribution of the authors to both publications is the same.
The publications are not subject of any further ongoing or completed dissertation.

(Max Greifenstein)

(Andreas Dreizler)

A.2 Permissions

A.2.1 ASME

Permission to reuse **Figure 13** from *Investigation of the Reacting Flow Field of a Lean Burn Injector With Varying Degree of Swirl at Elevated Pressure Condition* by Christoph Hassa, Ulrich Meier, Johannes Heinze, Eggert Magens, Michael Schroll, I. Bagchi, Paper No: GT2017-64280 [77] received via e-Mail on 17 December 2020.

Dear Mr. Greifenstein:

It is our pleasure to grant you permission to use the following
ASME Figures only listed:

> Figure 13 from "Investigation of the Reacting Flow Field
> of a Lean Burn Injector With Varying Degree of Swirl at
> Elevated Pressure Condition," by Christoph Hassa,
> Ulrich Meier, Johannes Heinze, Eggert Magens, Michael Schroll,
> I. Bagchi, Paper No: GT2017-64280
>
> Figure 8 from "Temperature Measurements at the Outlet of a
> Lean Burn Single-Sector Combustor by Laser Optical Methods,"
> by Ulrich Doll, Guido Stockhausen, Johannes Heinze, Ulrich Meier,
> Christoph Hassa, Imon Bagchi, J. Eng. Gas Turbines Power.
> February 2017, 139(2)

cited in your letter for inclusion in a doctoral thesis of
Mechanical Engineering to be published by Technical University of Darmstadt.

As is customary, we request that you ensure full acknowledgment of this
material, the author(s), source and ASME as original publisher.
Acknowledgment must be retained on all pages printed and distributed.

Many thanks for your interest in ASME publications.

Sincerely,

Beth Darchi
Publishing Administrator

ASME
2 Park Avenue
New York, NY 10016-5990
Tel 1.212.591.7700
darchib@asme.org

A.2.2 Copyright Transfer Statement Flow, Turbulence and Combustion

Copyright Transfer Statement for [E9]

Betreff: Copyright Transfer Statement (CTS) for your article in Flow, Turbulence and Combustion (9999)
Von: Springer <springerauthorquery@springeronline.com>
Datum: 29.11.2018, 09:03
An: greifenstein@rsm.tu-darmstadt.de

Springer

Copyright Transfer

29.11.2018

Besuchen Sie uns: springer.com

Copyright Transfer Statement

Lieber Autor, liebe Autorin,

Hinweis: Sie haben dem Copyright Transfer Statement (CTS) zugestimmt und erhalten diese E-Mail für Ihre persönliche Ablage.

1. Publication
The copyright to this article, (including any supplementary information and graphic elements therein (e.g. illustrations, charts, moving images) (the 'Article'), is hereby assigned for good and valuable consideration to Springer Nature B.V. (the 'Assignee'). Headings are for convenience only.

2. Grant of Rights
In consideration of the Assignee evaluating the Article for publication, the Author(s) grant the Assignee without limitation the exclusive (except as set out in clauses 3, 4 and 5 a) iv), assignable and sub-licensable right, unlimited in time and territory, to copy-edit, reproduce, publish, distribute, transmit, make available and store the Article, including abstracts thereof, in all forms of media of expression now known or developed in the future, including pre- and reprints, translations, photographic reproductions and extensions. Furthermore, to enable additional publishing services, such as promotion of the Article, the Author(s) grant the Assignee the right to use the Article (including the use of any graphic elements on a stand-alone basis) in whole or in part in electronic form, such as for display in databases or data networks (e.g. the Internet), or for print or download to stationary or portable devices. This includes interactive and multimedia use as well as posting the Article in full or in part or its abstract on social media, and the right to alter the Article to the extent necessary for such use. The Assignee may also let third parties share the Article in full or in part or its abstract on social media and may in this context sub-license the Article and its abstract to social media users. Author(s) grant to Assignee the right to re-license Article metadata without restriction (including but not limited to author name, title, abstract, citation, references, keywords and any additional information as determined by Assignee).

3. Self-Archiving
Author(s) are permitted to self-archive a pre-print and an author's accepted manuscript version of their Article.

a. A pre-print is the author's version of the Article before peer-review has taken place ("Pre-Print"). Prior to acceptance for publication, Author(s) retain the right to make a Pre-Print of their Article available on any of the following: their own personal, self-maintained website; a legally compliant, non-commercial pre-print server such as but not limited to arXiv and bioRxiv. Once the Article has been published, the Author(s) should update the acknowledgement and provide a link to the definitive version on the publisher's website: "This is a pre-print of an article published in [insert journal title]. The final authenticated version is available online at: https://doi.org/[insert DOI]".
b. An Author's Accepted Manuscript (AAM) is the version accepted for publication in a journal following peer review but prior to copyediting and typesetting that can be made available under the following conditions:
    a. Author(s) retain the right to make an AAM of their Article available on their own personal, self-maintained website immediately on acceptance,
    b. Author(s) retain the right to make an AAM of their Article available for public release on any of the following 12 months after first publication ("Embargo Period"): their employer's internal website; their institutional and/or funder repositories. AAMs may also be deposited in such repositories immediately on acceptance, provided that they are not made publicly available until after the Embargo Period.

An acknowledgement in the following form should be included, together with a link to the published version on the publisher's website: "This is a post-peer-review, pre-copyedit version of an article published in [insert journal title]. The final authenticated version is available online at: http://dx.doi.org/[insert DOI]".

4. Authors' Retained Rights
Author(s) retain the following non-exclusive rights for the published version provided that, when reproducing the Article or extracts from it, the Author(s) acknowledge and reference first publication in the Journal:

a. to reuse graphic elements created by the Author(s) and contained in the Article, in presentations and other works created by them;
b. they and any academic institution where they work at the time may reproduce the Article for the purpose of course teaching (but not for inclusion in course pack material for onward sale by libraries and institutions); and
c. to reproduce, or to allow a third party Assignee to reproduce the Article in whole or in part in any printed volume (book or thesis) written by the Author(s).

5. Warranties
The Author(s) warrant and represent that:

a. (i) the Author(s) are the sole copyright owners or have been authorised by any additional copyright owner(s) to assign the rights defined in clause 2, (ii) the Article does not infringe any intellectual property rights (including without limitation copyright, database rights or trade mark rights) or other third party rights and no licence from or payments to a third party are required to publish the Article, (iii) the Article has not been previously published or licensed, (iv) if the Article contains material from other sources (e.g. illustrations, tables, text quotations), Author(s) have obtained written permissions to the extent necessary from the copyright holder(s), to license to the Assignee the same rights as set out in Clause 2 but on a non-exclusive basis and without the right to use any graphic elements on a stand-alone basis and have cited any such

material correctly;
b. all of the facts contained in the Article are according to the current body of science true and accurate;
c. nothing in the Article is obscene, defamatory, violates any right of privacy or publicity, infringes any other human, personal or other rights of any person or entity or is otherwise unlawful and that informed consent to publish has been obtained for all research participants;
d. nothing in the Article infringes any duty of confidentiality which any of the Author(s) might owe to anyone else or violates any contract, express or implied, of any of the Author(s). All of the institutions in which work recorded in the Article was created or carried out have authorised and approved such research and publication; and
e. the signatory (the Author or the employer) who has signed this agreement has full right, power and authority to enter into this agreement on behalf of all of the Author(s).

6. Cooperation
The Author(s) shall cooperate fully with the Assignee in relation to any legal action that might arise from the publication of the Article, and the Author(s) shall give the Assignee access at reasonable times to any relevant accounts, documents and records within the power or control of the Author(s). The Author(s) agree that the distributing entity is intended to have the benefit of and shall have the right to enforce the terms of this agreement.

7. Author List
After signing, changes of authorship or the order of the authors listed will not be accepted unless formally approved in writing by the Assignee.

8. Edits & Corrections
The Author(s) agree(s) that the Assignee may retract the Article or publish a correction or other notice in relation to the Article if the Assignee considers in its reasonable opinion that such actions are appropriate from a legal, editorial or research integrity perspective.

Diese E-Mail wurde automatisch gesendet; Bitte antworten Sie nicht auf diese Adresse. Falls Sie Fragen haben, besuchen Sie bitte unsere Hilfe-Seiten.

Vielen Dank.

Mit freundlichen Grüßen,

Springer Autorenservice

Details des Artikels

Zeitschrift	Titel des Artikels
Flow, Turbulence and Combustion	Experimental investigation of global combustion characteristics in an effusion cooled single sector model gas turbine combustor
DOI	**Korrespondenzautor**
10.1007/s10494-018-9999-y	Max Greifenstein

Übertragung des Urheberrechts an	Übertragen am
Springer Nature B.V.	Thu Nov 29 09:03:13 CET 2018

Service Contacts

Springer Customer Service Center

Tiergartenstr. 15-17
69121 Heidelberg
Germany
phone: +49 6221 345 0
fax: +49 6221 345 4229
customerservice@springer.com

Springer New York, LCC

233 Spring Street
New York, NY 10013
USA
phone: +1 212 460 1500 or 800-SPRINGER
(Weekdays 8:30am - 5:30pm ET)
fax: +1 212-460-1700
customerservice@springer.com

A.2.3 Copyright Transfer Statement Experiments in Fluids

Copyright Transfer Statement for [E8]

Betreff: Copyright Transfer Statement (CTS) for your article in Experiments in Fluids (2656)
Von: Springer <springerauthorquery@springeronline.com>
Datum: 29.11.2018, 09:04
An: greifenstein@rsm.tu-darmstadt.de

Copyright Transfer

29.11.2018

Besuchen Sie uns: springer.com

Copyright Transfer Statement

Lieber Autor, liebe Autorin,

Hinweis: Sie haben dem Copyright Transfer Statement (CTS) zugestimmt und erhalten diese E-Mail für Ihre persönliche Ablage.

1. Publication
The copyright to this article, (including any supplementary information and graphic elements therein (e.g. illustrations, charts, moving images) (the 'Article'), is hereby assigned for good and valuable consideration to Springer-Verlag GmbH Germany, part of Springer Nature (the 'Assignee'). Headings are for convenience only.

2. Grant of Rights
In consideration of the Assignee evaluating the Article for publication, the Author(s) grant the Assignee without limitation the exclusive (except as set out in clauses 3, 4 and 5 a) iv), assignable and sub-licensable right, unlimited in time and territory, to copy-edit, reproduce, publish, distribute, transmit, make available and store the Article, including abstracts thereof, in all forms of media of expression now known or developed in the future, including pre- and reprints, translations, photographic reproductions and extensions. Furthermore, to enable additional publishing services, such as promotion of the Article, the Author(s) grant the Assignee the right to use the Article (including the use of any graphic elements on a stand-alone basis) in whole or in part in electronic form, such as for display in databases or data networks (e.g. the Internet), or for print or download to stationary or portable devices. This includes interactive and multimedia use as well as posting the Article in full or in part or its abstract on social media, and the right to alter the Article to the extent necessary for such use. The Assignee may also let third parties share the Article in full or in part or its abstract on social media and may in this context sub-license the Article and its abstract to social media users. Author(s) grant to Assignee the right to re-license Article metadata without restriction (including but not limited to author name, title, abstract, citation, references, keywords and any additional information as determined by Assignee).

3. Self-Archiving
Author(s) are permitted to self-archive a pre-print and an author's accepted manuscript version of their Article.

a. A pre-print is the author's version of the Article before peer-review has taken place ("Pre-Print"). Prior to acceptance for publication, Author(s) retain the right to make a Pre-Print of their Article available on any of the following: their own personal, self-maintained website; a legally compliant, non-commercial pre-print server such as but not limited to arXiv and bioRxiv. Once the Article has been published, the Author(s) should update the acknowledgement and provide a link to the definitive version on the publisher's website: "This is a pre-print of an article published in [insert journal title]. The final authenticated version is available online at: https://doi.org/[insert DOI]".
b. An Author's Accepted Manuscript (AAM) is the version accepted for publication in a journal following peer review but prior to copyediting and typesetting that can be made available under the following conditions:
    a. Author(s) retain the right to make an AAM of their Article available on their own personal, self-maintained website immediately on acceptance,
    b. Author(s) retain the right to make an AAM of their Article available for public release on any of the following 12 months after first publication ("Embargo Period"): their employer's internal website; their institutional and/or funder repositories. AAMs may also be deposited in such repositories immediately on acceptance, provided that they are not made publicly available until after the Embargo Period.

An acknowledgement in the following form should be included, together with a link to the published version on the publisher's website: "This is a post-peer-review, pre-copyedit version of an article published in [insert journal title]. The final authenticated version is available online at: http://dx.doi.org/[insert DOI]".

4. Authors' Retained Rights

Author(s) retain the following non-exclusive rights for the published version provided that, when reproducing the Article or extracts from it, the Author(s) acknowledge and reference first publication in the Journal:

a. to reuse graphic elements created by the Author(s) and contained in the Article, in presentations and other works created by them;
b. they and any academic institution where they work at the time may reproduce the Article for the purpose of course teaching (but not for inclusion in course pack material for onward sale by libraries and institutions); and
c. to reproduce, or to allow a third party Assignee to reproduce the Article in whole or in part in any printed volume (book or thesis) written by the Author(s).

5. Warranties

The Author(s) warrant and represent that:

a. (i) the Author(s) are the sole copyright owners or have been authorised by any additional copyright owner(s) to assign the rights defined in clause 2, (ii) the Article does not infringe any intellectual property rights (including without limitation copyright, database rights or trade mark rights) or other third party rights and no licence from or payments to a third party are required to publish the Article, (iii) the Article has not been previously published or licensed, (iv) if the Article contains material from other sources (e.g. illustrations, tables, text quotations), Author(s) have obtained written permissions to the extent necessary from the copyright holder(s), to license to the Assignee the same rights as set out in Clause 2 but on a non-exclusive basis and without the right to use any graphic elements on a stand-alone basis and have cited any such material correctly;
b. all of the facts contained in the Article are according to the current body of science true and accurate;

c. nothing in the Article is obscene, defamatory, violates any right of privacy or publicity, infringes any other human, personal or other rights of any person or entity or is otherwise unlawful and that informed consent to publish has been obtained for all research participants;
d. nothing in the Article infringes any duty of confidentiality which any of the Author(s) might owe to anyone else or violates any contract, express or implied, of any of the Author(s). All of the institutions in which work recorded in the Article was created or carried out have authorised and approved such research and publication; and
e. the signatory (the Author or the employer) who has signed this agreement has full right, power and authority to enter into this agreement on behalf of all of the Author(s).

6. Cooperation
The Author(s) shall cooperate fully with the Assignee in relation to any legal action that might arise from the publication of the Article, and the Author(s) shall give the Assignee access at reasonable times to any relevant accounts, documents and records within the power or control of the Author(s). The Author(s) agree that the distributing entity is intended to have the benefit of and shall have the right to enforce the terms of this agreement.

7. Author List
After signing, changes of authorship or the order of the authors listed will not be accepted unless formally approved in writing by the Assignee.

8. Edits & Corrections
The Author(s) agree(s) that the Assignee may retract the Article or publish a correction or other notice in relation to the Article if the Assignee considers in its reasonable opinion that such actions are appropriate from a legal, editorial or research integrity perspective.

Diese E-Mail wurde automatisch gesendet; Bitte antworten Sie nicht auf diese Adresse. Falls Sie Fragen haben, besuchen Sie bitte unsere Hilfe-Seiten.

Vielen Dank.

Mit freundlichen Grüßen,

Springer Autorenservice

Details des Artikels

Zeitschrift	Titel des Artikels
Experiments in Fluids	Flame-cooling-air-interaction in an effusion cooled model gas turbine combustor at elevated pressure
DOI	**Korrespondenzautor**
10.1007/s00348-018-2656-3	Max Greifenstein
Übertragung des Urheberrechts an	**Übertragen am**
Springer-Verlag GmbH Germany, part of Springer Nature	Thu Nov 29 09:04:15 CET 2018

Service Contacts

Springer Customer Service Center

Tiergartenstr. 15-17
69121 Heidelberg
Germany
phone: +49 6221 345 0
fax: +49 6221 345 4229
customerservice@springer.com

Springer New York, LCC

233 Spring Street
New York, NY 10013
USA
phone: +1 212 460 1500 or 800-SPRINGER
(Weekdays 8:30am - 5:30pm ET)
fax: +1 212-460-1700
customerservice@springer.com

A.2.4 Permission by Elsevier to Reuse Articles for Dissertation

Information extracted from Publishers website: https://www.elsevier.com/about/policies/copyright, Accessed on 18 December 2020. Relevant for reusing content from [E4] and [E5].

Authors can use their articles, in full or in part, for a wide range of scholarly, non-commercial purposes as outlined below:

> Use by an author in the author's classroom teaching
> (including distribution of copies, paper or electronic)
> Distribution of copies (including through e-mail) to
> known research colleagues for their personal use (but not for Commercial Use)
> Inclusion in a thesis or dissertation (provided that
> this is not to be published commercially)
> Use in a subsequent compilation of the author's works
> Extending the Article to book-length form
> Preparation of other derivative works (but not for Commercial Use)
> Otherwise using or re-using portions or excerpts in other works

These rights apply for all Elsevier authors who publish their article as either a subscription article or an open access article. In all cases we require that all Elsevier authors always include a full acknowledgement and, if appropriate, a link to the final published version hosted on Science Direct.

References

[1] Creative Commons Attribution License CC BY 4.0. http://creativecommons.org/licenses/by/4.0/.

[2] Creative Commons Attribution License CC BY-NC-ND 4.0. https://creativecommons.org/licenses/by-nc-nd/4.0/.

[3] Airbus S.A.S. Electric flight - Laying the groundwork for zero-emission aviation. https://www.airbus.com/innovation/zero-emission/electric-flight.html. Accessed 14-12-2020. Online.

[4] Y. M. Al-Abdeli and A. R. Masri. Review of Laboratory Swirl Burners and Experiments for Model Validation. *Experimental Thermal and Fluid Science*, 69:178–196, Dec. 2015.

[5] G. Amantini, J. H. Frank, M. D. Smooke, and A. Gomez. Computational and Experimental Study of Steady Axisymmetric Non-premixed Methane Counterflow Flames. *Combustion Theory and Modelling*, 11(1):47–72, 2007.

[6] C. Amiot, J.-Y. Roncin, and J. Verges. First Observation of the CO $E^1\Pi$ to $B^1\Sigma^+$ and $C^1\Sigma^+$ to $B^1\Sigma^+$ Band Systems. Predissociation in the $E^1\Pi$ (v=0) Level. *Journal of Physics B: Atomic and Molecular Physics*, 19(1):L19, 1986.

[7] A. Andreini, R. Becchi, B. Facchini, L. Mazzei, A. Picchi, and F. Turrini. Adiabatic Effectiveness and Flow Field Measurements in a Realistic Effusion Cooled Lean Burn Combustor. *Journal of Engineering for Gas Turbines and Power*, 138(3):31506, 2016.

[8] A. Andreini, R. Becchi, B. Facchini, A. Picchi, and A. Peschiulli. The Effect of Effusion Holes Inclination Angle on the Adiabatic Film Cooling Effectiveness in a Three-sector Gas Turbine Combustor Rig with a Realistic Swirling Flow. *International Journal of Thermal Sciences*, 121:75–88, Nov. 2017.

[9] A. Andreini, B. Facchini, A. Picchi, L. Tarchi, and F. Turrini. Experimental and Theoretical Investigation of Thermal Effectiveness in Multiperforated Plates for Combustor Liner Effusion Cooling. *Journal of Turbomachinery*, 136(9), Mar. 2014.

[10] G. E. Andrews and M. N. Kim. The Influence of Film Cooling on Emissions for a Low NOx Radial Swirler Gas Turbine Combustor. In *Volume 2: Coal, Biomass and Alternative Fuels; Combustion and Fuels: Oil and Gas Applications; Cycle Innovations*. American Society of Mechanical Engineers, jun 2001.

[11] B. Atakan, J. Heinze, and U. E. Meier. OH Laser-induced Fluorescence at High Pressures: Spectroscopic and Two-dimensional Measurements Exciting the A-X (1,0) Transition. *Applied Physics B: Lasers and Optics*, 64(5):585–591, 1997.

[12] B. O. Ayoola, R. Balachandran, J. H. Frank, E. Mastorakos, and C. F. Kaminski. Spatially Resolved Heat Release Rate Measurements in Turbulent Premixed Flames. *Combustion and Flame*, 144(1):1–16, Jan. 2006.

[13] R. Barlow, G. Fiechtner, C. Carter, and J.-Y. Chen. Experiments on the Scalar Structure of Turbulent $CO/H_2/N_2$ Jet Flames. *Combustion and Flame*, 120(4):549–569, 2000.

[14] T. Behrendt and C. Hassa. A Test Rig for Investigations of Gas Turbine Combustor Cooling Concepts under Realistic Operating Conditions. *Proceedings of the Institution of Mechanical Engineers, Part G: Journal of Aerospace Engineering*, 222(2):169–177, 2008.

[15] W. G. Bessler, C. Schulz, T. Lee, J. B. Jeffries, and R. K. Hanson. Strategies for Laser-induced Fluorescence Detection of Nitric Oxide in High-pressure Flames. I. A-X Excitation. *Applied Optics*, 41(18):3547–3557, 2002.

[16] W. G. Bessler, C. Schulz, V. Sick, and J. W. Daily. A Versatile Modeling Tool for Nitric Oxide LIF Spectra. In *Proceedings of the Third Joint Meeting of the US sections of the Combustion Institute*, volume 3, 2003.

[17] P. J. Bex and W. Makous. Spatial Frequency, Phase, and the Contrast of Natural Images. *JOSA A*, 19(6):1096–1106, June 2002.

[18] S. Böckle, J. Kazenwadel, T. Kunzelmann, D.-I. Shin, and C. Schulz. Single-shot Laser-induced Fluorescence Imaging of Formaldehyde with Xef Excimer Excitation. *Applied Physics B*, 70(5):733–735, 2000.

[19] A. Bohlin and C. Kliewer. Diagnostic Imaging in Flames with Instantaneous Planar Coherent Raman Spectroscopy. *The journal of physical chemistry letters*, 5(7):1243–1248, 2014.

[20] A. Bohlin, B. D. Patterson, and C. J. Kliewer. Communication: Simplified Two-beam Rotational CARS Signal Generation Demonstrated in 1D. 2013.

[21] J. Bouanich and C. Brodbeck. Vibration-rotation Matrix Elements for Diatomic Molecules; Vibration-rotation Interaction Functions Fv' V (m) for CO. *Journal of Quantitative Spectroscopy and Radiative Transfer*, 16(2):153–163, 1976.

[22] C. Brackmann, J. Nygren, X. Bai, Z. Li, H. Bladh, B. Axelsson, I. Denbratt, L. Koopmans, P.-E. Bengtsson, and M. Aldén. Laser-induced Fluorescence of Formaldehyde in Combustion Using Third Harmonic Nd:YAG Laser Excitation. *Spectrochimica Acta, Part A: Molecular and Biomolecular Spectroscopy*, 59(14):3347–3356, Dec. 2003.

[23] C. Brackmann, J. Sjöholm, J. Rosell, M. Richter, J. Bood, and M. Aldén. Picosecond Excitation for Reduction of Photolytic Effects in Two-photon Laser-induced Fluorescence of CO. *Proceedings of the Combustion Institute*, 34(2):3541–3548, Jan. 2013.

[24] J. Brand. 184. the Electronic Spectrum of Formaldehyde. *Journal of the Chemical Society (Resumed)*, pages 858–872, 1956.

[25] W. J. G. Bräunling. *Flugzeugtriebwerke: Grundlagen, Aero-Thermodynamik, ideale und reale Kreisprozesse, thermische Turbomaschinen, Komponenten, Emissionen und Systeme*. VDI-Buch. Springer Vieweg, Berlin, 2015.

[26] A. Buckingham and A. Szabo. Determination of Derivatives of the Polarizability Anisotropy in a Diatomic Molecule from Relative Raman Intensities. *Journal of Raman Spectroscopy*, 7(1):46–48, 1978.

[27] B. Bäuerle, J. Warnat, and F. Behrendt. Time-resolved Investigation of Hot Spots in the End Gas of an S. I. Engine by Means of 2-D Double-pulse LIF of Formaldehyde. *Symposium (International) on Combustion*, 26(2):2619–2626, 1996.

[28] A. Bülter, U. Lenhard, U. Rahmann, K. Kohse-Höinghaus, and A. Brockhinke. Laskin: Efficient Simulation of Spectra Affected by Energy Transfer. In *Laser Applications to Chemical and Environmental Analysis*, page TuE4. Optical Society of America, 2004.

[29] A. Burkert, D. Grebner, D. Müller, W. Triebel, and J. König. Single-shot Imaging of Formaldehyde in Hydrocarbon Flames by XeF Excimer Laser-induced Fluorescence. *Proceedings of the Combustion Institute*, 28(2):1655–1661, Jan. 2000.

[30] S. Candel, D. Durox, T. Schuller, J.-F. Bourgouin, and J. P. Moeck. Dynamics of Swirling Flames. *Annual Review of Fluid Mechanics*, 46(1):147–173, 2014.

[31] O. Carrivain. *Etude de la spectroscopie LIF à deux photons de la molécule CO pour des mesures en flammes à haute pression.* PhD thesis, 2015.

[32] A. Chang, M. DiRosa, and R. Hanson. Temperature Dependence of Collision Broadening and Shift in the NO A← X (0, 0) Band in the Presence of Argon and Nitrogen. *Journal of Quantitative Spectroscopy and Radiative Transfer*, 47(5):375–390, 1992.

[33] D. Clouthier and D. Ramsay. The Spectroscopy of Formaldehyde and Thioformaldehyde. *Annual Review of Physical Chemistry*, 34(1):31–58, 1983.

[34] D. T. Co, T. F. Hanisco, J. G. Anderson, and F. N. Keutsch. Rotationally Resolved Absorption Cross Sections of Formaldehyde in the 28100- 28500 cm^{-1} (351- 356 nm) Spectral Region: Implications for in situ LIF Measurements. *The Journal of Physical Chemistry A*, 109(47):10675–10682, 2005.

[35] F. Comes and E. Fink. Deactivation of CO ($A^1\Pi$) in Individual Vibrational Levels. *Chemical Physics Letters*, 14(4):433–437, 1972.

[36] B. Coriton, M. Zendehdel, S. Ukai, A. Kronenburg, O. T. Stein, S.-K. Im, M. Gamba, and J. H. Frank. Imaging Measurements and LES-CMC Modeling of a Partially-premixed Turbulent Dimethyl Ether/air Jet Flame. *Proceedings of the Combustion Institute*, 35(2):1251–1258, 2015.

[37] A. D. Cutler and G. Magnotti. CARS spectral fitting with multiple resonant species using sparse libraries. *Journal of Raman Spectroscopy*, 42(11):1949–1957, 2011.

[38] M. L. Da Silva and M. Dudeck. Arrays of Radiative Transition Probabilities for CO_2–N_2 Plasmas. *Journal of Quantitative Spectroscopy and Radiative Transfer*, 102(3):348–386, 2006.

[39] K. Dabov, A. Foi, V. Katkovnik, and K. Egiazarian. Image Denoising with Block-matching and 3D Filtering. In *Image Processing: Algorithms and Systems, Neural Networks, and Machine Learning*, volume 6064, page 606414. International Society for Optics and Photonics, 2006.

[40] M. Darecki, C. Edelstenne, T. Enders, E. Fernandez, P. Hartman, J.-P. Herteman, M. Kerkloh, I. King, P. Ky, M. Mathieu, et al. Flightpath 2050 Europe's vision for aviation. *Off. Eur*, 2011.

[41] W. Demtröder. *Laser Spectroscopy: Vol. 2: Experimental Techniques*, volume 2. Springer Science & Business Media, 2008.

[42] W. Demtröder. *Laser Spectroscopy 1: Basic Principles.* Springer, 2014.

[43] Deutsches Zentrum für Luft und Raumfahrt. Weltweiter Luftverkehr steigt in den nächsten 20 Jahren um rund 3.7 Prozent jährlich. https://www.dlr.de/content/de/artikel/news/2019/04/20191216_fast-zehn-milliarden-flugpassagiere-im-jahr-2040.htmlAccessed 14-12-2020. Online, Dec. 2019.

[44] M. Di Rosa and R. Farrow. Cross Sections of Photoionization and Ac Stark Shift Measured from Doppler-free B← X (0, 0) Excitation Spectra of CO. *JOSA B*, 16(5):861–870, 1999.

[45] M. D. Di Rosa and R. L. Farrow. Two-photon Excitation Cross Section of the B← X (0, 0) Band of CO Measured by Direct Absorption. *JOSA B*, 16(11):1988–1994, 1999.

[46] M. D. Di Rosa and R. L. Farrow. Temperature-dependent Collisional Broadening and Shift of Q-branch Transitions in the B← X (0, 0) Band of CO Perturbed by N_2, CO_2 and CO. *Journal of Quantitative Spectroscopy and Radiative Transfer*, 68(4):363–375, 2001.

[47] F. Di Teodoro and R. Farrow. CO+ $B^2\Sigma+(\nu=0)$ Emission Induced by Laser Excitation of Neutral CO at 230 Nm. *The Journal of Chemical Physics*, 114(8):3421–3428, 2001.

[48] G. Dieke and G. Kistiakowsky. The Structure of the Ultraviolet Absorption Spectrum of Formaldehyde. I. *Physical review*, 45(1):4, 1934.

[49] A. C. Eckbreth. BOXCARS: Crossed-beam phase-matched CARS generation in gases. *Applied Physics Letters*, 32(7):421, 1978.

[50] A. C. Eckbreth. *Laser Diagnostics for Combustion Temperature and Species*, volume 3. CRC Press, 1996.

[51] M. Eidelsberg, J.-Y. Roncin, A. Le Floch, F. Launay, C. Letzelter, and J. Rostas. Reinvestigation of the Vacuum Ultraviolet Spectrum of Co and Isotopic Species: The $B^1\Sigma^+ \leftarrow X^1\Sigma^+$ Transition. *Journal of Molecular Spectroscopy*, 121(2):309–336, 1987.

[52] F. Eitel, J. Pareja, A. Johchi, B. Boehm, D. Geyer, and A. Dreizler. Temporal Evolution of Autoignition of Ethylene and Methane Jets Propagating into a Turbulent Hot Air Co-flow Vitiated with NOx. *Combustion and Flame*, 177:193–206, 2017.

[53] M. Escudier. Vortex Breakdown: Observations and Explanations. *Progress in Aerospace Sciences*, 25(2):189–229, 1988.

[54] D. A. Everest, C. R. Shaddix, and K. C. Smyth. Quantitative Two-photon Laser-induced Fluorescence Imaging of CO in Flickering CH_4/air Diffusion Flames. In *Symposium (International) on Combustion*, volume 26, pages 1161–1162. Elsevier, 1996.

[55] J. Färber, R. Koch, H.-J. Bauer, M. Hase, and W. Krebs. Effects of Pilot Fuel and Liner Cooling on the Flame Structure in a Full Scale Swirl-Stabilized Combustion Setup. *Journal of Engineering for Gas Turbines and Power*, 132(9):91501, 2010.

[56] J. P. Feist, A. L. Heyes, and S. Seefelt. Thermographic Phosphor Thermometry for Film Cooling Studies in Gas Turbine Combustors. *Proceedings of the Institution of Mechanical Engineers, Part A: Journal of Power and Energy*, 217(2):193–200, 2003.

[57] J. H. Frank, S. A. Kaiser, and M. B. Long. Multiscalar Imaging in Partially Premixed Jet Flames with Argon Dilution. *Combustion and Flame*, 143(4):507–523, Dec. 2005.

[58] K. N. Gabet and J. A. Sutton. Narrowband Versus Broadband Excitation for CH_2O PLIF Imaging in Flames Using a Frequency-tripled Nd:YAG Laser. *Experiments in Fluids*, 55(7), July 2014.

[59] L. Gasnot, P. Desgroux, J. Pauwels, and L. Sochet. Detailed analysis of low-pressure premixed flames of CH_4+ O_2+ N_2: A study of prompt-no. *Combustion and flame*, 117(1-2):291–306, 1999.

[60] A. Gierulski, M. Noda, T. Yamamoto, G. Marowsky, and A. Slenczka. Pump-induced Population Changes in Broadband Coherent anti-Stokes Raman Scattering. *Optics letters*, 12(8):608–610, 1987.

[61] I. Glassman. *Combustion*. Academic Press, Amsterdam, 2014.

[62] R. J. Goldstein. Film Cooling. *Advances in Heat Transfer*, 7:321–379, 1971.

[63] D. G. Goodwin, H. K. Moffat, and R. L. Speth. Cantera: An Object-oriented Software Toolkit for Chemical Kinetics, Thermodynamics, and Transport Processes. http://www.cantera.org, 2015. Version 2.1.0.

[64] I. Gordon, L. Rothman, C. Hill, R. Kochanov, Y. Tan, P. Bernath, M. Birk, V. Boudon, A. Campargue, K. Chance, B. Drouin, J.-M. Flaud, R. Gamache, J. Hodges, D. Jacquemart, V. Perevalov, A. Perrin, K. Shine, M.-A. Smith, J. Tennyson, G. Toon, H. Tran, V. Tyuterev, A. Barbe, A. Császár, V. Devi, T. Furtenbacher, J. Harrison, J.-M. Hartmann, A. Jolly, T. Johnson, T. Karman, I. Kleiner, A. Kyuberis, J. Loos, O. Lyulin, S. Massie, S. Mikhailenko, N. Moazzen-Ahmadi, H. Müller, O. Naumenko, A. Nikitin, O. Polyansky, M. Rey, M. Rotger, S. Sharpe, K. Sung, E. Starikova, S. Tashkun, J. V. Auwera, G. Wagner, J. Wilzewski, P. Wcisło, S. Yu, and E. Zak. The HITRAN2016 Molecular Spectroscopic Database. *Journal of Quantitative Spectroscopy and Radiative Transfer*, 203:3–69, Dec. 2017.

[65] M. Gritsch, S. Baldauf, M. Martiny, A. Schulz, and S. Wittig. The Superposition Approach to Local Heat Transfer Coefficients in High Density Ratio Film Cooling Flows. In *ASME 1999 International Gas Turbine and Aeroengine Congress and Exhibition*, page V003T01A048, Monday 7 June 1999.

[66] M. Gritsch, W. Colban, H. Schär, and K. Döbbeling. Effect of Hole Geometry on the Thermal Performance of Fan-shaped Film Cooling Holes. *Journal of Turbomachinery*, 127(4):718, 2005.

[67] Guiness World Records Limited 2020. Fastest electric aircraft over a 3 km course. https://www.guinnessworldrecords.com/world-records/92771-fastest-electric-aircraft. Accessed 14-12-2020. Online, Dec. 2019.

[68] A. K. Gupta, D. G. Lilley, and N. Syred. Swirl Flows. *Tunbridge Wells, Kent, England, Abacus Press, 1984, 488 p.*, 1984.

[69] H. Haessler, H. Bockhorn, C. Pfeifer, and D. Kuhn. Formaldehyde-LIF of Dimethyl Ether during Auto-ignition at Elevated Pressures. *Flow, turbulence and combustion*, 89(2):249–259, 2012.

[70] R. Hall and A. Eckbreth. Coherent anti-Stokes Raman Spectroscopy (CARS): Application to Combustion Diagnostics. *Laser applications*, 5:213–309, 1984.

[71] R. Hall and D. Greenhalgh. Application of the Rotational Diffusion Model to Gaseous N_2 Cars Spectra. *Optics Communications*, 40(6):417–420, 1982.

[72] R. J. Hall and J. H. Stufflebeam. Quantitative CARS Spectroscopy of CO_2 and N_2O. *Applied Optics*, 23(23):4319–4327, Dec. 1984.

[73] R. D. Hancock, F. R. Schauer, R. P. Lucht, and R. L. Farrow. Dual-pump Coherent anti-Stokes Raman Scattering Measurements of Nitrogen and Oxygen in a Laminar Jet Diffusion Flame. *Applied Optics*, 36(15):3217–3226, 1997.

[74] R. K. Hanson, R. M. Spearrin, and C. S. Goldenstein. *Spectroscopy and Optical Diagnostics for Gases*. Springer, 2016.

[75] J. E. Harrington and K. C. Smyth. Laser-induced Fluorescence Measurements of Formaldehyde in a Methane/air Diffusion Flame. *Chemical Physics Letters*, 202(3-4):196–202, Jan. 1993.

[76] S. Hartl, D. Geyer, A. Dreizler, G. Magnotti, R. S. Barlow, and C. Hasse. Regime Identification from Raman/Rayleigh Line Measurements in Partially Premixed Flames. *Combustion and Flame*, 189:126–141, Mar. 2018.

[77] C. Hassa, U. Meier, J. Heinze, E. Magens, M. Schroll, and I. Bagchi. Investigation of the Reacting Flow Field of a Lean Burn Injector With Varying Degree of Swirl at Elevated Pressure Condition. In *ASME Turbo Expo 2017: Turbomachinery Technical Conference and Exposition*, volume 4B: Combustion, Fuels and Emissions, pages GT2017–64280, V04BT04A006, Charlotte, North Carolina, USA, 2017. International Gas Turbine Institute, ASME.

[78] C. Hasse, M. Bollig, N. Peters, and H. A. Dwyer. Quenching of Laminar Iso-octane Flames at Cold Walls. *Combustion and Flame*, 122(1):117–129, July 2000.

[79] J. Haumann, J. Seitzman, and R. Hanson. Two-photon Digital Imaging of CO in Combustion Flows Using Planar Laser-induced Fluorescence. *Optics letters*, 11(12):776–778, 1986.

[80] E. Hecht. *Optics*. Pearson custom library. Pearson Education, Harlow, Essex, 4. ed., paerson new internat. ed. edition, 2014.

[81] C. Heeger. *Flashback Investigations in a Premixed Swirl Burner by High-speed Laser Imaging*. Number 601. VDI Verlag GmbH, 2012.

[82] C. Heeger, R. L. Gordon, M. J. Tummers, T. Sattelmayer, and A. Dreizler. Experimental Analysis of Flashback in Lean Premixed Swirling Flames: Upstream Flame Propagation. *Experiments in Fluids*, 49(4):853–863, Oct. 2010.

[83] J. Heinze, U. Meier, T. Behrendt, C. Willert, K.-P. Geigle, O. Lammel, and R. Lückerath. PLIF Thermometry Based on Measurements of Absolute Concentrations of the OH Radical. *Zeitschrift für Physikalische Chemie*, 225(11-12):1315–1341, 2011.

[84] J. Hermann. *Laseroptische Untersuchung der Flamme-Kühlluft-Interaktion in einer Effusionsgekühlten Brennkammer*. PhD thesis, 2017.

[85] G. Herzberg. *Molecular Spectra and Molecular Structure: Volume 1- Spectra of Diatomic Molecules*. Krieger, Malabar, Fla., repr. ed. w/corrections, 2nd ed. edition, 1989.

[86] Y. Huang and V. Yang. Dynamics and Stability of Lean-premixed Swirl-stabilized Combustion. *Progress in Energy and Combustion Science*, 35(4):293–364, 2009.

[87] Z. Huang, Y.-B. Xiong, Y.-Q. Liu, P.-X. Jiang, and Y.-H. Zhu. Experimental Investigation of Full-coverage Effusion Cooling through Perforated Flat Plates. *Applied Thermal Engineering*, 76:76–85, 2015.

[88] IEEE Spectrum. GE Aviation Electrifies Airplane Engines to Meet Carbon Emission Goals. https://spectrum.ieee.org/the-institute/ieee-member-news/ge-aviation-electrifies-airplane-engines-to-meet-carbon-emission-goals. Accessed 14-12-2020. Online, June 2019.

[89] T. Jackowski, A. Schulz, H.-J. Bauer, M. Gerendás, and T. Behrendt. Effusion Cooled Combustor Liner Tiles With Modern Cooling Concepts: A Comparative Experimental Study. In *ASME Turbo Expo 2016: Turbomachinery Technical Conference and Exposition*, pages V05BT17A007–V05BT17A007. American Society of Mechanical Engineers, 2016.

[90] C. Jainski, M. Rißmann, B. Böhm, J. Janicka, and A. Dreizler. Sidewall Quenching of Atmospheric Laminar Premixed Flames Studied by Laser-based Diagnostics. *Combustion and Flame*, 183:271–282, 2017.

[91] T. James and W. Klemperer. Line Intensities in the Raman Effect of $^1\Sigma$ Diatomic Molecules. *Journal of Chemical Physics*, 31(1):130–134, 1959.

[92] J. Janicka, A. Sadiki, M. Schäfer, and C. Heeger. *Flow and Combustion in Advanced Gas Turbine Combustors*. Springer Netherlands, Oct. 2012.

[93] J. Jonuscheit, A. Thumann, M. Schenk, T. Seeger, and A. Leipertz. Accuracy and Precision of Single-pulse One-dimensional Vibrational Coherent anti-Stokes Raman-scattering Temperature Measurements. *Applied optics*, 36(15):3253–3260, 1997.

[94] R. Judge and D. J. Clouthier. Asyrotwin: A 32-bit Windows Version of Asyrot, a Program for the Analysis of High Resolution Singlet-singlet Band Spectra of Asymmetric Tops. *Computer physics communications*, 135(3):293–311, 2001.

[95] V. U. Kakade, S. J. Thorpe, and M. Gerendás. Effusion-cooling Performance at Gas Turbine Combustor Representative Flow Conditions. In *Volume 4: Heat Transfer, Parts A and B*. American Society of Mechanical Engineers, June 2012.

[96] N. Klarmann, B. T. Zoller, and T. Sattelmayer. Modeling of CO Emissions in Multi-Burner Systems With Fuel Staging. In *Turbo Expo: Power for Land, Sea, and Air*, volume 58615, page V04AT04A049. American Society of Mechanical Engineers, 2019.

[97] H. Kosaka, F. Zentgraf, A. Scholtissek, L. Bischoff, T. Häber, R. Suntz, B. Albert, C. Hasse, and A. Dreizler. Wall Heat Fluxes and CO Formation/Oxidation during Laminar and Turbulent Side-wall Quenching of Methane and DME Flames. *International Journal of Heat and Fluid Flow*, 70:181–192, 2018.

[98] H. Kosaka, F. Zentgraf, A. Scholtissek, C. Hasse, and A. Dreizler. Effect of flame-wall interaction on local heat release of methane and dme combustion in a side-wall quenching geometry. *Flow, Turbulence and Combustion*, pages 1–18, 2019.

[99] M. Koszykowski, L. Rahn, R. Palmer, and M. Coltrin. Theoretical and Experimental Studies of High-resolution Inverse Raman Spectra of Molecular Nitrogen at 1-10 Atm. *Journal of Physical Chemistry*, 91(1):41–46, 1987.

[100] R. Krewinkel. A Review of Gas Turbine Effusion Cooling Studies. *International Journal of Heat and Mass Transfer*, 66:706–722, Nov. 2013.

[101] L. Lange, J. Heinze, M. Schroll, C. Willert, and T. Behrendt. Combination of Planar Laser Optical Measurement Techniques for the Investigation of Pre-mixed Lean Combustion. (223):1–12, July 2012.

[102] P. V. Le Brocq, B. E. Launder, and C. H. Priddin. Discrete Hole Injection as a Means of Transpiration Cooling; an Experimental Study. *ARCHIVE: Proceedings of the Institution of Mechanical Engineers 1847-1982 (vols 1-196)*, 187(1973):149–157, 1973.

[103] A. Le Floch. *Etude Des Couplages Rotationnels Et Spin-orbite Dans L'etat a Singulet Pi De La Molecule CO*. PhD thesis, Paris 11, 1989.

[104] A. H. Lefebvre. *Gas Turbine Combustion*. CRC press, 1998.

[105] B. Leger, P. Miron, and J. Emidio. Geometric and Aero-thermal Influences on Multiholed Plate Temperature: Application on Combustor Wall. *International Journal of Heat and Mass Transfer*, 46(7):1215–1222, 2003.

[106] E. Lindholm. *Pressure Broadening of Spectral Lines*. Almqvist & Wiksells, 1946.

[107] S. Linow, A. Dreizler, J. Janicka, and E. Hassel. Comparison of Two-photon Excitation Schemes for CO Detection in Flames. *Applied Physics B*, 71(5):689–696, 2000.

[108] J. Luque and D. Crosley. LIFBASE: Database and simulation program (v 2.1.1). *SRI International Report MP*, pages 99–009, 1999.

[109] G. Magnotti. *Dual-pump CARS Development and Application to Supersonic Combustion*. PhD thesis, The George Washington University, 2012.

[110] M. Mann, C. Jainski, M. Euler, B. Böhm, and A. Dreizler. Transient Flame–wall Interactions: Experimental Analysis Using Spectroscopic Temperature and CO Concentration Measurements. *Combustion and Flame*, 161(9):2371–2386, 2014.

[111] M. Marrocco. Comparative Analysis of Herman-Wallis Factors for Uses in Coherent anti-Stokes Raman Spectra of Light Molecules. *Journal of Raman Spectroscopy*, 40(7):741–747, 2009.

[112] D. Martin and S. J. Thorpe. Experiments on Combustor Effusion Cooling under Conditions of Very High Free-stream Turbulence. In *Volume 4: Heat Transfer, Parts A and B*. American Society of Mechanical Engineers, June 2012.

[113] M. Martiny. *Wärmeübergang in Effusionsgekühlten Flammrohrwänden: Univ., Diss.–karlsruhe, 1998*, volume 6 of *Forschungsberichte aus dem Institut für Thermische Strömungsmaschinen*. Cuvillier, Göttingen, 1. aufl. edition, 1999.

[114] W. Meier, R. S. Barlow, Y.-L. Chen, and J.-Y. Chen. Raman/Rayleigh/LIF Measurements in a Turbulent $CH_4/H_2/N_2$ Jet Diffusion Flame: Experimental Techniques and Turbulence–Chemistry Interaction. *Combustion and Flame*, 123(3):326–343, 2000.

[115] D. Meschede. *Gerthsen Physik*. Springer-Verlag, 2015.

[116] D. E. Metzger, D. I. Takeuchi, and P. A. Kuenstler. Effectiveness and Heat Transfer with Full-coverage Film Cooling. *Journal of Engineering for Power*, 95(3):180, 1973.

[117] D. Moule and A. Walsh. Ultraviolet Spectra and Excited States of Formaldehyde. *Chemical Reviews*, 75(1):67–84, 1975.

[118] A. P. Nefedov, V. A. Sinel'shchikov, A. D. Usachev, and A. V. Zobnin. Photochemical Effect in Two-photon Laser-induced Fluorescence Detection of Carbon Monoxide in Hydrocarbon Flames. *Applied optics*, 37(33):7729–7736, 1998.

[119] S. O'Byrne, P. M. Danehy, A. D. Cutler, and S. Tedder. Dual-pump Coherent anti-Stokes Raman Scattering Measurements in a Supersonic Combustor. *AIAA journal*, 45(4):922–933, 2007.

[120] R. E. Palmer. The CARSFT Computer Code Calculating Coherent anti-Stokes Raman Spectra: User and Programmer Information. 1989.

[121] P. Paul. Calculation of Transition Frequencies and Rotational Line Strengths in the γ-bands of Nitric Oxide. *Journal of Quantitative Spectroscopy and Radiative Transfer*, 57(5):581–589, 1997.

[122] P. H. Paul, J. A. Gray, J. L. Durant, and J. W. Thoman. A Model for Temperature-dependent Collisional Quenching of NO $A^2\Sigma^+$. *Applied Physics B*, 57(4):249–259, Oct. 1993.

[123] P. H. Paul and H. N. Najm. Planar Laser-induced Fluorescence Imaging of Flame Heat Release Rate. *Symposium (International) on Combustion*, 27(1):43–50, Jan. 1998.

[124] P. Pixner, R. Schiessl, A. Dreizler, and U. Maas. Experimental Determination of PDFs of OH Radicals in IC Engines Using Calibrated Laser-Induced Fluorescence as a Basis for Modelling the End-Phase of Engine Combustion. *Combustion Science and Technology*, 158(1):485–509, 2000.

[125] S. B. Pope. Turbulent Flows, 2001.

[126] S. Popp, F. Hunger, S. Hartl, D. Messig, B. Coriton, J. H. Frank, F. Fuest, and C. Hasse. LES Flamelet-progress Variable Modeling and Measurements of a Turbulent Partially-premixed Dimethyl Ether Jet Flame. *Combustion and Flame*, 162(8):3016–3029, 2015.

[127] L. Rahn, R. Palmer, M. Koszykowski, and D. Greenhalgh. Comparison of Rotationally Inelastic Collision Models for Q-branch Raman Spectra of N_2. *Chemical Physics Letters*, 133(6):513–516, 1987.

[128] Rayleigh. XV. On the Theory of Optical Images, with Special Reference to the Microscope. *Philosophical Magazine Series 5*, 42(255):167–195, 1896.

[129] E. Rea Jr, A. Chang, and R. Hanson. Collisional Broadening of the $A^2\Sigma^+ \leftarrow X^2\Pi$ (0, 0) Band of OH by H_2O and CO_2 in Atmospheric-pressure Flames. *Journal of Quantitative Spectroscopy and Radiative Transfer*, 41(1):29–42, 1989.

[130] A. Rohatgi. Webplotdigitizer: Version 4.3. 2020.

[131] Rolls-Royce Holdings plc. Rolls-Royce unveils all-electric plane targeting the record books. https://www.rolls-royce.com/media/press-releases/2019/19-12-2019-rr-unveils-all-electric-plane-targeting-the-record-books.aspx. Accessed 14-12-2020. Online, Dec. 2019.

[132] J. Rosell, J. Sjöholm, M. Richter, and M. Aldén. Comparison of Three Schemes of Two-photon Laser-induced Fluorescence for CO Detection in Flames. *Applied spectroscopy*, 67(3):314–320, 2013.

[133] L. Sachs. *Angewandte Statistik, Methodensammlung mit R.* Springer, Berlin, 2006.

[134] R. Sadanandan, J. Fleck, W. Meier, P. Griebel, and C. Naumann. 2D Mixture Fraction Measurements in a High Pressure and High Temperature Combustion System Using NO Tracer-LIF. *Applied Physics B*, 106(1):185–196, 2012.

[135] R. Sadanandan, W. Meier, and J. Heinze. Experimental study of signal trapping of OH laser induced fluorescence and chemiluminescence in flames. *Applied Physics B*, 106(3):717–724, 2012.

[136] Safran S.A. Safran and Aviation's Electric Future - A Long Road to All-Electric Aircraft. https://www.safran-group.com/safran-and-aviations-electric-future?page=3. Accessed 14-12-2020. Online.

[137] R. Schießl, P. Pixner, A. Dreizler, and U. Maas. Formaldehyde Formation in the Endgas of Otto Engines: Numerical Simulations and Quantitative Concentration Measurements. *Combustion science and technology*, 149(1-6):339–360, 1999.

[138] P. Schreivogel, C. Abram, B. Fond, M. Straußwald, F. Beyrau, and M. Pfitzner. Simultaneous kHz-rate temperature and velocity field measurements in the flow emanating from angled and trenched film cooling holes. *International Journal of Heat and Mass Transfer*, 103:390–400, Dec. 2016.

[139] A. Schulz. Combustor liner cooling technology in scope of reduced pollutant formation and rising thermal efficiencies. *Annals of the New York Academy of Sciences*, 934(1):135–146, 2001.

[140] C. Schulz, J. Jeffries, D. Davidson, J. Koch, J. Wolfrum, and R. Hanson. Impact of UV Absorption by CO_2 and H_2O on NO LIF in High-Pressure Combustion Applications. *Proceedings of the Combustion Institute*, 29(2):2735–2742, 2002.

[141] J. J. Scrittore, K. A. Thole, and S. W. Burd. Investigation of Velocity Profiles for Effusion Cooling of a Combustor Liner. *Journal of Turbomachinery*, 129(3):518–526, aug 2006.

[142] J. M. Seitzman, J. Haumann, and R. K. Hanson. Quantitative Two-photon LIF Imaging of Carbon Monoxide in Combustion Gases. *Applied optics*, 26(14):2892–2899, 1987.

[143] T. Settersten, A. Dreizler, and R. Farrow. Temperature-and Species-dependent Quenching of CO B Probed by Two-photon Laser-induced Fluorescence Using a Picosecond Laser. *The Journal of chemical physics*, 117(7):3173–3179, 2002.

[144] T. B. Settersten, B. D. Patterson, and W. H. Humphries IV. Radiative Lifetimes of NO $A^2\Sigma^+(v' = 0, 1, 2)$ and the Electronic Transition Moment of the $A^2\Sigma^+ - X^2\Pi$ System. *The Journal of Chemical Physics*, 131(10):104309, 2009.

[145] D. Shin, T. Dreier, and J. Wolfrum. Spatially Resolved Absolute Concentration and Fluorescence-lifetime Determination of H_2CO in Atmospheric-pressure CH_4/air Flames. *Applied Physics B*, 72(2):257–261, 2001.

[146] A. Singh, M. Mann, T. Kissel, J. Brübach, and A. Dreizler. Simultaneous Measurements of Temperature and CO Concentration in Stagnation Stabilized Flames. *Flow, turbulence and combustion*, 90(4):723–739, 2013.

[147] K. Skalska, J. S. Miller, and S. Ledakowicz. Kinetics of Nitric Oxide Oxidation. *Chemical Papers*, 64(2):269–272, 2010.

[148] G. P. Smith, D. M. Golden, M. Frenklach, N. W. Moriarty, B. Eiteneer, M. Goldenberg, C. T. Bowman, R. K. Hanson, S. Song, W. Gardiner Jr, et al. GRI-Mech 3.0. *URL http://www. me. berkeley. edu/gri_mech*, 2011.

[149] K. Smith and A. Fahme. Back Side-Cooled Combustor Liner for Lean-Premixed Combustion. In *Volume 2: Coal, Biomass and Alternative Fuels; Combustion and Fuels: Oil and Gas Applications; Cycle Innovations*. American Society of Mechanical Engineers, jun 1999.

[150] S. Strickler and R. Barnhart. Absolute Vibronic Intensities in the $^1A_2 \leftarrow^1 A_1$ Absorption Spectrum of Formaldehyde. *The Journal of Physical Chemistry*, 86(4):448–455, 1982.

[151] W. Sun, G. Sha, B. Jiang, E. J. Hintsa, and C. Zhang. $M-$ and e/f-symmetry-resolved Cross Sections for CO ($A^1\Pi$)—He/Ar Collision-induced Energy Transfer from $J = 2$ to $J = 1$. *Chemical physics letters*, 218(5-6):515–522, 1994.

[152] M. Tamura, P. A. Berg, J. E. Harrington, J. Luque, J. B. Jeffries, G. P. Smith, and D. R. Crosley. Collisional Quenching of CH(A), OH(A), and NO(A) in Low Pressure Hydrocarbon Flames. *Combustion and Flame*, 114(3-4):502–514, 1998.

[153] S. A. Tedder, J. L. Wheeler, A. D. Cutler, and P. M. Danehy. Width-increased Dual-pump Enhanced Coherent anti-Stokes Raman Spectroscopy. *Applied optics*, 49(8):1305–1313, 2010.

[154] K. A. Thole, M. Gritsch, A. Schulz, and S. Wittig. Effect of a Crossflow at the Entrance to a Film-Cooling Hole. *Journal of Fluids Engineering*, 119(3):533, 1997.

[155] R. Tipping and J. Bouanich. On the Use of Herman–Wallis Factors for Diatomic Molecules. *Journal of Quantitative Spectroscopy and Radiative Transfer*, 71(1):99–103, 2001.

[156] T. D. Varberg and K. M. Evenson. Accurate Far-infrared Rotational Frequencies of Carbon Monoxide. *The Astrophysical Journal*, 385:763–765, 1992.

[157] G. Vedeshkin, E. Sverdlov, and A. Dubovitsky. Experimental Investigation of a Low-Emission Combustor Designed for MID Power Gas Turbine. *AerospaceLab Journal*, Issue 11:June 2016; ISSN: 2107–6596, 2016.

[158] L. Voigt, J. Heinze, T. Aumeier, T. Behrendt, and F. di Mare. Quantitative CO PLIF Measurements in Aeroengine Gas Turbine Combustion Chambers under Realistic Conditions. In *Turbo Expo: Power for Land, Sea, and Air*, volume 50916, page V006T05A004. American Society of Mechanical Engineers, 2017.

[159] L. Voigt, J. Heinze, M. Korkmaz, K. P. Geigle, and C. Willert. Planar measurements of CO concentrations in flames at atmospheric and elevated pressure by laser-induced fluorescence. *Applied Physics B*, 125(5), apr 2019.

[160] G. H. Wang and N. T. Clemens. Effects of Imaging System Blur on Measurements of Flow Scalars and Scalar Gradients. *Experiments in Fluids*, 37(2):194–205, may 2004.

[161] H. Wang, R. Xu, K. Wang, C. T. Bowman, R. K. Hanson, D. F. Davidson, K. Brezinsky, and F. N. Egolfopoulos. A Physics-based Approach to Modeling Real-fuel Combustion Chemistry - I. Evidence from Experiments, and Thermodynamic, Chemical Kinetic and Statistical Considerations. *Combustion and Flame*, 193:502–519, July 2018.

[162] J. Warnatz, U. Maas, and R. W. Dibble. *Verbrennung: Physikalisch-Chemische Grundlagen, Modellierung und Simulation, Experimente, Schadstoffentstehung.* Springer, Berlin [u.a.], 3., aktualisierte und erw. aufl. edition, 2001.

[163] N. Wiberg, E. Wiberg, and A. F. Hollemann. Lehrbuch der Anorganischen Chemie, 101. Auflage, 1995.

[164] K. Wieghardt. *Hot-air discharge for de-icing.* Wright Field, Air Materiel Command, 1946.

[165] C. Willert, M. Schroll, J. Heinze, and T. Soworka. High-speed PIV at the exit of a lean-burn combustion chamber operated at elevated pressure. In C. J. Kähler, R. Hain, S. Scharnowski, and T. Fuchs, editors, *Proceedings of the 13th International Symposium on Particle Image Velocimetry*, 2019.

[166] B. Wurm, A. Schulz, and H.-J. Bauer. A New Test Facility for Investigating the Interaction Between Swirl Flow and Wall Cooling Films in Combustors. In *ASME Turbo Expo 2009: Power for Land, Sea, and Air*, pages 1397–1408, 2009.

[167] B. Wurm, A. Schulz, H.-J. Bauer, and M. Gerendas. Impact of Swirl Flow on the Cooling Performance of an Effusion Cooled Combustor Liner. *Journal of Engineering for Gas Turbines and Power*, 134(12):121503, 2012.

[168] R. Xu, K. Wang, S. Banerjee, J. Shao, T. Parise, Y. Zhu, S. Wang, A. Movaghar, D. J. Lee, R. Zhao, X. Han, Y. Gao, T. Lu, K. Brezinsky, F. N. Egolfopoulos, D. F. Davidson, R. K. Hanson, C. T. Bowman, and H. Wang. A Physics-based Approach to Modeling Real-fuel Combustion Chemistry – II. Reaction Kinetic Models of Jet and Rocket Fuels. *Combustion and Flame*, 193:520–537, July 2018.

[169] Y. B. Zeldovich. The oxidation of nitrogen in combustion and explosions. *Acta Physicochim. USSR*, 21(4):577–628, 1946.

[170] A. Zschutschke, D. Messig, A. Scholtissek, and C. Hasse. Universal Laminar Flame Solver (ULF). 2017.

List of Publications

[E1] M. Agizza, S. Bürkle, L. Becker, M. Greifenstein, G. Bagheri, S. Doost, T. Faravelli, J. Janicka, S. Wagner, and A. Dreizler. Reactor Network Modelling of a Close to Reality Combustor Using Residence Time Measurements. *no. April*, pages 18–21, 2017.

[E2] S. Bürkle, M. Greifenstein, S. Wagner, A. Dreizler, and V. Ebert. Optical Sensing of Turbine Inlet Temperature in a Pressurized Gas Turbine Combustor. In *Laser Applications to Chemical, Security and Environmental Analysis*, pages LT4F–4. Optical Society of America, 2016.

[E3] M. Greifenstein and A. Dreizler. Influence of Effusion Cooling Air on CO+OH Chemistry in a Pressurized Single Sector Model Gas Turbine Combustor. *Publication in Preparation for Submission to Applications in Energy and Combustion Science*, 2020.

[E4] M. Greifenstein and A. Dreizler. Influence of Effusion Cooling Air on the Thermochemical State of Combustion in a Pressurized Model Single Sector Gas Turbine Combustor. *Combustion and Flame*, 226:455–466, Apr. 2021.

[E5] M. Greifenstein and A. Dreizler. Investigation of Mixing Processes of Effusion Cooling Air and Main Flow in a Single Sector Model Gas Turbine Combustor at Elevated Pressure. *International Journal of Heat and Fluid Flow*, 88:108768, Apr. 2021.

[E6] M. Greifenstein and A. Dreizler. MARSFT: Efficient Fitting of CARS Spectra Using a Library Based Genetic Algorithm. *Journal of Raman Spectroscopy*, pages 1–9, 2021.

[E7] M. Greifenstein, J. Heinze, C. Willert, L. Voigt, M. Zedda, C. Richter, and A. Dreizler. Time-resolved Temperature Profile Measurements in the Exhaust of a Single Sector Gas Turbine Combustor at Realistic Operating Conditions. *Experiments in Fluids*, 61(8):1–12, 2020.

[E8] M. Greifenstein, J. Hermann, B. Boehm, and A. Dreizler. Flame–cooling Air Interaction in an Effusion-cooled Model Gas Turbine Combustor at Elevated Pressure. *Experiments in Fluids*, 60(1):10, 2019.

[E9] J. Hermann, M. Greifenstein, B. Boehm, and A. Dreizler. Experimental Investigation of Global Combustion Characteristics in an Effusion Cooled Single Sector Model Gas Turbine Combustor. *Flow, Turbulence and Combustion*, 102(4):1025–1052, 2019.

[E10] T. Li, P. Farmand, C. Geschwindner, M. Greifenstein, J. Köser, C. Schumann, A. Attili, H. Pitsch, A. Dreizler, and B. Böhm. Homogeneous Ignition and Volatile Combustion of Single Solid Fuel Particles in Air and Oxy-fuel Conditions. *Fuel*, 291:120101, May 2021.

[E11] J. Weinkauff, M. Greifenstein, A. Dreizler, and B. Böhm. Time Resolved Three-dimensional Flamebase Imaging of a Lifted Jet Flame by Laser Scanning. *Measurement Science and Technology*, 26(10):105201, 2015.